

Distortion-Induced Fatigue of Rib-to-Crossbeam Joint in Orthotropic Steel Decks

Heng Fang

Doctoral dissertation submitted to obtain the academic degree of
Doctor of Civil Engineering

Supervisor

Prof. Hans De Backer, PhD

Department of Civil Engineering
Faculty of Engineering and Architecture, Ghent University

August 2021



**Distortion-Induced Fatigue of Rib-to-Crossbeam Joint in Orthotropic
Steel Decks**

Heng Fang

Doctoral dissertation submitted to obtain the academic degree of
Doctor of Civil Engineering

Supervisor

Prof. Hans De Backer, PhD

Department of Civil Engineering
Faculty of Engineering and Architecture, Ghent University

August 2021



ISBN 978-94-6355-511-1

NUR 956

Wettelijk depot: D/2021/10.500/59

Members of the Examination Board

Chair

Prof. Patrick De Baets, PhD, Ghent University

Other members entitled to vote

Prof. Bohumil Culek, PhD, Univerzita Pardubice, Czech Republic

Prof. Stijn Hertelé, PhD, Ghent University

Honorary Prof. Philippe Van Bogaert, PhD, Ghent University

Prof. Benjin Wang, PhD, Tongji University, China

Supervisor

Prof. Hans De Backer, PhD, Ghent University

“The universe is big, life is bigger.”

— Sophon, *The Three-Body Problem*

Acknowledgments

Doing a PhD in a medieval city on the other side of the continent is the craziest thing I have ever done in my life. When looking back at this specific moment near the end, the whole journey feels like a jungle hunting adventure, countless traps are waiting underneath the peaceful and harmless appearance. Luckily, I have been always receiving generous help from many sophisticated *hunters*.

First of all, I would like to thank my supervisor Prof. Hans De Backer for giving me the opportunity of pursuing a PhD. During past years, he was always ready to answer my questions, provide all the resources I need, and let me explore the research topic freely. The accomplishment of this dissertation cannot be realized without his great guidance.

Apart from Hans, I would also like to thank the other members of the examination board Prof. Patrick De Baets, Prof. Bohumil Culek, Prof. Stijn Hertelé, Honorary Prof. Philippe Van Bogaert and Prof. Benjin Wang for their valuable comments and suggestions. Special thanks go to Philippe, who kindly shared with me his profound knowledge and vigorous curiosity on history and museology.

The experimental work of this dissertation was performed with the help of Sam, Dave, Nouman and Gilles, which is gratefully acknowledged. The daily assistance from Lien and Ellen on administrative affairs is also gratefully appreciated. In addition, I would like to thank all enthusiastic users from the website Stack Overflow. Because of their unselfish sharing, I was always able to find a solution for the problem I met in programming no matter how strange it is.

When working, I have to deal with all kinds of unanticipated problems alone. While at most of the rest time, fortunately I do not have to. It is my privilege

Acknowledgments

to meet so many amazing people from all over the world. I would never forget those wonderful hours full of laughing and drinks during gatherings, parties or travels with my dear friends. These joyful memories just like sparkling stars that light up my adventure.

For those inevitable most difficult moments, the unconditional love and support from my family make me strong enough to pass through safely. My sincerest acknowledgements go to my parents Jiahua and Yurong. No words can express how much I owe them for bringing me to see the magnificent world.

Finally to the most important person, my lovely girlfriend Jia. The past year 2020 is quite tough. The great pandemic of COVID-19 is out of everyone's thought, which has deeply influenced every person's life on earth forever. However, also due to this crisis, we had more time staying together than ever. Without her accompanying and encouragement, I would never have a chance to finish this work. I cannot wait to hunt the next *monster* with the best teammate I can ever imagine. Let us go!

Heng Fang
7 August 2021

Summary

For long span bridges, the orthotropic steel deck (OSD) is a prior choice for the bridge deck of the main girder. A typical OSD normally has several components such as the steel deck plate, the longitudinal ribs and the horizontal crossbeams, which are combined together by numerous welds. These welds represent geometrical discontinuities that easily cause stress concentrations, which may lead to the fatigue damage under repetitive loading. Majority of previously reported research about OSDs mainly focuses on the rib-to-deck joint, even though fatigue cracks at the rib-to-crossbeam joint are more commonly seen. This indicates that the rib-to-crossbeam joint has not been paid enough attention. At present, the prevailing design of the rib-to-crossbeam joint is a continuous rib of the trapezoidal cross-section passing through the crossbeam with an additional cope hole. It has been discovered that fatigue cracks are likely to initiate from several possible locations, such as the free edge of the cope hole and the weld connecting the rib and the crossbeam. Unfortunately, the fatigue crack that initiates from the lower weld end on the rib wall induced by the rib distortion was more or less ignored before. Although the rib distortion induced fatigue crack controls the fatigue resistance of this joint, the corresponding fatigue detail category is still missing in current Eurocode. Hence, this research endeavors to have a better understanding of the rib distortion behavior and to enhance the fatigue performance of the rib-to-crossbeam joint accordingly.

In the first phase, the influences of different design parameters on the distortional behavior of ribs are investigated. In current major codes, the fatigue life assessments of OSDs are still based on the nominal stress method. However, due to the complex structure of the rib-to-crossbeam joint, it is rather difficult to have a clear definition of the nominal stress. Therefore, the structural hot spot stress method is more suitable and adopted accordingly. Five design parameters in total are analyzed, namely the rib thickness, the rib

distance, the crossbeam height, the crossbeam spacing and the weld length of rib-to-crossbeam joint. Among these parameters, the crossbeam spacing and the weld length of rib-to-crossbeam joint have positive correlations with the distortional stress. The rib thickness has a negative correlation with the distortional stress. The influence of the rib distance on distortional stress depends on the relative size between the width of load area and the rib distance. When considering the load patch size of the fatigue load model from Eurocode in this case, the distortional stress is generally negatively correlated with the rib distance. The crossbeam height does not have an obvious influence on the distortional behavior. Furthermore, based on the influence lines obtained from the parametric analysis, the most unfavorable load position of the distortional stress is determined by the dimensions of ribs, whereas other considered parameters do not show obvious effects. When the rib thickness gets larger, the most unfavorable load position will move towards the investigated crossbeam if other parameters remain the same.

Based on the results of the preliminary parametric analyses, static load tests on a full-scale OSD specimen is performed for validation. A concrete basin was constructed to place the specimen in. The deck plate is aligned with the road surface to allow for the real vehicle loading. To deal with the abnormal results of the raw data from measurements, especially for strain gauges applied at the high stress gradient area, the assumption that the deviations of strains are linearly dependent on time is proven to be efficient in eliminating the possible interfering signal of the measurements results. According to the measurement results, the most unfavorable load position as well as the positive correlation between the weld length of rib-to-crossbeam joint and the distortional stress are verified.

At the same time, the corresponding numerical simulations of the static load tests are conducted using the finite element analysis software Siemens NX. Initially, the solid element is selected. Through writing the manuscript of NX Open, one node is precisely defined at every location of a strain gauge for the convenience of exporting results. In general, similar trends as the measurement results are acquired. The calculation results of strain gauges that are far away from the stress concentration zone fit well with the measurement results. However, obviously divergent results appeared on strain gauges close to the weld toe. After the investigation of several possible factors, it is concluded that the deviation of strain gauges' locations and the deviation of load positions are the main causes that lead to the differences between measurement results and calculation results. Furthermore, it is found that the most unfavorable horizontal load position is not at the center between two ribs as considered before. If the center of tire load moves from the center between two ribs towards the rib-to-deck joint of the target rib, the distortional stress of the target rib

will first increase then decrease. Whereas the distortional stress at the adjacent rib will drop dramatically. This may be the explanation to the phenomenon that the differences between two ribs are larger in measurement results than in calculation results.

After validating the numerical models, fatigue life assessments based on influence lines are finished. During the assessments, it is assumed that the passing lorries will always drive along the same route. Results of the fatigue life assessments show that even through raising the termination location of cope hole on rib wall would decrease the distortional stress, its influence on the estimated fatigue life is still limited. Similarly, when the center of the tire load is divergent from the center between ribs, the distortional stress at the corresponding rib-to-crossbeam joint may be influenced, but the estimated fatigue life is only slightly affected.

In the next phase, the possibility of canceling the cope hole for the rib-to-crossbeam joint is discussed. On the one hand, the current prevailing design of the rib-to-crossbeam joint (i.e. the trapezoidal rib with additional cope holes) heavily relies on the manual welding. As a consequence, not only relevant fabrication costs are quite high but also the imperfections induced during fabricating procedures seem to be unavoidable. The introduced imperfections become the weak points where fatigue cracks initiate and decrease the fatigue performance of the joint. On the other hand, recently accomplished fatigue tests of OSD specimens with tight-fitted rib-to-crossbeam joints (i.e. without cope holes) indicate its high fatigue performance. Developed fabrication techniques such as the computerized numerical control cutting and the automatically robotic welding make the manufacturing of this joint type easier and more reliable.

Different modeling methods using the shell element and the solid element with or without the weld modeled are first compared. It shows that the shell element model and the solid element model would generate similar results under such conditions: a) the weld is modeled in the solid element model while omitted in the shell element model; and b) the distance from the weld toe to the reference point on the rib wall should be calculated from the corner point of the rib-to-crossbeam intersection. The results of the shell element model tend to be higher than the solid element model when getting closer to the intersection point of rib and crossbeam. Thus, the result of the shell element model may be more conservative when adopting the hot spot stress method.

Secondly, parametric analyses of the tight-fitted rib-to-crossbeam joint are performed. It is found that the most critical position for the rib-to-crossbeam joint without cope holes is at the curvature on the rib side. Increasing the thickness of the rib could reduce the maximum stress range on the rib side

meanwhile changing the stress distribution on the crossbeam side. When the thickness of deck increases, the maximum stress ranges on both sides decrease in general. The radius of rib has a local influence on the points at the curvature. A larger radius could effectively lower the maximum stress range. Lastly, the thickness of the crossbeam and the maximum stress range on the crossbeam side have an obvious negative correlation. A more flexible crossbeam, i.e. decreasing its thickness, would reduce the maximum stress range at the bottom of ribs on the rib side.

To include the influence of the stochastic traffic flow, fatigue life assessments based on influence surfaces are finished. The simulation procedure is programmed in Python. A normal distribution of vehicles is fitted in accordance with Eurocode. Relevant results show that the fatigue performance of the rib-to-crossbeam joint is sensitive to the position of the central line of the load distribution. For the rib-to-crossbeam joint with cope holes, it is preferred to place the central line of the load distribution closer to the center of the rib. In contrast, for the tight-fitted rib-to-crossbeam joint, it is preferred to place the central line of the load distribution closer to the center between two ribs. However, the load distribution mainly affects the controlling points on the rib side for both types of joints. Neither the rib dimensions nor the load distribution has an obvious improvement on the fatigue-prone details along the free edge of the cope hole. Hence, considering less possible fatigue-prone locations and reduced fabrication costs, the overall performance of the optimized tight-fitted rib-to-crossbeam joint is better.

In the last part of this research, a simplified calculation method for quick determining the dimensions of OSDs is developed. This method shares the same notion as the Pelikan-Esslinger method, which uses an idealized orthotropic plate to represent the actual OSD. By solving the idealized orthotropic plate, an approximation of the internal forces of the actual OSD may be acquired. In order to calculate the distortional stress, the shear deformation is treated as an independent variable and added to the simplified calculation method. The system of partial differential equations is derived through the equilibrium relationships of the substituting plate. Three rigidity coefficients are required in this method, namely the flexural rigidity coefficient, the torsional rigidity coefficient and the shear rigidity coefficient. The former two coefficients are the same as in the Pelikan-Esslinger method. By performing a frame analysis, the formulas of the shear rigidity coefficient are achieved. The solutions of the system of the partial differential equations are acquired by using the symbolic computing software Maple. Then, a simple local model is proposed for calculating the nominal distortional stress at the target point, which is under the lower weld end on the rib wall. All of the formulas for the simplified calculation method have been packed into three Python classes for the convenience of using.

Relevant codes generated during this research are provided in appendix for reference. To summarize, this research shows the possibility of optimizing the prevailing design of the rib-to-crossbeam joint in OSDs. The proposed fatigue life assessment method and simplified calculation method could be adopted by bridge designers in the future.

Samenvatting

Voor bruggen met een grote overspanning is het orthotrope stalen dek (OSD) een veelgebruikt type brugdek. Een typische OSD bestaat uit meerdere componenten, zoals de stalen dekplaat, de langsribben en de horizontale dwarsbalken. Deze worden door talrijke lassen met elkaar gecombineerd. De lassen vertegenwoordigen geometrische discontinuïteiten die belangrijke spanningsconcentraties veroorzaken, die vaak leiden tot vermoeiingsschade bij cyclische belasting. De meerderheid van het eerder gerapporteerd onderzoek naar OSD's richt zich op de langsverstijver-dekplaat, hoewel verveeiingsscheurtjes bij de langsverstijver -verbinding vaker worden opgemerkt. Dit geeft aan dat er niet voldoende aandacht is besteed aan de rib-tot-dwarsbalk. Op dit moment is het vaakst voorkomende ontwerp voor de verbinding tussen de ribben en dwarsbalk een doorlopende rib met een trapeziumvormige dwarsdoorsnede die door de dwarsbalk gaat met de hulp van een uitsnijding. Er is ontdekt dat vermoeiingsscheuren mogelijk ontstaan op verschillende locaties, zoals de vrije rand van de uitsnijdingen de las die de rib en de dwarsbalk verbindt. Helaas werd de vermoeiingsscheur die begint vanaf het onderste lasuiteinde op de ribwand, veroorzaakt door ribvervorming, voorheen min of meer genegeerd. Hoewel de vermoeiingsscheur door de ribvervorming de vermoeiingsweerstand van deze verbinding bepaalt, ontbreekt het corresponderende vermoeiingsdetail nog steeds in de huidige Eurocode. Daarom tracht dit doctoraat onderzoek een beter begrip te krijgen van het vervormingsgedrag van de ribben en als dusdanig het vermoeiingsgedrag van de rib-dwarsbalkverbinding te verbeteren.

In de eerste fase wordt de invloed van de verschillende ontwerpparameters op het vervormingsgedrag van ribben onderzocht. In de huidige ontwerpcodes zijn de beoordelingen van de levensduur van OSD's nog steeds gebaseerd op de nominale spanningsmethode. Vanwege de complexe structuur van de rib

-dwarsbalk-verbinding is het echter nogal moeilijk om een duidelijke definitie van de nominale spanning te vinden. Daarom is de structurele hotspot-stressmethode geschikter en wordt deze vaak toegepast. In totaal worden vijf ontwerpparameters geanalyseerd, namelijk de ribdikte, de ribafstand, de dwarsbalkhoogte, de dwarsbalkafstand en de laslengte van de rib-dwarsbalkverbinding. Van deze parameters heeft de afstand tussen de dwarsbalk en de laslengte van de verbinding tussen de ribben en de dwarsbalk een positieve correlatie met de spanning. De ribdikte heeft een negatieve correlatie met de spanning. De invloed van de ribbenafstand op de spanning hangt af van de relatieve grootte van de breedte van het laadgebied tot de ribafstand. Wanneer in dit geval het vermoeiingsbelastingsmodel van de Eurocode beschouwd wordt, is de spanning over het algemeen negatief gecorreleerd met de ribafstand. De hoogte van de dwarsbalk heeft geen duidelijke invloed op het vervormingsgedrag. Bovendien wordt op basis van de invloedslijnen die zijn verkregen met behulp van de parametrische analyse, de meest ongunstige belastingspositie van de spanningen bepaald door de afmetingen van de ribben. Dit terwijl de parameters die in overweging worden genomen geen duidelijk effect hebben. Als de ribdikte groter wordt, zal de meest ongunstige laadpositie naar de onderzochte dwarsbalk verschuiven als alle andere parameters hetzelfde blijven.

Op basis van de resultaten van de voorlopige parametrische analyses worden statische belastingstests uitgevoerd op een OSD-monster op ware grootte voor validatie. Er werd een betonnen kelder gebouwd om het exemplaar in te plaatsen. De dekplaat is uitgelijnd met het wegdek om een werkelijke belasting door een voertuig mogelijk te maken. Om abnormale resultaten van de ruwe meetgegevens te detecteren, met name voor rekstrookjes die worden toegepast in het gebied met hoge spanningsconcentraties, is het zo dat afwijkingen van de spanningen lineair afhankelijk zijn van de tijd, wat het elimineren van mogelijke storende meetresultaten toelaat. Door middel van de meetresultaten worden de meest ongunstige belastingsposities en de positieve correlatie tussen de laslengte van de rib-dwarsbalkverbinding en de spanning geverifieerd.

Tegelijkertijd worden de overeenkomstige numerieke simulaties van de statische belastingstests uitgevoerd met behulp van de eindige-elementenanalyse software Siemens NX. Aanvankelijk wordt een solid element geselecteerd. Door de variant van NX Open te gebruiken, wordt één knooppunt nauwkeurig gedefinieerd op elke locatie van een rekstrook voor de eenvoud van het exporteren van de resultaten. Over het algemeen worden vergelijkbare trends als bij de meetresultaten verkregen. De rekenresultaten van rekstrookjes die verwijderd zijn van de spanningsconcentratiezone sluiten goed aan bij de meetresultaten. Er verschenen echter duidelijk uiteenlopende resultaten bij rekstrookjes dicht bij de lasnaad. Na onderzoek van de verschillende mogelijke factoren wordt geconcludeerd dat de afwijking van de locatie van de rekstrookjes

en de afwijking van de belastingspositie de belangrijkste oorzaken zijn die leiden tot verschillen tussen meetresultaten en rekenresultaten. Verder blijkt dat de meest ongunstige horizontale laadpositie niet zoals eerder aangenomen in het midden tussen twee ribben ligt. Als het midden van de wielbelasting van het midden tussen twee ribben naar de rib -dekverbinding van de doelrib beweegt, zal de spanning van de doelrib eerst toenemen en dan afnemen. Terwijl de spanning op de aangrenzende rib dramatisch zal afnemen. Dit kan de verklaring zijn voor het fenomeen dat de verschillen tussen twee ribben groter zijn in de meetresultaten dan in de rekenresultaten.

Na validatie van de numerieke modellen, worden de levensduurbeoordelingen vermoeiing op basis van invloedslijnen afgerond. Bij de beoordelingen wordt ervan uitgegaan dat de passerende vrachtwagens altijd op hetzelfde traject zullen rijden. De resultaten van de beoordelingen van de vermoeiingslevensduur laten zien dat zelfs als de eindlocatie van het uitsnijding op de ribwand de vervormingsspanning zou verminderen, de invloed ervan op de geschatte levensduur van de vermoeidheid nog beperkt is. Eveneens kan, wanneer het midden van de wielbelasting afwijkt van het midden tussen de ribben, de vervormingsspanning bij de corresponderende rib- dwarsbalkverbinding worden beïnvloed, maar wordt de geschatte levensduur door vermoeiing slechts in geringe mate beïnvloed.

In de volgende fase wordt de mogelijkheid besproken om de uitsnijding voor de rib-dwarsbalk-verbinding op te heffen. Enerzijds is het huidige ontwerp van de dwarsbalkverbinding sterk afhankelijk van handmatig lassen. Als gevolg hiervan zijn niet alleen de relevante fabricagekosten vrij hoog, maar lijken ook onvolkomenheden die tijdens fabricageprocedures worden veroorzaakt onvermijdelijk te zijn. De geïntroduceerde onvolkomenheden worden de zwakke punten waar vermoeiingscheuren de vermoeiingsprestaties van het detail initiëren en verminderen. Aan de andere kant duiden recent uitgevoerde vermoeiingstests van OSD-monsters met nauw aansluitende rib-dwarsbalkverbindingen (d.w.z. zonder uitsnijdingen) op hoge vermoeidheidsprestaties. Ontwikkelde fabricagetechnieken zoals computergestuurd snijden met numerieke besturing en het automatisch robotlassen maken de fabricage van dit type verbinding gemakkelijker en betrouwbaarder.

Allereerst worden dan verschillende modelleermethoden met schaalementen en massieve elementen met of zonder gemodelleerde las, vergeleken. Het toont aan dat het schaal elementmodel en het volume-elementmodel consistente resultaten zouden genereren onder gelijkaardige omstandigheden: a) de las wordt gemodelleerd in het volume-elementmodel terwijl deze weggelaten wordt in het schaalementmodel; en b) de afstand van de lasteen tot het referentiepunt op de ribwand moet worden berekend vanaf het hoekpunt van het snijpunt

van de ribbe met de dwarsbalk. De spanningen van het schaalementmodel zijn meestal hoger dan het volume-elementmodel wanneer men dichterbij het snijpunt van rib en dwarsbalk komt. Het resultaat van het schaalementmodel kan dus conservatiever zijn bij het toepassen van de hotspot-stressmethode.

Ten tweede worden parametrische analyses van de nauwsluitende rib-dwarsbalkverbinding uitgevoerd. Gebleken is dat de meest kritische positie voor de rib-dwarsbalkverbinding zonder uitsnijding de kromming aan de ribzijde is. Het vergroten van de dikte van de rib zou het maximale spanningsbereik aan de ribzijde kunnen verkleinen, terwijl ook de spanningsverdeling op de dwarsbalkzijde kan veranderen. Wanneer de dikte van het dek toeneemt, neemt het maximale spanningsbereik aan beide zijden in het algemeen af. De ribstraal heeft een lokale invloed. De grotere straal zou het maximale spanningsbereik effectief kunnen verlagen. Ten slotte hebben de dikte van de dwarsbalk en het maximale spanningsbereik aan de dwarsbalkzijde een duidelijk negatieve correlatie. Een flexibeler dwarsbalk, d.w.z. een kleinere dikte, zou het maximale spanningsbereik aan de onderkant van de ribben aan de ribzijde verkleinen.

Om de invloed van een stochastische verkeersstroom mee te nemen, worden de vermoeingslevensduurbeoordelingen op basis van invloedsoppervlakken afgerond. De simulatieprocedure is geprogrammeerd in Python. Een normale verdeling van voertuigen is aangebracht in overeenstemming met de Eurocode. Relevante resultaten laten zien dat de vermoeingsprestaties van de rib-dwarsbalkverbinding gevoelig zijn voor de positie van de hartlijn van de lastverdeling. Voor de rib-dwarsbalkverbinding met uitsnijdingen is het voordelig om de hartlijn van de lastverdeling dichterbij het midden van de rib te plaatsen. Daarentegen heeft het voor de nauw aansluitende rib-dwarsbalk verbinding de voorkeur om de hartlijn van de lastverdeling dichterbij het midden tussen twee ribben te plaatsen. De belastingverdeling heeft echter vooral invloed op de controlepunten aan de ribzijde voor beide types verbindingen. Noch de ribafmetingen, noch de belastingverdeling hebben een duidelijke verbetering ten opzichte van de details die gevoelig zijn voor vermoeing langs de vrije rand van het boorgat. Gezien het kleiner aantal mogelijke locaties die gevoelig zijn voor vermoeing en de lagere fabricagekosten, zijn de algehele prestaties van de geoptimaliseerde nauwsluitende rib-dwarsbalkverbinding dus beter.

In het laatste deel van dit onderzoek is een vereenvoudigde rekenmethode ontwikkeld om snel de dimensies van OSD's te bepalen. Deze methode deelt hetzelfde basisidee als de Pelikan-Esslinger-methode, waarbij een geïdealiseerde orthotrope plaat wordt gebruikt om de werkelijke OSD weer te geven. Door de geïdealiseerde orthotrope plaat wiskundig op te lossen, kunnen de interne krachten van de werkelijke OSD worden verkregen.

Om de spanningen te berekenen, wordt de afschuifvervorming behandeld als een onafhankelijke variabele en toegevoegd aan de vereenvoudigde berekeningsmethode. Het systeem van partiële differentiaalvergelijkingen wordt afgeleid. Bij deze methode zijn drie stijfheidscoëfficiënten vereist, namelijk de buigstijfheidscoëfficiënt, de torsiestijfheidscoëfficiënt en de afschuifstijfheidscoëfficiënt. De eerste twee coëfficiënten zijn dezelfde als bij de Pelikan-Esslinger-methode. Door een raamwerkanalyse uit te voeren, worden de formules van de afschuifstijfheidscoëfficiënt afgeleid. De oplossing van het systeem van de partiële differentiaalvergelijkingen worden verkregen met behulp van de computersoftware Maple. Vervolgens wordt een eenvoudig lokaal model voorgesteld voor het berekenen van de nominale spanning op het punt, dat zich onder het onderste lasuiteinde op de ribwand bevindt. Alle formules voor de vereenvoudigde berekeningsmethode zijn voor het gebruiksgemak verpakt in drie Python-klassen.

Relevante codes die tijdens dit onderzoek zijn gegenereerd, worden ter referentie in de bijlage verstrekt. Samenvattend toont dit onderzoek de mogelijkheid aan om het heersende ontwerp van de rib-dwarsbalkverbinding in OSD's te optimaliseren. De voorgestelde methode voor het beoordelen van de vermoeiingslevensduur en de vereenvoudigde berekeningsmethode zouden in de toekomst door brugontwerpers kunnen worden overgenomen.

Nomenclature

Symbols

A	area enclosed by a rib	$[mm^2]$
a	crack length; upper width of the rib	$[mm]$
α	rotational angle about X axis	$[rad]$
α_n	parameter of the general solution	$[-]$
β	rotational angle about Y axis	$[rad]$
β_n	parameter of the general solution	$[-]$
C	constant depending on detail category; parameter depending on material	$[-]$
$C1_{mn}$	parameter of the particular solution	$[-]$
$C1_n$	integration coefficient of the general solution	$[-]$
$C2_{mn}$	parameter of the particular solution	$[-]$
$C2_n$	integration coefficient of the general solution	$[-]$
$C3_n$	integration coefficient of the general solution	$[-]$
$C4_n$	integration coefficient of the general solution	$[-]$
ΔK_{sif}	stress intensity factor range	$[-]$
ΔK_{th}	threshold stress intensity factor value	$[-]$
$\Delta\sigma$	constant amplitude stress range	$[MPa]$
$\Delta\sigma_D$	constant amplitude fatigue limit	$[MPa]$
e	gap between two adjacent ribs	$[mm]$
η_n	parameter of the general solution	$[-]$
h_j	vertical height of the rib	$[mm]$
h_w	actual length of the rib wall	$[mm]$
I_R	moment of inertia of one rib	$[mm^4]$
j	bottom width of the rib	$[mm]$

Nomenclature

κ_n	carry-over factor	[-]
K_c	critical stress intensity factor	[-]
K_s	stress concentration factor	[-]
K_{sif}	stress intensity factor	[-]
K_{xy}	torsional rigidity coefficient	[Nmm]
K_{xz}	shear rigidity coefficient	[N]
K_y	flexural rigidity coefficient	[Nmm]
l_{pl}	length of the load patch	[mm]
l_{pw}	width of the load patch	[mm]
m	inverse of the slope of S-N curve; parameter depend on material	[-]
M_{xy}	torsional moment per unit width in the X direction	[Nmm]
M_y	bending moment per unit width in the X direction	[Nmm]
n	number of load cycles	[-]
N	number of cycles	[-]
Q_{1d}	1-D Fourier series of tire load	[-]
Q_{2d}	2-D Fourier series of tire load	[-]
r	effective radius	[mm]
ρ	rotational angle about Z axis	[rad]
σ_{cc}	stress perpendicular to normal direction of cope hole	[MPa]
σ_{eqv}	equivalent stress	[MPa]
σ_{hs}	(structural) hot spot stress	[MPa]
σ_{lr}	longitudinal stress on rib wall	[MPa]
σ_{nom}	nominal stress	[MPa]
σ_{tc}	stress perpendicular to weld toe on crossbeam	[MPa]
σ_{vr}	vertical stress on rib wall	[MPa]
σ_x	normal stress in the X direction	[MPa]
σ_y	normal stress in the Y direction	[MPa]
t	plate thickness	[mm]
t_d	thickness of the deck	[mm]
t_r	thickness of the rib	[mm]
τ_{xy}	shear stress in the XY plane	[MPa]
τ_{xz}	shear stress in the XZ plane	[MPa]
u_0	horizontal displacement of the middle surface	[mm]
v_0	horizontal displacement of the middle surface	[mm]
V_{xz}	shearing force per unit width in the Y direction	[N]
V_{yz}	shearing force per unit width in the X direction	[N]
w_0	vertical displacement of the middle surface	[mm]
x_p	X coordinate of the load center	[mm]
y_p	Y coordinate of the load center	[mm]
ζ_n	parameter of the general solution	[-]

Abbreviations

AISC	American Institute of Steel Constructions
API	Application Programming Interface
CAFL	Constant Amplitude Fatigue Limit
CJP	Complete Joint Penetration
DBN	Dynamic Bayesian Network
DOF	Degree of Freedom
FEA	Finite Element Analysis
GUI	Graphical User Interface
HPC	High Performance Concrete
IIW	International Institute of Welding
OSD	Orthotropic Steel Deck
PE	Pelikan-Esslinger (method)
SCF	Stress Concentration Factor
SIF	Stress Intensity Factor
UHPC	Ultra-High Performance Concrete

Contents

- Symbols xv
- Abbreviations xvii

- 1 Introduction 1**
- 1.1 Brief history of orthotropic steel decks 2
- 1.2 Outline 4

- 2 Fatigue in OSDs 5**
- 2.1 Overview of fatigue problems in OSDs 6
- 2.2 Fatigue behavior of the rib-to-crossbeam joint 7
 - 2.2.1 Continuous ribs with cope holes 7
 - 2.2.2 Continuous ribs without cope holes 8
 - 2.2.3 Discontinuous ribs fitted between crossbeams 9
- 2.3 Mechanical behavior of the rib-to-crossbeam joint 10
 - 2.3.1 In-plane behavior of the crossbeam 11
 - 2.3.2 Out-of-plane behavior of the crossbeam 11
 - 2.3.3 Rib distortion 12
- 2.4 Fatigue life assessment methods 13
 - 2.4.1 Approaches based on S-N curves 13
 - 2.4.2 Approaches based on fracture mechanics 25
 - 2.4.3 Other approaches 27
- 2.5 Structural optimizations 28
 - 2.5.1 Using bulkheads or other attachments 28
 - 2.5.2 Optimizing the cope hole shape 31
 - 2.5.3 Applying post weld improvement 33
 - 2.5.4 Introducing global reinforcement system 37
- 2.6 Aim and objectives 39

- 3 Parametric analysis 41**
- 3.1 Introduction 42
- 3.2 Finite element model 43

- 3.3 Boundary condition and load cases 46
- 3.4 Results and discussion 48
 - 3.4.1 First analysis 48
 - 3.4.2 Second analysis 54
- 3.5 Conclusions 58

- 4 Experimental study 61**
- 4.1 Introduction 62
- 4.2 Instrumentation of tests 64
- 4.3 Load cases and test procedure 70
- 4.4 Data processing 72
- 4.5 Results and discussion 74
- 4.6 Conclusions 80

- 5 Numerical simulation of experiments 83**
- 5.1 Introduction 84
- 5.2 FEA models 84
 - 5.2.1 Method for defining specific nodes 84
 - 5.2.2 Mesh sensitivity tests 86
- 5.3 Post-processing of the calculation results 87
- 5.4 Calculation results 88
- 5.5 Background of differences between measurements and calculations 92
 - 5.5.1 Different boundary condition 93
 - 5.5.2 Different weld shape and size 93
 - 5.5.3 Deviation of load position 95
 - 5.5.4 Deviation of strain gauge position 98
- 5.6 Fatigue assessment based on influence lines 100
 - 5.6.1 Influence lines of different weld length 102
 - 5.6.2 Influence lines of different horizontal load position 103
 - 5.6.3 Estimated fatigue life 104
- 5.7 Conclusions 108

- 6 Structural optimization 111**
- 6.1 Motivation 112
- 6.2 Comparison of different modeling method 116
 - 6.2.1 Different models 117
 - 6.2.2 Results and discussion 118
- 6.3 Parametric study 120
 - 6.3.1 FEA model 120
 - 6.3.2 Boundary conditions and load cases 123
 - 6.3.3 Results and discussion 123
- 6.4 Structural optimization 131
 - 6.4.1 Fatigue life assessment based on influence surfaces 135

6.4.2	Results and discussion	146
6.5	Conclusions	154
7	Investigation of simplified calculation method	157
7.1	Introduction	158
7.2	Analytical model	159
7.2.1	Basic assumptions	159
7.2.2	Relevant expressions	160
7.2.3	Equilibrium equations	162
7.2.4	Relationships between stress, strain and displacement	164
7.2.5	Rigidity coefficients	165
7.2.6	Partial differential equations	170
7.2.7	Carry-over factor	176
7.2.8	Influence line	178
7.2.9	Local model	179
7.3	Case study	180
7.3.1	Trial calculation using the analytical method	180
7.3.2	Comparison of results from analytical method and FEA	187
7.4	Conclusions	191
8	Conclusions and future research	193
8.1	Conclusions	194
8.2	Future research	200
A	Manuscripts and templates	203
A.1	Process measurement data	204
A.2	Generate nodes at specific coordinates	205
A.2.1	Required template of NX Open	205
A.2.2	Coordinate transformation for large amount of points	206
A.3	Export results using NX Open	208
A.4	Class <code>FatigueLoadModel4</code>	211
A.5	Functions for fatigue life assessment	213
A.6	Example of simulation procedure	218
A.7	Analytical method	221
A.7.1	Class <code>TrapezoidalSection</code>	221
A.7.2	Class <code>LoadCase</code>	225
A.7.3	Class <code>AnalyticalModel</code>	226
B	Supplementary calculation results	233

1

Introduction

1.1 Brief history of orthotropic steel decks

The early prototypes of orthotropic steel decks (OSD) can be traced back to the 1930s. Similar steel bridge deck systems appeared in Germany and the United States at almost the same time. In Germany, a light steel bridge was designed by engineer Leonhardt (Weber, 2012), as shown in Figure 1.1(a). The steel deck plate was supported by a grid composed of L-section beams in the longitudinal direction and closely spaced transverse stiffeners. While the strength of the steel plate was still ample, the deck was subjected to large local deflections which caused cracking in the asphalt wearing surface. Meanwhile in the United States, the *battle deck floor* system (Lyse & Madsen, 1938) was introduced by the American Institute of Steel Construction (AISC) in an attempt to reduce the dead weight of highway bridges as presented in Figure 1.1(b). The deck plate was welded together with longitudinal I-beams. The local wheel loads introduced to the deck plate were transmitted to the main girders through transverse stiffeners or crossbeams. By that time, the design of the battle deck floor was quite conservative and uneconomic since all structural components were treated separately to achieve a simple analysis.

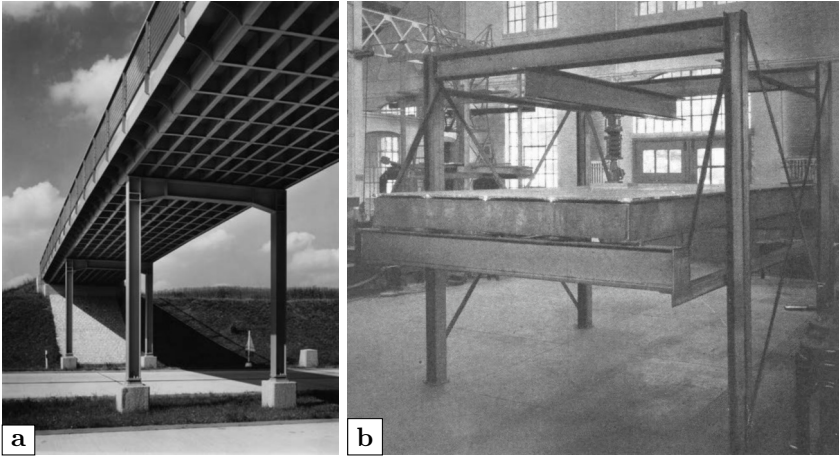


Figure 1.1: Early prototypes of OSDs: (a) fly-over in German; (b) experiments of a battle deck floor in the United States

After the second World War, the principle of OSDs became more and more prevailing to deal with the insufficient supply of steel. Compared with prewar bridges, the steel consumption was reduced by 50%. The merits of OSDs, which are well-known nowadays e.g. the light self-weight, rapid construction speed, high load carrying capacity, etc. were also gradually discovered. Benefiting from these merits, OSDs become an excellent choice not only for long span bridges

but also for movable bridges of short spans, both of which require a light main girder. This can be proven by recent applications of OSDs, as presented in Figure 1.2.

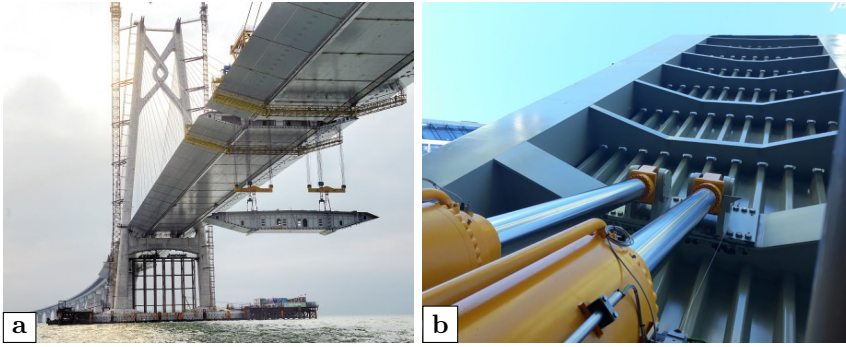


Figure 1.2: Recent applications of OSDs: (a) Hongkong-Zhuhai-Macau bridge in China; (b) movable bridge in the United Kingdom

After decades of evolution, two basic types of longitudinal ribs are used nowadays, namely the open ribs (e.g. bulb cross-sections) and the closed ribs (e.g. trapezoidal cross-sections) as shown in Figure 1.3. The characteristic difference between open and the closed ribs is their resistance to torsion. The torsional rigidity of the closed ribs is considerable, while that of the open ribs is very small (AISC, 1963). Nowadays, the trapezoidal cross-section is the most popular cross-section for longitudinal ribs which represents almost half of the total types of longitudinal ribs used in OSDs (Kolstein, 2009).

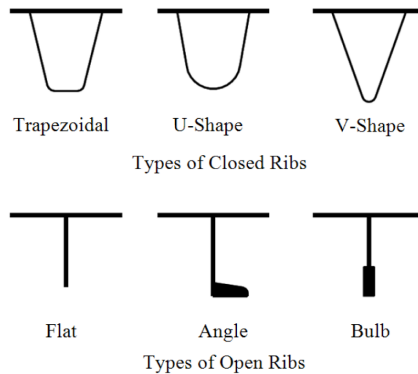


Figure 1.3: Typical rib types for OSDs including closed and open ribs

1.2 Outline

Chapter 2 starts with an overview of the fatigue problem in OSDs. Then, a literature review of recent research is given with the emphasis placed on the rib-to-crossbeam joint.

Chapter 3 presents the parametric analyses about a number of classical design parameters of OSDs to clarify their influences on the stress concentrations induced by rib distortion.

Chapter 4 shows a series of static load tests on a full-scale OSD specimen, which were conducted with the purpose of validating the acquired results of the parametric analyses.

Chapter 5 gives the corresponding numerical simulations of the tests. Possibilities that may lead to the differences between the measurement results and calculation results are also discussed. After validating the numerical models, the fatigue life assessments based on influence lines are introduced.

Chapter 6 discusses the possibility of canceling the cope hole for rib-to-crossbeam joints to deal with the fatigue problem induced by rib distortion. Firstly, different modeling methods are compared. Secondly, parametric analyses of tight-fitted rib-to-crossbeam joints are performed. Lastly, fatigue life assessments of different rib-to-crossbeam joints are conducted considering the stochastic traffic flow.

Chapter 7 introduces a simplified calculation method for the estimation of stress concentrations in the prevailing design with cope holes.

Chapter 8 summarizes the findings of this research and the recommendations for future research.

Appendix A exhibits the source code of programs generated for different tasks during this research.

Appendix B exhibits part of the calculated influence surfaces of rib-to-crossbeam joints with or without cope holes from the models used in chapter 6.

2

Fatigue in OSDs

2.1 Overview of fatigue problems in OSDs

At the time when OSDs were developed, it was already known that steel structures with fluctuating stresses might suffer from fatigue (Leendertz, 2008). In 1971, the first observation of fatigue cracks in an OSD structure was reported about the Severn bridge in the United Kingdom (S Chatterjee, 1992). Wolchuk (1990) stated that these cracks were caused by inappropriate details and welds not suitable for transmitting stresses between the deck components at the intersections of the discontinuous ribs with the floor beams and at the rib-to-deck welds. Ever since that moment, a great amount of fatigue damage had been found in OSD structures all around the world. These fatigue cracks may be divided into four main categories (de Jong, 2007) as shown in Figure 2.1:

- ① cracks in the weld connecting two ribs;
- ② cracks in the longitudinal weld between deck plate and rib wall;
- ③ cracks in the connection between rib and crossbeam;
- ④ cracks in the deck plate.

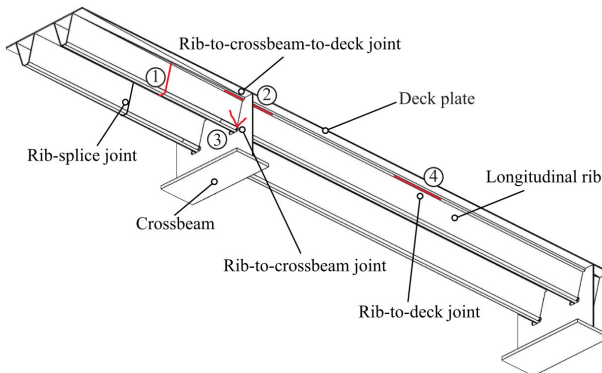


Figure 2.1: Typical fatigue-prone locations (adapted from Nagy (2017))

At present, most of the reported research about the OSDs focuses on the rib-to-deck joint. This joint is considered to be the most dangerous one since the fatigue cracks in this connection remain undetectable by visual inspection unless the resulting damage of the wearing courses becomes visible (Nagy, 2017). Nevertheless, fatigue cracks that happened in the rib-to-crossbeam joint may be evenly common. According to Yokozeki (2017), investigations of Japanese urban expressways detected approximately 7000 and 3500 cracks in closed-rib and open-rib OSDs respectively, and 41% and 91% of these cracks were found

in the longitudinal rib to transverse rib (i.e. crossbeam) connections separately. Therefore, the rib-to-crossbeam joint could be considered as the most vulnerable detail that has not drawn enough attentions.

2.2 Fatigue behavior of the rib-to-crossbeam joint

The rib-to-crossbeam joint is the most complex joint in the OSD structure as two highly stressed members cross each other, and it is impossible to provide a continuous load path for both (Kolstein, 2009). Accompanying the development of OSDs, different designs of the rib-to-crossbeam joint have been used. As stated in section 1.1, this research mainly focuses on the longitudinal rib with a trapezoidal cross-section since this rib type represents the majority of OSD applications at present. Generally, the designs of the rib-to-crossbeam joint can be divided into two main categories, which are

- continuous ribs passing through the crossbeam, with or without an additional cope hole;
- discontinuous ribs fitted between crossbeams.

2.2.1 Continuous ribs with cope holes

The designs of continuous ribs passing through the crossbeam with an additional cope hole take the largest proportion of designs nowadays. As illustrated in Figure 2.2, the weld can either be a two-sided fillet weld or a complete joint penetration (CJP) weld with termination ground smooth. The fabrication cost of the fillet weld is less but the CJP weld offers superior fatigue strength for rib wall distortional cracking (Connor *et al.*, 2012). To utilize the fillet weld, the rib may require stiffening or the spacing of the crossbeams may require reduction.

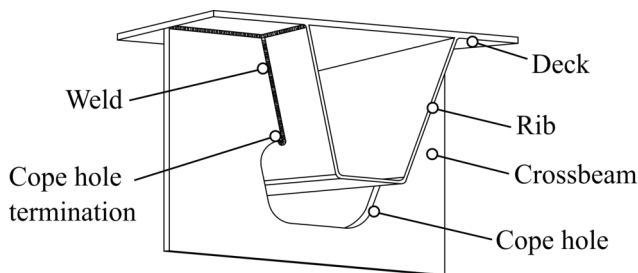


Figure 2.2: Continuous ribs with copes holes

According to previous research (Connor *et al.*, 2012; Kolstein, 2009; Leendertz, 2008), the following modes of fatigue cracking would possibly appear when adopting this design:

- vertical cracks in the rib wall starting from the weld toe (Figure 2.3(a));
- longitudinal cracks in the rib wall starting from the weld end at the weld toe of the cope hole termination (Figure 2.3(b));
- cracks in the crossbeam starting from the weld toe of the cope hole termination (Figure 2.3(c));
- cracks in the crossbeam at the free edge of cope hole (Figure 2.3(d)).

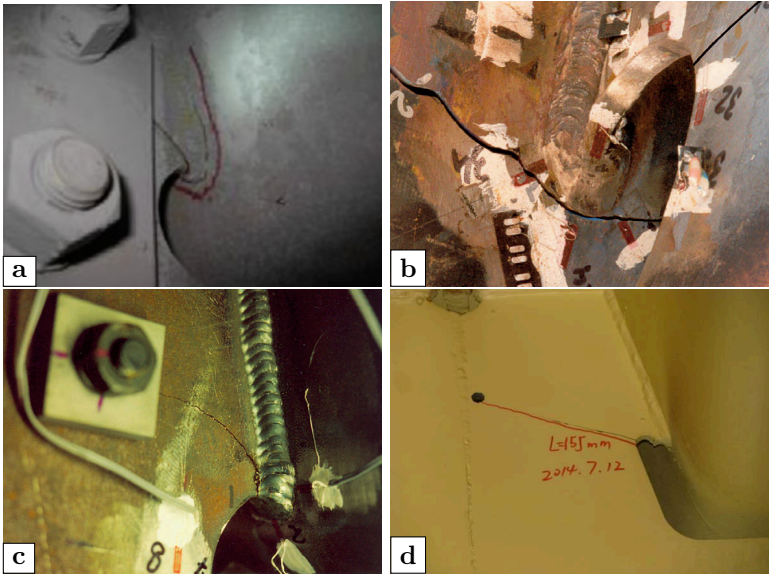


Figure 2.3: Failure modes of continuous ribs with cope holes: (a) vertical crack in the rib wall (Huang *et al.*, 2019a); (b) longitudinal crack in the rib wall (Kolstein, 2009); (c) crack in the crossbeam starting from the cope hole termination (Kolstein, 2009); (d) crack in the crossbeam at the free edge of the cope hole (Chen *et al.*, 2016)

2.2.2 Continuous ribs without cope holes

The other alternative for connecting the ribs and the crossbeam does not utilize the cope hole at the bottom of the rib as shown in Figure 2.4. In this case, a weld is placed around the outer perimeter of the rib on both sides of the crossbeam web plate.

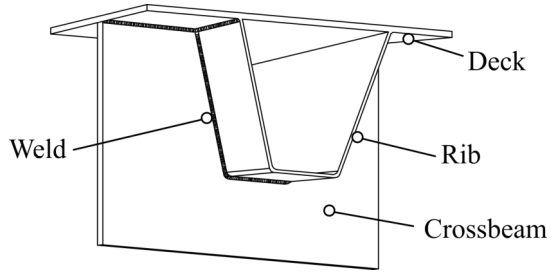


Figure 2.4: Continuous ribs without cope holes

There are two modes of fatigue cracking possible:

- cracks in the rib soffit starting from the weld toe (Figure 2.5(a));
- cracks in the crossbeam web plate near the bottom of the rib (Figure 2.5(b)).

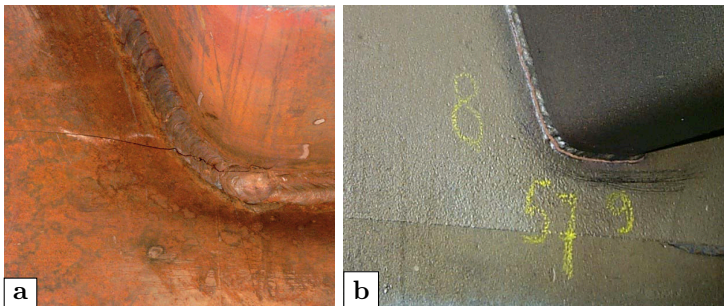


Figure 2.5: Failure modes of continuous ribs without cope holes: (a) cracks in the rib soffit (Kolstein, 2009); (b) cracks in the crossbeam web plate (de Jong, 2004)

2.2.3 Discontinuous ribs fitted between crossbeams

The designs of discontinuous ribs fitted between crossbeams are more commonly seen in earlier designs of OSDs as illustrated in Figure 2.6. At first, the ribs and crossbeams were welded together by fillet welds, which were later proven to have relatively low fatigue strength. The improved version of the detail has full penetration welds which increases the fatigue strength considerably (de Jong, 2007).

Besides the two similar modes as the design of continuous ribs without cope holes, the fatigue crack initiated from the weld root and further developed

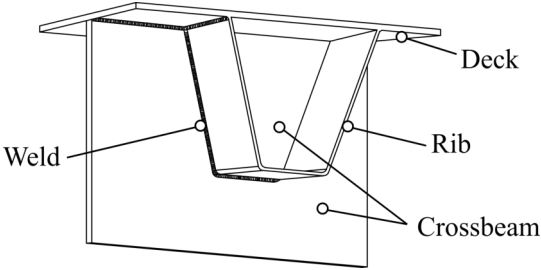


Figure 2.6: Discontinuous ribs fitted between crossbeams

through the weld throat is the third mode of fatigue cracking if the fillet welds are adopted as shown in Figure 2.7.

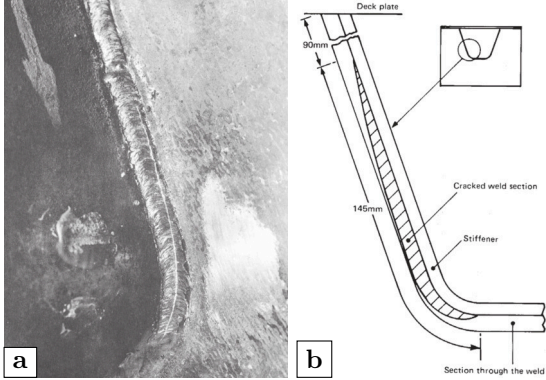


Figure 2.7: Failure modes of discontinuous rib fitted between crossbeams: (a) photo of weld throat failures; (b) corresponding illustration (Kolstein, 2009)

2.3 Mechanical behavior of the rib-to-crossbeam joint

Prior to the widespread availability of modern finite element analysis (FEA) software, it was proposed to decompose the OSD structure into a series of pseudo sub-systems that are more easily understood and analyzed individually by simplified (non-computerized) methods (Connor *et al.*, 2012). The stresses may be calculated from analyses of the sub-systems. In the next step, these stresses can be combined under the principle of linear superposition for the verification of the applicable design limit states.

The rib-to-crossbeam joint consists of welds that transfer the loads from the ribs with the deck plate into the crossbeam or transfer internal forces from the rib through the crossbeam web to the adjacent rib. Due to its unique location, the rib-to-crossbeam joint is influenced by the in-plane and out-of-plane behavior of the crossbeam as well as the rib distortion.

2.3.1 In-plane behavior of the crossbeam

When the tire load is in the plane of the crossbeam (i.e. over the crossbeam), the whole crossbeam can be seen as a simply supported beam subjected to in-plane bending moment and shear. When adopting continuous ribs passing through the crossbeam, the corresponding part of the crossbeam (i.e. the cope hole) is missing. The remaining part can be divided into different zones, which can be considered as chords. For example, the partial crossbeam web below the cope hole together with the bottom flange can be treated as a lower chord with an inverted T section. The upper chord reflects the crossbeam web between the ribs, which is also called the *tooth*, and the effective deck plate is the upper part. Therefore, the whole crossbeam is transferred to a truss structure, which is so-called *Vierendeel* model as shown in Figure 2.8. By using this model, the shear and flexural stresses can be determined by simple mechanical calculations. This model was first proposed by Haibach in 1983 (Haibach & Plasil, 1983) and was later included in the current Eurocode. It provides a simplified 2-D analysis of the in-plane behavior of the crossbeam.

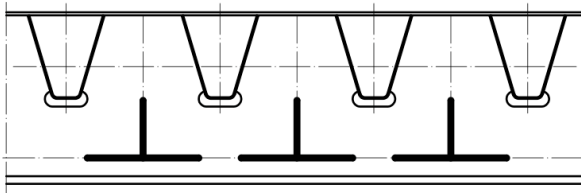


Figure 2.8: Illustration of the Vierendeel model (Leendertz, 2008)

2.3.2 Out-of-plane behavior of the crossbeam

When the tire load is out of the plane of the crossbeam (i.e. over the rib at a distance to the crossbeam), it would cause flexural deformation of the ribs. The flexural deformation results in rib rotation at the rib-to-crossbeam joint. Furthermore, the rib rotation leads to out-of-plane deformation of the crossbeam as shown in Figure 2.9. This behavior was one of the early industry concerns since the out-of-plane deformation would cause high compression stresses at the crossbeam close to the bottom of the rib when adopting discontinuous ribs or

continuous ribs without cope holes. However, cope holes with carefully selected geometries have demonstrated experimentally that the out-of-plane stresses can be kept below 25 percent of the in-plane stress (Tsakopoulos & Fisher, 2005). Therefore, it has not been counted as the most important effect any more.

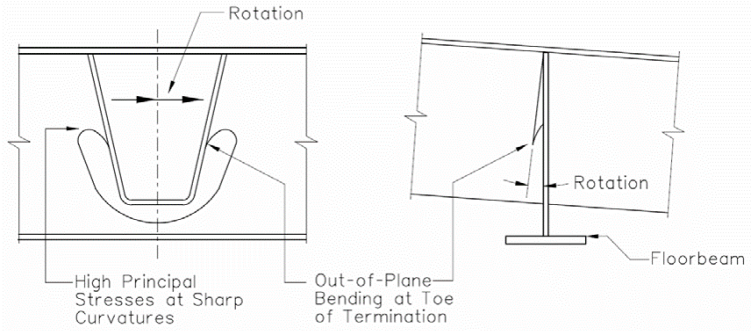


Figure 2.9: Out-of-plane deformation of crossbeam (Connor *et al.*, 2012)

2.3.3 Rib distortion

The influence of rib distortion was more or less ignored in previous research (Connor *et al.*, 2012; Leendertz, 2008; Yokozeki, 2017). This very important phenomenon has a large influence, especially when adopting the design of continuous ribs with cope holes. When the tire load is at a distance away from the crossbeam and eccentric about the axis of the rib, it causes rotation and distortion of the rib. At the position of the rib-to-crossbeam joint, the rotation and distortion of the rib is impeded by the heavy crossbeam web which represents a fixed boundary. As a consequence, the vertical deformation of the rib wall appeared at the zone close to the end of the weld connecting the rib and the crossbeam as presented in Figure 2.10.

What makes this effect even worse is that the stresses appearing at each side due to this effect have an opposite sign. While one stem displays *tension* stresses on the outer surface of the rib wall, the opposite stem displays *compression* stresses on the other outer surface. Meanwhile, the stresses at the inner surfaces of each stem are inverted. If the vehicles alternatively pass through this joint on opposite sides of the rib, the reverse of these stresses will accordingly occur which makes this detail easier prone to fatigue damage. This phenomenon may be associated with the longitudinal crack in the rib wall below the cope hole termination as shown in Figure 2.3(b).

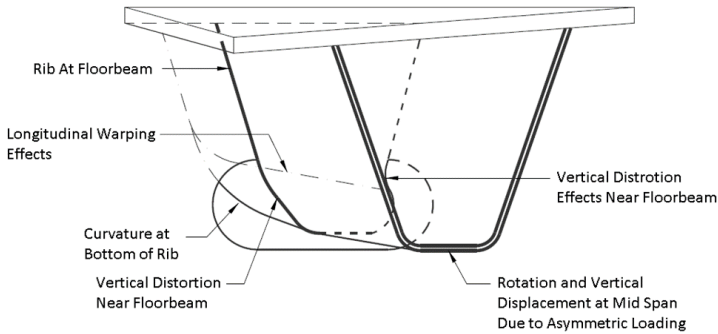


Figure 2.10: Rib distortion effects causing high stress concentrations below the cope hole termination (Connor *et al.*, 2012)

2.4 Fatigue life assessment methods

2.4.1 Approaches based on S-N curves

The main fatigue life assessment methods in current codes (i.e. AASHTO and Eurocode) are all based on S-N curves. As stated at the beginning of this section, it is realized that the fatigue behavior of structures is tightly associated with the applied stress range, the number of cycles and the type of detail. During the procedure of investigating the fatigue behavior, numerous fatigue tests of different weld details have been performed. The resulting data consists of the magnitude of the stress ranges and the number of cycles to failure when subjected to a particular constant amplitude load (Connor & Fisher, 2006). Then, it is found that the logarithm of the number of cycles is approximately normally distributed at a particular stress range. In the last step, an *S-N* curve can be acquired by doing a linear regression analysis of the data of a specific detail. Normally, the derived *S-N* curve is assumed to represent a survival probability of at least 95%, calculated from the mean value on the basis of two-sided 75% tolerance limits of the mean. Other existing definitions, e.g. a survival probability of 95% on the basis of 95% one-sided limit of the mean or mean minus two standard deviations corresponding to a survival probability of 97.7% (see Figure 2.11), are practically equal for engineering applications (Hobbacher, 2019). The *S-N* curves are expressed by:

$$C = N\Delta\sigma^m \quad (2.1)$$

where C is the constant depending on the detail category; N is the number of cycles; $\Delta\sigma$ is the constant amplitude stress range; and m is the inverse of the slope of the *S-N* curve.

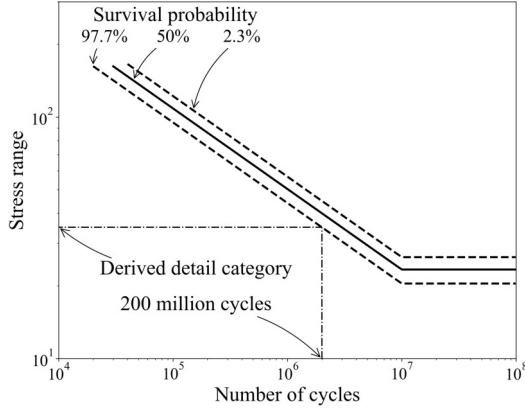


Figure 2.11: Scatter band in S - N curve (adapted from Hobbacher (2019))

In current Eurocode (CEN, 2005), the different S - N curves (i.e. different fatigue detail categories) are presented in Figure 2.12(a). It is regulated that the detail category $\Delta\sigma_C$ corresponds to the fatigue strength at 2 million cycles. For the constant amplitude nominal stresses, the fatigue strengths can be calculated by

$$\Delta\sigma_R^m N_R = \Delta\sigma_C^m 2 \times 10^6 \quad \text{with } m = 3 \text{ for } N \leq 5 \times 10^6 \quad (2.2)$$

Note that the constant amplitude fatigue limit (CAFL) is calculated as

$$\Delta\sigma_D = \left(\frac{2}{5}\right)^{1/5} \Delta\sigma_C = 0.737 \Delta\sigma_C \quad (2.3)$$

By definition, the CAFL corresponds to the fatigue strength at 5 million cycles. It assumes that the target structure is fatigue-free if the applied constant amplitude stress range is under the CAFL. Unfortunately, this is usually not the case in reality since different types of vehicles will cause variable stress ranges. Hence, for nominal stress spectra with stress ranges above and below the CAFL, $\Delta\sigma_D$ the fatigue strength should be calculated based on the extended fatigue strength curves expressed as

$$\begin{aligned} \Delta\sigma_R^m N_R &= \Delta\sigma_C^m 2 \times 10^6 & \text{with } m = 3 \text{ for } N \leq 5 \times 10^6 \\ \Delta\sigma_R^m N_R &= \Delta\sigma_D^m 5 \times 10^6 & \text{with } m = 5 \text{ for } 5 \times 10^6 \leq N \leq 10^8 \end{aligned} \quad (2.4)$$

In current AASHTO (AASHTO, 2012), the detail categories are named as letters, yet the general notion remains the same. The S - N curves for fatigue design in AASHTO are shown in Figure 2.12(b). Note that the constant-amplitude fatigue thresholds (i.e. the same meaning as CAFL in Eurocode) of different detail categories are defined at different number of cycles.

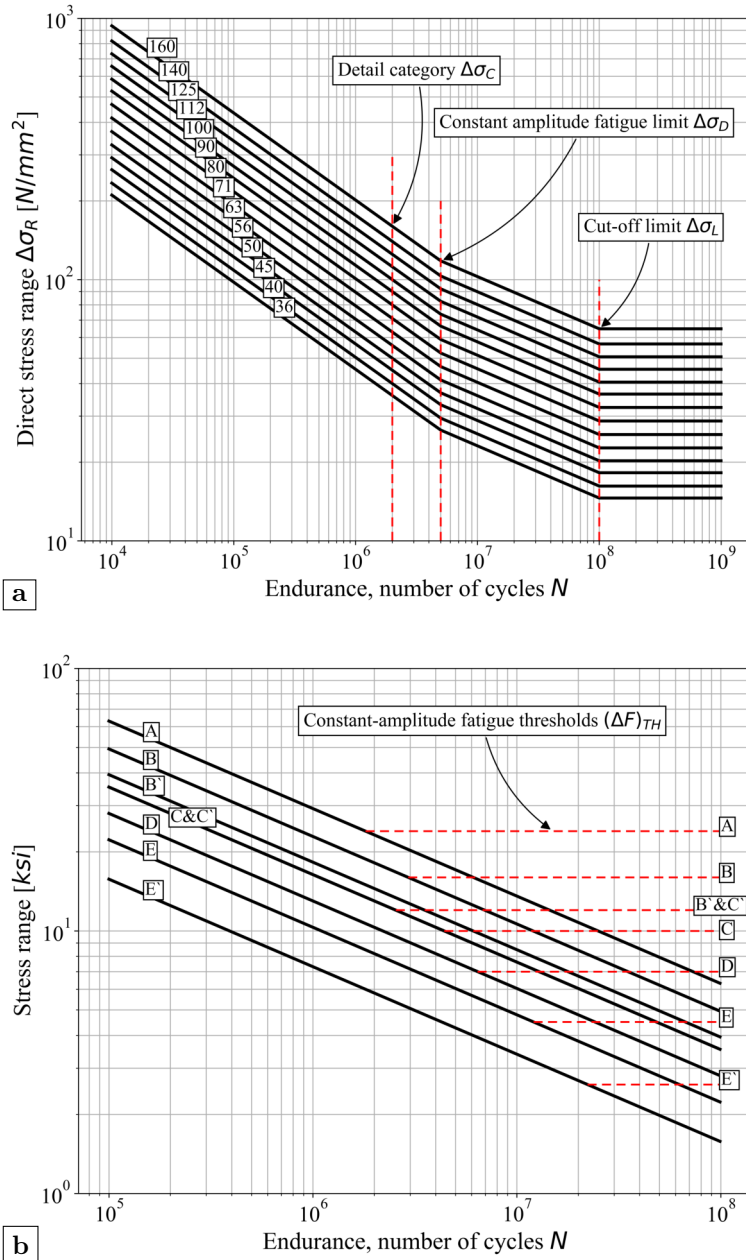
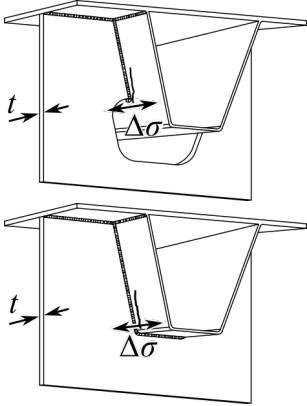
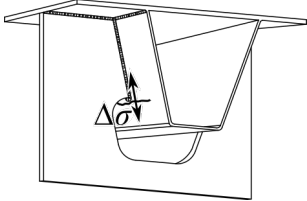
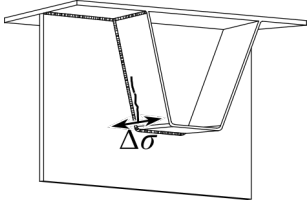


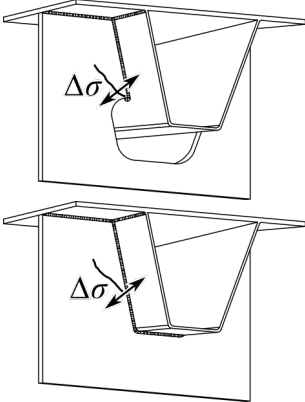
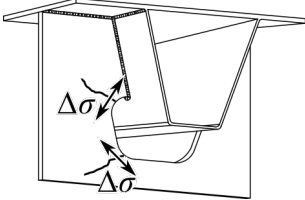
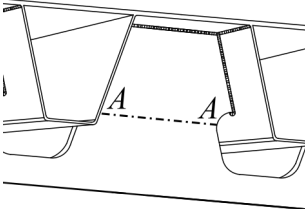
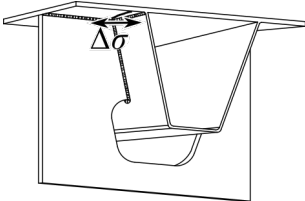
Figure 2.12: S - N curves for fatigue design in current codes: (a) Eurocode (CEN, 2005); (b) AASHTO (AASHTO, 2012)

The detail categories related to the rib-to-crossbeam joint in current codes are summarized in Table 2.1. It should be noted that the potential crack initiation points are not totally identical. The detail categories *A* and *C* in AASHTO correspond approximately to the detail categories of 160 (MPa) and 90 (MPa) in Eurocode if the same definition of the detail category (i.e. the fatigue strength at 2 million cycles) is adopted.

Table 2.1: Detail categories related to the rib-to-crossbeam joint in current codes

Description	Detail category		Illustrative examples
	Eurocode	AASHTO	
1) Rib wall at rib to crossbeam weld - Continuous rib with or without additional cope holes	80 ($t \leq 12\text{mm}$)	C	
	71 ($t > 12\text{mm}$)		
2) Rib wall at rib to crossbeam weld - Continuous rib with additional cope holes	-	C	
3) Rib wall at rib to crossbeam weld - Separate rib each side of the crossbeam	36	-	

(To be continued)

Description	Detail category		Illustrative examples
	Eurocode	AASHTO	
4) Crossbeam web at rib to crossbeam weld	-	C	
5) Base metal at edge of cope hole	-	A	
6) Critical section in web of crossbeam due to cope holes	71	-	
7) Rib to deck plate weld at crossbeam	-	C	

2.4.1.1 Nominal stress approach

In Eurocode, it is stated that the fatigue life assessment should be carried out using nominal stress ranges for details in OSDs (CEN, 2005). However, due to the complexity of the rib-to-crossbeam joint, it is rather difficult to get the definition of the nominal stress, especially for the details in the rib wall close to the welds, e.g. the constructional details 1 to 3 in Table 2.1. Nevertheless, the Vierendeel model could be employed when analyzing the critical positions around the cope hole, i.e. the constructional detail 6 in Table 2.1.

In AASHTO, three design levels are defined in total (Connor *et al.*, 2012):

- level 1 is based on full-scale laboratory testing and may be completed without considerations of levels 2 and 3;
- level 2 is based on simplified 1-D or 2-D analysis of certain panel details for which there is little experimental data and acceptance of certain details that are similar to previous tested details as described in level 1;
- level 3 is based on 3-D finite element modeling of the panel and the supporting bridge superstructure (where applicable).

In line with the definitions, the nominal stress approach should be adopted when level 2 design is considered. However, the approximate 2-D analysis presented by the Pelikan-Esslinger (PE) method (AISC, 1963) is not capable of getting the nominal stresses at the rib-to-crossbeam joint. The PE method can, however, be appropriately used to evaluate locations such as the longitudinal bending stress in a rib-splice joint.

Apart from the codes, Leendertz (2008) proposed several local numerical models for the rib-to-crossbeam joint based on the principle of Vierendeel models. The in-plane and out-of-plane behavior of the crossbeam is analyzed, and the nominal stresses are determined accordingly. In the thesis of Leendertz, an analytic radial beam model is proposed for the purpose of getting the geometrical stress concentration factor (SCF), which will be further discussed in the next section.

2.4.1.2 Structural hot spot stress method

With reference to the definition of the International Institute of Welding (IIW) (Hobbacher, 2019), the structural or geometrical hot spot stress σ_{hs} at the hot spot includes all stress raising effects of a structural detail excluding that due to the local weld profile itself as presented in Figure 2.13. Here the term *hot spot* is used to represent the locations where the fatigue cracks are most likely to appear. The structural hot spot stress (SHSS) approach is typically used where there is no clearly defined nominal stress due to complex geometric effects, or

where the structural discontinuity is not comparable to a classified structural detail.

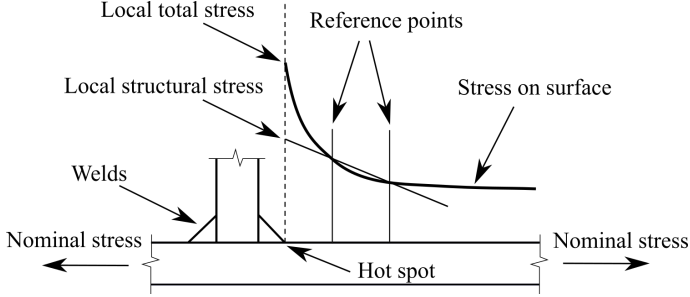


Figure 2.13: Illustration of structural hot spot stress

The hot spot stress σ_{hs} can be derived in two ways. The first one is multiplying the nominal stress σ_{nom} with a SCF denoted as K_s :

$$\sigma_{hs} = \sigma_{nom} K_s \quad (2.5)$$

Although there are some SCFs published for steel structures e.g. tubular joints, etc. limited data is available on SCFs in OSD details for simplified evaluations. As stated in previous section, Leendertz (2008) proposed the radial beam model to calculate the SCFs for hot spots near the termination of the rib-to-crossbeam joint as shown in Figure 2.14. The SCFs for hot spots in the rib-to-crossbeam joint with cope holes of 25 & 35 mm radius as well as in the closely fitted rib-to-crossbeam joint are calculated. However, it should be noted that since only the in-plane and out-of-plane behavior of the crossbeam are considered in the work of Leendertz, the derived SCFs for the hot spots on the rib wall might be on underestimation.

The other way to determine the hot spot stress is through extrapolation of stresses at reference points to the weld toe under consideration, as shown in Figure 2.13. According to the recommendations of IIW (Hobbacher, 2019), two types of hot spots (see Figure 2.15) are defined depending on their location and orientation with respect to the weld, as summarized in Table 2.2. The hot spots at the fatigue crack locations of the rib-to-crossbeam joint can be divided into type *a* hot spots with respect to the classification, which indicates that the potential cracking positions are at the weld toe on plate surface.

The stresses at reference points are generally determined through FEA. Since the stress state of the rib-to-crossbeam joint is quite complex, the stress which acts approximately in line with the perpendicular direction to the weld toe is suggested when evaluating this detail. Either shell elements or solid

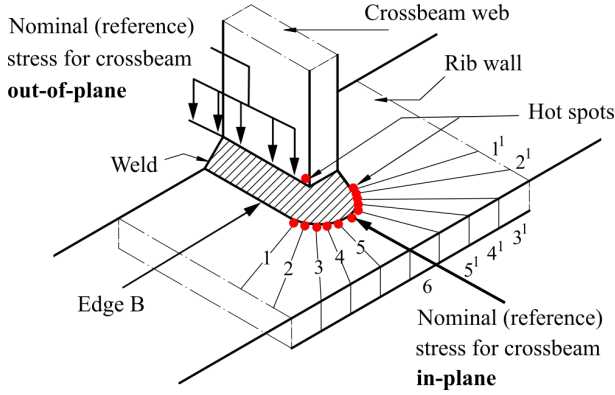


Figure 2.14: Stress concentration factor locations for crossbeam in-plane and out-of-plane loading (adapted from Leendertz (2008))

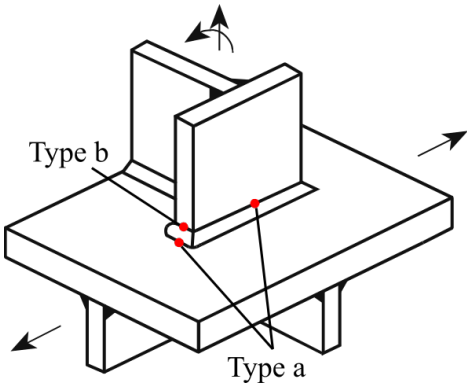


Figure 2.15: Types of hot spots (adapted from Hobbacher (2019))

Table 2.2: Types of hot spots (Hobbacher, 2019)

Type	Description	Determination
a	Weld toe on plate surface	FEA or measurement and extrapolation
b	Weld toe at plate edge	FEA or measurement and extrapolation

elements could be adopted when calculating the hot spot stress. Past research (Hobbacher, 2019) has demonstrated that the mesh quality, especially at locations close to the zone of stress concentration, has a relatively large impact on the results. For type *a* hot spots, IIW suggests using different extrapolation methods corresponding to different mesh qualities. It should be noted that here t is the plate thickness in which the hot spot is located.

- Fine mesh with the element length not more than $0.4t$ at the hot spot: evaluation of nodal stresses at two reference points $0.4t$ and $1.0t$ as shown in Figure 2.16(a), and the linear extrapolation method is adopted as in equation 2.6.

$$\sigma_{hs} = 1.67\sigma_{0.4t} - 0.67\sigma_{1.0t} \quad (2.6)$$

- Fine mesh with the same element length defined above: evaluation of nodal stresses at three reference points $0.4t$, $0.9t$ and $1.4t$ as shown in Figure 2.16(b), and the quadratic extrapolation method is adopted as in equation 2.7. This method is recommended for cases of pronounced non-linear structural stresses increasing towards the hot spot, which are induced by sharp changes of direction of the applied force or for thick-walled structures.

$$\sigma_{hs} = 2.25\sigma_{0.4t} - 2.24\sigma_{0.9t} + 0.72\sigma_{1.4t} \quad (2.7)$$

- Coarse mesh with higher-order elements having lengths equal to the plate thickness at the hot spot: evaluation of stresses at mid-side points or surface centers respectively, i.e. at two reference points $0.5t$ and $1.5t$ as shown in Figure 2.16(c), and linear extrapolation method is adopted as in equation 2.8.

$$\sigma_{hs} = 1.50\sigma_{0.5t} - 0.50\sigma_{1.5t} \quad (2.8)$$

In Eurocode, the detail categories for use with the SHSS method are only given in annex B (CEN, 2005). The relevant extrapolation method and the mesh requirement are not given in details. In AASHTO, the SHSS design approach belongs to Level 3 design. The specified mesh density is $t \times t$ and reference points are at a distance of $0.5t$ and $1.0t$ respectively. The recommended extrapolation method of AASHTO is the same as equation 2.8 from IIW. With respect to the recommendation of IIW, the classification reference to $S-N$ curves of the SHSS is denoted by $FATx$, in which x is the stress range in MPa at 2×10^6 cycles.

2.4.1.3 Effective notch stress method

The effective notch stress is the total stress at the root of a notch, assuming linear-elastic material behavior. Compared with the hot spot stress, the notch

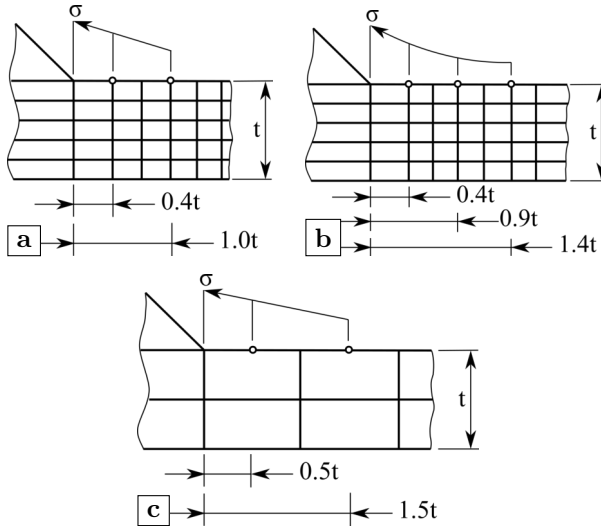


Figure 2.16: Different extrapolation methods: (a) fine mesh with linear extrapolation; (b) fine mesh with quadratic extrapolation; (c) coarse mesh with linear extrapolation

stress concentration due to the weld bead notches is included. To take account of the variation of the weld shape parameters, as well as of the non-linear material behavior at the notch root, the actual weld contour is replaced by an effective radius, which is 1 mm for structural steels as shown in Figure 2.17 (Hobbacher, 2019).

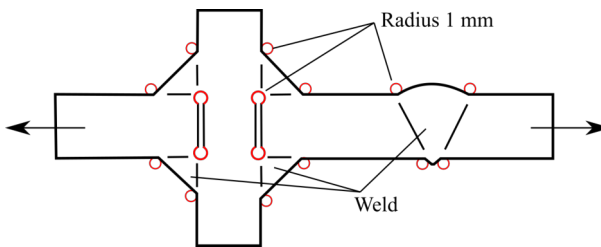


Figure 2.17: Fictitious rounding of weld toes and roots (adapted from Hobbacher (2019))

The calculation of the effective notch stress is normally performed by FEA. Similar to the hot spot stress, the effective notch stress is also influenced by the local mesh quality. The recommendation about the sizes of elements on the surface from IIW is presented in Table 2.3. The first principal stress around the

notch could be exported as the effective notch stress.

Table 2.3: Recommended sizes and number of elements on the surface (Hobbacher, 2019)

Element type	Element size	No. of elements in 45° arc	No. of elements in 360° arc
Quadratic with mid-side nodes	$\leq 0.25 \text{ mm } (r/4)^*$	≥ 3	≥ 24
Linear	$\leq 0.15 \text{ mm } (r/6)^*$	≥ 5	≥ 40

* r is the effective radius as defined in Figure 2.17.

However, a few limitations about the effective notch stress method should be noted. Firstly, the method is restricted to the assessment of possible fatigue failures initiated from the weld toe or weld root. The fatigue performance of the parent material at the weld toe should be evaluated by the SHSS method. Secondly, the method is limited to situations with thickness of plate $t \geq 5$ mm, since the method has not been verified for smaller thickness. Lastly, the effective notch stress cannot be measured directly in the welded component since the effective notch radius is an idealization (Hobbacher, 2019).

2.4.1.4 Recent research of S-N curve based approaches

Shi *et al.* (2019) conducted preliminary FEA of an OSD with U-ribs and V-ribs using the hot spot stress method. The element grid size adopted was 1 to 4 mm, and the linear extrapolation method from IIW was adopted. The results of FEA indicate that V-ribs exhibit better fatigue performance than U-ribs on typical fatigue details. Relevant full-scale fatigue tests were then conducted. It was concluded that the rib-to-diaphragm (i.e. rib-to-crossbeam) joints in the U-ribs were more prone to fatigue cracks than those in V-ribs. The results indicate that the FAT90 fatigue class is the most suitable for estimating the fatigue resistance of rib-to-crossbeam welded connections in a railway OSD.

Huang *et al.* (2019a) tested nine large-scale specimens using static and fatigue loading to explore the failure mode, fatigue life, and failure process. The hot spot stress was computed by linear extrapolation. The minimum mesh size at the welded joint was 0.8 mm and gradually increased to the global mesh size (30 mm) beyond the weld region. Design $S - N$ curves is derived with a characteristic fatigue strength of 85.4 MPa for the hot spot stress approach. Then, the $S - N$ curves are developed with a 75% confidential level of 95% probability of survival. The paper concludes that the FAT90 fatigue resistance curve can be used to assess the fatigue performance of the rib-to-crossbeam joint.

Yokozeki & Miki (2016, 2017) investigated rib-to-crossbeam joints of various types (i.e. U, V or plate ribs with or without cope holes) by FEA and fatigue tests. The influences of the out-of-plane bending and the thickness of steel plate were considered through the bending stress reduction factor of 0.8 and the thickness exponent of 0.25. Therefore, the computed hot spot stress was modified accordingly. The FEA model was built by shell elements and the weld was not modeled. The increased stiffness introduced by welds was considered by increasing the thickness of local shell elements. Based on the results of fatigue tests, the FAT80 is found to be conservative estimations for evaluating the rib-to-crossbeam joint through the hot spot stress method. The non-slit (i.e. without cope hole) connection with the plate rib is considered to be the most suitable among the connections evaluated in the study.

Zhang *et al.* (2015) carried out fatigue tests of full-scale orthotropic steel decks focusing on determining actual fatigue resistance for the rib-to-diaphragm (i.e. rib-to-crossbeam) joint. Three different assessment methods were compared: the consistent nominal stress approach, the hot spot stress approach and the notch stress approach. The fatigue crack that initiates from the weld end at the weld toe and propagates along the rib wall was predominant for rib-to-crossbeam joints. For the hot spot stress approach, the element size was 1 mm at hot spots and the linear extrapolation method was adopted. Based on the comparison results, the evaluation results of hot spot stress and notch stress approaches correlated with model tests better than consistent nominal stress approach. The fatigue strength design class FAT90 was suggested when using the hot spot stress approach. The FAT225 fatigue resistance curves could be used when adopting the effective notch stress approach. It is also found that the scatter of fatigue experimental data is higher using the effective notch stress approach than using the hot spot stress approach in terms of the model testing results. The main reasons behind the divergence in evaluation results is whether local stress condition could be accurately simulated or not. Actually, the effective notch stress is primarily influenced by the element size at the notch of an un-welded root gap, the tip of the radius at the root of the real notch, and possible misalignment having been neglected.

Aygül *et al.* (2012) performed fatigue life assessment of the rib-to-crossbeam joint with open ribs. Different element types e.g. tetrahedral and hexahedral and various geometrical shapes were used to examine their effects. The results of different modeling methods with shell element were compared with the results of the solid element model and experiments. Research results indicate that the shape of the root geometry has no significant effect on the stress at the weld toe. The stress distribution at the welded joint is primarily influenced by the cope hole. Using smaller tetrahedral solid elements facilitate the modeling work and the differences between the results when using hexahedral and tetrahedral

elements are very small. The modeling work of using the effective notch stress approach requires much more effort than the work involved in using the structural hot spot stress approach. The results of the FEA reveal that the structural hot spot stresses obtained from the shell element models are unrealistically high when welds were omitted. Moreover, the way in which the welds were represented had a substantial influence on the magnitude of the hot spot stresses. For models incorporating shell elements, it is important to represent the welds in complex welded joints, not only in the form of stiffness (thickness) but also in the form of shape (geometry). The shell model with oblique shell elements to model the weld was recommended.

Wang (2014) investigated the diaphragm-to-rib (i.e. rib-to-crossbeam) welded connection in an OSD using the effective notch stress approach. Two kinds of specimens with different shapes of cope holes were designed. Specimen s1 had the form of the circular arc transition and specimen s2 had the form of the vertical transition. According to the results of the fatigue tests, the fatigue strength of s1 and s2 met the design level FAT225 in IIW. The vertical transition had the higher fatigue strength. The FEA showed that the maximum first principal stress of s1 and s2 at the weld toe were significantly larger than those at the weld root. The exact location of the fatigue crack along the weld toe line was determined according to the first principal stress distribution which corresponded to the fatigue test results.

Choi & Kim (2008) evaluated the stress characteristics and the fatigue crack behavior of the longitudinal rib-to-crossbeam joints. To measure the geometric stress concentration and residual stresses around the longitudinal rib-to-crossbeam joints, strain gauges were installed at 5 mm and 15 mm distant from the weld toe of the rib-to-crossbeam joint. It is found that the stress adjacent to the rib-to-crossbeam joint is greatly increased above the nominal stress when very close to the weld toe of the joint. Meanwhile, the stop-hole repair method was introduced attempting to delay the crack growth. However, the stop-hole repair method is not effective enough in delaying the fatigue crack growth in the longitudinal rib if the strains around the crack were greater than the yield strain limit.

2.4.2 Approaches based on fracture mechanics

Approaches based on $S-N$ curves are quite suitable for the purpose of design due to their simplicity. However, only the point of fatigue failure is defined in these approaches. For example, these methods can only predict after how many cycles, under a series of certain stress ranges, the fatigue failure would occur, yet the actual fatigue progress is not covered by these approaches.

Fracture mechanics has therefore been developed to give a better understanding

of crack propagation. In order to understand the use of fracture mechanics, a very important principle needs to be clarified first, which is the stress intensity factor (SIF). Taking the example of a center crack in an infinite plate (Hobbacher, 2019), the stress intensity factor denoted by K_{sif} is defined by the formula

$$K_{sif} = \sigma\sqrt{\pi a} \tag{2.9}$$

where σ is the remote stress in the plate and a is the half of the crack length.

However, there are various crack configurations and geometrical shapes in practice. Hence, a correction parameter $f(a)$ is introduced, which is related to the crack length, the geometry of the construction which contains the defect and the load condition (Nagy, 2017). The formula for K_{sif} becomes

$$K_{sif} = f(a)\sigma\sqrt{\pi a} \tag{2.10}$$

Past research has revealed that the stress intensity factor range denoted as ΔK_{sif} can be used to describe the fatigue action at a crack tip in terms of the crack propagation. The fatigue crack propagation is defined by a characteristic S-shaped curve as shown in Figure 2.18.

Three different regions of a crack propagation can be identified. In the first region, there is a threshold value ΔK_{th} . Below ΔK_{th} , there is no or extremely slow crack propagation in the detail. Above ΔK_{th} , the crack propagation rate da/dn increases relatively rapidly until the second region. In the second region, normally a linear relationship can be found between the crack growth rate da/dn and the stress intensity factor range ΔK_{sif} in the logarithmic scale. Finally, in the third region, the unstable crack propagates swiftly until the critical stress intensity factor K_c is reached.

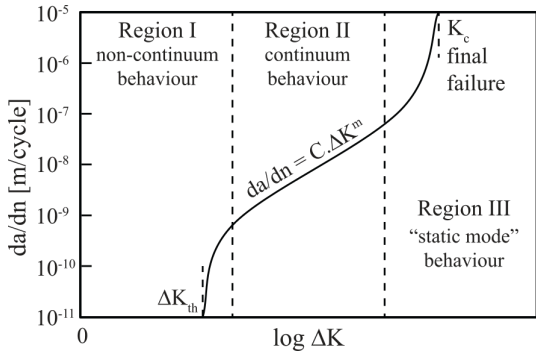


Figure 2.18: Characteristic sigmoidal fatigue crack growth curve (adapted from Nagy (2017))

Many researchers tried to describe the crack growth rate curve. The most widely known method is the Paris equation, as also shown in the Figure 2.18, given by

$$\frac{da}{dn} = C \cdot (\Delta K)^m \quad (2.11)$$

where the a is the crack length and n is the number of load cycles; C and m are the parameters depending on material; ΔK_{sif} is the SIF range.

Since the Paris law only describes part of the crack growth rate curve (i.e. the second region), other crack propagation laws are proposed to fit the whole S-shaped curve by including more parameters e.g. ΔK_{th} , ΔK_c or other material/empirical constants.

The prerequisite for fracture mechanics based approaches to yield realistic predictions of the fatigue life is to have an accurate prediction of the crack growth, even at the threshold level. Unfortunately, experimental data near the threshold growth rates is sensitive to many variables. One of these is the actual crack length and shape, one of the most readily quantified parameters (Connor & Fisher, 2006). Other parameters e.g. residual stresses and stress gradients are not so easy to quantify. Furthermore, data from full-scale tests are still required to accurately calibrate the results. At present, the approaches based on fracture mechanics are more common when analyzing relatively simple construction details such as the rib-to-deck joint. Relevant research on the rib-to-crossbeam joint is not reported.

2.4.3 Other approaches

Except for the two main categories mentioned above, a few innovative fatigue life assessment approaches for OSDs are reported in recent years. Even though they are not specific for the rib-to-crossbeam joint, a brief introduction is beneficial for expanding the possible application of these approaches to the rib-to-crossbeam joint.

Heng *et al.* (2019b) and Zhu *et al.* (2019a) both proposed a dynamic Bayesian network (DBN) based model which is capable of assessing the fatigue reliability of OSDs at system-level. According to Heng *et al.* (2019b), the fatigue reliability of welded joints can be predicted and updated with the inspection and monitoring results by using the DBN model. A case study using the proposed method on a typical OSD bridge is finished. The fatigue fracture of the rib-to-deck joints is considered. Zhu *et al.* (2019a) stated that the proposed framework aims to fulfill two independent tasks: (1) track the crack growth and calibrate the time-independent variables (i.e. the geometric parameters and the multiplier for the crack shape factor); and (2) predict the crack growth in the future.

The proposed framework is illustrated by a numerical example of fatigue crack growth on the OSD subjected to truck load.

Ladinek *et al.* (2018b) reported a strain-life approach for the assessment of welded joints considering the real weld geometry. The real weld geometry is obtained by 3D laser scanning. By doing so, the effect of additional stress concentration from the weld profile itself can be studied, leading to the predictions of fatigue lifetime which take the individual features of the weld into account. By taking the strain-life concept, different methods for the mean stress and the plasticity correction are available into consideration. It proves that the predicted fatigue lifetimes vary from being unrealistic to pretty accurate.

Cui *et al.* (2020) and Zhou *et al.* (2016b) both presented the approaches based on dynamic analyses of the coupled vehicle/train-bridge system. Cui *et al.* (2020) presented a framework for vehicle-induced dynamic stress analysis of rib-to-deck joints in a cable-stayed bridge. The influence of the bridge dynamics, vehicle dynamics, asphalt pavement temperature, roughness and vehicle velocity are assessed. The results show that the dynamically coupled vehicle-bridge system should be considered and that pavement temperature and roughness are two profound factors affecting the stress responses of rib-to-crossbeam joints. Zhou *et al.* (2016b) carried out an enhanced fatigue assessment of critical welded details in a steel-concrete composite railway bridge based on fracture mechanics through global-local dynamic analysis. The stress intensity factor histories of the cracks are calculated through dynamic analysis of the bridge due to the high-speed train passages. The fatigue crack growth curve is obtained through crack propagation analysis, and fatigue propagation life is therefore predicted.

2.5 Structural optimizations

In previous sections, the current major fatigue life assessment methods are discussed. However, the fatigue life assessment methods can only point out the problems rather than solving them. The stress concentrations that eventually cause fatigue problems are the intrinsic character of OSDs, which cannot be thoroughly resolved without structural optimizations.

2.5.1 Using bulkheads or other attachments

Historically, the rib-to-crossbeam joint has undergone the most dramatic evolution. Evolution of this joint determined that in some cases a stress-relieving cope hole was needed in the crossbeam web to exclude high localized out-of-plane stresses at the bottom of the rib and to remove the weld from a point of maximum stress. The need for a cope hole was correctly recognized but the limited understanding about stress flow in the connection steered engineers

to conceive of the detail called *bulkhead* (Connor *et al.*, 2012). The so-called bulkhead is a plate installed inside the rib at the intersection of the rib to the crossbeam as shown in Figure 2.19. It was thought before that the distortion of the rib stem created by the crossbeam stiffening from outside should be balanced by providing a resistance from the inside of the rib. Unfortunately, later research showed that the bulkheads do not provide sufficient benefits. The new welds required for attaching the bulkhead are prone to fatigue and relevant cracks could eventually propagate into the rib stem. Not to mention that the bulkheads are not only costly to fabricate (i.e. grinding of the abrupt terminations) but also difficult to install (i.e. alignment with the crossbeam). Therefore, the bulkhead is recommended to be avoided when possible (Connor *et al.*, 2012).

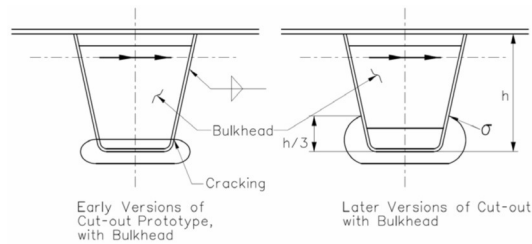


Figure 2.19: Illustration of bulkhead and stress flow (Connor *et al.*, 2012)

Nevertheless, recent reports about the bulkheads or other types of inner stiffeners are still available. Li *et al.* (2020) investigated the fatigue performance of the rounded welding region between the diaphragm plate and closed rib (i.e. rib-to-crossbeam joint) of an orthotropic steel bridge deck using experiments and FEM. According to the research results, the stress concentration of the rounded welding region could be effectively reduced by attaching two reinforcing plates at the corresponding location of the termination as shown in Figure 2.20. Nonetheless, fatigue tests of the optimized models are missing.

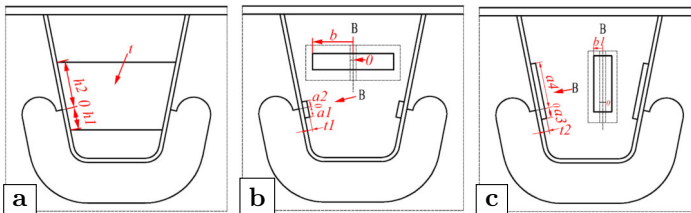


Figure 2.20: Different schemes: (a) bulkhead; (b) reinforcing plates; (c) reinforcing plates (Li *et al.*, 2020).

Zhu *et al.* (2018a) conducted fatigue tests to investigate the effects of inner bulkheads as displayed in Figure 2.21. The tensile stresses and stress amplitudes in the rib-to-crossbeam joint weld are reduced significantly by the installation of an inner bulkhead. Therefore, the fatigue cracks near the weld end of the rib-to-crossbeam joint are delayed significantly. However, fatigue cracking in the rib-to-bulkhead details are introduced by installing the inner bulkhead. Overall, the effectiveness of a bulkhead on the fatigue life of the OSD may be limited.

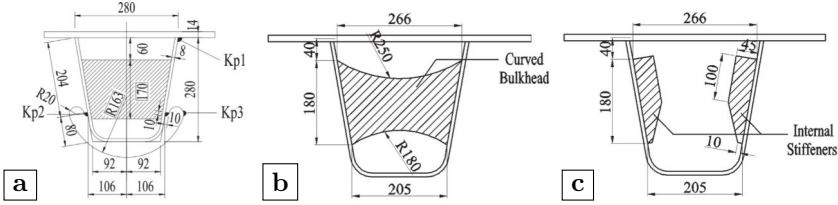


Figure 2.21: Different designs: (a) normal bulkhead tested; (b) curved bulkhead; (c) internal stiffeners (Zhu *et al.*, 2018a)

Following the notion of bulkheads, the attempts of adding external attachments to the rib-to-crossbeam are also reported. Zhi *et al.* (2018) analyzed the stress range and service life of a bridge based on the actual strain data collected from sensors. The optimization method of setting an extra short stiffener along the cope hole was analyzed as shown in Figure 2.22. The calculation results show that the extra stiffener could decrease the stress ranges of the rib-to-crossbeam weld ending and cope hole, therefore reducing the possibility of fatigue cracks.

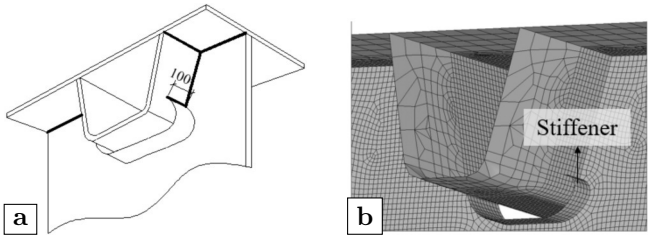


Figure 2.22: Setting stiffener on the arc gap: (a) illustration; (b) FEA model (Zhi *et al.*, 2018)

Wang *et al.* (2018a) proposed cold reinforcement techniques to stop fatigue cracking of the critical details of OSDs and web gap zones. The cold reinforcement techniques refer to reinforcement methods that produce no or only low tensile residual stresses in structural details, avoiding new fatigue vulnerable details. The research shows that cold bonding of steel plates or bonding and bolting of steel angles can effectively decrease local stresses, increase local

rigidity, and extend fatigue life as shown in Figure 2.23. Even though the technique is for repairing old bridges, it is also possible for newly constructed bridges.

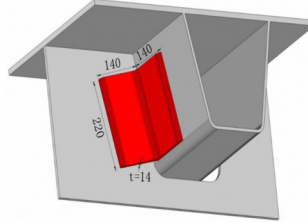


Figure 2.23: Bonding of angle steel at rib-to-crossbeam joint (Wang *et al.*, 2018a)

2.5.2 Optimizing the cope hole shape

Since continuous ribs with cope holes represent the majority of current designs of the intersection between rib and crossbeam, the shape of the cope hole should be carefully considered. The shape of the cope hole influences not only the welds but also the free edge of the cope hole itself. At present, there is not a worldwide consensus. In Eurocode, the minimum dimensions of cope holes are given in annex C (CEN, 2006), as shown in Figure 2.24. Relevant regulations are not directly shown in AASHTO, but a few recommendations are given in the manual from AISC (Connor *et al.*, 2012) as:

- the radius of curvature in each point of the free edge of the cope hole must be large to decrease the stress concentration at the free edge;
- the dimension of the crossbeam web tooth between ribs must be large to minimize the in-plane stresses due to shear and bending of the tooth;
- the cope hole must terminate high enough on the rib wall to avoid the highly stresses area of the rib and provide out-of-plane flexibility for rib rotations;
- the cope hole must terminate low enough on the rib wall to prevent excessive distortion in the rib walls.

Zhu *et al.* (2020) investigated the stress behavior and the fatigue performance of two types of cope hole geometry based on the simultaneous field monitoring and FEM analyses as shown in Figure 2.25. Results of the study reveal that the two types of cope hole geometry present high stress response and severe stress concentration at the crossbeam cope hole. Compared to the original cope hole geometry, the new cope hole geometry with large radius increases the stress level at the crossbeam cope hole, resulting in a further low fatigue life at this detail.

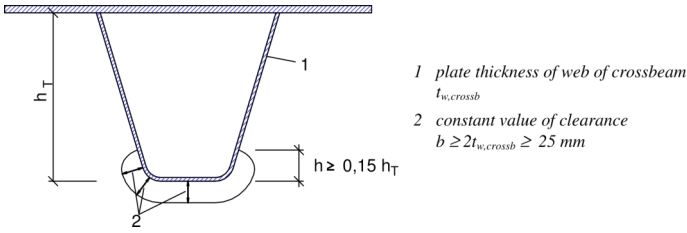


Figure 2.24: Minimum dimensions of cope holes (CEN, 2006)

Meanwhile, the fatigue resistance at the rib-to-crossbeam weld connection is deteriorated by the new cope hole geometry, especially at the detail of rib wall.

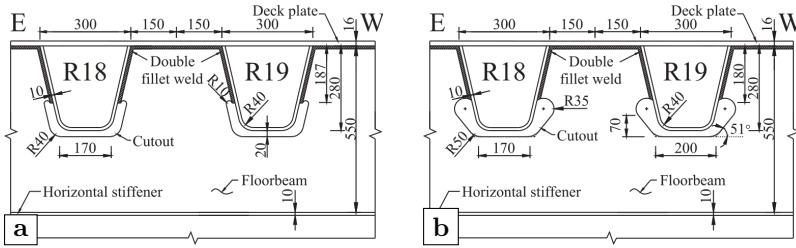


Figure 2.25: Cope hole geometry: (a) original design; (b) new design (Zhu *et al.*, 2020)

Zhu & Xiang (2019) built multi-scale finite element models to investigate the mechanism of base-metal cracking on diaphragm cope hole. The results indicate that the length of the longitudinal influence line for the detail stress to the tire load approximately equal twice the diaphragm (i.e. crossbeam) spacing. The nominal stress is hard to define at cope hole detail for high stress concentration, and the hot spot stress is preferred to be used in the fatigue assessment based on S-N curve of FAT125. Also, the nominal stress is suggested to be extracted at the location 5 mm from the cope hole edge.

Zhou *et al.* (2016b) conducted three fatigue tests to evaluate the fatigue performance of rib-to-crossbeam connections with various cope hole configurations as shown in Figure 2.26. In the tests, cracks are more likely to initiate from the perimeter of the cope holes in the crossbeam webs rather than the rib-to-crossbeam web fillet welds. By using the FEA, the characteristic stresses based on the theory of critical distances are calculated for the stress concentrations along the cope holes. The method based on the theory of critical distances could further form a basis of fatigue crack propagation analysis using the fracture mechanics approaches.

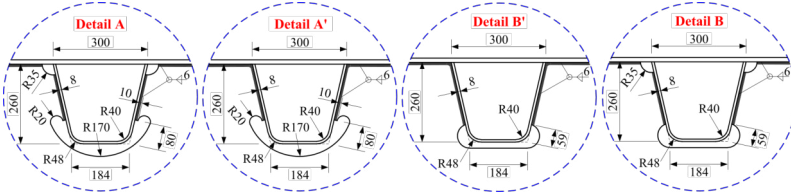


Figure 2.26: Geometries of the cope holes (Zhou *et al.*, 2016b)

2.5.3 Applying post weld improvement

The welding procedure has a large influence on the fatigue performance of welds. On the one hand, the residual stresses are introduced after the complex temperature changes due to the welding operations. On the other hand, the weld defects are quite common after welding. The irregular surface of welds or the abrupt transition from the weld material to the base material would cause stress concentrations and reduce the fatigue life. IIW published a series of recommendations (Haagensen & Maddox, 2006) for post weld improvement of weld components. In general, the suggested approaches are divided into two categories, which are the introduction of compressive residual stresses and the modification of weld toe geometry.

2.5.3.1 Introduction of compressive residual stress

The first approach of introducing compressive residual stresses is suitable for the welded joints that are most likely to fail from the weld toe. The compressive residual stresses have the effect of *clamping* the weld toe in compression. Therefore, when the welded joints are bearing tensile stresses, the residual compressive stresses have to be overcome before the tensile stresses become damaging (Haagensen & Maddox, 2006). For using this approach, the compressive residual stresses are induced by mechanical plastic deformation of the weld toe region, which can be achieved by techniques such as hammer peening, needle peening, high pressure water pounding, etc. Because of the simplified operation and portable equipment used, the hammer peening is more commonly used. An illustration of the hammer peening procedure is given in Figure 2.27. In order to have an effective treatment, a reasonably accurate positioning of the tip of the hammer gun over the weld toe is important. Therefore, both the weld metal and the parent metal can be deformed. Meanwhile, repeated peening is also needed to achieve full coverage and a smooth surface. The surface of a weld toe before and after the hammer peening is presented in Figure 2.28.

To investigate the application of hammer peening on the rib-to-crossbeam joint,

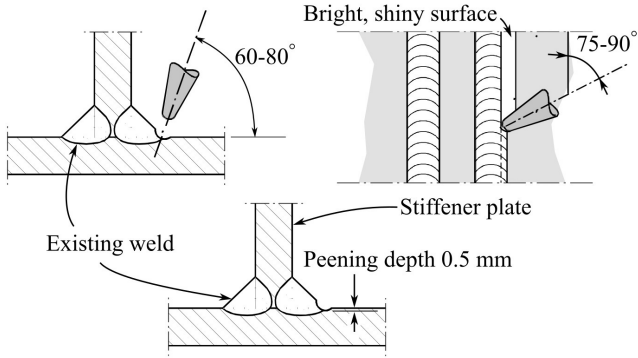


Figure 2.27: Hammer peening procedure (adapted from Haagensen & Maddox (2006))

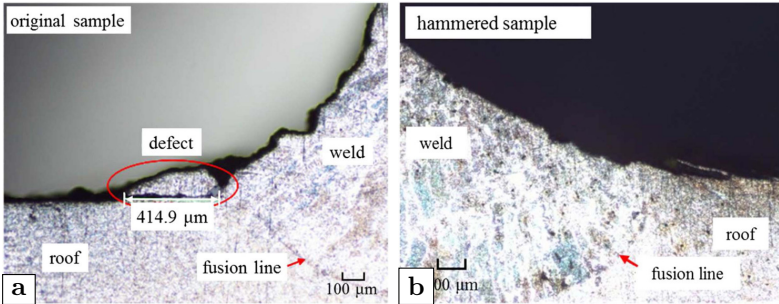


Figure 2.28: Surface of weld toe: (a) original sample; (b) hammered sample (Fu *et al.*, 2018)

Wang *et al.* (2018b) developed the simplified FEM of hammer-peened specimen to investigate the local stress variation after hammer peening. Three local specimens were peened and the subsequent fatigue tests were conducted for comparison. The results show that the crack initiation life of hammer peened specimen is enhanced significantly, while the crack propagation pattern still remained unchanged. Significant compressive stress is induced by hammer peening, and the effective tensile stress under the bending load could be decreased effectively, which is beneficial to the fatigue performance of the rib-to-crossbeam welds.

2.5.3.2 Modification of weld toe geometry

The primary aim of the improvement techniques that modify the weld toe geometry is to remove or reduce the size of minute crack-like flaws, which will enhance the stress concentration effect. A secondary aim is to reduce the local stress concentration due to the weld profile by achieving a smooth blend at the transition between the plate and the weld face (Haagensen & Maddox, 2006).

As recommended by IIW, the modification of weld toe geometry can be finished by the burr grinding or the tungsten inert gas (TIG) dressing. Figure 2.29 gives an illustration of the burr grinding technique. Since the quality of grinding depends on the skill of the operator, only general advice is given in the recommendations of IIW. For example, the axis of the tool should be $45 - 60^\circ$ to the main plate, and approximately 45° to the direction of travel. The TIG dressing technique removes the weld flaws by re-melting the material at the weld toe. The present specifications are not applicable to connections with main plate thickness less than 6 mm for steel. For an optimum result, the remelted zone has to be positioned carefully with respect to the existing weld toe. Normally, the best result is acquired when the arc center is located at a small distance away from the weld toe as shown in Figure 2.30.

Van Es *et al.* (2013) reported the results of extensive measurements on weld toe geometry of as-welded and TIG-dressed butt welded connections in high strength steels and very high strength steels. Four weld toe parameters have been formulated to characterize the weld toe: weld toe radius, weld toe angle, weld height and undercut. It is concluded that TIG dressing, on average, has a beneficial effect on the geometry of the weld toe. However, TIG-dressed weld toes have different appearances and as a result, weld toe parameters show more variation after TIG dressing. An improvement of the weakest link is therefore not guaranteed.

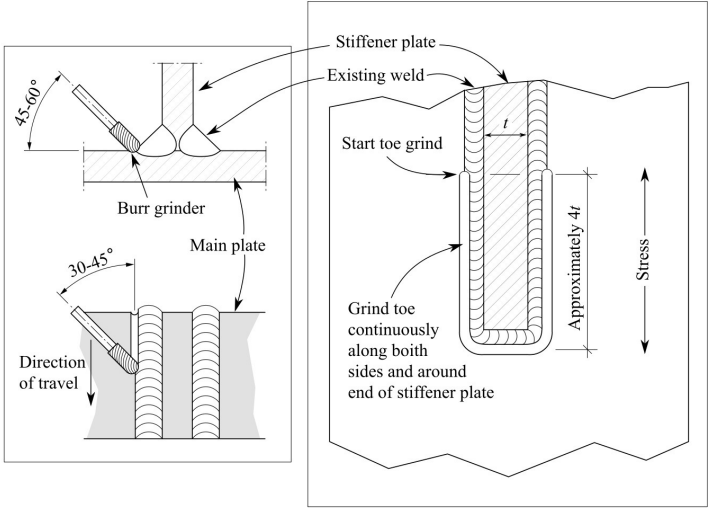


Figure 2.29: Burr grinding technique (adapted from Haagensen & Maddox (2006))

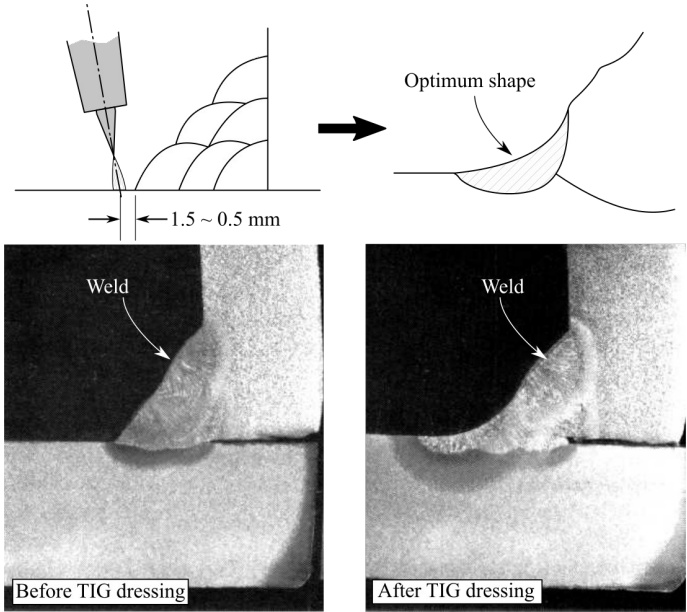


Figure 2.30: Effect of TIG dressing (adapted from Haagensen & Maddox (2006))

2.5.4 Introducing global reinforcement system

One important reason of vehicle-induced fatigue problems for OSDs is the insufficient local stiffness. The insufficient local stiffness leads to relatively larger deformations of the steel plates and further causes fatigue cracks. Except for the intrinsic property of OSD, such as the relatively thin deck plate, another important factor is the influence of the pavement. The conventional pavement of OSD is normally the asphalt concrete, which has a much lower elastic modulus than steel. When the environment temperature increases such as during summer time, the stiffness of the asphalt concrete will further decrease. As a consequence, the contribution of the conventional pavement to the local stiffness is quite low. The idea of replacing the conventional pavement by a layer with higher stiffness to increase the local stiffness and lower the stress ranges at fatigue-prone details seems promising. The reported reinforcement systems can be divided into two categories, which are the cement based overlays and the second steel plate reinforcement.

2.5.4.1 Cement based overlays

In 2004, Buitelaar *et al.* (2004) reported the use of heavily reinforced high performance concrete (HPC) and ultra-high performance concrete (UHPC) as the overlay. The UHPC overlay could increase the local stiffness of the OSD and decrease the stress concentration induced by the vehicle loading. The results of strain measurements on the pilot project show a stress reduction with a factor 4 to 5 in the fatigue critical details. Later on, more and more research has demonstrated the efficiency of this method in reducing the stress ranges at fatigue-prone details. An illustration of a typical OSD-UHPC composite structure is shown in Figure 2.31.

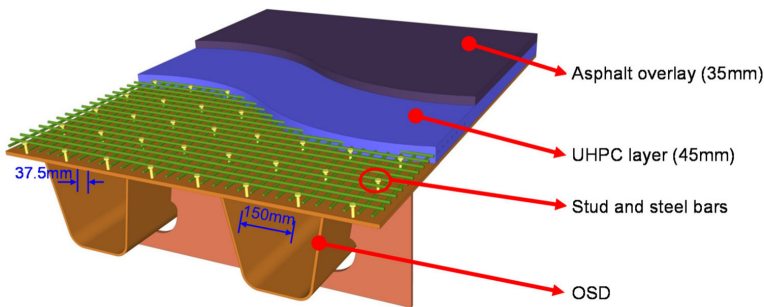


Figure 2.31: OSD with UHPC overlay (Shao & Cao, 2018)

In recent reports, Abdelbaset *et al.* (2020) carried out experimental work to investigate the effect of employing UHPC overlay on the hot spot stresses at

fatigue prone details of OSDs. Three full scale rib-to-deck-to-crossbeam welded connections were fabricated and tested. The effect of in-plane and out-of-plane distortions of crossbeam web were considered. Experimental results indicate that the stresses around the crossbeam cope hole are slightly higher than the hot spot stresses at considered locations on U-rib due to in-plane and out-of-plane distortions of the crossbeam under central loading. The application of 60 mm UHPC layer effectively reduces the hot spot stresses by 26-83% at the considered locations of the test specimens.

Zhu *et al.* (2019b) performed numerical simulations of an orthotropic steel bridge stiffened with UHPC layer. The stress response of the fatigue-prone details under tire loads is obtained, and the fatigue performance is also evaluated. The stress tendencies observed by the FEMs are compared to the stress response data from field measurements. It is observed that an application of 45 mm thick UHPC layer on the OSD can reduce the stress range at deck side of rib-to-deck joint by up to 70.9%, achieving an infinite fatigue life. However, the stress ranges for the other three details are still significant, including the stress range at rib side of rib-to-deck joint (with both membrane and bending stresses), the stress range on rib wall at weld end of rib-to-crossbeam joint (with both rotational and Poisson's effects), and the stress range at crossbeam side of rib-to-crossbeam joint (due to the in-plane deformations and out-of-plane twist).

2.5.4.2 Second steel plate reinforcement

The need for more efficient light-weight solutions to reinforce movable bridges led to another system which consists of adding a second steel plate to the existing bridge deck. The second steel plate can be simply bonded to the existing deck. Alternatively, a sandwich structure can be created utilizing the second steel plate. The second steel plate is generally 5 to 8 mm thick.

Teixeira de Freitas (2012) investigated the reinforcement of OSD by adding a second steel plate to the existing deck based on multi-scale approach. Two reinforcement systems are considered, the bonded steel plates system and the sandwich steel plates system as shown in Figure 2.32. In the bonded steel plates system, the existing OSD is reinforced by adding the second steel plate using a thin epoxy adhesive layer, which is approximately 2 mm thick. In the sandwich steel plates system, a polyurethane core of 15 to 30 mm thick is set between the second steel plate and the existing deck plate forming a sandwich structure. Both reinforcements are considered lightweight solutions for application on movable bridges. Through the research based on a multi-scale approach, the performance of these two light-weight solutions are proven to be efficient and durable.

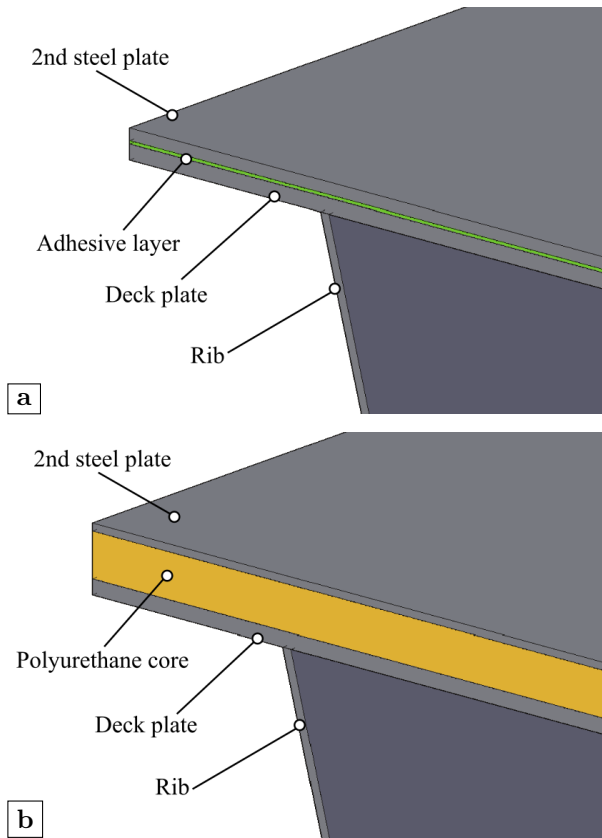


Figure 2.32: Detail of the steel plate reinforcement system: (a) bonded steel plates system; (b) sandwich steel plate system (adapted from Teixeira de Freitas (2012))

A very important condition for the global reinforcement system to operate continuously is the tight and solid connection between the original deck plate of OSDs and the reinforcement layer. Once the connection is deteriorated, the repair of such structures will be quite costly given the high strength of the reinforcement layer. The durability of the global reinforcement system requires more time to verify.

2.6 Aim and objectives

When summarizing recent research about OSDs, it is found that most of them focus on the rib-to-deck joint. The rib-to-crossbeam joint does not attract the

same amount of attentions, even though this detail is rather important. As mentioned before, designers prefer to use the rib with the trapezoidal cross-sections passing through the crossbeam continuously with an additional cope hole. The performance of this design scheme has shown that the fatigue failure mode of cracks initiating from the lower end of the rib-to-crossbeam joint weld on the rib wall is quite common. However, this failure mode caused by the rib distortion phenomenon is not considered in current version of Eurocode as the relevant design criterion is still missing. Furthermore, due to the complexity of the rib-to-crossbeam joint, designers aim at reducing the number of crossbeams by maximizing the crossbeam spacing. This leads to a trend of using higher and slender ribs to achieve an optimal use of the constructional steel. When applying high and slender ribs, the torsional rigidity of rib is easy to be lost through the distortion of the closed cross-section. This distortion generates large non-rotational deformation thus reducing the effective development of full torsional rigidity of the rib, which further impedes the load dispersal through adjacent ribs and finally more severe stress concentrations. The overall fatigue life of the structure is therefore vastly reduced.

This research aims at a thorough investigation of the influence of the rib distortion on the fatigue performance of the rib-to-crossbeam joint, as well as the recommendations for the design of the rib-to-crossbeam joint including the design criteria and the design procedure.

To achieve the aim, the objectives are to:

- generate numerical models accurately describing the distortion of closed ribs;
- carry out detailed measurements from tests for verification of numerical models;
- analyze the classical parameters of OSDs which may or may not have an influence on the distortional behavior;
- investigate possible alternatives for OSDs to reduce distortion and improve fatigue performance;
- develop a simplified calculation method for estimation of stress concentrations;
- formulate guidance and design criteria for distortion-free orthotropic plates.

3

Parametric analysis

This chapter is based on:

Fang H., Van Puymbroeck E., Iqbal N., et al. (2018). Numerical simulation of rib distortion in orthotropic steel decks. *IOP Conference Series-Materials Science and Engineering*, 419:012012.

3.1 Introduction

In this chapter, parametric analyses are performed to determine the influences of classic design parameters on the distortional behavior of the ribs of an OSD. It is already known from the previous chapter that the trapezoidal section is one of the most widely adopted geometries for the ribs. When the load is eccentric from the axis of the rib, the rib will be subjected to torsion and distortion. On the one hand, the torsional rigidity of the ribs is essentially reduced which impedes the load dispersal. On the other hand, the rib distortion causes high stress concentrations in the rib wall at the rib-to-crossbeam joint. Moreover, the eccentric load that causes the tension stress on one stem of the rib always causes the compression stress on the other stem of the rib at the same time. Thus, the rib-to-crossbeam joint carries positive and negative stresses alternately, when vehicles pass by, which makes the joint more vulnerable to fatigue damage. The typical crack locations and associated stresses close to the rib-to-crossbeam joint are shown in Figure 3.1. Among these stresses, the rib distortion will mainly cause the stress denoted as σ_{vr} which is along the vertical direction of the rib wall and perpendicular to the lower end of the weld. The correlated crack will initiate in the rib wall from the lower weld toe and propagate longitudinally. The stress σ_{lr} is in the rib along the longitudinal direction and perpendicular to the weld toe, which is mainly due to the longitudinal bending of the rib. Normally, it will lead to a vertical crack on the rib wall. The stresses denoted as σ_{tc} and σ_{cc} are related to the in-plane and out-of-plane behavior of the crossbeam. The stress σ_{tc} is in the crossbeam and along direction perpendicular to the weld toe. The relevant crack usually initiates from the the weld toe close to the termination and evolves upwards. The cracks that appear at the free edge of the cope hole can be related to the stress σ_{cc} which is perpendicular to the normal direction of the cope hole.

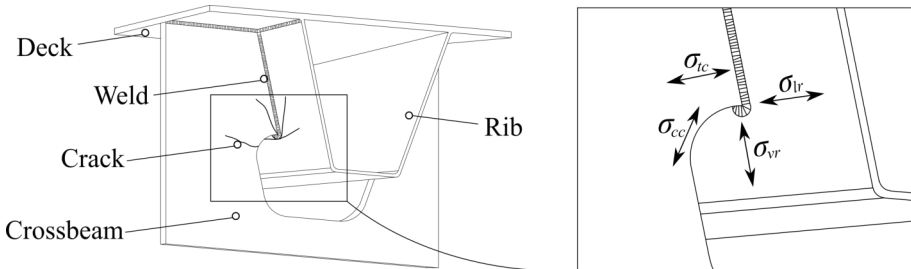


Figure 3.1: Typical crack locations and associated stresses close to the rib-to-crossbeam joint

3.2 Finite element model

Initially, a standard OSD is designed, the dimensions of which will be adopted as a reference for the verification tests introduced later in chapter 4. It is composed of 6 ribs, 3 crossbeams and 2 main girders. The longitudinal trapezoidal ribs are 300 mm high, 300 mm wide at the top and 125 mm wide at the bottom. The distance between adjacent ribs is also 300 mm. The height of the crossbeam and of the main girder is 600 mm and 1000 mm respectively. The thickness of the deck, the rib and the crossbeam are 15 mm, 6 mm and 15 mm respectively. The radius of the cope hole is 50 mm and the radius of the curvature at the bottom of the rib is 25 mm. The spacing between crossbeams (i.e. span) is 4000 mm. The height of the weld between the longitudinal rib and crossbeam is 200 mm. Relevant dimensions are shown in Figure 3.2.

The FEA is performed using the software ANSYS. According to the design of the standard OSD, a global model is built first using shell elements SHELL63 with a relatively coarse mesh as shown in Figure 3.3(a). In order to take the influence of welds into account and to get a more accurate distribution of stresses, a submodel is built using solid elements SOLID45 as presented in Figure 3.3(b). The submodel is composed of part of the deck, rib, crossbeam and welds. The location of the submodel is at the intersection of rib 3 and the middle crossbeam as the part marked by a red color in the middle of Figure 3.3. The cross-section of the weld in the submodel is modeled as a triangular, and the throat thickness of weld is set to 4 mm.

Linear-elastic material properties are used in both models. The Young's modulus of steel is 210 GPa and the Poisson's ratio in the elastic range is 0.3. As stated in section 2.4, the definition of the nominal stress is not very clear at this joint due to the influence of the secondary stresses induced by rib distortion. Meanwhile, the effective notch stress cannot be measured directly, which is impossible for the verification. Therefore, the hot spot stress method is finally adopted. Based on the recommendations of IIW (Hobbacher, 2019), a refined mesh is required to adopt the linear extrapolation method. The mesh of the submodel is displayed in Figure 3.3(c). Two reference points are at a distance of $0.4t$ and $1.0t$ away from the weld toe, where t is the thickness of rib. The mesh size of the elements close to the target line is controlled at $0.1t$ which equals 0.6 mm. The requirement of the linear extrapolation method is fulfilled, which is the element length should be no more than $0.4t$ as stated in section 2.4.1.2.

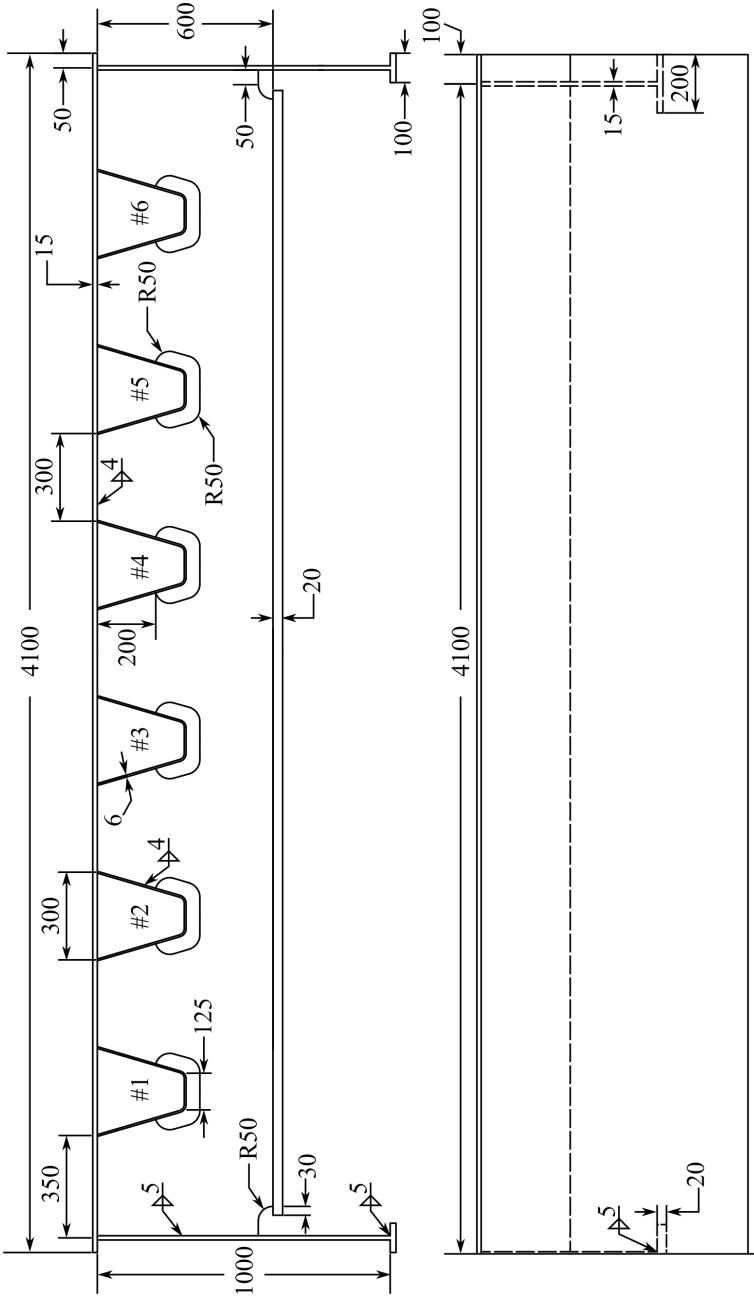


Figure 3.2: Dimensions of the standard OSD (unit: mm)

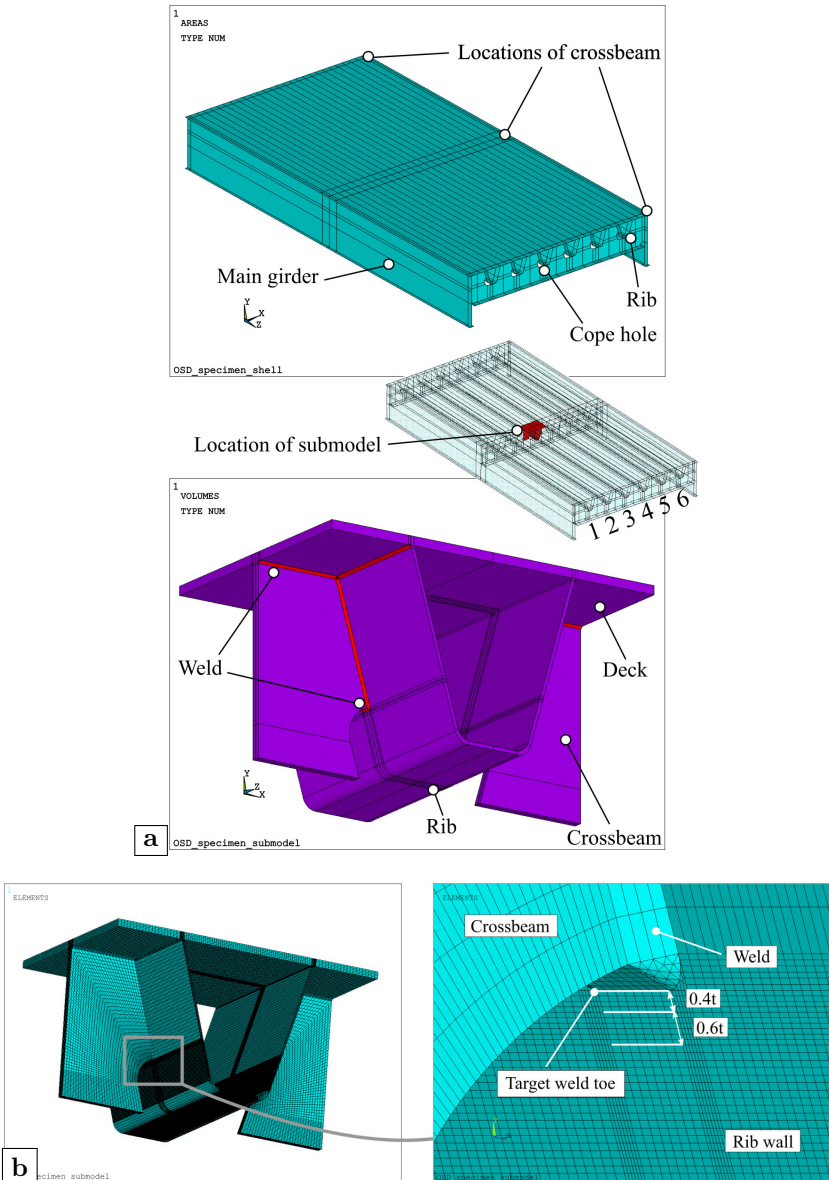


Figure 3.3: Finite element models of parametric analyses: (a) global model and submodel; (b) mesh of submodel

3.3 Boundary condition and load cases

The boundary conditions of the global model are similar to the bearing settings of a normal bridge. Six virtual bearings in total are placed at the middle and both ends of the two main girders separately, as shown in Figure 3.4. The fixed bearing is at the lower left corner in the figure. The arrows at the other locations indicate that the movement along the corresponding directions are not restricted. The contact area of a bearing is 80×80 mm.

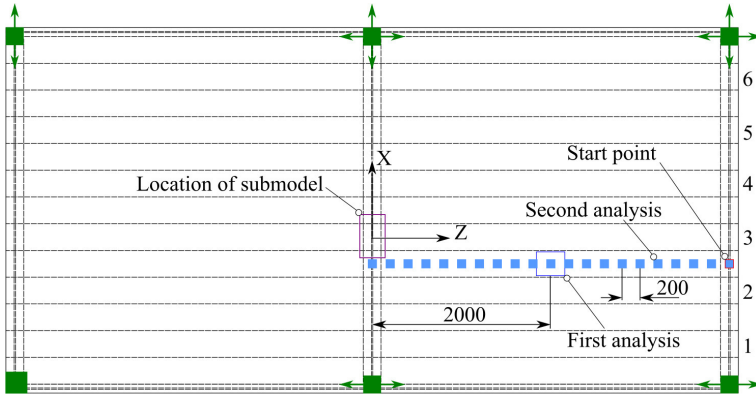


Figure 3.4: Boundary conditions and load cases (unit: mm)

The boundary conditions for the submodel are extracted from the calculation results of the global model. Since the global model and the submodel use different elements, the shell-to-solid submodeling technique is adopted. Figure 3.5 presents an illustration of a refined solid submodel superimposed on a coarse shell model. It should be noted that the shell element planes are at the middle plane of the corresponding positions in the solid submodel. In another word, the submodel is approximately centered on the shell model. Meanwhile, the same coordinate system should be used in both models. The procedure of shell-to-solid submodeling is as follows:

- open the submodel. Cut boundaries on the submodel are the end planes that are normal to the shell plane. Relevant information of nodes on these cut boundaries are written to the node file by the command `NWRITE`;
- switch to the global model. To determine the degree of freedom (DOF) values of a node on the cut boundary plane, the program first projects the node onto the nearest element in the shell plane. The DOF values of this projected point are then calculated by interpolation and assigned to the corresponding node. Once the translations and rotations of the

projected points are acquired, the translational displacements of the cut boundary node is calculated accordingly. Thus, a `.cbdo` file including the DOF information of all cut boundary nodes is generated by the command `CBD0F`;

- switch back to the submodel. The DOF specifications of cut boundary nodes are applied on the submodel as constraints using the command `INPUT`. Therefore, the submodel can be solved to get final results.

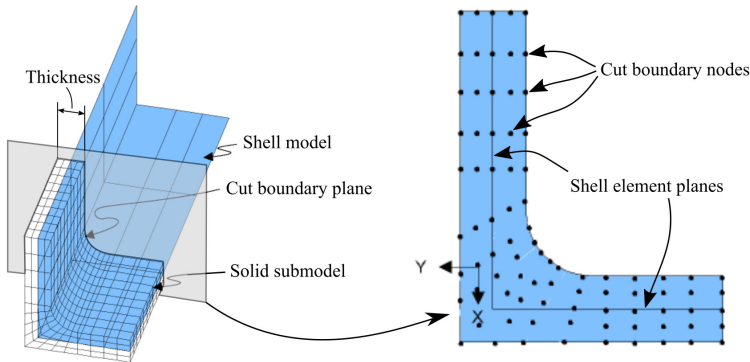


Figure 3.5: Illustration of a refined solid model superimposed on a coarse shell model (adapted from ANSYS Help manual (ANSYS Inc., 2007))

Two analyses in total are performed, and different load cases are adopted respectively. In the first analysis, a fixed single tire load is considered. It should be emphasized that the purpose of the analyses is to determine the influence of classic design parameters on the distortional behavior. Given the adopted linear-elastic material assumption, the magnitude of load may be arbitrarily selected. With a reference to Eurocode (CEN, 2003), Fatigue Load Model 1 to 3 are intended to be used to determine the maximum and minimum stresses resulting from the possible load arrangements on the bridge of any of these models. Meanwhile, Fatigue Load Model 2 is more suitable when the simultaneous presence of several lorries on the bridge can be neglected for the fatigue verification. Hence, a heavy rear axle from the set of lorries of Fatigue Load Model 2 is considered. The axle load of 110 kN with tire type C is chosen. Besides, an additional dynamic amplification factor of 1.3 is selected from a conservative perspective. Therefore, one fixed tire load of 70 kN is placed at midspan longitudinally and at the center between rib 2 & 3 horizontally, as marked by an empty rectangle in Figure 3.4. The contact area of tire type C is 270 mm wide and 320 mm long.

In order to verify the most unfavorable load positions for the distortional

stresses, a movable unit load is considered to get the influence lines of the distortional stresses in the second analysis. A pressure of 1 MPa is adopted with load area of 100×100 mm and the total load of 10 kN. The load path is at the central line between rib 2 & 3, as marked by the series of small solid rectangles in Figure 3.4. The interval distance between two load points is 200 mm. The starting point of the load path is above the crossbeam at the right end of the model.

3.4 Results and discussion

3.4.1 First analysis

As a trial calculation, the calculation result of the standard design is shown in Figure 3.6. Due to the eccentric load, obvious rib distortion is observed on rib 2 and rib 3. Taking a closer look at rib 3, it can be seen that tension stresses appear at the rib wall of the left side which is also closer to the horizontal position of the load, and compression stresses appear at the rib wall of the right side. A symmetrical situation can be found on rib 2. Figure 3.6(b) displays the equivalent stress (i.e. Von Mises stress) distribution closer to the rib-to-crossbeam joint on the tension side from the result of submodel. Strictly speaking, the stresses that are normal to the direction of welds should be adopted when performing fatigue life assessments using the hot spot stress method. But the equivalent stress is selected to give a general examination of the distortional behavior. It can be observed from the figure that the stress concentration appears at the weld toe on the rib wall as anticipated. The maximum stress point is at the transition point from the curvature part to the bottom part as annotated by *MX*. One possible explanation is that the transition point represents a point of geometrical discontinuity and it is also closer to the load position. Except for the maximum stress of 190.35 MPa, stresses at the lower weld toe are around 105 to 120 MPa. Due to the relatively large stress gradient, the stress concentration would quickly diminish in only a couple of millimeters away from the weld toe. It should be noted that the coordinate system shown in Figure 3.6(b) will be further used to display the stress distribution along the weld toe later in this section.

For the first analysis, 5 classic design parameters are considered, namely the thickness of the rib, the transversal spacing of the rib, the height of the crossbeam, the longitudinal spacing of the crossbeam and the weld length of the rib-to-crossbeam joint. Only one parameter changes each time, which means the other dimensions would be kept the same as the standard design. Note that the thickness of the rib is normally determined by the stiffness of rib. Therefore, the moment of inertia of one single rib plus the corresponding deck plate is treated

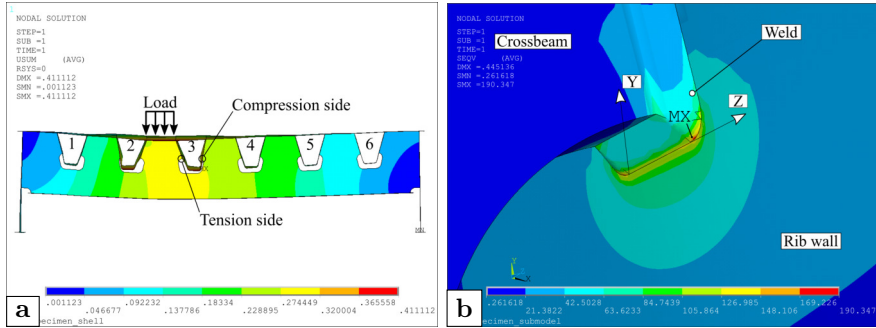


Figure 3.6: Result of the standard design: (a) displacement of the global model; (b) stress distribution close to weld toe on tension side

as a constant reference when adjusting the thickness of rib. Hence, the height of the rib will change in accordance with the thickness of rib. Relevant model numbers with variable parameters are shown in Table 3.1.

3.4.1.1 Rib thickness

Figure 3.7 shows the influence of the rib thickness on the distortional stress. According to the figure, the distortional stress decreases as the rib thickness increases. On the tension side, the average distortional stress decreases from 89.10 MPa to 40.09 MPa when the rib thickness changes from 6 mm to 10 mm. On the compression side, the average distortional stress decreases from 69.72 MPa to 37.05 MPa when the rib thickness increases. Using a thicker rib could reduce the distortional stress, but the effect would gradually decline with the further increase of the rib thickness. Comparing the scheme of 9 mm to 10 mm, the decrease amplitude of the distortional stresses from the scheme 6 mm to 7 mm is more obvious especially on the tension side. As for the stress distribution, the stresses at the end that is closer to the load direction (i.e. where the distance equals 15 mm) are slightly bigger than the opposite end (i.e. where the distance equals 0) on both sides. However, the stress distributions of different rib thickness remain the same. Therefore, the stress distribution is not affected by this parameter.

3.4.1.2 Rib distance

Figure 3.8 presents the influence of the rib distance on the distortional stress. In general, the distortional stress and the rib distance are positively correlated. On the tension side, the average distortional stress rises from 75.76 MPa to 94.22 MPa as the rib distance increases from 200 mm to 375 mm. Meanwhile, the average distortional stress climbs from 61.89 MPa to 72.51 MPa on the

Table 3.1: Dimensions for first analysis (unit: mm)

Model number	Rib height	Rib thickness	Rib distance	Crossbeam height	Crossbeam spacing	Weld length*
Standard	300	6	300	600	4000	200
1	285	7				
2	275	8				
3	265	9	300			
4	255	10				
5			200	600		
6			250			
7			350		4000	
8			375			
9				500		200
10				700		
11				800		
12				900		
13	300	6			2500	
14					3000	
15			300		3500	
16					5000	
17				600		150
18						180
19					4000	210
20						240

* Weld length means the vertical weld length of the rib-to-crossbeam joint.

compression side. Nevertheless, it should be noted that when the rib distance changes from 300 mm through 350 mm to 375 mm, the distortional stresses first decrease then increase on both sides. One possible explanation is that the relative size of contact area, which is 270 mm, to the rib distance will affect the load dispersion. Similar to the rib thickness, the rib distance does not have an obvious influence on the stress distribution.

3.4.1.3 Crossbeam height

Figure 3.9 displays the influence of the crossbeam height on the distortional stress. Compared to the other parameters, the influence of the crossbeam height on the rib distortion is rather small. On the tension side, the distortional stress decreases by 2.5 MPa as the crossbeam height increases from 500 mm to 900 mm. On the compression side, the distortional stresses remain almost the same when

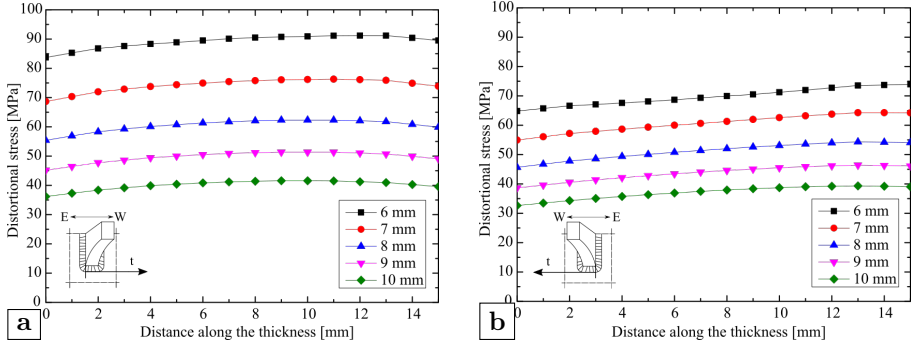


Figure 3.7: Influence of the rib thickness: (a) tension side; (b) compression side

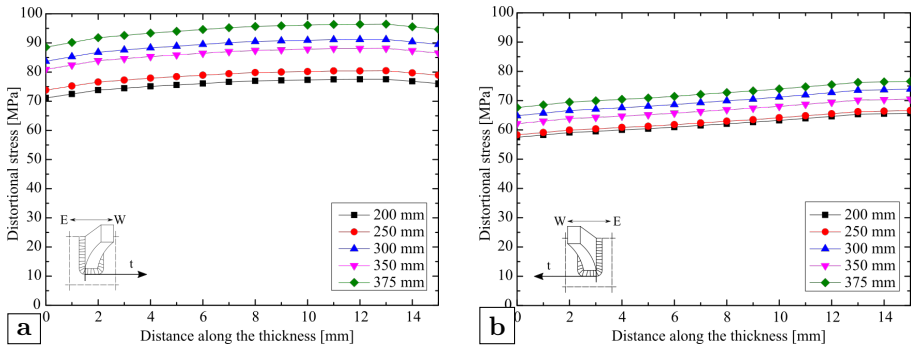


Figure 3.8: Influence of the rib distance: (a) tension side; (b) compression side

the crossbeam height changes. According to Leendertz (2008), the crossbeam height is a very important factor that affects the crossbeam’s in-plane and out-of-plane behavior. A higher crossbeam represents a more rigid support that will affect the bending moment and shear on the crossbeam. However, its influence on the rib distortion is quite limited.

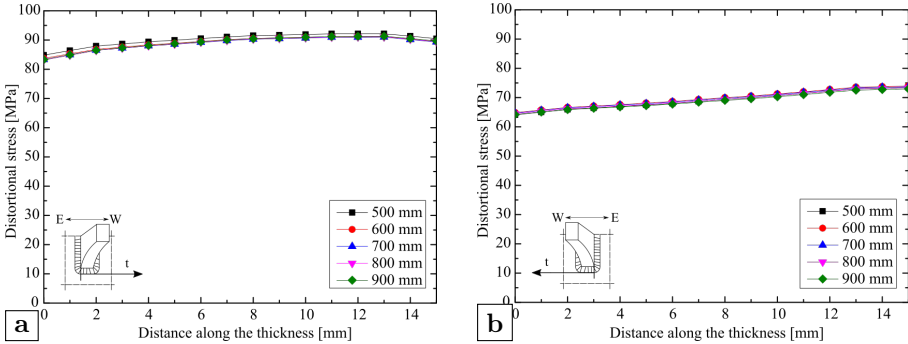


Figure 3.9: Influence of the crossbeam height: (a) tension side; (b) compression side

3.4.1.4 Crossbeam spacing

Figure 3.10 shows the influence of the crossbeam spacing on the distortional stress. In general, the distortional stress and the crossbeam spacing are positively correlated. When the spacing of the crossbeam decreases from 5000 mm to 2500 mm, the average distortional stress of the tension side declines from 95.04 MPa to 66.06 MPa and the average distortional stress of the compression side drops from 76.99 MPa to 46.78 MPa. The calculation results also indicate that the stress distribution may be affected by the crossbeam spacing. When the crossbeam spacing goes down, the distortional stress tends to be more uniformly distributed along the weld toe. Compared with the tension side, this phenomenon is more outstanding on the compression side, which is proven by the flatter curve of distortional stresses when the crossbeam spacing equals 2500 mm.

3.4.1.5 Weld length of the rib-to-crossbeam joint

Figure 3.11 presents the influence of the weld length of the rib-to-crossbeam joint on the distortional stress. The distortional stress and the weld length show a positive correlation. If the weld length of the rib-to-crossbeam joint increases from 150 mm to 240 mm, the average distortional stress rise from 81.50 MPa to 95.73 MPa on the tension side. On the compression side, this parameter appears relatively larger influence. The average distortional stress

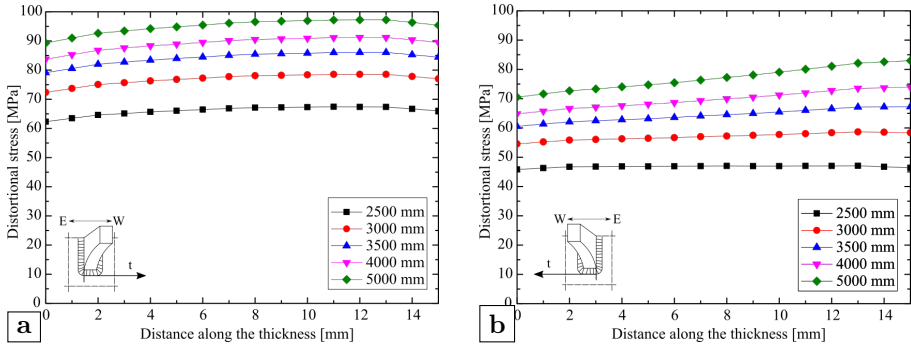


Figure 3.10: Influence of the crossbeam spacing: (a) tension side; (b) compression side

enlarges from 55.50 MPa to 82.28 MPa when the weld length changes the same. On the other hand, the influence of this parameter on the stress distribution is not very obvious.

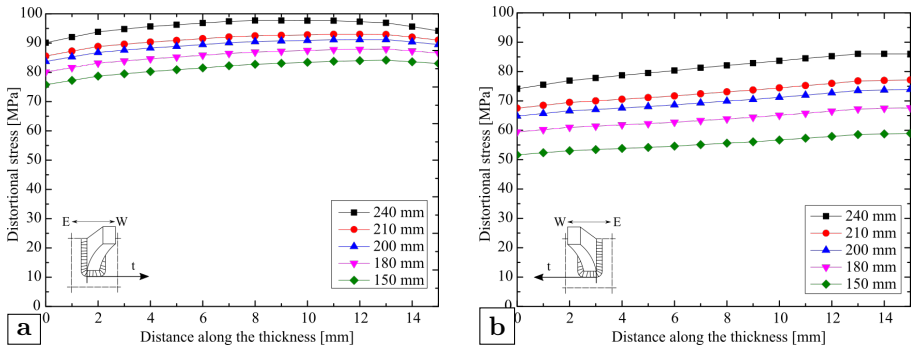


Figure 3.11: Influence of the weld length of the rib-to-crossbeam joint: (a) tension side; (b) compression side

3.4.1.6 Concluding remarks for first analysis

When examining the calculation results, it is found that some combinations of parameters e.g. using a thicker rib or a shorter crossbeam spacing could reduce the distortional stress at rib-to-crossbeam joint, meanwhile the stress concentration transfers to other locations as well. The results of model 4 and model 13 are presented in Figure 3.12 and 3.13, for a rib thickness of 10 mm. The stress peak appears on the rib wall close to the rib-to-deck joint instead of the rib-to-crossbeam joint. However, it should be noted that this situation can

also be induced by interpolations of the nodal displacement since the appeared stress concentration is quite close to the cut boundary plane.

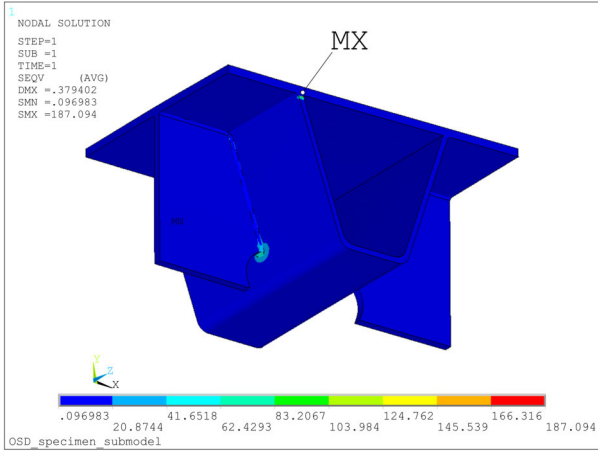


Figure 3.12: Calculation results of model 4 with rib thickness of 10 mm

3.4.2 Second analysis

According to the first analysis, the parameter crossbeam height does not have an obvious influence, therefore it is eliminated from the second analysis. Using the same boundary conditions as the first analysis, a unit load is adopted to verify whether midspan is the most critical load position by determining the influence lines of distortional stress. Due to the fact that there is no dramatic change of the distortional stress along the target weld toe as illustrated in Figure 3.6, the average distortional stress along the target weld toe is exported as a representative in the second analysis. The other four parameters are considered as summarized in Table 3.2. Note that the interval distance between two sequential load points is 200 mm. When the crossbeam spacing increases, the corresponding number of load points are added to ensure that the load path still covers the whole span.

3.4.2.1 Rib thickness

Figure 3.14 shows the influence lines of different rib thickness. On the tension side, the maximum distortional stress decreases from 10.27 MPa to 5.27 MPa when the rib thickness changes from 6 mm to 10 mm. On the compression side, the maximum distortional stress declines from 7.94 MPa to 4.19 MPa as the rib thickness changes similarly. The most unfavorable load position is the location where the distortional stress reaches the peak value. It can be

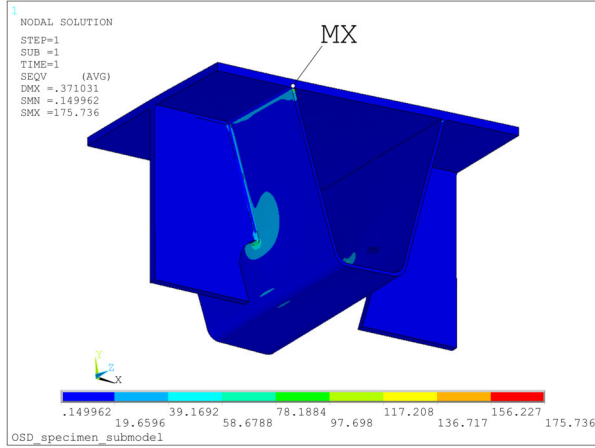


Figure 3.13: Calculation results of model 13 with crossbeam spacing of 2500 mm

Table 3.2: Dimensions for second analysis (unit: mm)

Model number	Rib height	Rib thickness	Rib distance	Crossbeam spacing	Weld length*
Standard	300	6	300	4000	200
1	275	8	300		
2	255	10	300		
3			200	4000	
4			375		200
5				2500	
6	300	6		5000	
7			300	4000	150
8				4000	240

* Weld length means the vertical weld length of the rib-to-crossbeam joint.

seen from the figure that the most unfavorable load position is affected by this parameter. When the rib thickness is 6 mm, the most unfavorable load position is at 2500 mm from the target crossbeam (i.e. the location of the submodel). If the thickness rises to 10 mm, the most unfavorable load position would move towards the target crossbeam by 600 mm.

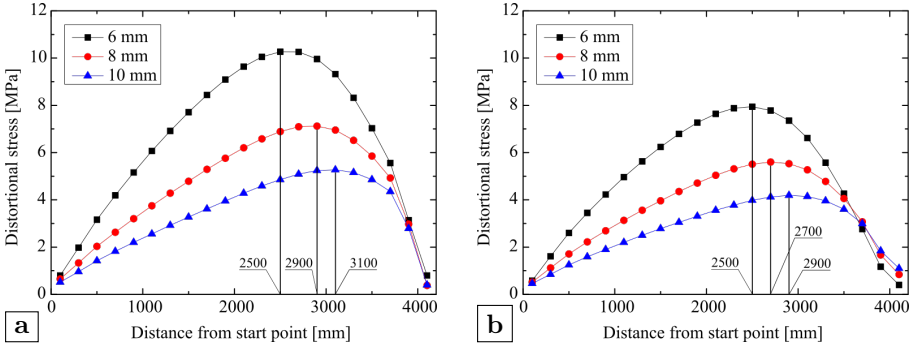


Figure 3.14: Influence lines of different rib thickness: (a) tension side; (b) compression side

3.4.2.2 Rib distance

Figure 3.15 displays the influence lines for different rib distance. The maximum distortional stress increases from 9.30 MPa to 10.18 MPa on the tension side and from 7.07 MPa to 8.16 MPa on the compression side if the rib distance is reduced from 375 mm to 200 mm. The distortional stress and the rib distance have a negative correlation. However, according to the results from the first analysis, the distortional stress would increase when the rib distance increases. The relative size between the rib distance and the width of the load area would influence the load dispersal which has a further impact on the distortional stress. The most unfavorable load positions on both sides are not influenced by the changes of the rib distance, which shows an offset of about 400 mm from the midspan to the target crossbeam.

3.4.2.3 Crossbeam spacing

Figure 3.16 presents the influence lines of different crossbeam spacing. The distortional stress and the crossbeam spacing are also positively correlated. On the tension side, the maximum distortional stress goes down from 11.57 MPa to 6.90 MPa as the crossbeam spacing decreases from 5000 mm to 2500 mm. Meanwhile, the maximum distortional stress diminishes from 9.14 MPa to 5.28 MPa. As for the most unfavorable load position, the influence of the crossbeam

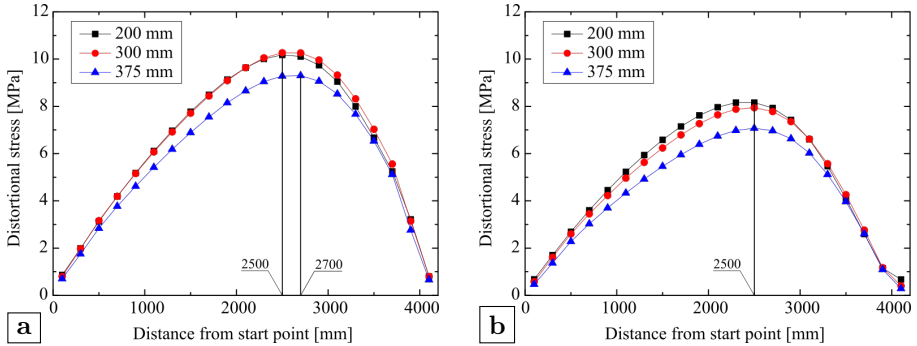


Figure 3.15: Influence lines of different rib distance: (a) tension side; (b) compression side

spacing is not obvious. The most unfavorable load position is always located at around 1600 mm away from the target crossbeam no matter how the crossbeam spacing changes.

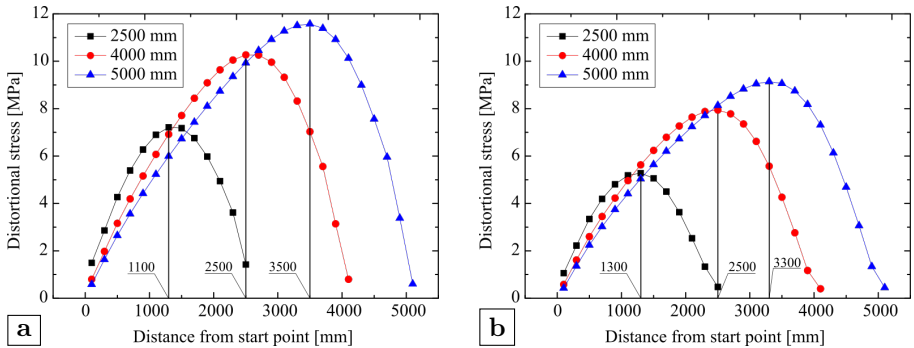


Figure 3.16: Influence lines of different crossbeam spacing: (a) tension side; (b) compression side

3.4.2.4 Weld length of rib-to-crossbeam joint

Figure 3.17 shows the influence lines of different weld length of the rib-to-crossbeam joint. The same result as the first analysis is observed. In general, the distortional stress and the weld length of the rib-to-crossbeam joint are positively correlated. When the weld length of the rib-to-crossbeam joint increases from 150 mm to 240 mm, the maximum distortional stress also increases from 9.32 MPa to 11.18 MPa on the tension side. At the same time, the maximum distortional stress increases from 6.20 MPa to 9.44 MPa on the

compression side. The most unfavorable load position is not affected by the weld length of rib-to-crossbeam joint, which stays at the same distance away from the target crossbeam.

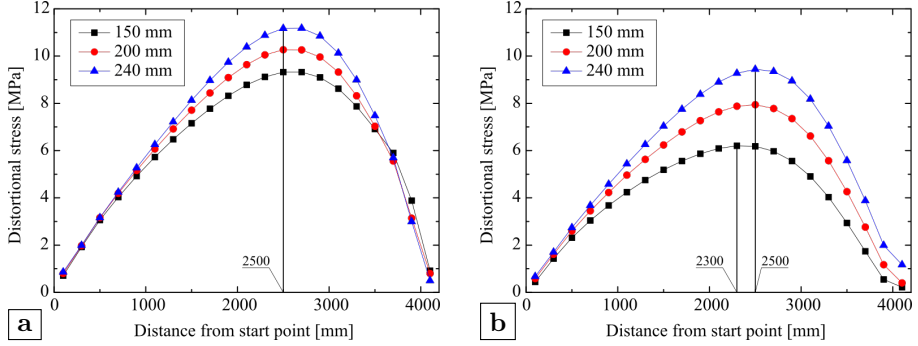


Figure 3.17: Influence lines of different weld lengths of the rib-to-crossbeam joint: (a) tension side; (b) compression side

3.5 Conclusions

In this chapter, the influence of different design parameters on the distortional behavior of the ribs is discussed. The distortional stresses that distribute at the lower weld toe of the termination between two transition points are chosen as the reference for comparison. 5 design parameters in total are analyzed, namely the rib thickness, the rib distance, the crossbeam height, the crossbeam spacing and the weld length of the rib-to-crossbeam joint. Among these parameters, the crossbeam spacing and the weld length of the rib-to-crossbeam joint have positive correlations with the distortional stress. The rib thickness has a negative correlation with the distortional stress. The influence of the rib distance on the distortional stress depends on the relative size between the width of load area and the rib distance. When adopting the tire load with a load width of 270 mm, the distortional stress is generally negatively correlated with the rib distance. The crossbeam height does not have an obvious influence on the distortional behavior.

Based on the influence lines obtained from the second analysis, the most unfavorable load position for the distortional stress is determined by the dimensions of the ribs, whereas the other considered parameters do not show an obvious effect. In this case, the most unfavorable load position for the distortional stress is at a distance of about 1600 mm away from the investigated crossbeam rather than at the midspan when the crossbeam distance is equal or

larger than 4000 mm. When the rib thickness gets larger, the most unfavorable load position moves towards the investigated crossbeam.

In the first analysis, it is found that some approaches e.g. increasing the rib thickness or decreasing the crossbeam spacing could reduce the distortional stress, but the stress concentration at the rib-to-deck joints also becomes more prominent at the same time. This phenomenon is harmful for the rib-to-deck joint, hence it should be paid attention when designing an OSD.

4

Experimental study

This chapter is based on:

Fang H., Iqbal N., Van Staen G., et al. (2021). Experimental and numerical investigation of stress concentration at rib-to-crossbeam joint. *International Journal of Steel Structures*, 21(1):360-380.

4.1 Introduction

In previous chapter, the influence of different design parameters on the distortional behavior of the rib is discussed. Based on the influence lines acquired from simulations, the most unfavorable load position is also derived. In order to validate the numerical models and the calculation results, a full-scale OSD specimen is constructed and tested.

The dimensions of the OSD specimen are modified with respect to the standard design that was used in the parametric analysis. It is also composed of two main girders, three crossbeams and six ribs. The total length of the specimen is 8.2 m and the total width is 4.2 m. The trapezoidal section of the ribs is 300 mm high, 300 mm wide at the top and 125 mm wide at the lower soffit. The center-to-center distance of adjacent ribs is 600 mm. Each rib-to-crossbeam joint has a different cope hole height. The weld length varies from 127 mm to 252 mm as shown in Figure 4.1. Different weld lengths lead to different termination locations on the rib wall which may have a certain influence on the load dispersal behavior, but the mutual influence of the varying weld length is sufficiently small to conclude that the stresses in the individual ribs are representative as each rib in the deck has the same weld length. The specimen is made of S235 steel with a yield strength of 235 MPa and an ultimate strength of 360 MPa (CEN, 2006). The deck plate has a thickness of 15 mm while the rib has a thickness of 6 mm. The thickness of the crossbeams is also 15 mm. The throat thickness of the welds at the rib-to-crossbeam joint and rib-to-deck joint is approximate 4 mm. For the other connections e.g. the welds between the crossbeam and the main girder as well as the welds between the main girder and the bottom flange, the throat thickness of 5 mm is therefore adopted. There is no asphalt layer added on the deck plate. A relative thick layer of paint is used instead to protect the specimen from corrosion.

A concrete basin is constructed to house the specimen. The deck plate is aligned with the road as shown in Figure 4.2. The specimen is simply supported by six concrete columns, which are placed under two main girders at the intersection location with crossbeams as marked by green color. The OSD specimen is accessible underneath through the stair entrance in order to attach the strain gauges. The rib at the closest position to the entrance corresponds to rib 1 in Figure 4.1, which has a weld length of 127 mm. The rib at the furthest location to rib 1 is rib 6 which has a weld length of 252 mm. Ribs in between rib 1 and rib 6 are rib 2 to 5 accordingly. The difference of the weld length of two adjacent ribs is 25 mm.

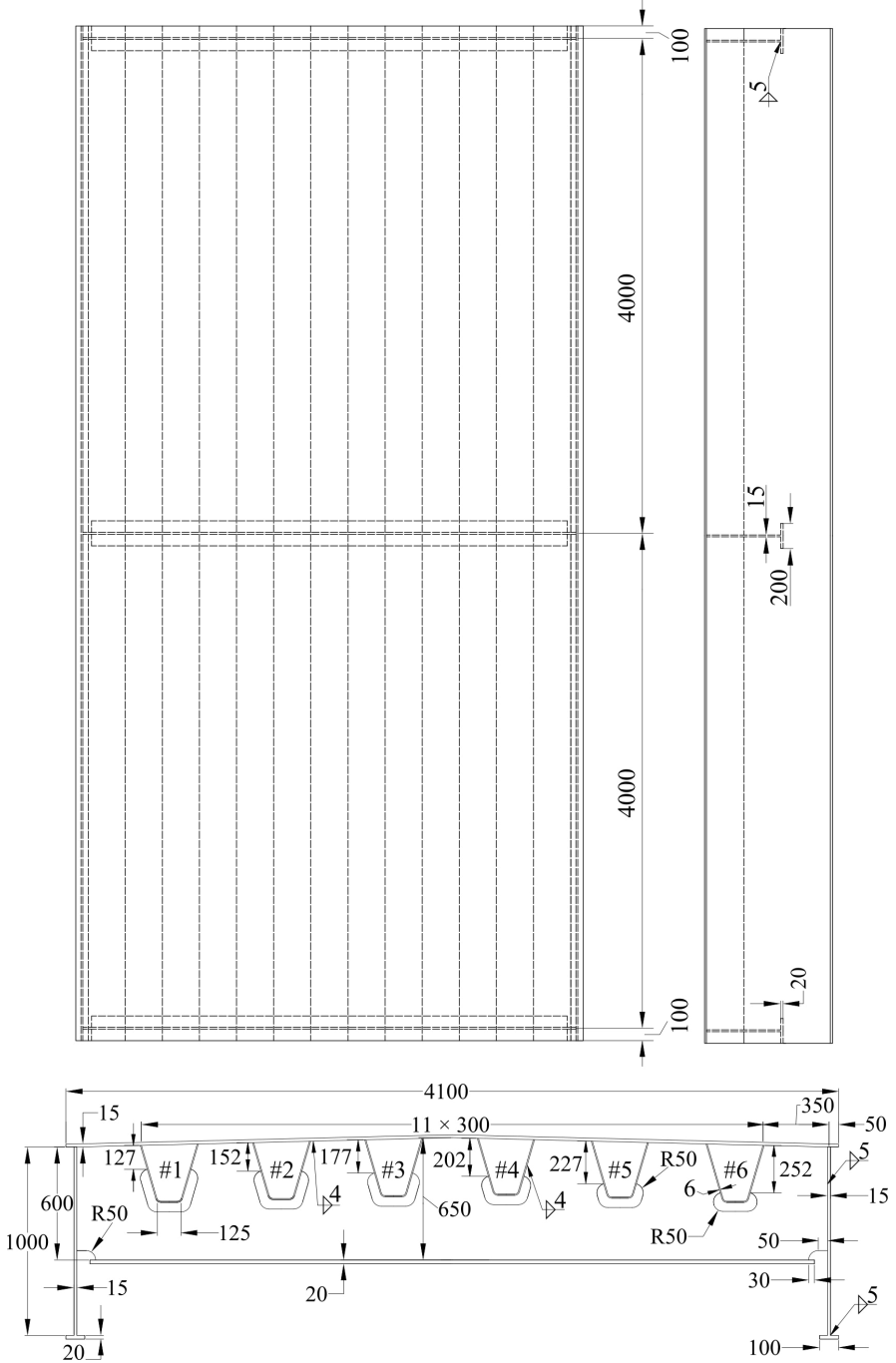


Figure 4.1: Dimensions of the OSD specimen (unit: mm)

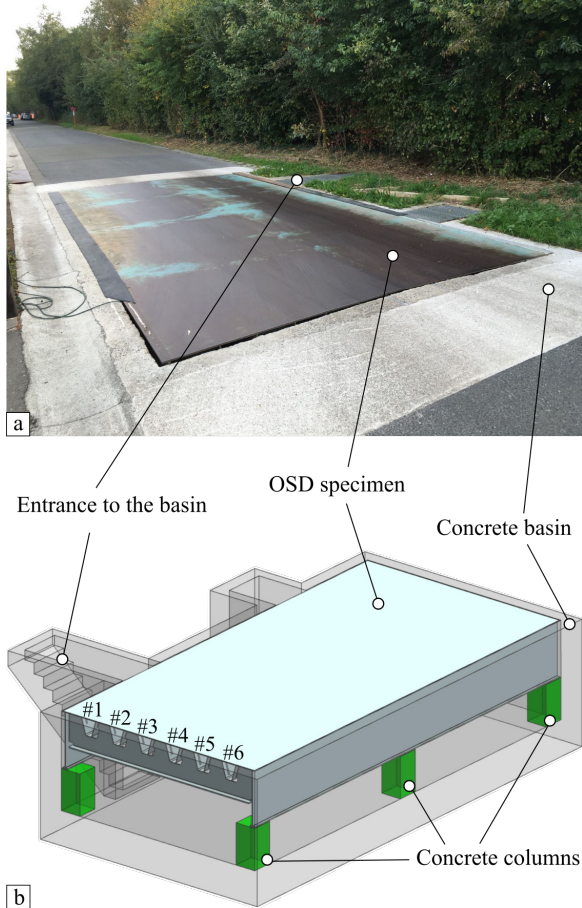


Figure 4.2: OSD specimen and the concrete basin: (a) on-site photo; (b) 3-D view

4.2 Instrumentation of tests

With respect to the discussion in chapter 2, the structural hot spot stress method seems to be more suitable for the rib-to-crossbeam joint since it is rather difficult to have a clear definition of the nominal stresses. Therefore, the structural hot spot stress method is adopted in the experimental study as well. According to the recommendations of IIW (Hobbacher, 2019), the reference points for measurement of the structural hot spot stress are the same as for the numerical calculation. For hot spot type a, which is defined in section 2.4.1.2, the structural hot spot stress could use either linear extrapolation with

two reference points (see Figure 4.3(a)) or quadratic extrapolation with three reference points (see Figure 4.3(b)). The recommendations also suggest that the strain gauge length should not exceed $0.2t$, where t is the thickness of the plate under consideration. The central point of the first strain gauge is located at a distance of $0.4t$ from the weld toe. If this was not possible for example due to a small plate thickness, the leading edge of the gauge should be placed at a distance of $0.3t$ from the weld toe as illustrated in Figure 4.3(c).

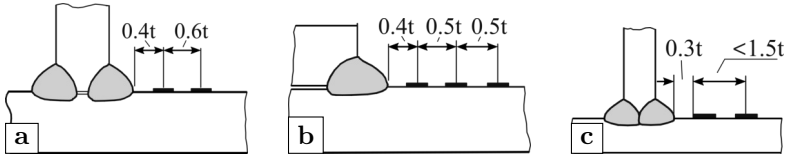


Figure 4.3: Examples of strain gauges in plate structures: (a) linear extrapolation; (b) quadratic extrapolation; (c) small plate thickness (adapted from Hobbacher (2019))

The rib distortion induced stress is related to the vertical stress on the rib wall at the vicinity of lower weld end. If the rib thickness is 6 mm, the distance from the reference points to the weld toe should be 2.4 mm and 6 mm respectively when using the linear extrapolation method. Nevertheless, direct measurements of stresses at these two points especially at the first reference point were rarely reported. Kolstein (2009) presented static and fatigue tests about the connection of ribs to crossbeam finished in 1995 as shown in Figure 4.4(a). Stresses are measured at points located between 4 mm, with an increment of 2 mm until 12 mm, away from the weld toe. The adopted rib thickness is 6 mm. Except the stresses at the central plane of the crossbeam, the stresses along the longitudinal direction are also measured. Choi & Kim (2008) reported tests about two full-scale OSD specimens with the rib thickness of 8 mm as shown in Figure 4.4(b). To measure the geometric stress concentration and residual stresses around the rib-to-crossbeam joint, strain gauges were installed at 5 mm and 15 mm distance from the weld toe. Yokozeki & Miki (2016) conducted fatigue tests on the OSD specimen with different construction details as shown in Figure 4.4(c). The rib thickness of the specimen is 6 mm whereas the measurement point is at 20 mm away from the curve end of the cope hole on the rib wall. Abdelbaset *et al.* (2020) performed tests on three full-scale rib-to-deck-to-crossbeam welded connections to investigate the effect of employing UHPC overlay on the hot spot stresses at fatigue prone details of OSDs as shown in Figure 4.2(d). Given the rib thickness of 8 mm, a similar scheme to the tests from Kolstein is used. Stresses are measured at distances of 4 to 12 mm away from the weld toe with a interval distance of 2 mm. Unfortunately, the results of strain gauges at 4 mm and a few other locations are missing due to errors in strain gauge data recording as stated in the article.

With reference to previous tests and the recommendations of IIW, the final arrangement of strain gauges are determined. Tests are conducted focusing on rib 2 and rib 3. Strain gauges are mainly distributed at two sections, the midspan section and the crossbeam section respectively as shown in Figure 4.5.

Three types of strain gauges are employed in total as summarized in Table 4.1. All strain gauges adopted in this research are produced by HBM. The 14.5 mm long strain gauge chains (model: 1-KY11-1/120) are placed on the vicinity below the weld of the rib-to-crossbeam joint. It comprises 11 measuring grids with a length of 0.6 mm, parallel to the chain axis. The last one can be cut off for temperature compensation if the temperature changes a lot during measurements. The leading edge of the plastic carrier board is supposed to be parallel to the target weld toe, and the central axis should be aligned with the central plane of crossbeam. Therefore, the distance from the first strain gauge to the weld toe is 2.75 mm, which is calculated based on the dimensions given in Table 4.1, under the ideal circumstance. The other reference point which is at 6 mm (i.e. $1.0t$) away from the weld toe is within the measurement range of the strain gauge chain. The rectangular rosette strain gauges (model: 1-RY81-1.5/120) are attached on the crossbeam. Based on the stress distribution acquired from the parametric analysis, stress concentrations appear at the lower curvature of the cope hole. The edge of the rosette strain gauge is parallel to the corresponding curvature, and its central line is along the angle's bisector. The rosette strain gauges are placed on the side of crossbeam that is towards the midspan section. The measurement of other positions at midspan section and crossbeam section is done by the 1.5 mm long single strain gauges (model: 1-LY11-1.5/350). The single strain gauges are mainly installed on the middle and lower end of the rib wall as well as the bottom of the soffit at both the midspan section and the crossbeam section. Detailed locations of the single strain gauges can be found in Figure 4.5.

The surface preparation before applying strain gauges includes the following steps: solvent degreasing, abrading, marking the gauge layout lines, conditioning the surface and finally neutralizing the surface (Nagy, 2017). For the convenience of installing, a relatively large area around the predefined location of strain gauges are abraded. After the surface abrading, the exact locations of the strain gauges are marked by the intersections of reference lines. Then, the contact area is cleaned and neutralized by using an effective degreasing solvent, water based acid and alkaline surface cleaners. The result of surface preparation generates a smooth and clean surface that is beneficial for the bonding of strain gauges and improving the accuracy of the strain results.

Although some strain gauges e.g. the single strain gauges and the rosette strain gauges have already been installed the solder taps for connecting the lead wires, an independent solder terminal is used. The advantage of using the

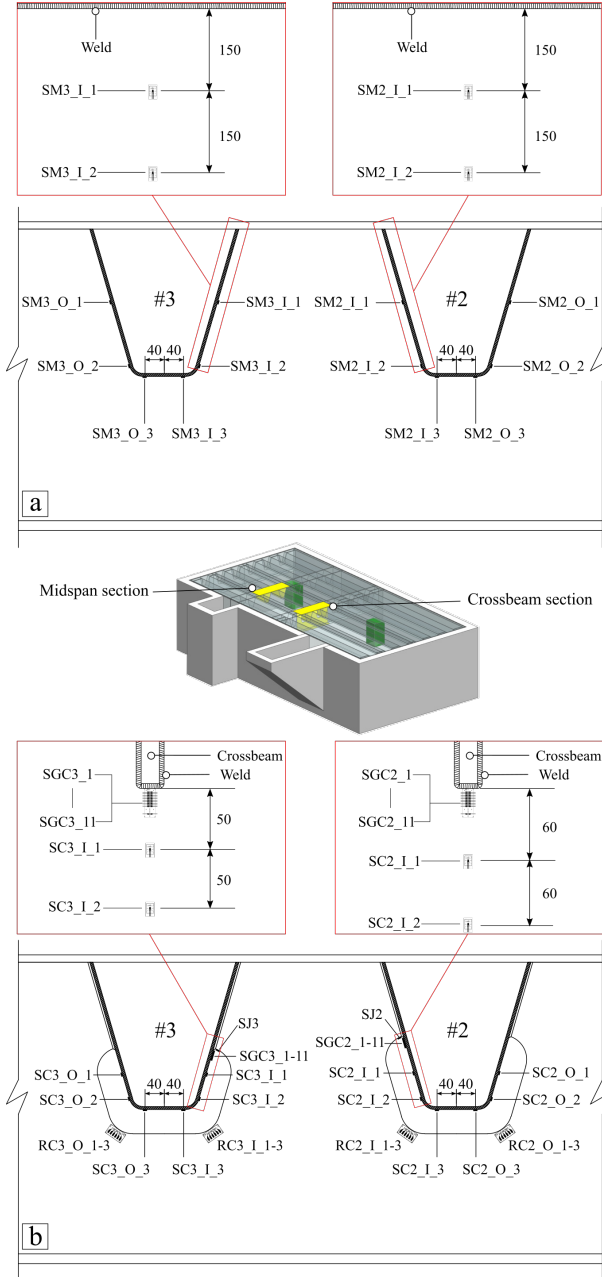
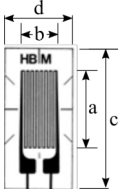
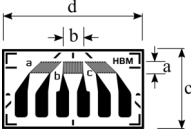
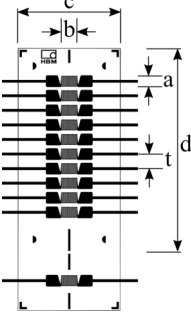


Figure 4.5: Locations of strain gauges: (a) at midspan section; (b) at crossbeam section (unit: mm)

Table 4.1: Adopted strain gauges for tests

Type	1-LY11-1.5/350	1-RY81-1.5/120	1-KY11-1/120
Illustration			
Nominal resistance	350 Ω	120 Ω	120 Ω
Measuring grid length (a)	1.5 mm	1.5mm	0.6 mm
Measuring grid width (b)	1.2 mm	1.4 mm	1 mm
Carrier length (c)	5.7 mm	8.2 mm	7.2 mm
Carrier width (d)	4.7 mm	14.6 mm	14.5 mm
Pitch (t)	-	-	1 mm

solder terminal is that it provides strain relief for the strain gauge connections since the wires may tear the strain gauges during soldering. Once the surface preparation is done, the strain gauge with the corresponding solder terminals are installed together using a short transparent tape as shown in Figure 4.6(a). A fast-drying and creep-free cyanoacrylate glue is smeared on the contact surface of strain gauge as well as the solder terminals. Then, the strain gauge with solder terminal is placed at the exact location. The next step is removing the tape and soldering the cables as shown in Figure 4.6(b). Depending on the data acquisition system, a quarter, half or full Wheatstone bridge completion can be used. For the experimental study, the data acquisition system Quantum X MX1615 from HBM is used. This system allows for a four-wire configuration. Compared to the three-wire configuration, the four-wire configuration has the advantage of directly compensating the lead wire resistance during measurement. The resistance of wires may change during measurement which would influence the results. Therefore, the four-wire quarter bridge completion is eventually adopted. In addition to the four-wire

configuration, the shielded cables are adopted which are able to protect the signals against external electromagnetic interference.

After the soldering of cables to the solder terminals, a rosin solvent is used to cover the whole strain gauge and solder terminal to prevent degradation of the protective coatings, corrosion of the metals and to eliminate conductive flux residues as shown in Figure 4.6(g). Finally, a nitrile rubber protective coating is applied on the strain gauges, solder terminals and all connections as shown in Figure 4.6(h). The numbers of the strain gauges are summarized in Table 4.2.

Table 4.2: Strain gauges numbers

Number	Type	Location
SGC2_1-11 SGC3_1-11	Strain gauge chain	Rib wall of rib 2 close to the weld toe
		Rib wall of rib 3 close to the weld toe
SC2_I/O_1-3 SC3_I/O_1-3	Single strain gauge	Rib 2 at the crossbeam section
SM2_I/O_1-3 SM3_I/O_1-3		Rib 3 at the crossbeam section
		Rib 2 at the midspan section
SJ2-3		Rib 3 at the midspan section
		Crossbeam side of rib-to-crossbeam joint
R2_I/O_1-3 R3_I/O_1-3	Rosette strain gauges	Curvature of cope hole at rib 2
		Curvature of cope hole at rib 3

4.3 Load cases and test procedure

A car of the model Peugeot 807 is used for loading. The total weight of the car is 1760 kg. As for the weight distribution, the weight of the front axle is 1080 kg and the weight of the rear axle is 680 kg. The distance of two axles is 2823 mm and the transversal distance between tires is 1570 mm for the front axle, 1550 mm for the rear axle. For all axles, the same type of tire is adopted. The contact area of one single tire is measured as about 220×180 mm.

In total 21 load positions are tested with an interval center-to-center distance of 400 mm as presented in Figure 4.7. Facing the forward direction, the right side tires of the loading car are located in the central line between rib 2 and rib 3. The left side tires are above one stem of rib 5. Note that only the locations of the front tires are drawn in the figure. Therefore, only the front axle is actually plated on the specimen for the first several load cases. The specimen is loaded by the whole car from load case 8 until load case 21 given the distance of two axles is about 2800 mm.

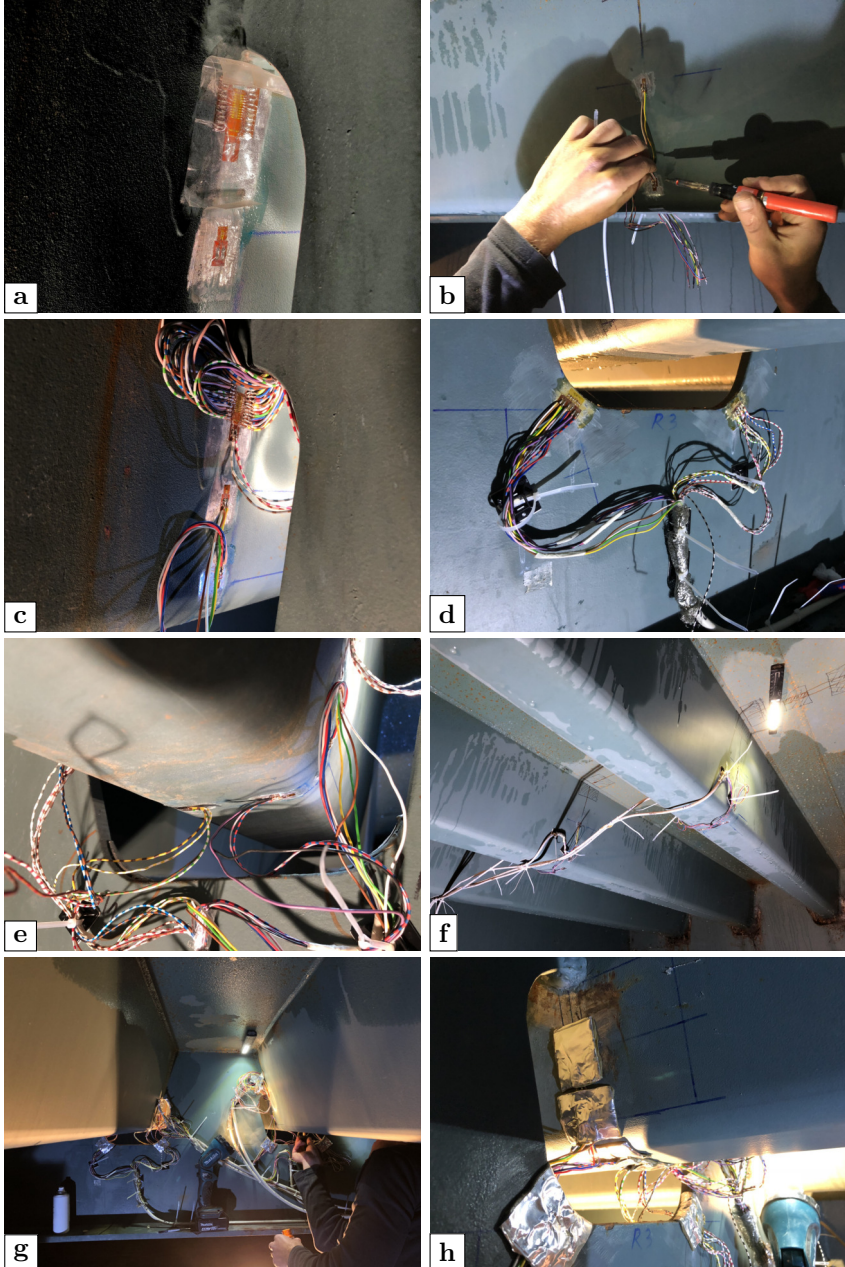


Figure 4.6: On-site photos of strain gauge installment: (a) preliminary bond; (b) cable soldering; (c) strain gauge chain; (d) rosette strain gauges; (e) single strain gauges at crossbeam section; (f) single strain gauges at midspan section; (g) applying rosin solvent; (h) protective coating attached

When preparing the tests, the measurement system runs for 5 minutes in advance to warm up all strain gauges and secure connections. Then, the loading car is sequentially stopped at every designed load position for 3 minutes, during which time the measurement results of the strain gauges are recorded continuously with a frequency of 50 Hz.

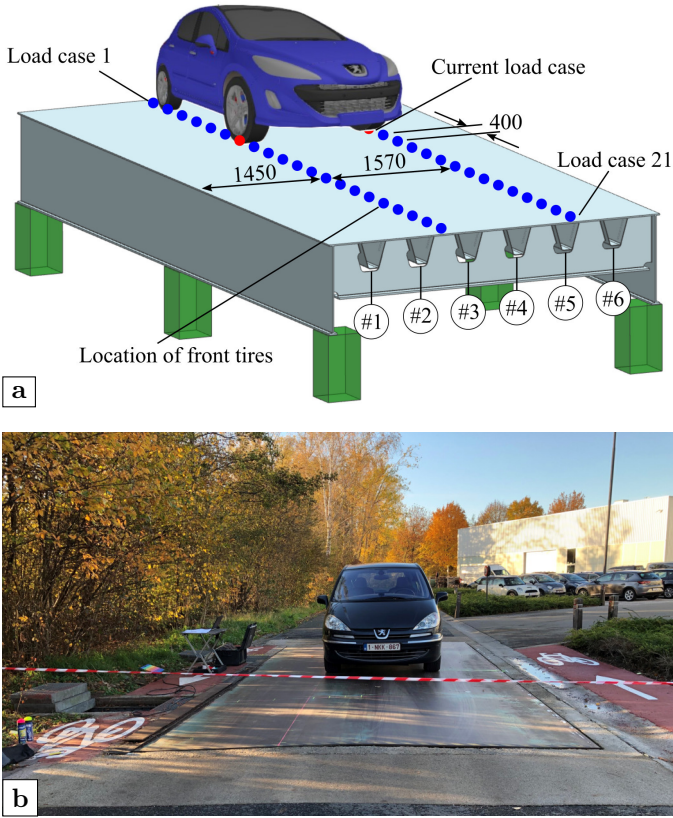


Figure 4.7: Arrangement of load cases: (a) illustration; (b) on-site photo (unit: mm)

4.4 Data processing

60 independent measurement points in total are recorded. The whole measurement lasted for about 75 minutes which generates a raw data file of 118 MB. The raw data is shown in Figure 4.8. There are two strain gauges that give obviously abnormal results. The results of other strain gauges are within -50 to $50 \mu\epsilon$ and show different stages that correspond to different load cases.

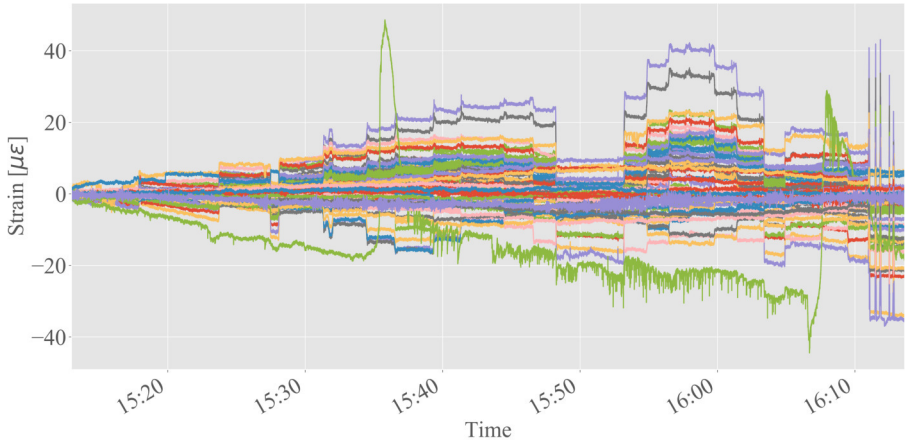


Figure 4.8: Raw data of tests

The open source Python libraries Pandas and Matplotlib are utilized to further processing and visualizing the data. The manuscript for processing the data of HBM measurement system is given in appendix A.1. The whole data is first re-sampled to seconds by the mean method. Since the data of three minutes are recorded for each load case, only the data points from the middle one minute are selected to eliminate the influence induced by moving the loading car, which is illustrated in Figure 4.9. According to the preliminary investigation of the raw data, this strategy is capable to get stable results. However, when checking the final results, some of them are quite divergent from the anticipated ones especially for the strain gauge chains. With reference to the results of FEA in previous chapter, the stress concentration is supposed to reach the peak at the target weld toe and to gradually decrease with the increment of the distance away from the weld toe. Nevertheless, the relative relationship is out of order for specific locations if the raw data was presented directly. Relevant results will be presented in the next section.

One possible explanation for this phenomenon is that a kind of interfering signal exists. The interfering signal may be induced by factors other than the structural deformation. The principal of strain measurement is that the strain gauge is a small electrical resistance. Either elongation or contraction of the structural surface would be captured by the strain gauge and eventually reflected in the changes of electrical resistance since the strain gauge is tightly attached on the structure surface. Apart from the structural behavior, the possible interfering signal induced by other factors e.g. the local temperature changes, the moving of cables etc. is also recorded and affects the final results.

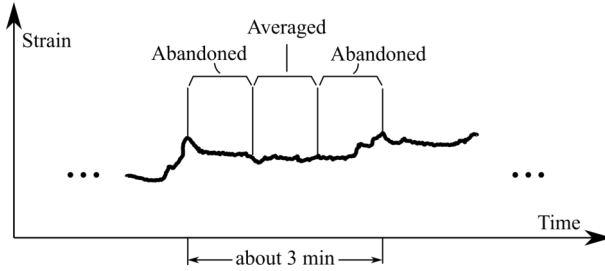


Figure 4.9: Illustration of the data processing of one load case

In order to eliminate the interfering signal, the assumption that the deviations of the strain are linearly depending on time is finally adopted as illustrated in Figure 4.10). Two time points before and after the measurement are chosen separately as the reference points. At these two time points, the structural strain is assumed to be zero, therefore the measured strains are all caused by the interfering signal. For every time point during the measurement, the corresponding measurement deviation is calculated through linear interpolation. Finally, the deviations are compensated from the raw data.

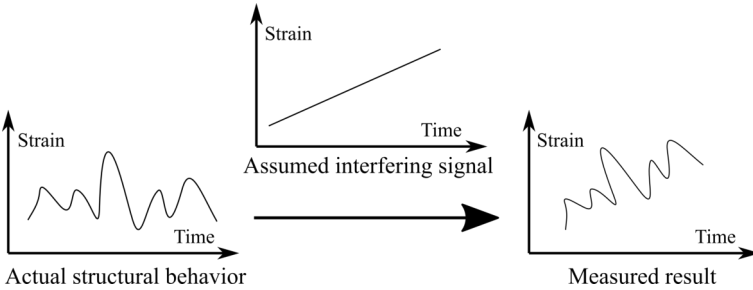


Figure 4.10: Illustration of interfering signal

4.5 Results and discussion

For every group of strain gauges, the raw data and the filtered result are presented side-by-side for comparison. Figure 4.11 and Figure 4.12 are the results of strain gauge chains at rib 2 and rib 3. The name of a strain gauge with a smaller post-fix means it is closer to the target weld toe. Before filtering the interfering signal, the disordered results are observed in both two locations. The strain gauge SGC2_1 is the closest strain gauge to the weld toe but its result is much smaller than the others. A similar situation is found on rib 3

as the results of SGC3_4 and SGC3_6 are deviating from the adjacent strain gauges and are smaller than the rest of the strain gauges. Moreover, stresses appearing at these two locations should always be tension stresses according to the simulations, however negative strains are recorded which is theoretically impossible. After the processing, a clearer stress gradient is shown in both locations, even though the results of SGC3_9 to SGC3_10 are still abnormally located in between SGC3_6 and SGC3_7. When getting closer to the weld toe, the stress gradient is gradually increasing, which is reflected in the relatively larger difference in strain gauges ending with index 1 to 3. The overall trends of these two locations are very similar. The peak value appears at load cases 14 or 15. Note that the load case 11 is when the front tire is just above the middle crossbeam. For load cases 14 and 15, the front tires are at 1200 mm and 1600 mm away from the middle crossbeam respectively, meanwhile the rear tires are at about 1600 mm and 1200 mm distance to the target crossbeam accordingly. This corresponds to the results of the numerical simulations with the same rib geometry as the most unfavorable load position is about 1600 mm away from the investigated crossbeam. Furthermore, the positive correlation between the weld length of rib-to-crossbeam joint and the distortional stress is also observed in the measurement results. In general, the results of SGC3_1 are higher than the results of SGC2_1 given the weld length of the rib-to-crossbeam joint is 152 mm on rib 2 and 177 mm on rib 3.

Figure 4.13 and Figure 4.14 show the results of single strain gauges at the midspan section and the results of single strain gauges at the crossbeam section respectively. In the names of strain gauges, *I* means the inner side of the rib and *O* means the outer side of the rib as shown in Figure 4.5. *M* and *C* represent the midspan section and crossbeam section respectively.

For strain gauges at the midspan section, the influence of the interfering signal is not obvious. Therefore, the results before and after elimination of the interfering signal are almost identical. Due to the same structures and measurement locations, the shapes of strain-loadcase curves are very close. The peak value appears when the tire load is directly above the corresponding location. For example, the first peak is reached when the front tires are at middle of span for load case 6 and the second peak is reached when the rear tires are at middle of span as load case 13. Since the weight of the front axle is larger than that of the rear axle, the strain induced by the rear axle is about half of the strain induced by the front axle. It should also be noted that the influence lines of the stresses in the rib are quite short. Once the tire load is moved away from the corresponding position, the strain would quickly diminish to around zero. The distortional deformation of ribs can be proven by the results of the strain gauges at the lower corner of the ribs, which are ending with O_2 or 3 and I_2 or 3. The measured strains have opposite signs at these two locations.

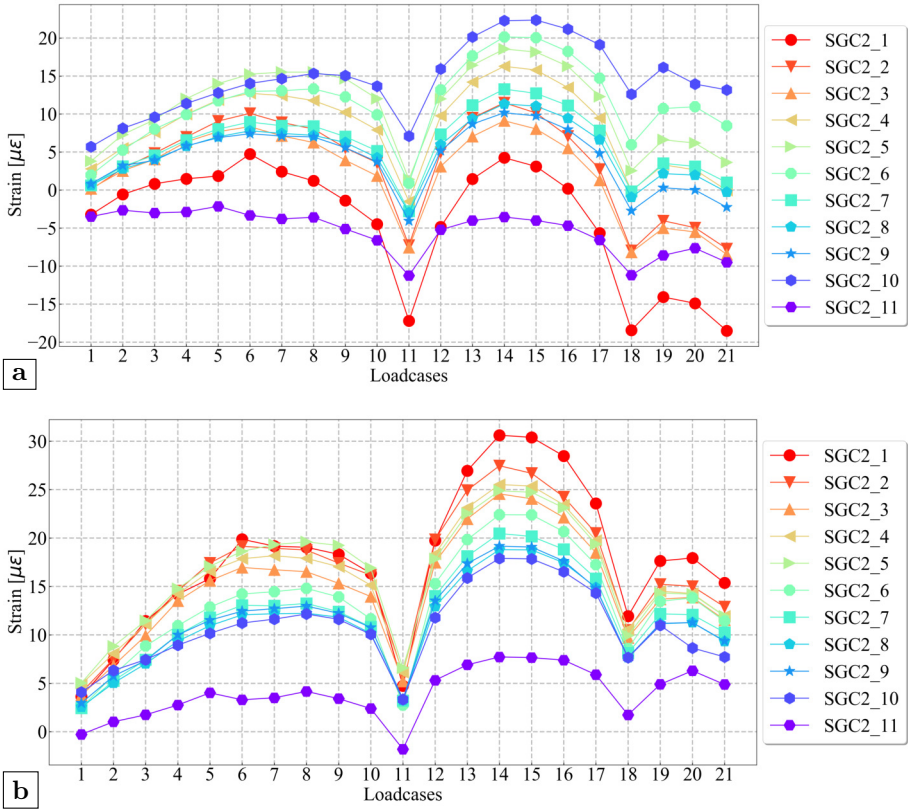


Figure 4.11: Results of the strain gauge chain at rib 2: (a) raw data; (b) filtered result

For single strain gauges at the crossbeam section, the influence of the interfering signal is also not obvious as presented in Figure 4.14. The result of SC2_O_1 changes to almost zero after eliminating the interfering signal which is quite close to SC3_O_1. Except this one, the changes of other strain gauges are rather small. The strain gauge SC3_I_1 may be broken since it gives an irregular result compared to the result of SC2_I_1 which is at a similar position. Similar to the results of strain gauge chains, the first peak value appears at load case 6 for strain gauges on rib 2 and load case 7 for strain gauges on rib 3. The second peak value appears at load case 15 on both ribs. This phenomenon illustrates that the distortional deformation arrives the maximum under aforementioned load cases. Meanwhile, the trough value appears at two load cases which are load case 11 and load case 18. As stated before, the front axle is above the central plane of the target crossbeam for load case 11 and the rear axle is very

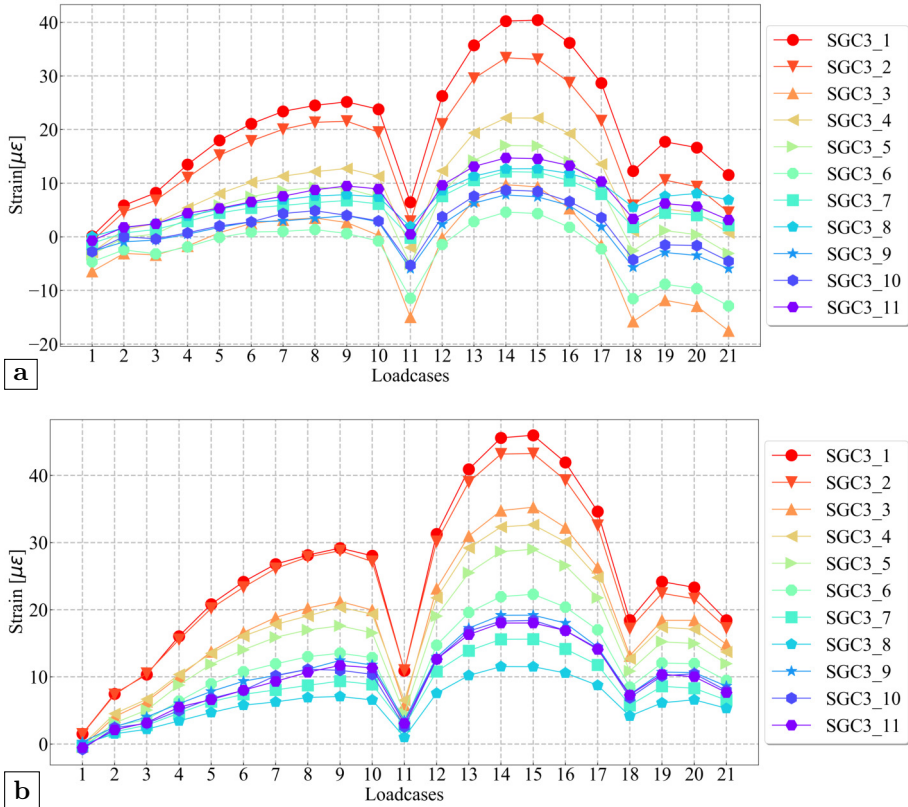


Figure 4.12: Results of the strain gauge chain at rib 3: (a) raw data; (b) filtered result

close to the same central plane for load case 18 given the spacing of axle is 2823 mm. For these two load cases, the crossbeam in-plane behavior is dominant. Therefore, the rib distortion does not have an obvious impact. Compared to the results from rib 2, the results of rib 3 are larger in absolute values which can be explained by the stronger constraints induced by the longer weld length.

The results of rosette strain gauges are displayed in Figure 4.15. Minor adjustments are made after the process of filtering, but the general trends remain the same. Since the strain gauge R3_O_3 gives abnormal results and is assumed to be broken, its measurement result is removed from the results for better illustration. Compared with rib 2, the results of rosette strain gauges at the location of rib 3 are lack of a recognizable rule. On the other hand, the measured strains are also very small which shows that the stress concentration does not

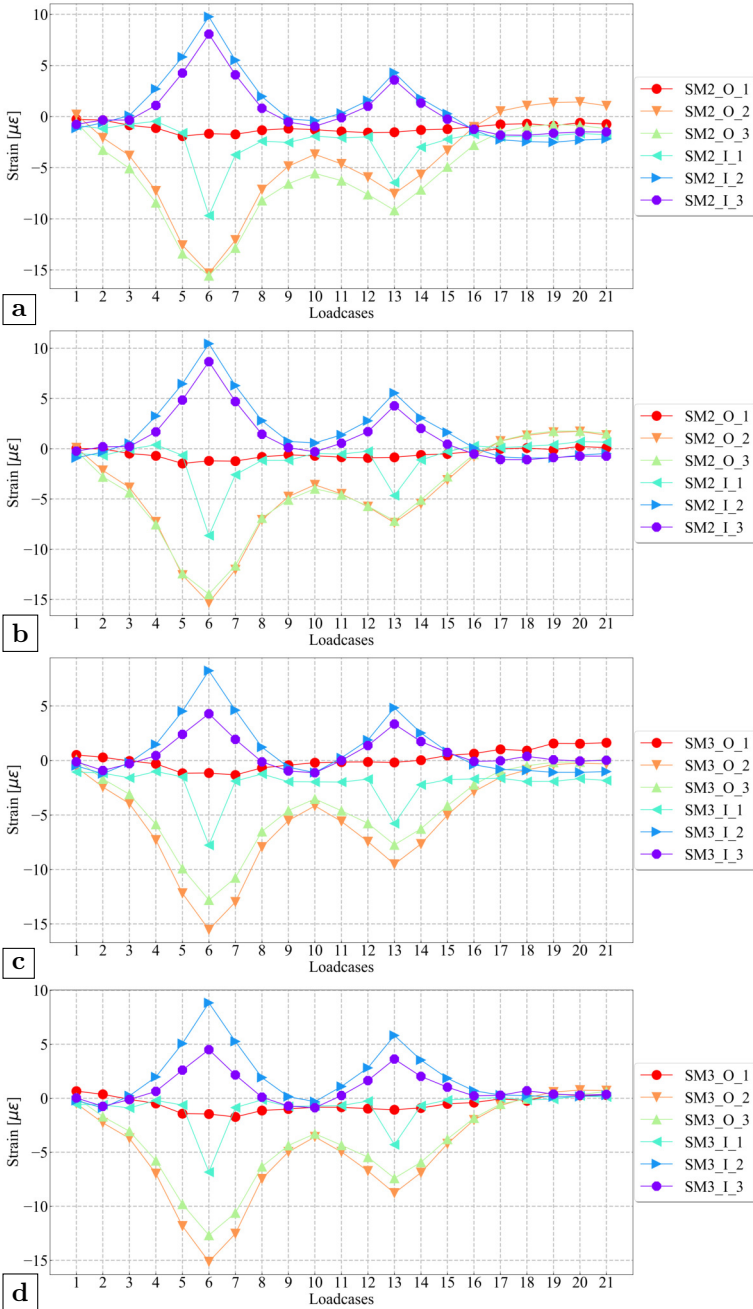


Figure 4.13: Results of single strain gauges at the midspan section: (a) raw data of rib 2; (b) filtered result of rib 2; (c) raw data of rib 3; (d) filtered result of rib 3

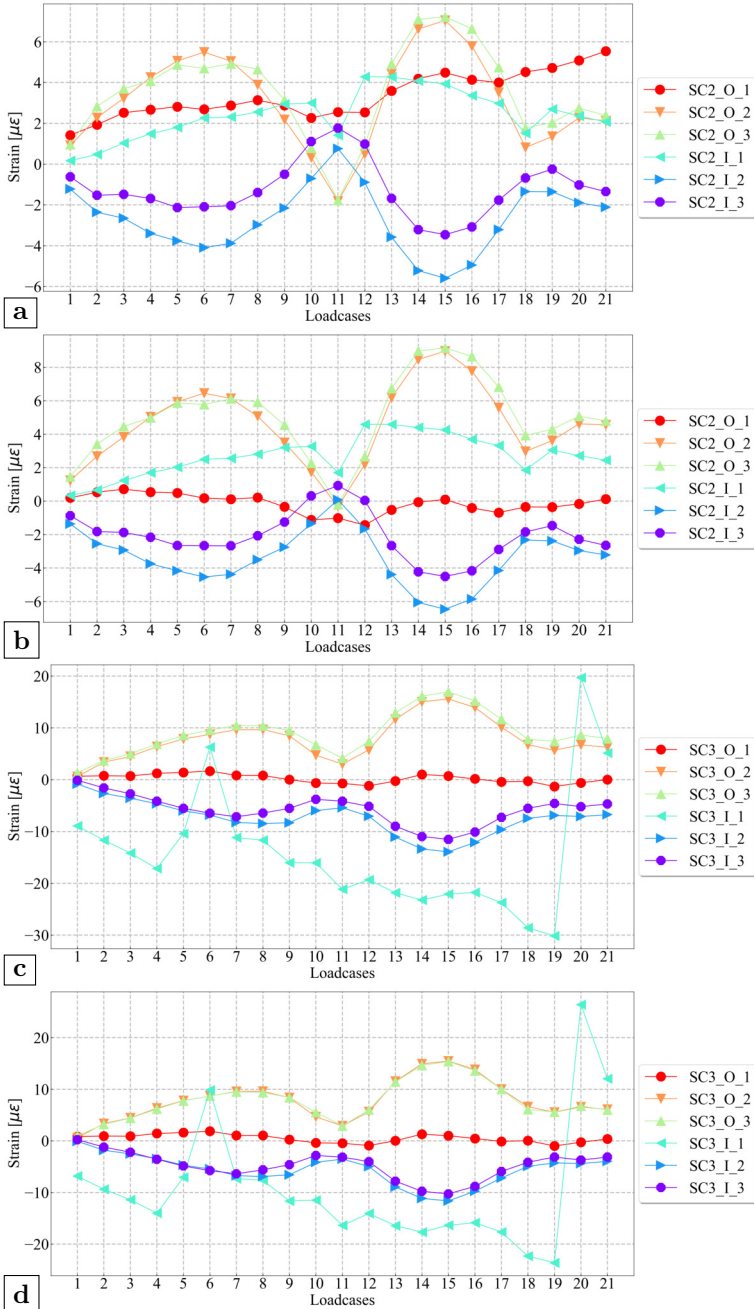


Figure 4.14: Results of single strain gauges at the crossbeam section: (a) raw data of rib 2; (b) filtered result of rib 2; (c) raw data of rib 3; (d) filtered result of rib 3

appear at the corresponding cope hole. Considering the rosette strain gauges at the location of rib 2, the peak value appears when the axle load is directly above the middle crossbeam which is load case 11. This phenomenon proves that the crack initiated from the free edge of cope hole is closely associated with the crossbeam in-plane behavior. Based on the results, the direction of the principal tension stress at the inner side (i.e. derived from R2_I_1-3) is along the radius of the curve whereas the direction of the principal tension stress at the outer side (i.e. derived from R2_O_1-3) is parallel to the curvature.

Figure 4.16 presents the results of two single strain gauges on the crossbeam of rib-to-crossbeam joint. In general, the result of SJ3 is larger than the SJ2, and the measured stresses at these two locations are both compression stresses. The maximum compression stress appears when the load is very close to the section, which are load cases 10 & 12 caused by the front axle, and load cases 17 & 19 caused by the rear axle. However, if the tire load is directly above the central plane of the crossbeam (i.e. load case 11 and 18), the results of these two positions return to nearly zero. With reference to the result, it can be found that the position of the cope hole termination determined by the weld length would also influence the stress status on the crossbeam side. Lower height of the termination represents a stronger constraint which could increase the stress concentration.

4.6 Conclusions

In this chapter, a full-scale OSD specimen is tested to investigate the rib distortional behavior based on previous parametric analyses. Since the raw data has some irregular results especially for strain gauge chains applied at the high stress gradient area, the assumption that the interfering signal is linearly dependent on time is adopted for processing the raw data. Comparing the raw data and the filtered results, the assumed interfering signal has more influence on the strain gauge chains than other single strain gauges or rosette strain gauges.

Based on the measurement results, two conclusions from the parametric analyses are verified. The most unfavorable load position for the distortional stress on the rib wall is determined by the geometries of ribs. For the same rib geometry as adopted in the tests, the most unfavorable load position is at 1600 mm away from the investigated crossbeam according to simulations, which is supported by the measurement results. Meanwhile, the positive correlation between the weld length of rib-to-crossbeam joint and the distortional stress is also verified. A longer weld length, or a lower termination position of cope hole curve, would increase the stress induced by the rib distortion.

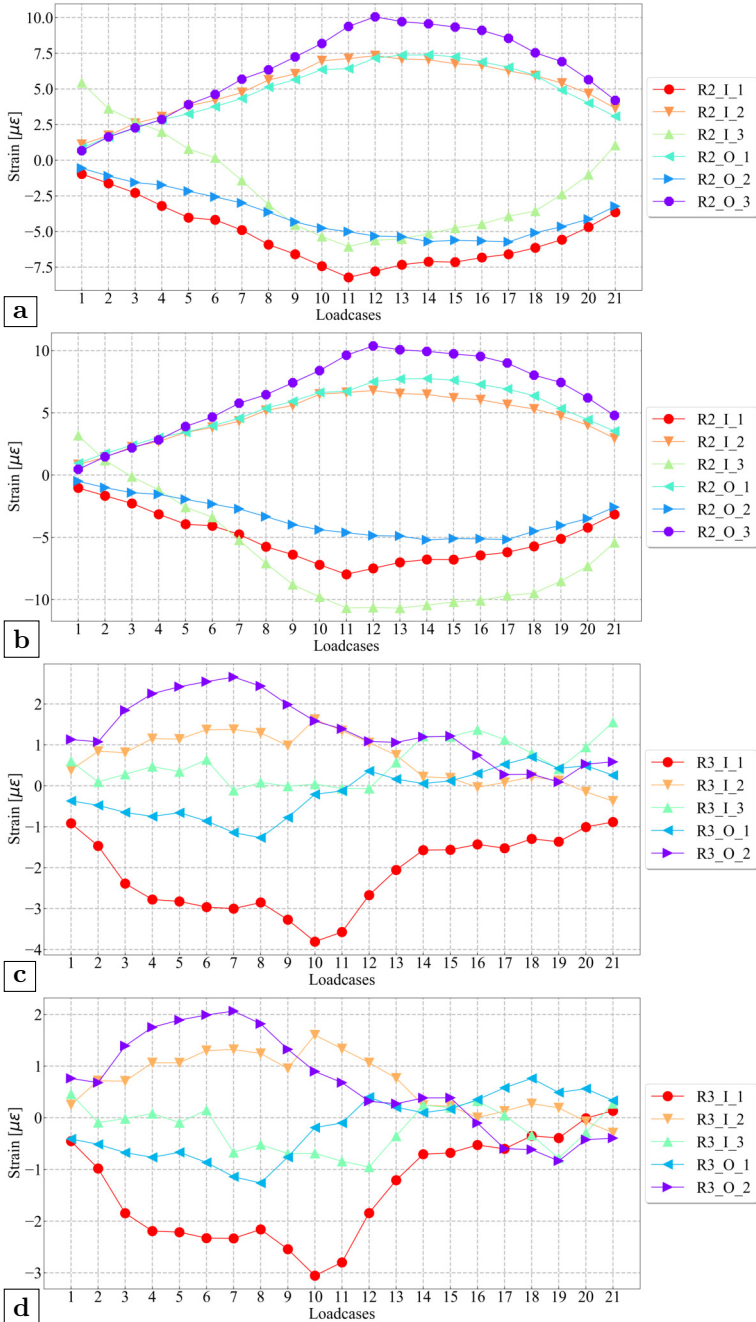


Figure 4.15: Results of rosette strain gauges on crossbeam: (a) raw data of rib 2; (b) filtered result of rib 2; (c) raw data of rib 3; (d) filtered result of rib 3

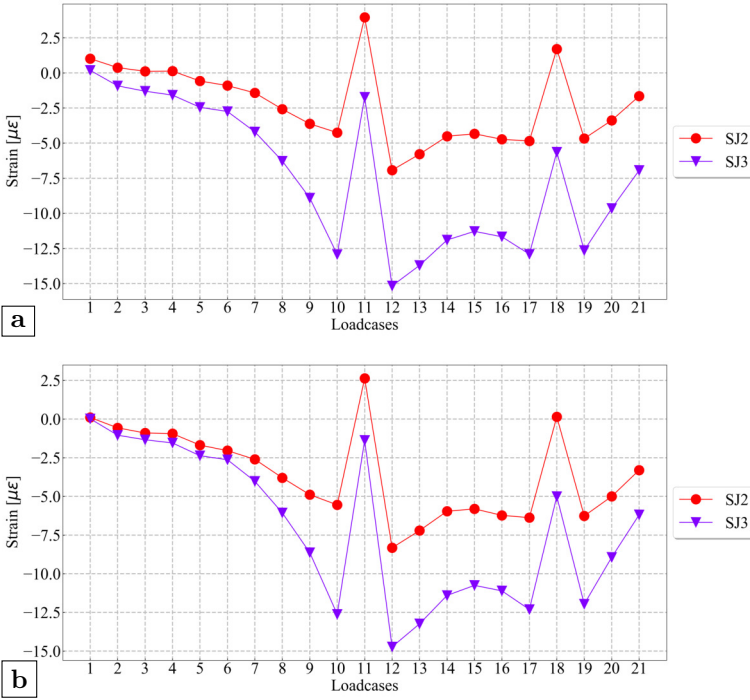


Figure 4.16: Results of single strain gauges on crossbeam: (a) raw data; (b) filtered result

During the tests, it is observed that the weld length of rib-to-crossbeam joint would influence the stresses on rib wall and lower soffit as well as the stresses on inner surface of cope hole close to the weld toe. A longer weld length, which represents a stronger constraint, would increase the stress level at these points. The stresses of corresponding points on ribs at midpan section are not influenced by the weld length. The stress concentration close to the curvature of cope holes is associated with the in-plane behavior of crossbeams as the peak value is achieved when the tire load is directly above the crossbeam.

5

Numerical simulation of experiments

5.1 Introduction

After performing the tests, the corresponding numerical simulations of the measurements are further conducted. On the one hand, the comparison of measurement results and calculation results will reveal that if the consistent results could be acquired when adopting the structural hot spot stress method to assess the rib-to-crossbeam joint. On the other hand, the influences of different choices in simulations are also discussed.

5.2 FEA models

The corresponding numerical simulations of the experiments are performed using the commercial FEA software Siemens NX. Based on the dimensions of the OSD specimen, the global model is shown in Figure 5.1. The submodel analysis technique is also adopted. The location of the submodel is at the intersection of the middle crossbeam and rib 2 & 3 which is marked by a yellow color in the figure. Initially, the models are built by volumes for using solid elements and all welds are finely modeled by using an assumed triangular cross-section, yet the influences of the element type and the welds will be discussed later in this chapter. The initial boundary condition of the global model is one fixed support at the middle up corner and five roller supports at other locations as marked by a green color. The boundary condition of the submodel comes from the calculation results of the relevant global model. The nodal displacements along the cutting boundary are applied back to the submodel as enforced constraints.

5.2.1 Method for defining specific nodes

In general, there are two methods for building a finite element model. The first method is called the direct method. In this method, all of required nodes are defined first. Then, the elements are defined based on the coordinates of the nodes and the whole finite element model is therefore built. The other method is called the indirect method, in which a geometrical model is built first. Based on the geometrical model, the nodes and elements needed are meshed accordingly. Nowadays, commonly-used FEA software would tend to use the indirect method since it is much more convenient. However, defining a node with specific coordinates is usually rather difficult when adopting the indirect method. For comparing the calculation results with the measurement results, relevant results at the specific locations of the strain gauges should be able to be exported. If it is not possible to define nodes at the desired specific locations, exporting relevant results can be achieved by writing a macro script. For a given coordinate where no node exists, the macro script can find three nodes which are the closest to the specific coordinate. The target results are

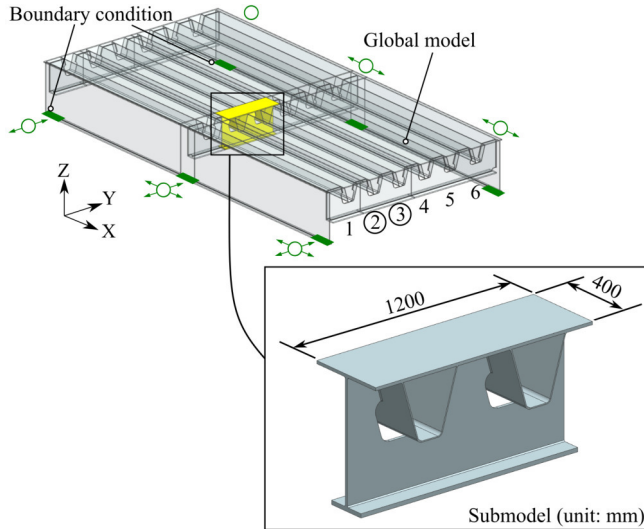


Figure 5.1: Global model and submodel

therefore calculated through interpolations from these three nodes.

In Siemens NX, it is possible to define nodes according to coordinates directly. Firstly, a geometrical point can be defined according to the coordinate when building the geometrical model (i.e. in `.prt` file). Then, the geometrical point is used as a reference point for defining a mesh point when meshing (i.e. in `.fem` file). The mesh point is generated through the projection of the geometrical point to the target surface. Once the mesh point is defined, a corresponding node would be generated at this specific location during meshing. Nevertheless, there are still two problems to be solved. The first problem is how to get the coordinates of the strain gauges. Direct hand calculation is rather difficult and time-consuming. Therefore, the notion of a local coordinate system is utilized. The local coordinate system could be defined at the plane of the rib wall, and the coordinates of the strain gauges on the rib wall can be easily expressed in the local coordinate system. In the next step, the relevant coordinates in the global coordinate system can be calculated through a coordinate transformation. The programming language Python is adopted to realize the algorithm of the coordinate transformation. The second problem is how to input these coordinates into the model. The graphical user interface (GUI) method in Siemens NX is not easy especially when the number of points is quite large. Luckily, the NX open can be employed to finish this task. NX Open is an application programming interface (API) that lets the user writes programs to customize or extend NX. NX Open supports major programming languages

such as Visual Basic (VB), C++, Java and Python. In order to use NX Open, the **Developer** tab has to be turned on and the programming language can be chosen in the option **User Interface Preferences**. Therefore, the process of adding points can be written as a function that calls the Python library of NX Open. One example of the NX Open manuscript is given in appendix A.2.

5.2.2 Mesh sensitivity tests

By writing the NX Open manuscript, one node is precisely defined at the location of each strain gauge. The simulation is based on linear-elastic material assumption. According to Eurocode (CEN, 2005), the modulus of elasticity is 210 GPa, the Poisson’s ratio in the elastic stage is 0.3 for steel material. The weld material is assumed to have the same material property as the base metal. The 10-nodes 3D CTETRA10 element is utilized in both the global model and the submodel. In order to determine the appropriate element size, mesh sensitivity tests are performed in advance. Among the strain gauges used in the tests, only the results of single strain gauges at the midspan section are exported from the global model. Results of the other strain gauges are acquired from the submodel. Therefore, the evaluation criterion for the global model is the average strain of the 12 measurement points from the relevant single strain gauge at the midspan section, which are strain gauges SM2_I/O_1-3 and SM3_I/O_1-3. Meanwhile, the evaluation criterion for the submodel is the average strain of 22 measurement points from the relevant strain gauge chains, which are strain gauges SGC2_1-11 and SGC3_1-11. For the mesh sensitivity tests, load case 14 and the initial boundary condition are adopted, which are also used for further calculations and discussed later in section 5.5. The results of the mesh sensitivity test are shown in Figure 5.2, in which each curve represents a given mesh size of the global model. According to the results, the element sizes of 20 mm and 5 mm for the global model and the submodel respectively are able to give convergent results which are therefore selected.

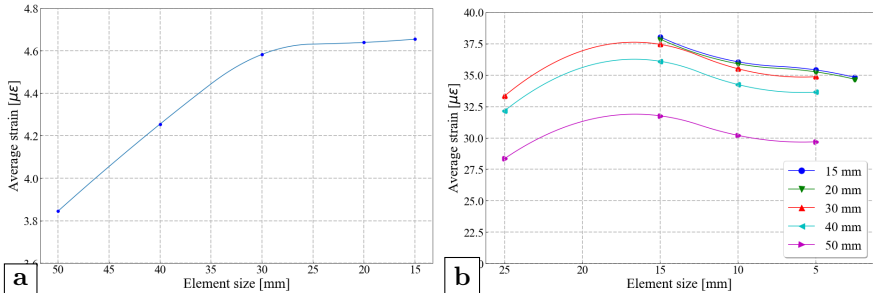


Figure 5.2: Mesh sensitivity tests: (a) global model; (b) submodel

5.3 Post-processing of the calculation results

For strain gauges installed on the rib wall, e.g. the strain gauge chains, the direction of the measured strain is along the surface perpendicular to the target weld toe. However, the strain or stress component along this perpendicular direction cannot be exported directly from the finite element models. As illustrated in Figure 5.3(a), the Z axis and Y axis come from the coordinate system used in the simulations. The N axis denotes the direction of the measured strain component. A tiny cube is used to represent the node at the location of one strain gauge close to the weld as shown in Figure 5.3(b). Six independent strain components that correspond to six stress components are exported, in which ε_{XX} , ε_{YY} and ε_{ZZ} correspond to three principal stresses; ε_{XY} , ε_{YZ} and ε_{ZX} correspond to three shear stresses. Based on the force equilibrium function, the strain component ε_{NN} that is normal to the plane A is calculated by equation 5.1, which is therefore compared with the measurement results. This processing is applied to the results of all strain gauges that relevant results cannot be read directly. For strain gauges at other locations, corresponding strain components are exported. For example, the strain component ε_{XX} is adopted for single strain gauges that are placed at the soffit of the ribs, which is the same as the measurement direction.

$$\varepsilon_{NN} = \varepsilon_{XX}l^2 + \varepsilon_{YY}m^2 + \varepsilon_{ZZ}n^2 + 2(\varepsilon_{XY}lm + \varepsilon_{YZ}mn + \varepsilon_{ZX}ln) \quad (5.1)$$

where l is the cosine of angle between N axis and X axis; m is the cosine of angle between N axis and Y axis (e.g. $\cos \beta$ in Figure 5.3(a)); n is the cosine of angle between N axis and Z axis (e.g. $\cos \alpha$ in Figure 5.3(a)).

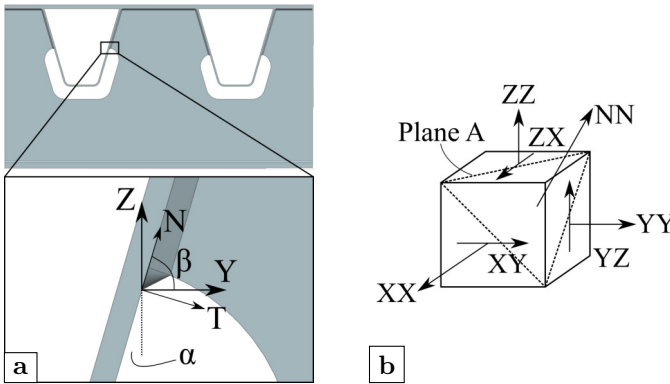


Figure 5.3: Post-processing of calculation results: (a) illustration of the local coordinate; (b) components of calculation results

5.4 Calculation results

Figure 5.4 presents the calculation results of the strain gauge chains. In general, compared with the measurement results (see Figure 4.11 and Figure 4.12), the overall trends are very close. The peak value also appears at load case 14 or 15. When getting closer to the weld toe, the stress gradient gradually increases, which can be proven by the larger gap between the results of two adjacent strain gauges when getting closer to the weld toe (i.e. the strain gauges' names end with 1 to 3). It should be noted that the results of strain gauges on rib 3 are larger than those on rib 2 around the peak value zone (i.e. from load case 12 to load case 17). This relationship is the same as acquired from the measurement results. For the other load cases, the calculation results from different ribs are quite close, which may be because of the relatively light load. The last observation is that the calculation results are obviously larger than the measurement results. Possible reasons that cause the differences will be further discussed in the next section.

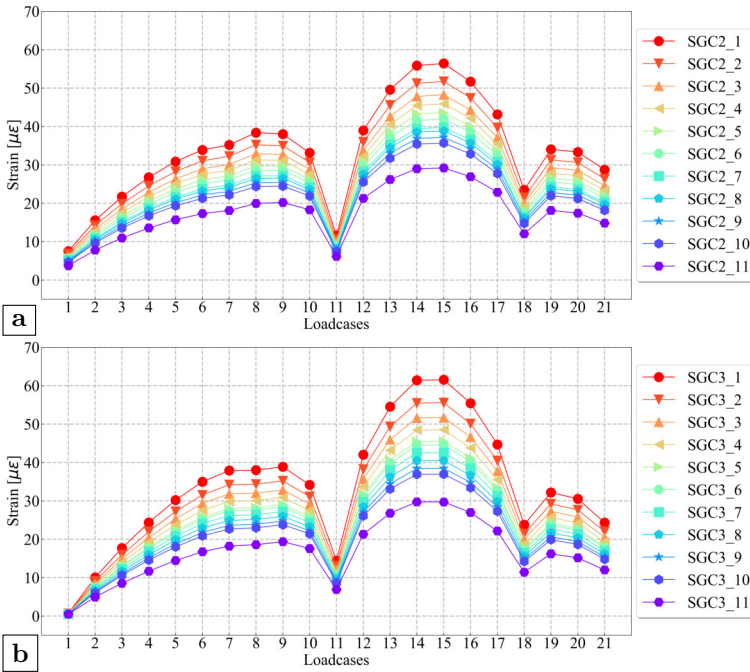


Figure 5.4: Calculation results of the strain gauge chains: (a) rib 2; (b) rib 3

The calculation results of the single strain gauges at the midspan section are presented in Figure 5.5. For the reference of relevant measurement results,

see Figure 4.13. As stated before, the peak value appears when the tire load is directly above the location where the strain gauges are (i.e. the middle point of the span). Due to the symmetry of the structure and the very short horizontal influence lines, the simulation results of rib 2 and 3 are almost identical. However, it should be noted that the small increments of rib 2 starting from load case 17 until load case 21 are also captured by the numerical model if a comparison is made between Figure 5.5(a) and Figure 4.13(b). Compared with calculation results of rib 2, the calculation results of rib 3 generally fit better with the corresponding measurement results.

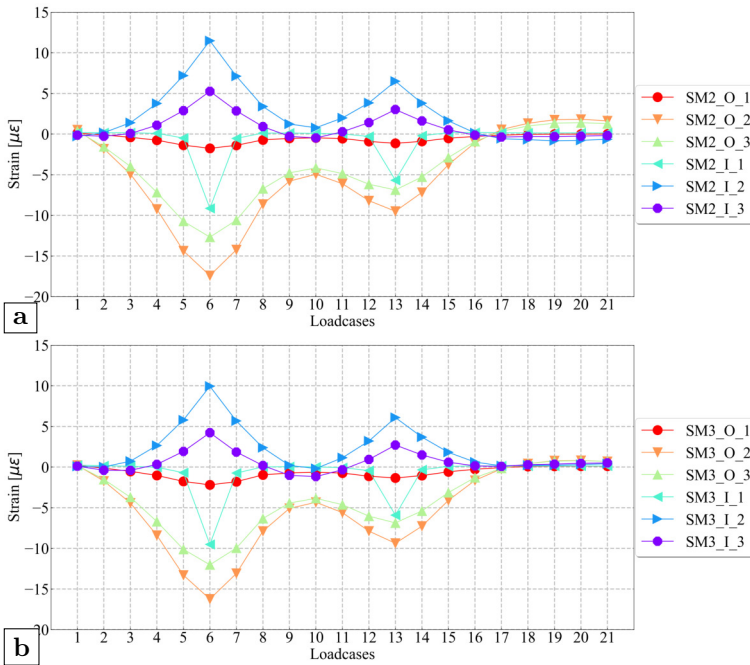


Figure 5.5: Calculation results of the single strain gauges at midspan section: (a) rib 2; (b) rib 3

Figure 5.6 shows the calculation results of single strain gauges at crossbeam section. Corresponding measurement results are given in Figure 4.14. Similarly, the first peak value appears at load case 6 for rib 2, and load case 7 for rib 3. The second peak value appears at load case 15 on both ribs. The peak values may be related to the distortional behavior of the ribs, which reaches the maximum for load 6 and 15. When the tire load is directly above the crossbeam (i.e. load case 11 for the front axle or load case 18 for the rear axle), the distortional behavior of ribs is negligible if compared to the crossbeam in-plane behavior.

For both ribs, the results of strain gauges on the inner side (i.e. strain gauges end with I_2 and I_3) are higher than those on the outer side (i.e. strain gauge names end with O_2 and O_3). Based on the calculation results, SC3_I_1 is supposed to have the same trend as SC2_I_1. Although the calculation result of SC2_I_1 is a bit bigger than the measurement results, the overall trend is the same. The irregular measurement result of SC3_I_1 demonstrates that the strain gauge is actually broken.

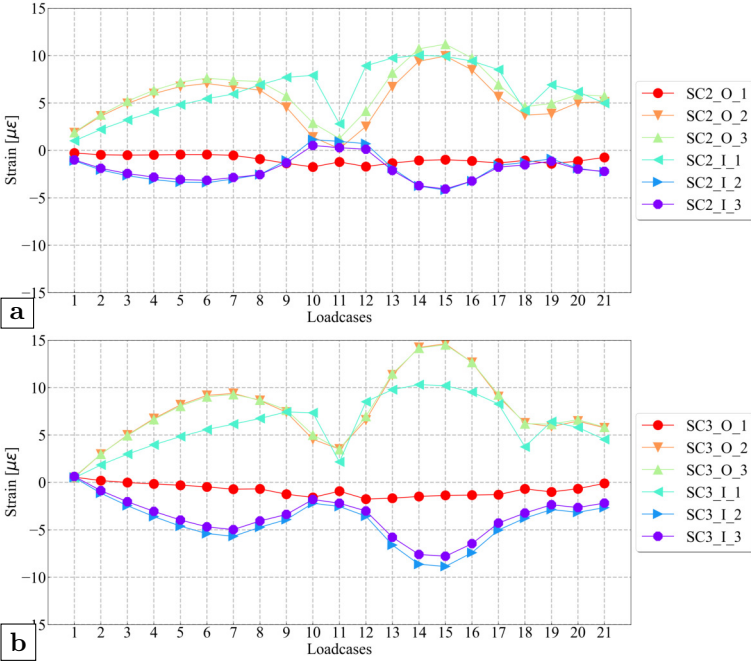


Figure 5.6: Calculation results of the single strain gauges at crossbeam section: (a) rib 2; (b) rib 3

The calculation results of the rosette strain gauges are presented in Figure 5.7, the corresponding measurement results can be found in Figure 4.15. For rosette strain gauges at the location of rib 2, the calculation results generally fit well with the measurement results. The directions of stresses are the same, and the absolute values of the calculation results are slightly larger than the measurement results. For strain gauges at the location of rib 3, the strains are very small which equal almost zero, therefore the fluctuating results do not offer any meaningful information.

Figure 5.8 shows the calculation results of single strain gauges on the crossbeam side. As opposed to the measurement results, which are shown in Figure 4.16,

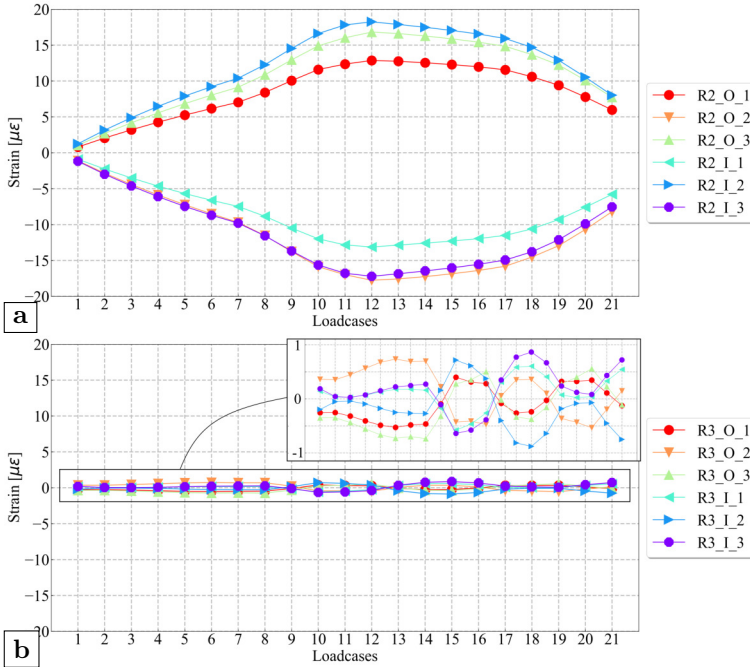


Figure 5.7: Calculation results of the rosette strain gauges on crossbeam: (a) rib 2; (b) rib 3

the calculation results of SJ2 and SJ3 are mostly tensile. Only for specific load cases e.g. when the tire load is above the middle crossbeam, their results change to compression strain. The results on both locations are quite small when compared with the measurement results. Nevertheless, on the one hand, their relative relationship is still the same. The result of SJ2 is larger than SJ3. On the other hand, the simulation results of these two position still show a local inflection point when the tire load is directly above the central plane of the crossbeam (i.e. load case 11 and 18).

In general, the FEA model is able to correctly reflect the structural behavior of the OSD specimen. Hence, the overall trends for all strain gauges are the same as the measurement results. However, when the magnitudes of strains are closely compared, the calculation results does not fit very well with the measurement results in values, especially for the target detail (i.e. the strain gauge chains). For that reason, several possibilities that may cause differences between measurement results and calculation results are investigated in the next section.

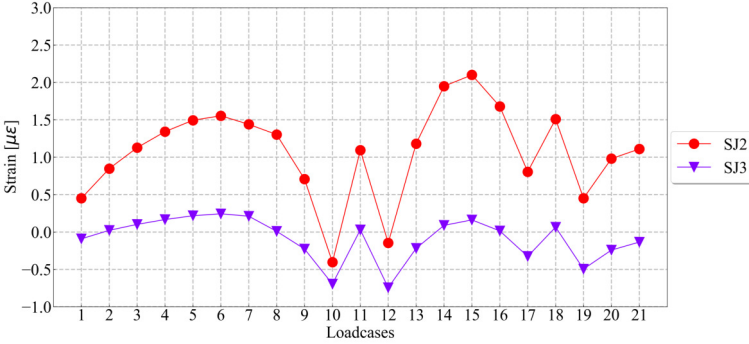


Figure 5.8: Calculation results of the single strain gauges on crossbeam

5.5 Background of differences between measurements and calculations

According to the measurement results and relevant simulations, load case 14 or 15 is the most unfavorable load position for the rib-to-crossbeam joint in this case. Therefore, load case 14 is chosen as the reference load case for the following considerations.

From the perspective of numerical simulations, the boundary conditions could have an influence on the simulation results since the constraints applied on the specimen in reality are hard to be perfectly simulated. Meanwhile, the modeling of the welds is accomplished by an ideal geometry i.e. a triangular. However, the actual welds of the rib-to-crossbeam joint are normally finished by manual welding. The irregular shape of the weld is unavoidable, which is not reflected in the numerical models. Moreover, the imperfect shape of the welds would also have an influence on the experimental aspect. The locations of the strain gauges are rather difficult to be determined precisely since the target weld toe is not a straight line as assumed in numerical models. Due to the particular locations of the measuring points at the rib-to-crossbeam joint, installing strain gauges is much more difficult than other joints e.g. the rib-to-deck joint. Given the high stress gradients at the weld toe vicinity, the deviation of the strain gauges is an important factor that may lead to the differences. The last possibility is the deviation of the load position. Even though the load car is positioned as precisely as possible, a small deviation, especially on the horizontal direction, may cause the differences given the relatively short influence lines.

5.5.1 Different boundary condition

Figure 5.9 presents the influence of different boundary condition, where BC is the abbreviation of “Boundary Condition”. When performing the tests, the specimen is directly placed on the concrete columns. Accordingly, the rotations along three directions as well as the vertical displacement (i.e. along the Z axis) are constrained at the corresponding surface area. In the numerical simulations presented in previous section, the classical boundary condition was adopted which allows the specimen to expand in two directions. To investigate the influence of the boundary conditions, three extra boundary conditions are considered. For boundary condition 2 (BC2), all displacement of nodes on the boundary area are constrained. For boundary condition 3 or 4 (BC3 or BC4), the specimen is allowed to expand along Y axis or X axis respectively. Based on the comparison presented in Figure 5.10, the boundary condition has no obvious influence on the simulation results of all strain gauges. Hence, the boundary condition *Classic* will still be used in later analyses.

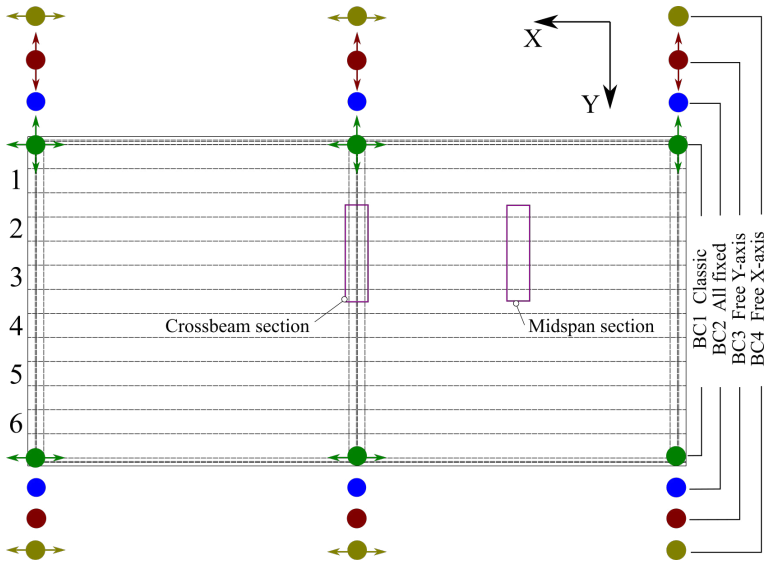


Figure 5.9: Different boundary conditions

5.5.2 Different weld shape and size

Normally, the cross-section of a weld is modeled as a triangular section in numerical simulation, yet the construction quality of the specimen is far from perfect. A closer look of the rib-to-crossbeam joint weld from the OSD specimen can be found in Figure 5.11. The weld shape and the weld toe line are both

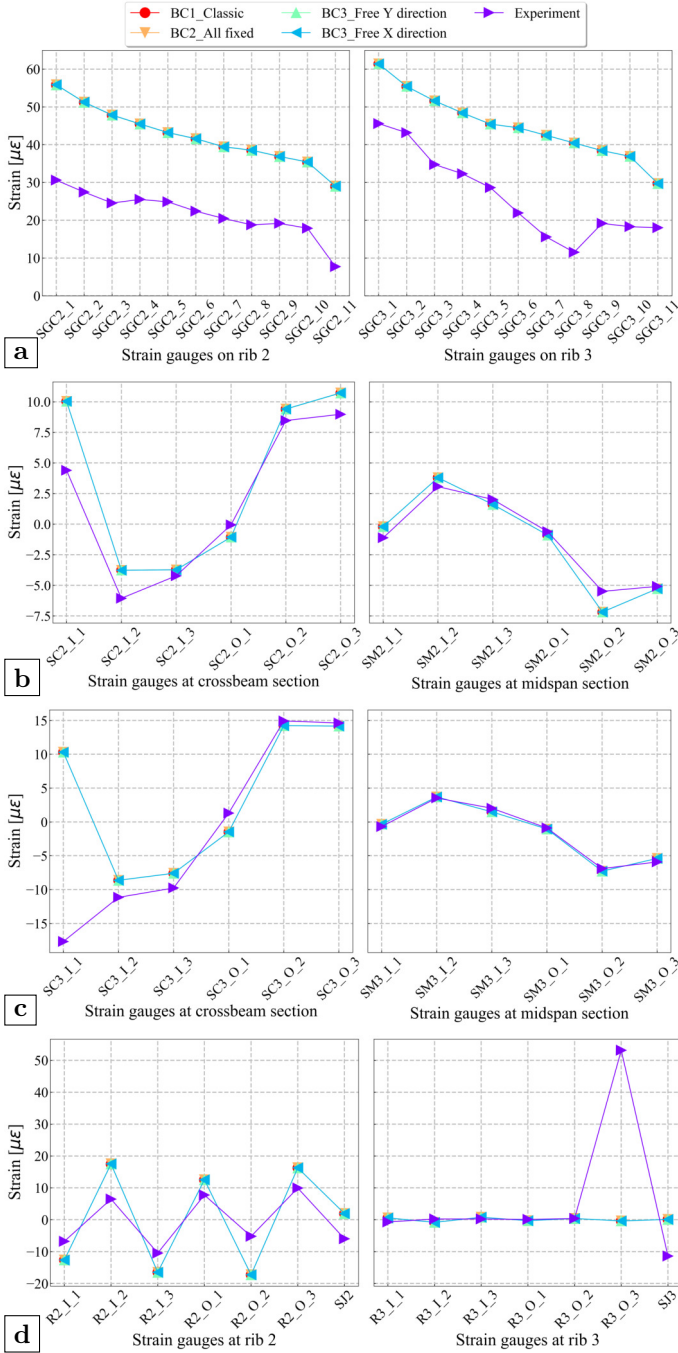


Figure 5.10: Influence of different boundary conditions: (a) strain gauge chains; (b) single strain gauges on rib 2; (c) single strain gauges on rib 3; (d) strain gauges on crossbeam

obviously irregular. The actual contour of the weld could be miter, convex, concave or even in-between these situations. The throat thickness of the weld is not precise even though it was set to 4 mm in design. Due to these reasons, it is rather difficult to judge whether the prerequisite (i.e. the leading edge of the carrier board of strain gauge chains is in tangent with the target weld toe) is fulfilled or not. To check the influences of different weld profiles, three different idealized weld profiles are considered as shown in Figure 5.12. In which a is the throat thickness and h is the contour height. The contour height is set to 1.875 mm in following examples. Different throat thickness is also considered, such as 4 mm, 5 mm and 6 mm.

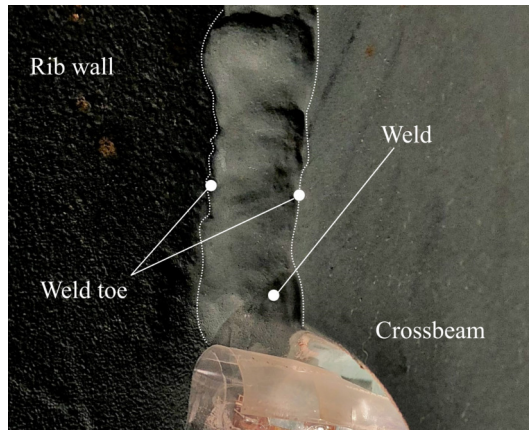


Figure 5.11: Irregular weld shape and weld toe

The influence of different cross-sections and throat thickness of welds are presented in Figure 5.13. According to the results, the weld profile is a local factor which only affects the points in the vicinity of the weld toe (i.e. strain gauge chains and single strain gauges on the crossbeam). Among these three weld profiles, the concave weld profile leads to the smallest results given a certain throat thickness. Compared with the miter profile, the convex weld profile causes the same or larger strains for the same throat thickness. Given a certain weld profile, the influence of the throat thickness is not obvious.

5.5.3 Deviation of load position

The difference between the experimental results and the numerical simulations could also be induced by a deviation of the load position. Figure 5.14 gives the illustration of possible horizontal deviations of the loading tire. The center of the tire is supposed to be at the central line between rib 2 and rib 3. The deviation is shown as positive when the load center moves towards the direction

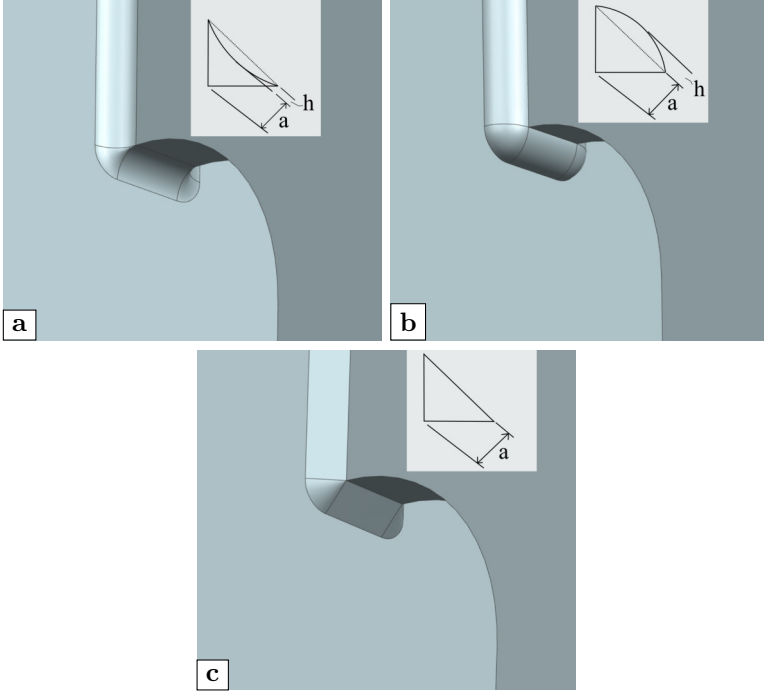


Figure 5.12: Different weld profiles: (a) concave; (b) convex; (c) miter

of the Y axis and vice versa. When the deviation is 150 mm, the center of the loading tire is just above the rib-to-crossbeam-to-deck joint of one stem given the spacing between ribs is 600 mm and the upper width of the ribs is 300 mm.

Figure 5.15 shows the influence of the deviation of the load position. According to the results, the horizontal load position has a relatively large influence on the distortional stresses of all points. When the tire load moves from the center between two ribs (e.g. the *NoDeviation* scheme) towards the center of one rib (e.g. the *150mmDeviation* scheme), the stress on the corresponding rib wall (e.g. strain gauge chain on rib 3) will first increase then decrease whereas the stress of the other side (e.g. strain gauge chain on rib 2) will drop dramatically. Due to this reason, the relative difference between the stresses of two sides would get larger with the increment of the horizontal deviation. Note that the maximum values of strain gauge chains appear when the tire load is 100 mm away from the central line for both sides. However if the strain gauges at other locations were checked simultaneously, a 50 mm or 100 mm positive deviation has the highest possibility. For larger positive deviations, clear deviations appear on single strain gauges at inner side (i.e. strain gauge names end with I_1-3).

5.5 Background of differences between measurements and calculations

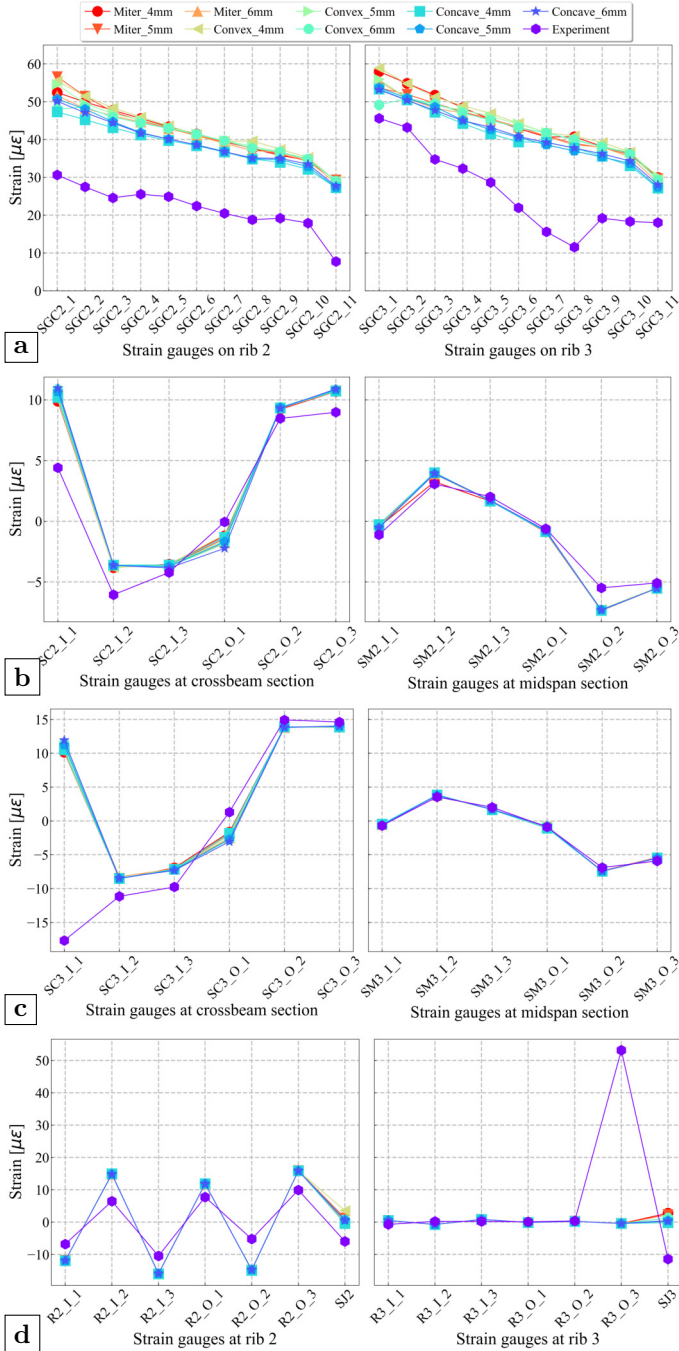


Figure 5.13: Influence of different weld profile: (a) strain gauge chains; (b) single strain gauges on rib 2; (c) single strain gauges on rib 3; (d) strain gauges on crossbeam

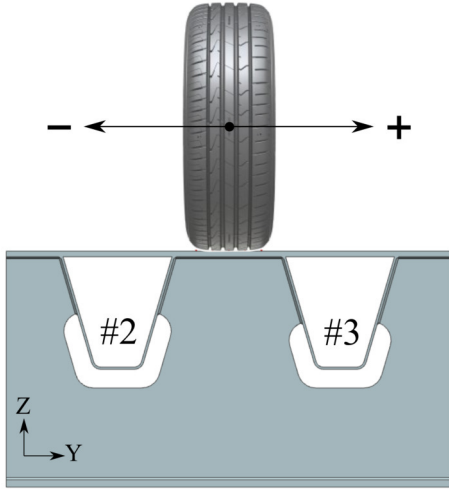


Figure 5.14: Deviation of the load position

Whereas for negative deviations, pronounced differences can be found on single strain gauges at outer side (i.e. strain gauge names end with O_1-3).

5.5.4 Deviation of strain gauge position

Due to the location of the rib-to-crossbeam joint, installing the strain gauge chains is more difficult than installing strain gauges at other locations. When designing the experiments, the leading edge of the carrier of the strain gauge chain is supposed to be tangent with the lower weld toe. Under this assumption, the distance between the first strain gauge and the target weld toe equals the distance from the first strain gauge to the leading edge of the strain gauge carrier which is 2.75 mm. However, the shape of the weld is more or less irregular because of manual welding as shown before in Figure 5.11. The target weld toe is not a straight line as in the numerical model. The exact position of the strain gauge chain is very difficult to locate. Therefore, the distance between strain gauges and the weld toe could be larger than anticipated. Meanwhile, it is also possible that the direction of the strain gauge chain is not perfectly aligned with the central line of the crossbeam. Figure 5.16 gives an illustration of the location of the strain gauge chain. In the figure, the distance S_f is the distance between the first strain gauge and the weld toe which is supposed to be 2.75 mm in an ideal situation. The strain gauge chain at different distances to the weld toe is also assumed to simultaneously rotate about its center. The rotation angle is positive when it rotates towards the midspan section (see Figure 5.9) and vice versa.

5.5 Background of differences between measurements and calculations

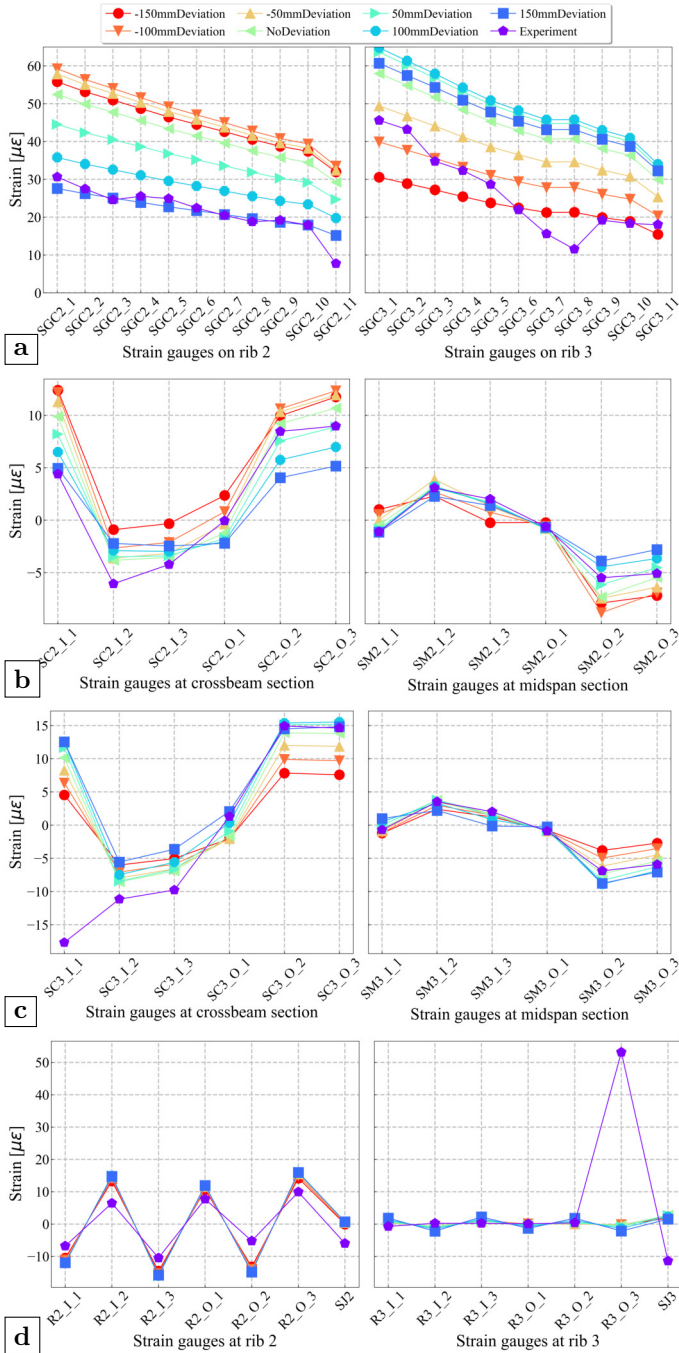


Figure 5.15: Influence of load position deviation: (a) strain gauge chains; (b) single strain gauges on rib 2; (c) single strain gauges on rib 3; (d) strain gauges on crossbeam

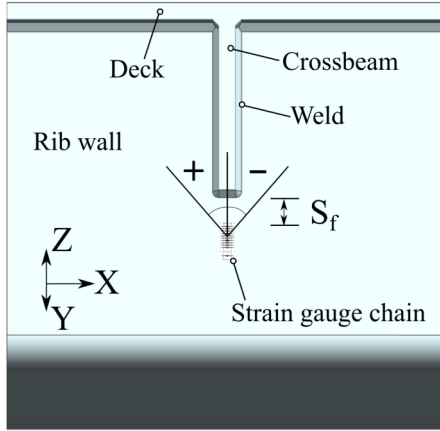


Figure 5.16: Deviation of the strain gauge position

Since this possibility affects the results of strain gauge chains solely, only relevant results are presented. Figure 5.17 shows the influence of the translation deviation of strain gauges. A large gradient appears in the vicinity of the weld toe. A relatively large gap can be found between the distance of 4 mm and 6 mm. Figure 5.18 displays the influence of the rotation of the strain gauge chains. A range between 15 degrees and -15 degrees are considered for the distance of 2.75 mm and 10 mm. Either positive rotation or negative rotation will lead to a smaller result if compared to the vertical direction. The reductions of the strains at two rotation directions are almost identical, which indicates the distribution of stress is almost symmetrical to the central plate of crossbeam. Due to the large stress gradient, the results of strain gauge chain are more sensitive to the possible rotation when it is getting closer to the weld toe.

5.6 Fatigue assessment based on influence lines

After validating the numerical models, a fatigue assessment is further conducted to investigate the influence of different weld length and the influence of different horizontal deviation of loads. In the first step, a series of influence lines are acquired. The models for fatigue assessments are updated from the numerical models of the OSD specimen. The general dimensions remain the same except that a uniform weld length is adopted for all ribs. The uniform weld length equals one of the weld lengths used in the specimen. As stated in section 5.5, the influences of the boundary condition and the weld shape on distortional stresses are not obvious. Hence, the boundary condition *classic* and the *miter* weld profile are selected.

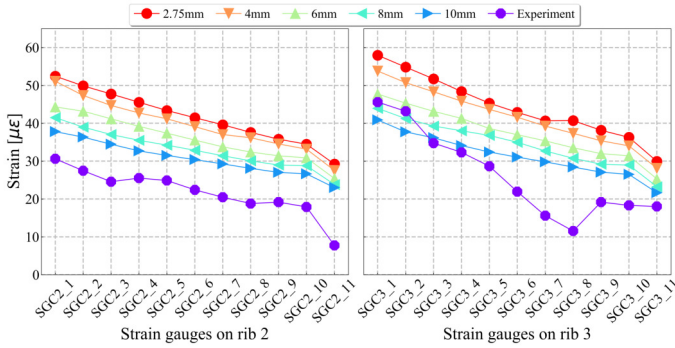


Figure 5.17: Influence of the the translational deviation of strain gauge chains

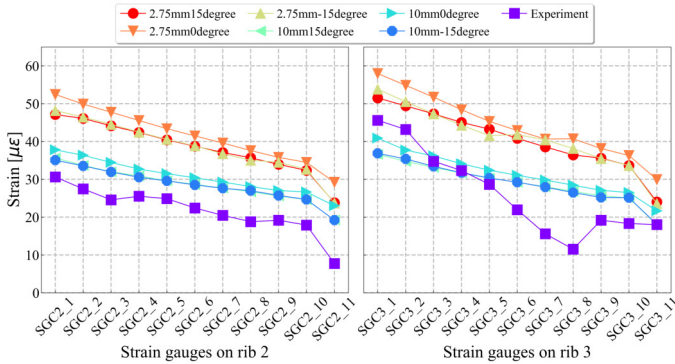


Figure 5.18: Influence of the rotation of strain gauge chains

As stated before, the nominal stress method is not suitable for the rib-to-crossbeam joint, so the structural hot spot stress method is adopted. In total 21 locations around the lower weld end are considered. With respect to linear extrapolation (Hobbacher, 2019), 42 reference points are defined on the left side of rib 3 as shown in Figure 5.19. Fatigue Load Model 4 from Eurocode is considered (CEN, 2003). To derive the influence lines, a single tire load with type C is chosen. The contact area of one tire is 270 mm wide and 320 mm long. The equivalent axle load is 90 kN, thus the tire load is 45 kN. In total 19 load points are considered with an interval distance of 400 mm.

Two calculations in total are finished. Calculation 1 investigates the influences of different weld lengths on the fatigue life. Based on the simulation results in section 5.5, the horizontal deviation of 100 mm is more unfavorable for the distortional stress of the corresponding rib. Therefore, the center of the tire load

is first set to 100 mm away from the central line between rib 2 and 3, which is 1550 mm to the edge of deck plate. 6 schemes correspond to the weld lengths of the OSD specimen are considered. On the basis of the calculation 1, Calculation 2 is conducted to verify the influences of different horizontal deviations on the fatigue life. 4 schemes are considered with a increment of 50 mm, namely *NoDeviation*, *50mmDeviation*, *100mmDeviation* and *150mmDeviation*. During both calculations, similar processing procedure as described in section 5.3 is used to export the corresponding stress that is normal to the weld toe. It should be noted that the extrapolation directions would change accordingly with the location of reference points.

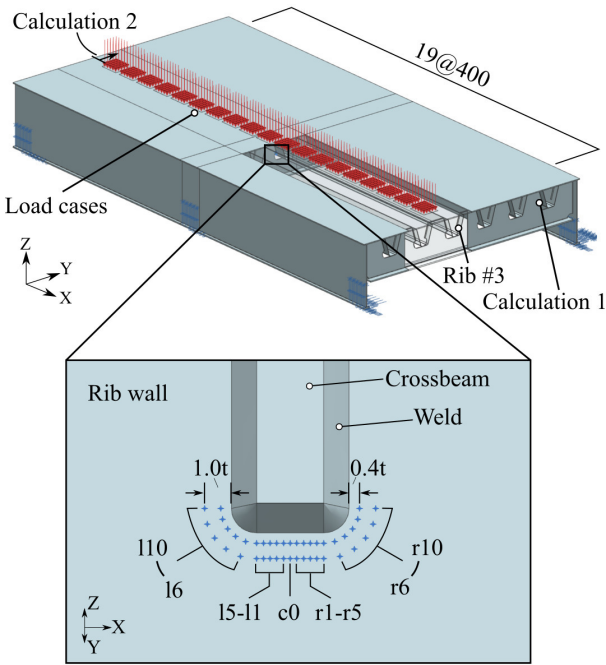


Figure 5.19: Reference points close to the lower weld toe (unit: mm)

5.6.1 Influence lines of different weld length

The influence lines of the models with different weld length are presented in Figure 5.20 to 5.25. In general, the overall trends for all schemes are quite similar. The most critical load position appears at 1200 mm away from the middle crossbeam for most points. When the tire load is at 1600 mm away from the middle crossbeam, the distortional stresses of points close to two ends (i.e. *l8-10* and *r8-10*) reach their peak values even though the results

are relatively small. The stress concentrations mainly appear at the locations close to the crossbeam center (i.e. point $c0$). Meanwhile, the small differences between points at the lower end indicate that the distortional stresses are evenly distributed. Comparing the influence lines from different models, the maximum hot spot stress will gradually rise with the increment of the weld length.

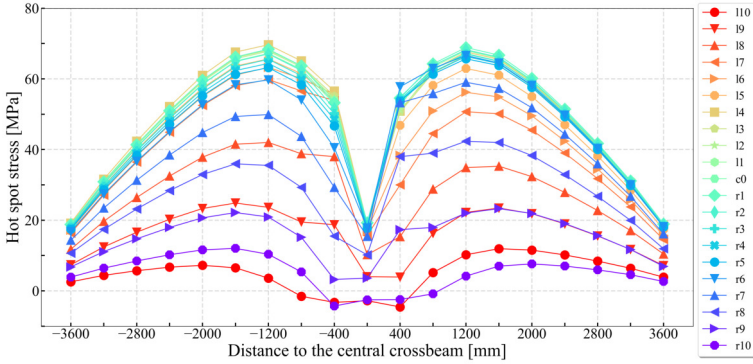


Figure 5.20: Influence lines of model with 127 mm weld length

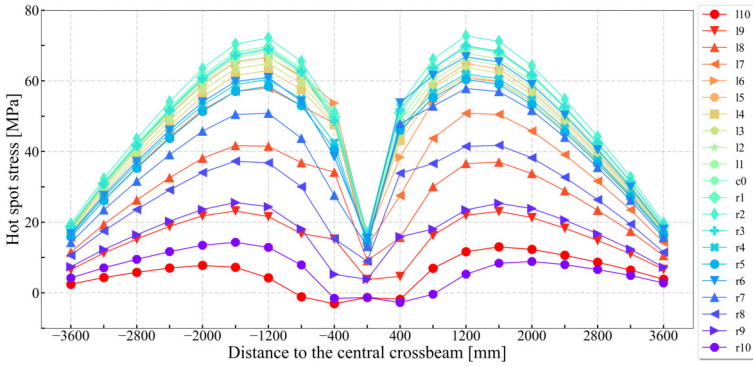


Figure 5.21: Influence lines of model with 152 mm weld length

5.6.2 Influence lines of different horizontal load position

The influence lines of different horizontal load position are given in Figure 5.26 to 5.29. In general, the overall shapes of the influence lines are similar. However, the most unfavorable load position in the longitudinal direction moves from 1600 mm away to 1200 mm away when the center of the load path moves from the center between ribs (i.e. the scheme *NoDeviation*) to the corresponding rib-to-deck joint (i.e. the scheme *150mmDeviation*). During this procedure, the same

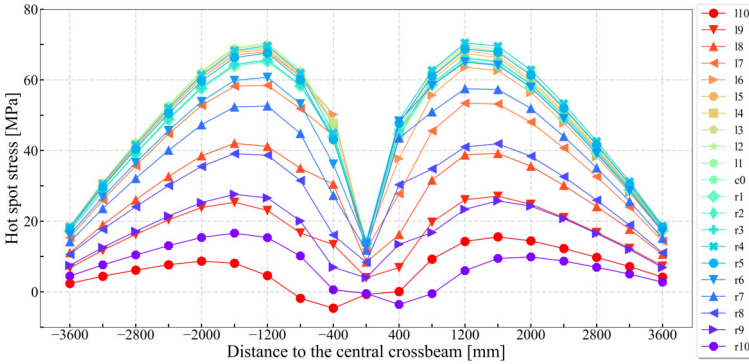


Figure 5.22: Influence lines of model with 177 mm weld length

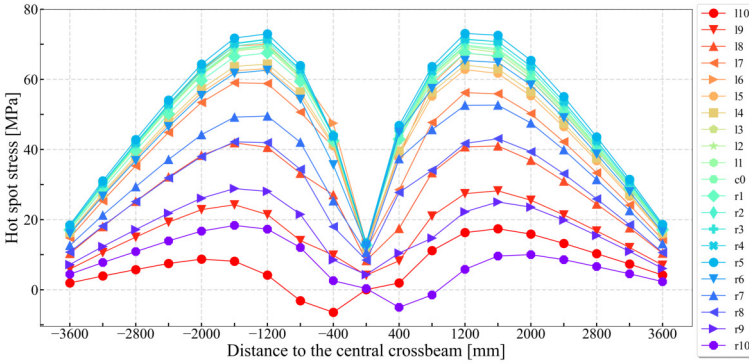


Figure 5.23: Influence lines of model with 202 mm weld length

rule as derived in section 5.5 is observed. The distortional stress would first increase then decrease. The most unfavorable load position in the horizontal direction appears when the horizontal deviation equals 100 mm.

5.6.3 Estimated fatigue life

After getting the influence lines, the corresponding calculations of the fatigue life are performed. The sets of standard lorries from Fatigue Load Model 4 (CEN, 2003) are utilized. Given the principal of linear superposition, the total stress induced by one lorry is acquired by the sum of stresses induced by tire loads from one side. Since the horizontal influence line is quite short, tires of the other side of the lorry would not have a huge impact on the results. The stress induced by a specific tire load is calculated through the linear interpolation of the corresponding influence line. Based on the assumptions mentioned above,

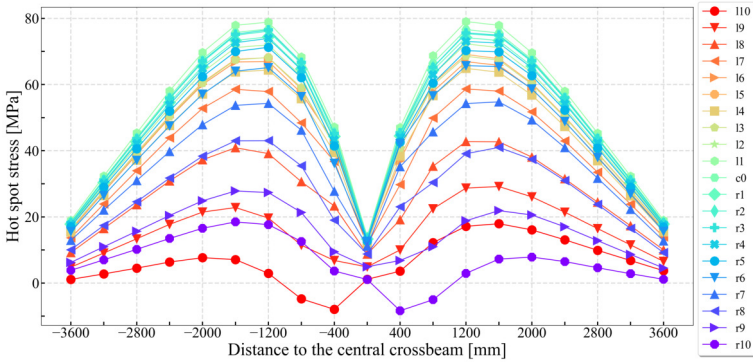


Figure 5.24: Influence lines of model with 227 mm weld length

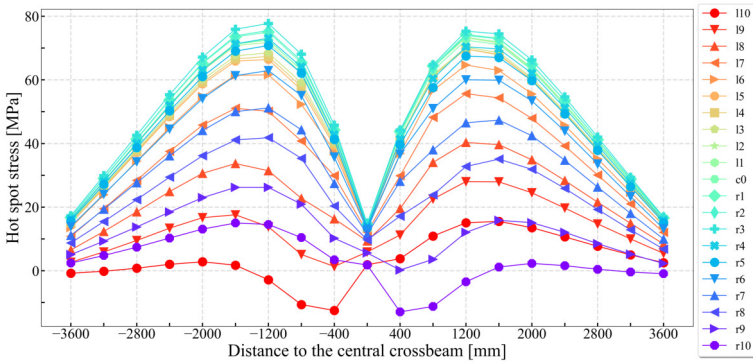


Figure 5.25: Influence lines of model with 252 mm weld length

the simulated stress histories of all target points can be acquired. Because the load routes are fixed, the stress cycles induced by a given lorry can be easily acquired. The traffic type of *local traffic* is selected which determines the percentages of lorries. *Traffic category 1* is chosen which indicates that the number of heavy vehicles (i.e. observations) expected per year and per slow lane is 200 million. Based on the stress cycles, the annually traffic volume and the percentages of lorries, the estimated fatigue life can be calculated according to the Palmgren-Miner method (Hobbacher, 2019). The detail category of 125 is adopted based on the recommendation of previous research (Kolstein, 2009).

Figure 5.31 displays the estimated fatigue life of models with different weld length when the center of the load path is inbetween two rib. In the names, *WL* is the abbreviation of “Weld Length”, which is followed by the vertical lengths of the connecting welds as illustrated in Figure 5.30. According to the results,

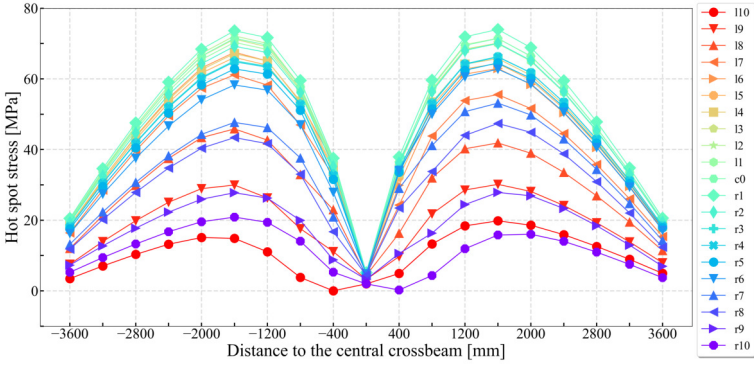


Figure 5.26: Influence lines of NoDeviation

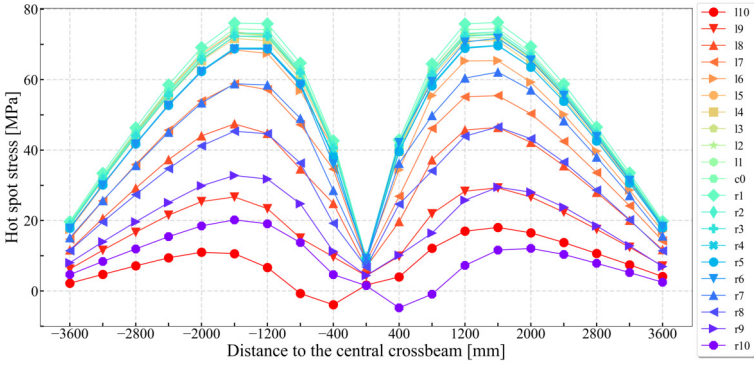


Figure 5.27: Influence lines of 50mmDeviation

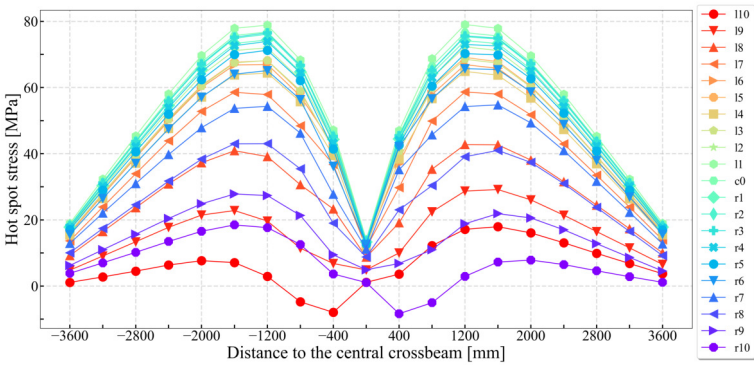


Figure 5.28: Influence lines of 100mmDeviation

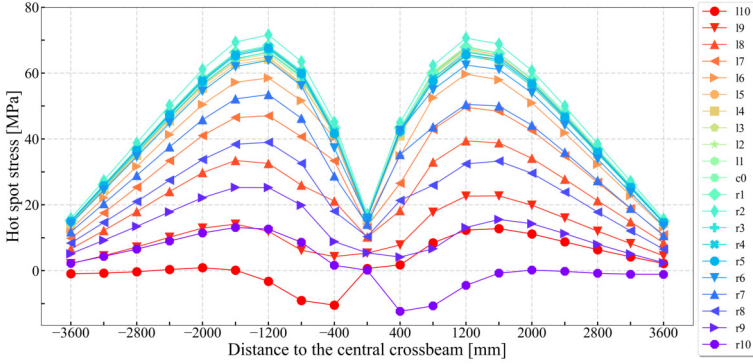


Figure 5.29: Influence lines of 150mmDeviation

fatigue cracks are most likely to initiate from the lower weld toe close to the center of crossbeam. Along the lower weld toe, the estimated fatigue lives of different points are almost identical. Therefore, point $c0$ could be adopted as the representative point when assessing the distortion-induced fatigue performance of the rib-to-crossbeam joint based on influence lines. The estimated fatigue life of points close to the two ends (i.e. point names ending with 8 to 10) are normally unlimited. When using a higher termination of the cope hole on rib wall (i.e. adopting shorter weld length), the estimated fatigue life would increase. Nevertheless, the influence of this parameter is limited. For $WL227$, the shortest fatigue life appears at point $l1$ which is 12.24 year. Meanwhile, the point $l4$ from $WL127$ has an estimated fatigue life of 17.94 year.

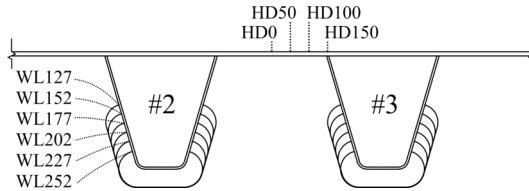


Figure 5.30: Illustration of the names of models

Figure 5.32 presents the estimated fatigue life of models with different load position when the weld length is 227 mm. In the names, HD is the abbreviation of “Horizontal Deviation”, which is followed by the horizontal distance from the center of the load path to the center between two ribs as shown in Figure 5.30. In general, $HD150$ has the highest estimated fatigue life. For points closer to the crossbeam center, $HD100$ would lead to the lowest fatigue life. Meanwhile, for points at two ends, $HD50$ would cause a shorter fatigue life.

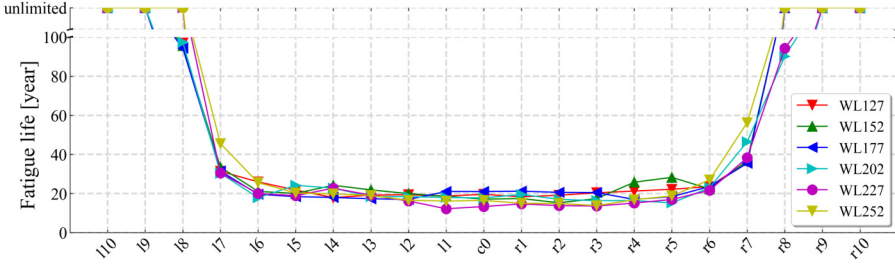


Figure 5.31: Estimated fatigue life of models with different weld lengths

This is related to the pattern of influence lines. Since there are two peaks for the influence lines of rib-to-crossbeam joint, the stress range is related to the distance between axles. In general, when the load center is more divergent from the center between ribs (i.e. from *HD0* to *HD150*), the most unfavorable load position of one tire load would move closer to the crossbeam. However, since the results of different schemes are still close to each other, the center between ribs could still be adopted as the reference load position when performing fatigue assessments for rib-to-crossbeam joint based on influence lines.

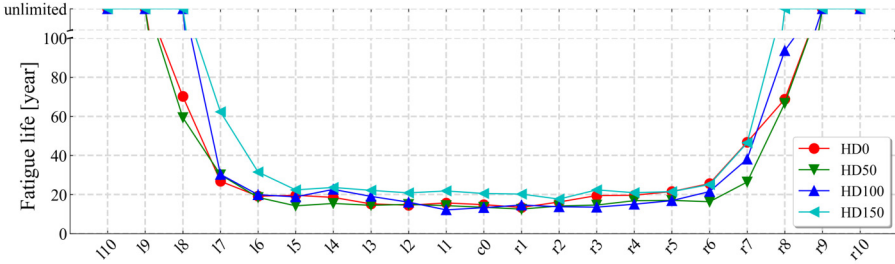


Figure 5.32: Estimated fatigue life of models with different load positions

5.7 Conclusions

In this chapter, the corresponding numerical simulations of the static load experiments are presented first. In general, similar trends as the tests are acquired. The calculation results of strain gauges that are far away from the stress concentration zone fit well with the measurement results. However, divergent results appear in strain gauges close to the weld toe (i.e. strain gauge chains). Four possible factors that may cause these differences are discussed one by one. According to the comparison of the measurement results and the

calculation results, the boundary condition has no influence on the simulation results. The weld profile (i.e. the weld cross-section and the throat thickness) has an influence on the calculation results but not prominent enough. The deviation of the strain gauges and the deviation of the load positions are the main causes that lead to the differences between measurement results and calculation results.

The deviation of the strain gauges is mainly caused by the irregular weld shape. On the one hand, the target weld at the rib-to-crossbeam joint that passes through the cope hole heavily relies on manual welding. Therefore, the target weld toe line is not as straight as normally seen at other joints that may be finished by automatic welding i.e. the rib-to-deck joint. This situation makes it very hard to precisely define the exact location of the strain gauges, especially when adopting the hot spot stress method. Meanwhile, this could be the explanation of the phenomenon that the measurement results are smaller than the simulation results on both sides. On the other hand, the irregular weld shape cannot be perfectly modeled in FEA. When performing numerical simulations using solid elements, the actual weld shape is replaced by an idealized weld shape. Under a certain weld throat thickness, the concave weld profile would tend to decrease the calculated stress meanwhile the convex weld profile would tend to increase the calculated stress. On the contrary, the influence of different throat thickness is limited under a certain weld profile.

When investigating the influence of the load deviation, it is found that the most unfavorable horizontal load position is not at the center between two ribs as considered before. If the center of the tire load moves from the center between two ribs towards the rib-to-deck joint of the target rib, the distortional stress of the target rib will first increase then decrease, whereas the distortional stress at the adjacent rib will drop dramatically. This may be the explanation of the phenomenon that the relative difference between two ribs is larger in measurement results than in calculation results.

The results of the fatigue assessments based on influence lines show that even through raising the termination location of the cope hole on the rib wall would decrease the distortional stress, its influence on the estimated fatigue life is limited. Meanwhile, if the center of the tire load was divergent from the center between ribs, the distortional stress at the corresponding rib-to-crossbeam joint may be influenced. However, the estimated fatigue life is almost the same. Therefore, the center between ribs could be used as the reference transverse load position when conducting the fatigue assessments based on influence lines. The reference points that are closer to the crossbeam center have a similar fatigue life. Hence, the reference point at the central plane of crossbeam could be chosen as the representative point for assessing the fatigue performance induced by distortional stresses.

6

Structural optimization

6.1 Motivation

In section 2.2, it was introduced that a continuous rib passing through the crossbeam is the prevailing form of the rib-to-crossbeam joint, and there are two accepted approaches when dealing with the intersection of the rib to the crossbeam. The first approach is to design a cope hole in the crossbeam web under the rib. The other approach is to provide a tight fit between the continuous rib and the crossbeam with a continuous weld all-around. The majority of current designs adopts the former approach. However, the existence of cope holes introduces several problems.

On the one hand, fatigue cracks initiating around the cope holes of the crossbeam are very common. The shape of the cope holes has a direct influence on the fatigue performance itself. Even though a large number of different cope hole shapes has been investigated (Connor, 2004; Zhu *et al.*, 2019a), an overall optimal shape has not been found yet. Meanwhile, the cope hole also represents a geometrical discontinuity at the bottom end of the weld connecting the crossbeam and the rib. As presented so far, the geometrical discontinuity causes stress concentrations which lead to a very low fatigue performance at this detail. Some approaches such as decreasing the weld length could lower the stress range but the influence on the fatigue life is still limited as shown in previous chapter.

On the other hand, the cost spent on welding the rib-to-crossbeam joint with cope holes is extremely high. That is because this weld cannot be finished by automatic welding. The fabrication relies heavily on manual welding. According to previous research (Tang, 2011), the total cost of orthotropic steel bridge decks is composed of material cost, fabrication cost, transportation cost and installation cost. Normally, the material cost presents less than 35% of the total cost. The major cost is spent in fabrication, in which the major expenses are the welds at the intersection of the rib and the crossbeam as illustrated in Figure 6.1.

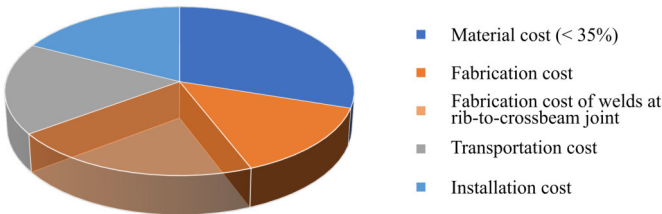


Figure 6.1: The cost composition of orthotropic steel bridge decks (according to the description of Tang (2011))

Canceling the cope hole at rib-to-crossbeam joint may save up to 15% of the fabrication cost of an OSD (Wolchuk, 2004). Except for the high fabrication cost, the manual welding plus the narrow space of manipulation makes it rather hard to ensure a stable weld quality. As presented in Figure 5.11, the irregular weld shape represents numerous imperfections that aggravate the stress concentrations, which further reduces the fatigue life of this joint.

As introduced before, the reported research aiming at improving the fatigue performance of the rib-to-crossbeam joint includes such aspects as follows:

- introducing additional attachments to enhance the local rigidity (Connor *et al.*, 2012; Zhu *et al.*, 2018a);
- optimizing the shape of cope holes (Connor, 2004; De Corte, 2009; Zhu & Xiang, 2019; Zhu *et al.*, 2020);
- using post-weld treatment to release residual stress and enhance the performance (Wang *et al.*, 2018b);
- introducing the cement-based material as a rigid pavement to improve the rigidity of OSD and decrease stress range at fatigue details (Abdelbaset *et al.*, 2020; Chen *et al.*, 2019a; Shao & Cao, 2018; Su *et al.*, 2018; Zhang *et al.*, 2020b; Zhu *et al.*, 2019b), etc.

Among these approaches, installing additional attachments e.g. bulk heads would introduce new fatigue prone details and further increase the fabrication cost which is therefore not recommended anymore. Optimizing the shape of cope holes mainly affects the fatigue cracks along the free edge, whereas its influence on the lower weld end on the rib wall is quite limited. Through the comparison presented in the previous chapter, increasing the position of the cope hole termination is able to decrease the distortional stress, yet the influence on the fatigue life is not obvious. Applying post weld treatment could eliminate the micro imperfections caused by the welding procedures and eventually improve the fatigue life. However, this approach does not change the structural behavior itself. Therefore, it cannot reduce the stress range induced by vehicles, which means the possibility of fatigue cracks is still very high. By far, the most promising approach is to introduce rigid pavements. A rigid pavement could effectively enhance the local rigidity of an OSD which is beneficial for the load dispersion. Thus, almost all fatigue prone details could get a reduction of stress ranges under different ratios. As a relatively new technique, the durability of this new structure requires more time to prove its efficiency. The prerequisite for a composite structure to achieve successes relies on the combination of the pavement and the OSD. Typically, the inter-facial connection is finished by high strength epoxy adhesive or shear connectors e.g. studs. Once there is deterioration on the connection, the necessary repairing process would be

very laborious due to the high strength of pavement material and the dense reinforcements.

In 2011, Tang (2011) proposed a new concept of OSDs as shown in Figure 6.2. The new concept is based on the use of a hot-rolled rib with variable thickness. Initially, the hot-rolled rib is proposed to reduce the residual stress created by the cold bending process. However, the optimization of the rib shape could be finished simultaneously. The thickness at the bottom is 20 mm. Meanwhile, rounded rib bottom is adopted. Use of a rounded shape without a cope hole has performed well in a number of earlier bridges. To improve the rib-to-deck joint, a local thickening is introduced at the top portion of the rib stem. The rib thickness gradually increases from 8 mm to 11 mm at the top. Then, it will be easy to produce an 8 mm or 9 mm weld from one side only without risking blow-through. The paper claims that when the crossbeam span could go up to 8 meters, there is no need for intermediate floor beam in most cases. According to the paper, the thickness of the deck plate is 18 mm which is thought to reduce stress concentrations at the rib-to-deck joint. Meanwhile, the stress problems in the pavement should be eliminated with the thicker deck plate and a span to depth ratio of 22.22 based on previous experience.

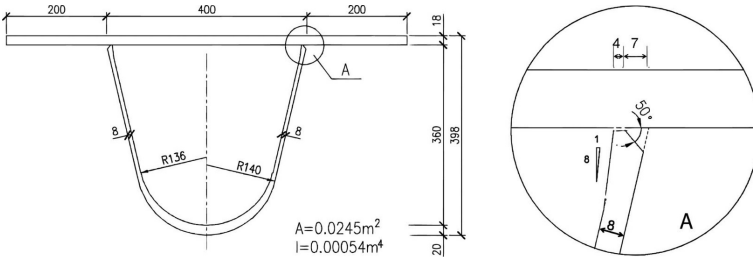


Figure 6.2: The proposed hot-rolled rib (unit: mm) (Tang, 2011)

Recently reported, the rounded rib was also investigated by researchers from the United States (Kitner, 2016; Marks, 2018; Saunders *et al.*, 2019). An illustration of the investigated rib-to-crossbeam joints is presented in Figure 6.3. In total three types of connections are studied. Except these two types shown in the figure, the other type is with a conventional cope hole. Parametric studies based on FEA are performed on all three types of connections, but only these two fitted connections are fabricated and tested. As stated in the reports, the motivation of the research is to improve manufacturability of the often labor-intensive rib-to-crossbeam joint by using automated fabrication method. Different from the suggestion of Tang, cold-bent ribs are adopted because of two main reasons. On the one hand, the hot-rolled ribs are more complicated and expensive to fabricate than cold-formed ribs (Mangus, 2015). Manufacturers must have pre-

made dies and rolls to hot roll a rib shape. Without standardized rib profiles, custom roll and dies would be a significant investment for the fabrication of the ribs for a new OSD. On the other hand, cold-bent ribs using a die created for a specific OSD rib geometry are likely to have less deviation from the specified rib shape, compared to ribs that are cold-bent using a break press in a series of bends, or ribs that are cold rolled or hot rolled. When ribs are rolled, rather than pressed, achieving appropriate tolerances has been difficult, with variations up to 0.12 inch (3.048 mm) as reported by Saunders *et al.* (2019). Therefore, cold-bent ribs are continuously adopted. The automated fabrication process is also introduced in the reports. After the ribs are welded to the deck plate, laser tracking of the rib-deck panel at the intersection with the crossbeam web can be used to create a two-dimensional (2D) digital representation of the rib-deck panel profile. With the help of computer numerically controlled (CNC) equipment, the 2D representation can be used to program cutting tool to cut the crossbeam web. This process will ensure that the crossbeam will tightly fit the rib-deck panel if the measurement and cutting equipment is sufficiently accurate. According the report (Saunders *et al.*, 2019), the rib-to-crossbeam connection welds of the two fitted are made with a robotic welding process. Based on the laboratory tests, these two types of connections both demonstrate good fatigue performance. In accordance with the recommendations, the fitted rib-to-crossbeam connection type is preferred for new bridges due to its potential for automated fabrication and for good fatigue performance. For deck replacement applications, where the crossbeams of the OSD may be restrained by the existing superstructure, the slit rib-to-crossbeam connection type is more suitable.

At almost the same time, the tight-fitted rib-to-crossbeam joint was also studied by researchers from Japan (Yokozeki, 2017; Yokozeki & Miki, 2016, 2017). Yokozeki tested the fatigue strength and the fatigue lives of several types of OSDs. At first, different OSDs are investigated based on hot spot stress approach. Then, a series of static and fatigue load tests are performed including the slit or none-slit (i.e. with or without cope hole) trapezoidal ribs as shown in Figure 6.4. In the figure, *US* represents slit U rib and *UN* means none-slit U rib. Three constant amplitude fatigue tests are conducted. The loading positions are marked by *USa*, *UWa* and *UNa* in Figure 6.4(a). The test results show that surface fatigue cracks were detected at slit connections of models U, while no cracks were detected in non-slit connections of models U by both visual inspections and strain monitoring. It is concluded that eliminating the slit on the crossbeam webs can improve the fatigue strength of the longitudinal rib to crossbeam connections. The hot spot stress ranges of connection UN is smaller than those of US by 65 %, where the inner diaphragms are attached in the U ribs at 400 mm from the crossbeam.

In retrospect, the tight-fitted rib-to-crossbeam joint appeared earlier in the

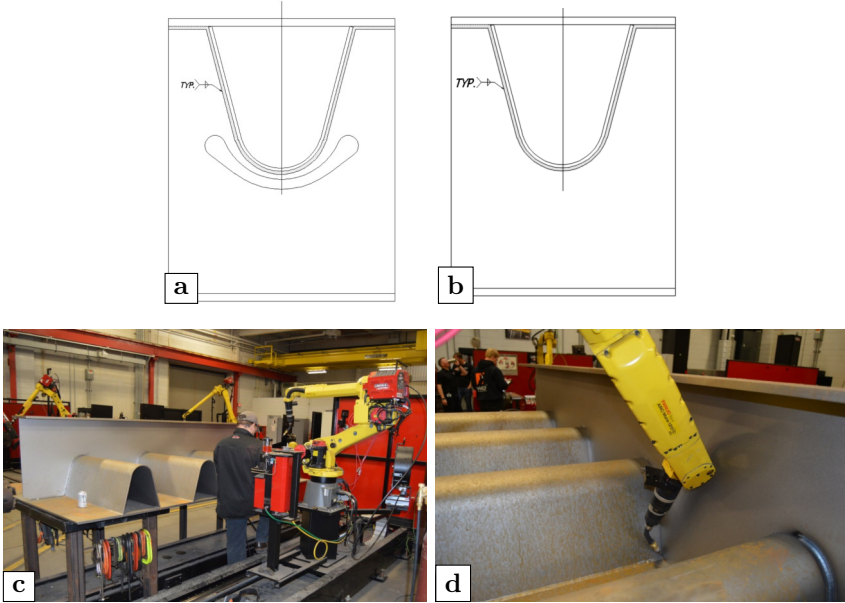


Figure 6.3: Investigated rib-to-crossbeam joint: (a) slit connection; (b) fitted connection; (c) robotic welding station; (d) welding procedure (Saunders *et al.*, 2019)

development history of OSDs than those with cope holes. However, two main problems impeded the application of this tight-fitted form. On the one hand, the fabrication accuracy of steel plates was quite low, which increased the assembly difficulties. On the other hand, the deck plate thickness of early OSDs was usually much thinner than those used nowadays. This led to larger deformations under concentrated tire loads which caused high stresses at the bottom of the rib. Therefore, tight-fitted joints were gradually replaced by those with cope holes. Nevertheless, the fabrication accuracy has been improved with the help of modern CNC equipment. The commonly-used thickness of deck plates is also much thicker than before. These developments may encourage engineers to reconsider the applications of tight-fitted rib-to-crossbeam joints given the disadvantages of adopting cope holes as stated before.

6.2 Comparison of different modeling method

In the prevailing codes, the simulation methods of OSD structures are not regulated. Up till now, the numerical simulations of this thesis are all based on solid elements. When adopting solid elements, the weld is normally modeled as a prism that has a triangular cross-section. However, on the one hand, the actual

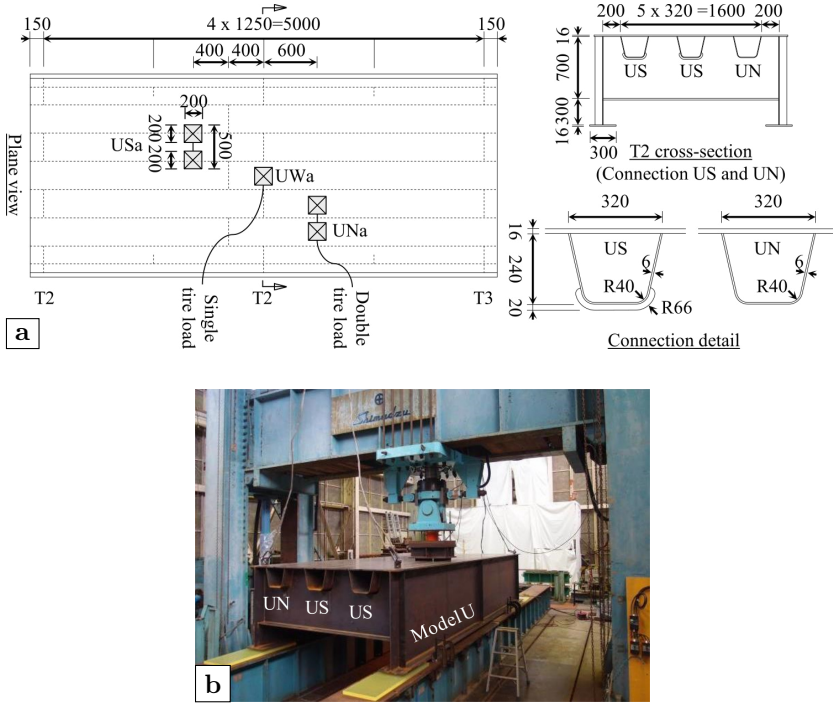


Figure 6.4: Specimen dimensions and on-site photo: (a) dimensions of specimen; (b) fatigue tests (units: mm) (Yokozeki, 2017)

weld shape of the rib-to-crossbeam joint is quite irregular as demonstrated in the section 5.5. The unpredictable weld shape makes it very difficult to derive a guideline when performing FEA. On the other hand, the computation of solid models especially when using higher order solid elements and relatively small element sizes is very time-consuming. For numerical models using solid elements presented in the previous chapter, the computation time for one load case including the global model and the submodel is around 1.5 hours. Due to these reasons, different modeling methods are first investigated.

6.2.1 Different models

The numerical simulation is still performed using the software Siemens NX. Two finite element models are built using solid elements and shell elements respectively. The division of global model and submodel for the shell model is the same as the solid model used before. The details close to the target weld toe of the rib-to-crossbeam joint are presented in Figure 6.5. In this

figure, the frontier distance S_f is defined to represent the distance from the weld toe to the strain gauge in reality. In section 5.5.4, the influence of the deviation of strain gauges is discussed. Ideally, the frontier distance equals the distance from the first strain gauge to the leading edge of the carrier which is 2.75 mm. Even though it shows that the actual frontier distance may be larger than the ideal situation, the frontier distance in simulations is still set to 2.75 mm. The simulated results can therefore be used as references when adopting the structural hot spot stress method (i.e. the frontier distance of the first reference point is 2.4 mm). S_{wl} represents the length of the weld leg which is 5.65 mm as the throat thickness of the weld is 4 mm. The letters W or NW in model names are the abbreviations of “Weld” and “No Weld”, which means the influence of welds is considered or not considered respectively. With reference to the conclusion in section 5.5, the influence of different weld profiles is limited. Therefore, all welds are finely modeled using the triangular cross-section in *SolidW* but omitted in *SolidNW*. As for the shell models, the weld geometry is not modeled, so two schemes are adopted. In *ShellW*, the frontier distance is calculated from the supposed location of the weld toe. Hence, the distance from the strain gauge to the edge point equals the frontier distance plus the length of the weld. In *ShellNW*, the frontier distance is calculated from the edge point of the crossbeam.

Similar to the solid models, mesh sensitivity tests are conducted. In shell models, the 8-nodes 2D CQUAD8 element with full integration is adopted in both the global model and the submodel. Relevant sensitivity tests are also performed adopting the same evaluation criterion as the solid element models. The results of the mesh sensitivity tests are given in Figure 6.6. Similarly in Figure 6.6(b), each curve represents a given mesh size of the global model since the boundary condition of the submodel is derived from the global model. Based on the results, the element size of the global model is chosen as 10 mm. For the submodel, the trend is different if compared with solid model, but the influence of the mesh size is much smaller. The element size of 2 mm is finally adopted. For solid models, the 10-nodes 3D CTETRA10 element is adopted. Element sizes are 20 mm and 5 mm for the global model and the submodel respectively. The results of the mesh sensitivity tests may be checked in Figure 5.2.

6.2.2 Results and discussion

Figure 6.7 displays the comparison of the measurement results and the calculation results from different models. Among these four schemes, the results of *ShellW* are the closest to the experimental results at the location of the strain gauge chains as shown in Figure 6.7(a). In the same figure, the results of *SolidW* and *ShellNW* are quite close but they are all higher than the experimental results, and *SolidNW* gives the highest estimation. With

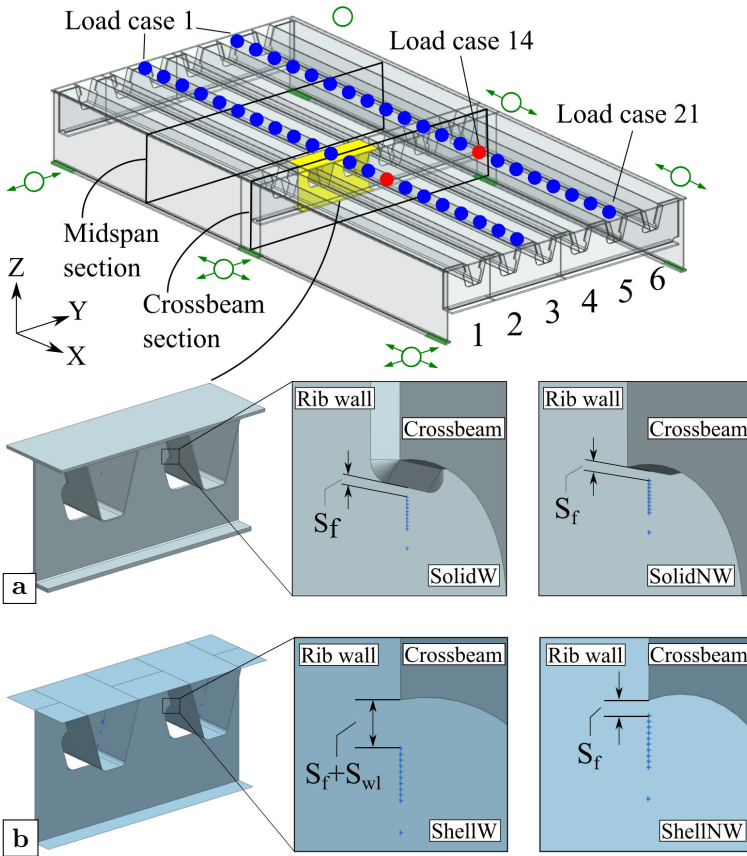


Figure 6.5: Different modeling methods: (a) solid models; (b) shell models

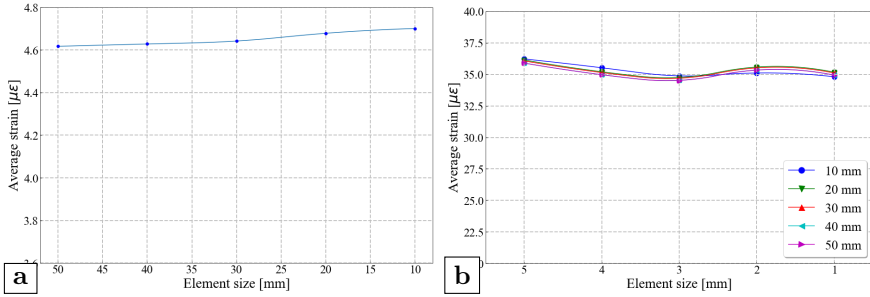


Figure 6.6: Mesh sensitivity tests of shell models: (a) global model; (b) submodel

reference to the results presented in the previous chapter, the difference could be explained by the deviation of experiments e.g. the horizontal deviation of load position or the position of strain gauges. Due to the steep stress gradient at this location, a displacement of only a few millimeters or a rotation of a few degrees may influence the calculation results. Figure 6.7(b) to (d) present the results of other strain gauges on the rib and on the crossbeam. In general, for these locations that are not within the stress concentration zone, both the solid models and the shell models give estimations that fit well with the measurement results.

Given that the computation time of the solid models is 3 to 4 times higher than the shell models and that their results are quite close, the shell element model seems to be a better choice when performing analysis for the rib-to-crossbeam joint. Even though the result of *ShellW* is closer to the experimental results, the scheme of *ShellNW* is adopted in the following sections since it gives the same results as the solid model with the welds modeled. Thus, using either solid elements or shell elements would lead to a consistent result. Besides, the results of *ShellNW* tend to be larger than the results of *SolidW* when the frontier distance decreases. Consequently, *ShellNW* is more conservative when adopting the hot spot stress method.

6.3 Parametric study

6.3.1 FEA model

As stated before, the existence of cope holes not only increases the cost of fabrication but also introduces several fatigue prone details which are difficult to eliminate. To investigate the possibility of canceling the cope hole, the parametric analysis of a tight-fitted rib-to-crossbeam joint is first performed to investigate the influence of a few design parameters as shown in Figure 6.8.

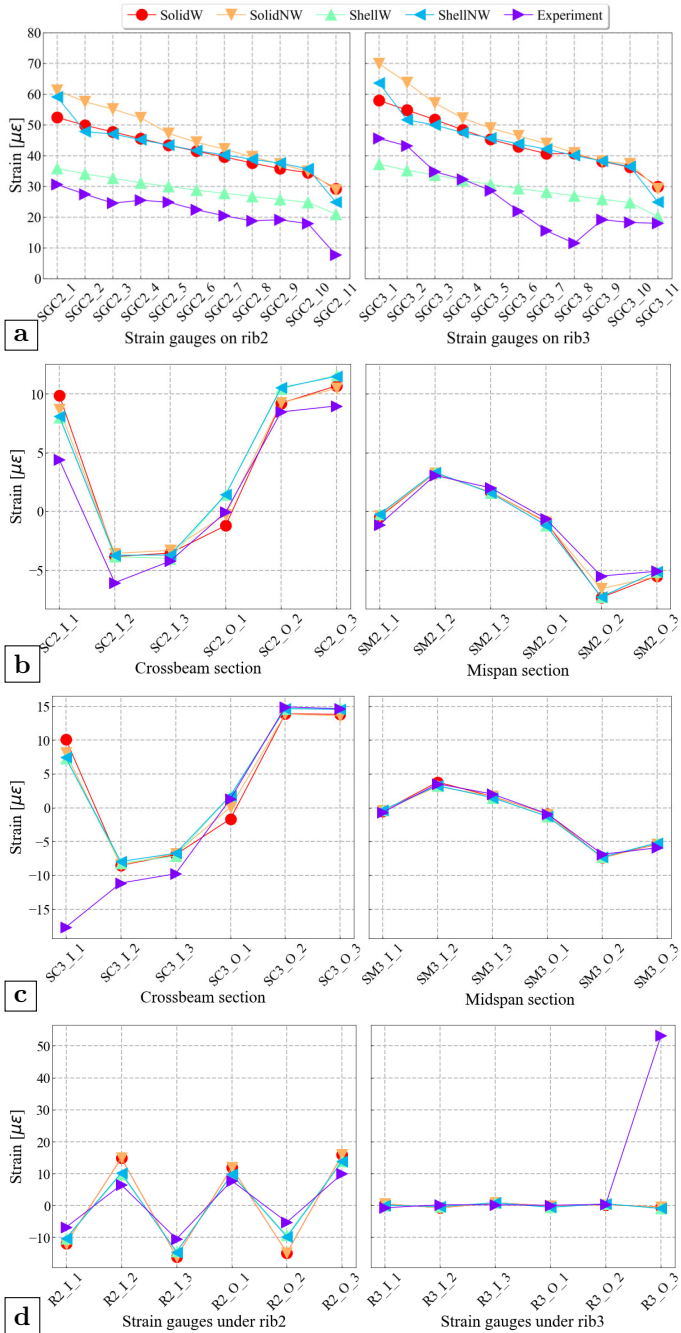


Figure 6.7: Results comparison of different models: (a) strain gauge chains; (b) single strain gauges on rib 2; (c) single strain gauges on rib 3; (d) strain gauges on crossbeam

The general dimensions of the baseline design come from the specimen of the static load experiments as shown in Figure 4.1. Major design parameters such as the shape of the ribs, the span of the crossbeams and the span of the ribs remain the same, but all cope holes are canceled.

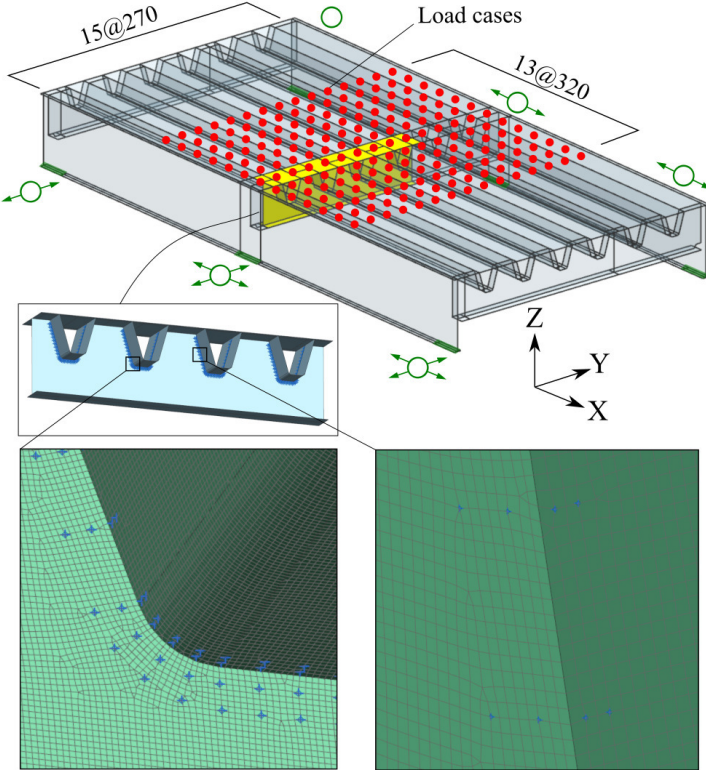


Figure 6.8: FEA model of OSD with the tight-fitted rib-to-crossbeam joint (unit: mm)

The hot spot stress method with the linear extrapolation method are still adopted. For the tight-fitted rib-to-crossbeam joint, there are two weld toes on each plate surface (i.e. the rib plate and the crossbeam plate). Investigated points on both plates are defined as hot spot type *a* in accordance with the recommendation from IIW (Hobbacher, 2019). Two reference points are located at $0.4t$ and $1.0t$ respectively as stated before. Therefore, the hot spot stress is calculated by equation 2.6. For each intersection of the rib to the crossbeam, 36 inquiry locations are defined all around the joint as shown in Figure 6.9.

The inquiry locations are symmetrically arranged around the central line of rib. For each inquiry location, 4 reference points are defined, two of which are on the crossbeam side and the other two are on the rib side. It should be noted that the points from crossbeam side and the points from rib side share the same names since both of them actually refer to the same location but different extrapolation paths. For the target zone, being the rib-to-crossbeam joint, a refined element size of 2 mm is adopted. For the rest of the model, the element size is 10 mm. According to the results in previous section, the element size is small enough to get convergent results.

6.3.2 Boundary conditions and load cases

The boundary conditions adopted are the same as in the previous section. It has been verified that the influence of boundary conditions is not obvious since the rib-to-crossbeam joint is far from the supports. As for the load cases, the single tire load of Fatigue Load Model 4 from Eurocode 1 (CEN, 2003) is adopted. The wheel type C with a contact area of 270×320 mm is chosen. The equivalent axle load is 90 kN. Thus, the single tire load is 45 kN. The impact factor is included in the load model therefore it is not considered separately. To get the influence surface, the predefined load positions are distributed over a distance of half a span to both sides from the target crossbeam. The interval distances between load cases are 320 mm longitudinally and 270 mm transversely, which are the same sizes as the length and width of the contact area. In total $13 \times 15 = 195$ load cases are calculated. An illustration of all load cases is shown in Figure 6.8.

6.3.3 Results and discussion

Four design parameters are investigated: the thickness of the deck, the thickness of the rib, the thickness of the crossbeam and the radius at the bottom of the rib. Table 6.1 gives the overview of the investigated parameters. Only one parameter is modified to investigate relevant influences at each time. The stress component that is perpendicular to the weld is utilized to calculate the hot spot stress. Hence, when calculating the hot spot stresses of the weld toe on the rib side, the stress component along the X axis is used (see Figure 6.8). Meanwhile, when calculating the hot spot stresses of the weld toe on the crossbeam side, the stresses are calculated along the extrapolation paths that are normal to the direction of the welds by the method described in section 5.3.

It should be noted that the possible maximum stress range for each investigated location is acquired by using the maximum stress (i.e. maximum tension stress) minus the minimum stress (i.e. maximum compression stress) throughout all load cases. When comparing the calculation results from the three ribs on the

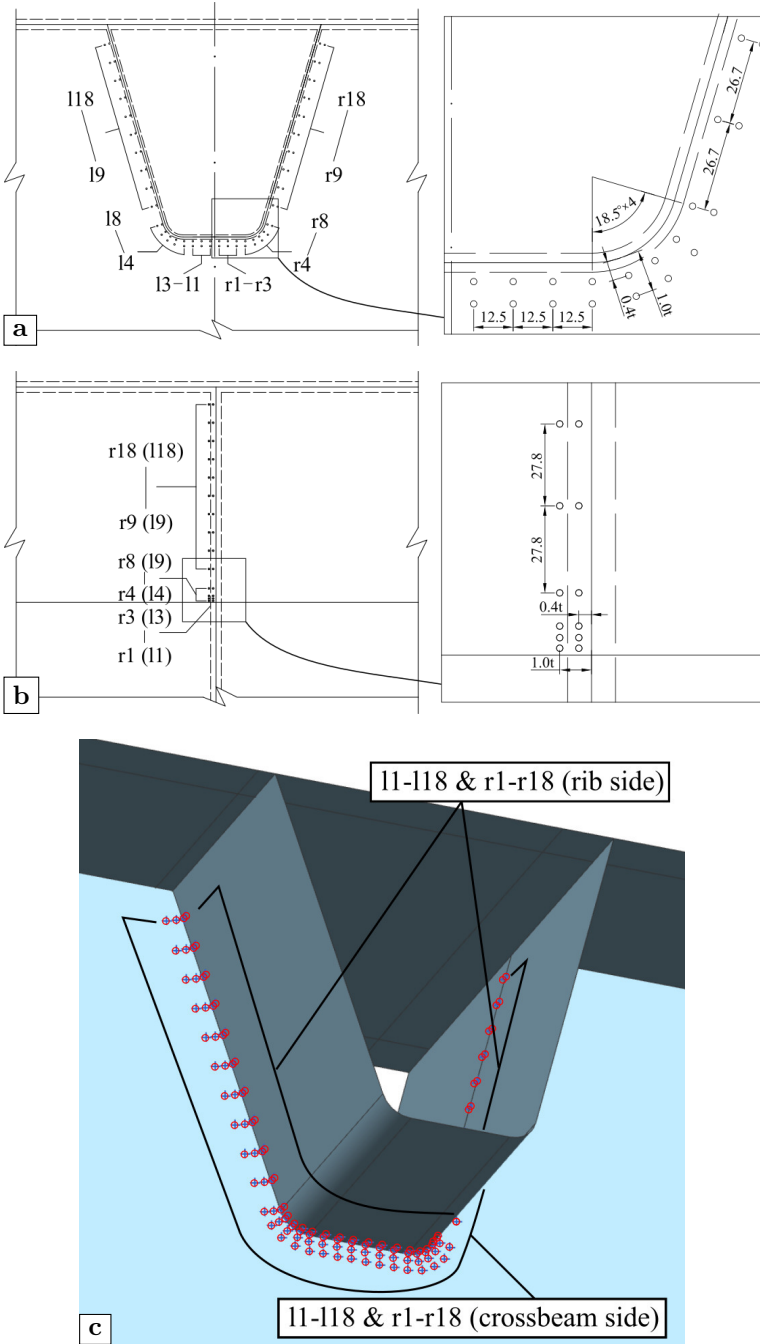
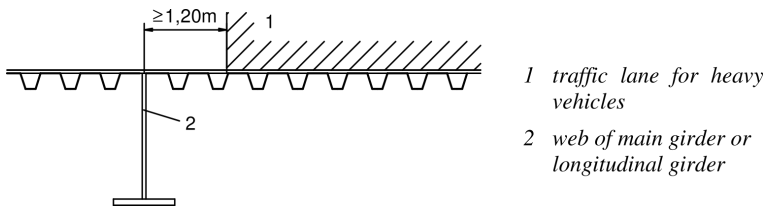


Figure 6.9: Locations of investigated points: (a) crossbeam side; (b) rib side; (c) 3-D illustration (unit: mm)

Table 6.1: Summary of the investigated parameters (unit: mm)

Thickness of deck	Thickness of rib	Thickness of crossbeam	Radius of rib
15	6	12	25
18	8	15	35
20	10	18	45

same side, the stress range of the same location is larger when the rib is getting closer to the web of the main girder. It may be explained by the fact that the load dispersion is impeded by the web of the main girder, which leads to more severe stress concentrations. The stress distributions of rib 3 and rib 4 are symmetrical due to the symmetry of the structure itself. Based on the suggestion of Eurocode 3 CEN (2006), the minimum distance from the edge of the traffic lane for heavy vehicles to the web of the main girder is 1.2 m as shown in Figure 6.10. When the distance is within 1.2 m, the stiffness of the ribs needs to increase to prevent cracking of the surfacing due to differential deflections. Therefore, the calculation results from rib 3 are chosen as the representative results in the following sections.

**Figure 6.10:** Condition for the curve of minimum stiffness (adapted from CEN (2006))

6.3.3.1 The thickness of the deck plate

Figure 6.11 presents the influence of the deck plate thickness on the maximum stress ranges. In general, increasing the thickness of the deck would decrease the stress range. On the crossbeam side, the average decreasing amplitude is 28.12%. Meanwhile on the rib side, the average decreasing amplitude is 22.89%. It should be noted that the maximum stress ranges on the rib side are much larger than the stress ranges on the crossbeam side. However, the most critical points remain the same. For both sides, the peak values appear at the middle point of the curvatures (i.e. points $l6$ and $r6$). Figure 6.12 shows the influence surface of point $l6$ on rib side for different deck thickness. In the figures of influence surfaces, the zero tick of the Y axis denotes the

position of the middle crossbeam. The intersection of the rib wall with the deck (i.e. the rib-to-deck joint) is marked by dashed lines. The projected location of the point on the deck plane is marked by the rectangular symbol. The positions that generate the maximum and minimum stress are denoted by the cross and circle symbol respectively. The same annotation method is adopted in following similar figures. It can be seen from the comparison that the pattern of the influence surface does not change with an increase of the deck thickness. The load positions that cause the maximum tension and compression stress are located between two ribs.

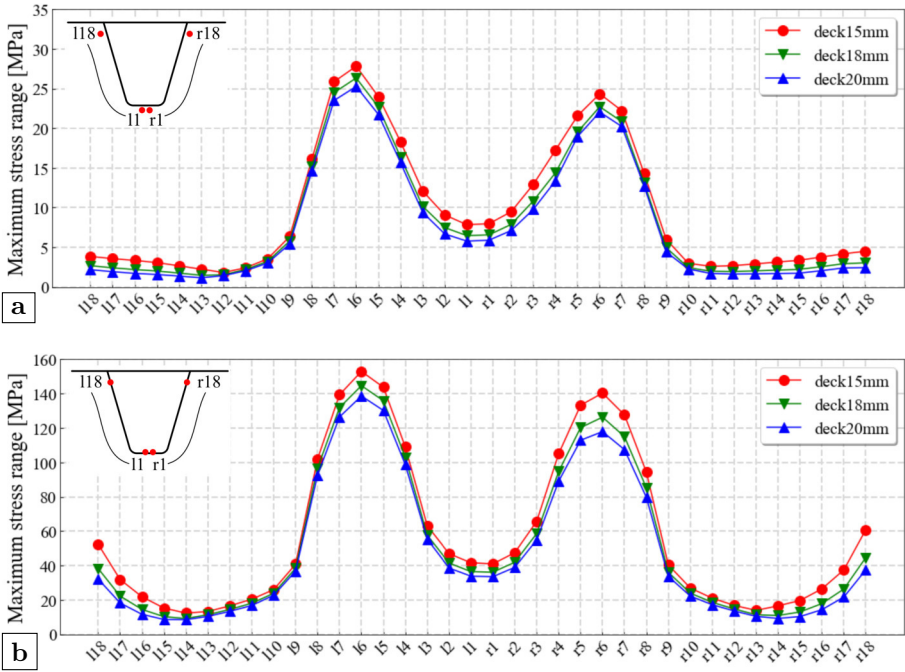


Figure 6.11: Influence of the deck plate thickness: (a) crossbeam side; (b) rib side

6.3.3.2 The thickness of the rib

Figure 6.13 displays the influence of the rib thickness on the maximum stress ranges. On the crossbeam side, raising the rib thickness could diminish the maximum stress range at the curvature. However, the maximum stress ranges of points at the stem (i.e. points $l/r10-18$) and the bottom (i.e. points $l/r1-4$) would also get larger at the same time. On the rib side, the thickness of the rib has an obvious influence on the maximum stress ranges of points at the curvature (i.e. points $l/r4-8$). When the thickness of the rib increases from 6

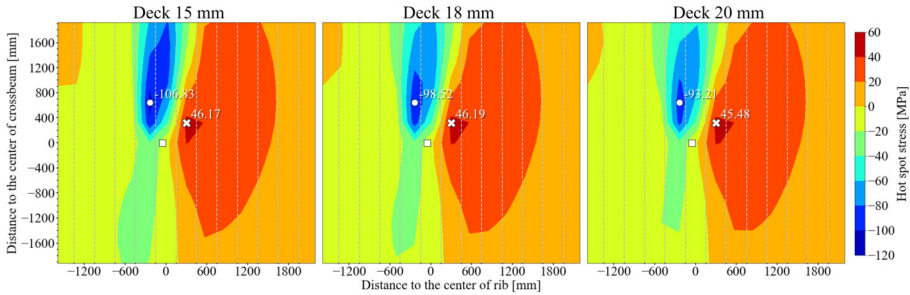


Figure 6.12: The influence surface of point $l6$ for different deck thickness

mm to 8 mm, the maximum stress range drops dramatically from 153 MPa to 63 MPa at point $l6$. The decreasing amplitude is 58.6%. Nevertheless, the influence of the rib thickness on the maximum stress ranges of points at the stem of rib (i.e. points $l/r13-18$) is not obvious. Figure 6.14 shows the influence surfaces of point $l6$ on the rib side for different rib thickness. As seen in the figure, this parameter would influence the most unfavorable load position of either the tension stress or the compression stress. For the tension stress, the most unfavorable load position is at 320 mm away from the crossbeam longitudinally when the rib thickness is 6 mm. If the rib thickness is larger than 8 mm, the most unfavorable load position would move to the center of the crossbeam longitudinally and remain the same horizontally. For the compression stress, if the rib thickness changes from 8 mm to 10 mm, the most unfavorable load position would change from the center between rib 2 and rib 3 to the center of rib 3 transversely, and from 600 mm to 1400 mm away from the target crossbeam longitudinally.

6.3.3.3 The thickness of the crossbeam

Figure 6.15 presents the influence of the crossbeam thickness on the maximum stress ranges. In general, this parameter mainly affects the points on the crossbeam side while having little influence on the rib side. On the crossbeam side, the maximum stress ranges decrease with an average decreasing amplitude of 39.93% when the crossbeam thickness increases from 12 mm to 18 mm. On the rib side, when the crossbeam thickness changes the same amount, only the points at the curvature are influenced (i.e. points $l/r5-7$). It should be noted, however, that the maximum stress ranges on the rib side are still much larger than at the crossbeam side. The influence surfaces of point $l6$ on the rib side for different crossbeam thickness are displayed in Figure 6.16. It can be concluded from the figure that although the maximum stress range of this point do not show large changes, the maximum compression stress increases (i.e. from 98.02

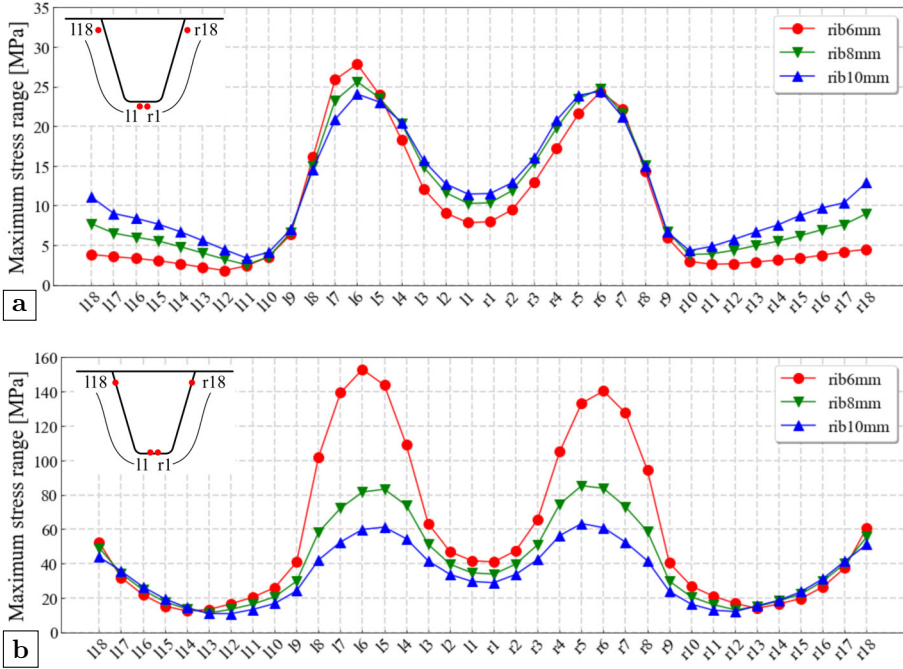


Figure 6.13: Influence of the rib thickness: (a) crossbeam side; (b) rib side

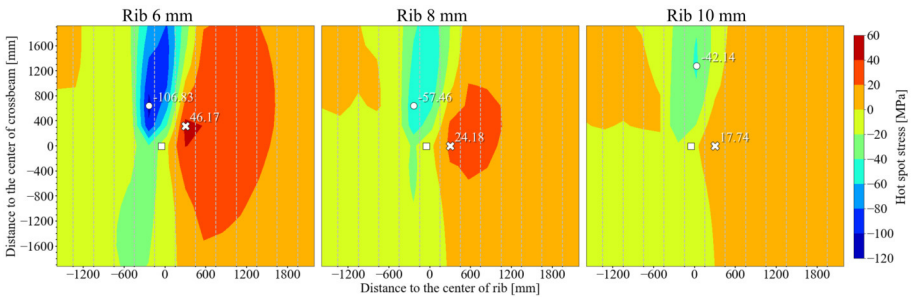


Figure 6.14: The influence surface of point l6 for different rib thickness

MPa to 108.09 MPa) and the maximum tension stress decreases (i.e. from 49.59 MPa to 45.81 MPa) when the crossbeam thickness changes from 12 mm to 18 mm. Finally, this parameter does not affect the most unfavorable load position.

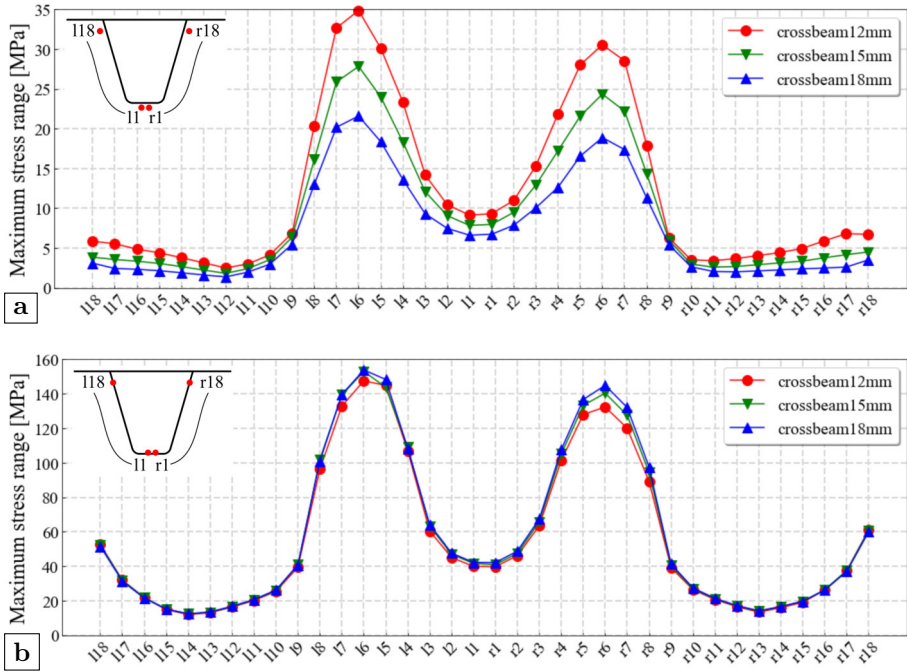


Figure 6.15: Influence of the crossbeam thickness: (a) crossbeam side; (b) rib side

6.3.3.4 The radius of the rib

Figure 6.17 shows the influence of the rib radius on the maximum stress ranges. On both the crossbeam and the rib side, the rib radius mainly affects the points at the bottom of the rib (i.e. points $l/r1-8$). In general, the maximum stress ranges of these influenced points are tend to be more evenly distributed when using a larger rib radius. Meanwhile, the difference between the two peak values that appear on the two curvatures (i.e. point $l6$ and $r6$) respectively also decreases. The decreasing amplitude of point $l6$ is 28.2% and 16.54% on the crossbeam side and the rib side separately. Figure 6.18 displays the influence surfaces of point $l6$ for different rib radius. it can be seen from the figure that the most unfavorable load positions are not influenced by this parameter. The maximum tension and compression stresses are both reduced when the radius of rib gets larger.

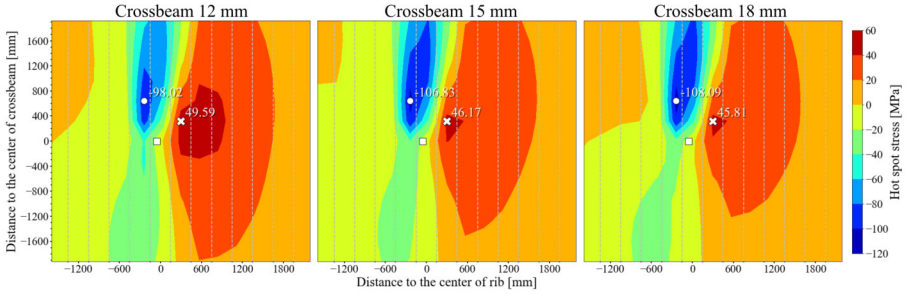


Figure 6.16: The influence surface of point l6 for different crossbeam thickness

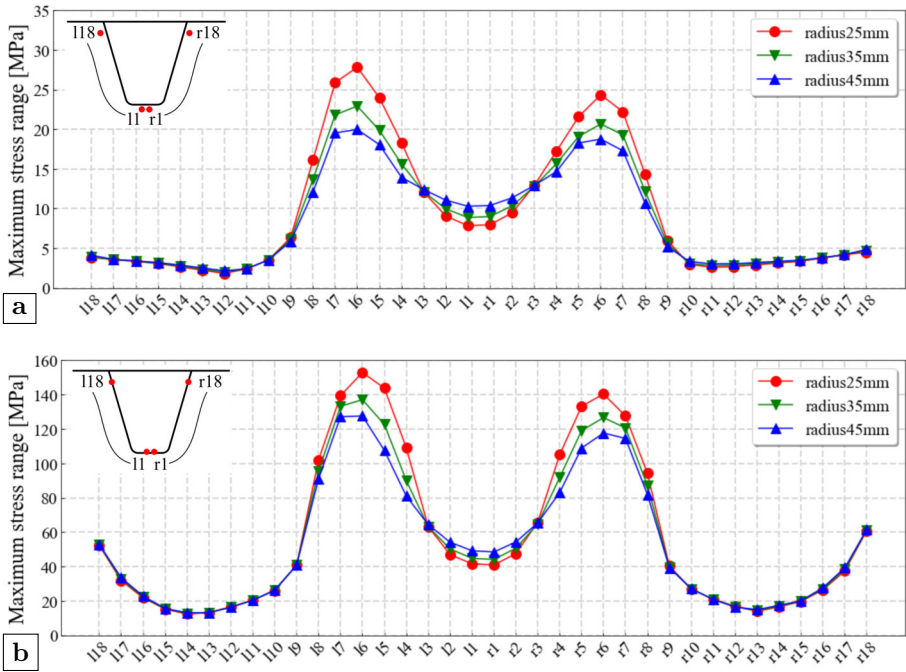


Figure 6.17: Influence of the rib radius: (a) crossbeam side; (b) rib side

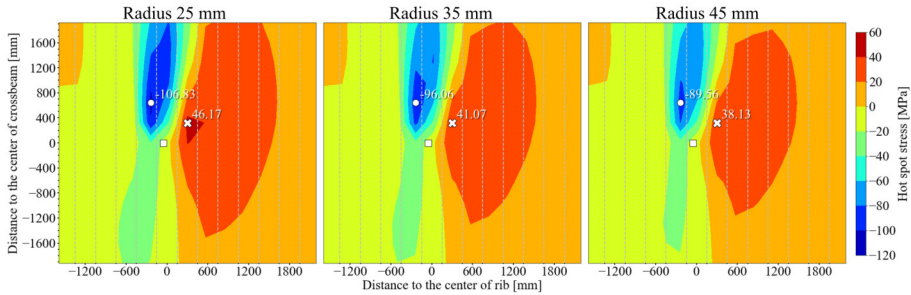


Figure 6.18: The influence surface of point 16 for different rib radius

6.4 Structural optimization

In this section, the fatigue assessments of an OSD with or without cope holes are conducted and compared. The purpose of the comparison is to verify the possibility of canceling the cope hole. For the OSD without cope holes, a similar model as described in previous section is considered. Nevertheless, the dimensions of the OSD are adjusted in accordance with the results of the parametric analysis. As for the OSD with cope holes, Figure 6.19 shows the illustration of a typical OSD with trapezoidal closed ribs and cope holes. The basic dimensions are selected from the OSD specimen adopted in the tests as presented in chapter 3. The radius for the cope hole is 50 mm and the height of the weld between rib and crossbeam is 227 mm, which is the same as rib 5 in Figure 4.1. Relevant dimensions of the OSD model with cope holes will be explained in detail later in this section.

Different assessment methods are adopted for different parts of the structures. For assessing the fatigue performance of the welds, the hot spot stress method is adopted. The same reference points from the linear extrapolation method are selected. The investigated points of the tight-fitted rib-to-crossbeam joint are still distributed around the whole section of the joint, which can be found in Figure 6.9. As for the rib-to-crossbeam joint with cope holes, the investigated points are placed along the weld connecting the rib and the crossbeam as shown in Figure 6.19. It should, however, be noted that the investigated points from the crossbeam side and the rib side do not share the same names anymore since their numbers are not identical. More specifically, the points $l/r3-13$ from the rib side and the points $l/r16-26$ from the crossbeam side actually represent the hot spot stress reference points of the same locations. Points $l/r1-2$ are defined on the rib wall at the bottom of the rib-to-crossbeam joint as shown in Figure 6.19(b). For assessing the fatigue performance of the curvature of the cope holes (i.e. points $l/r1-15$ from the crossbeam side), no explicit guideline

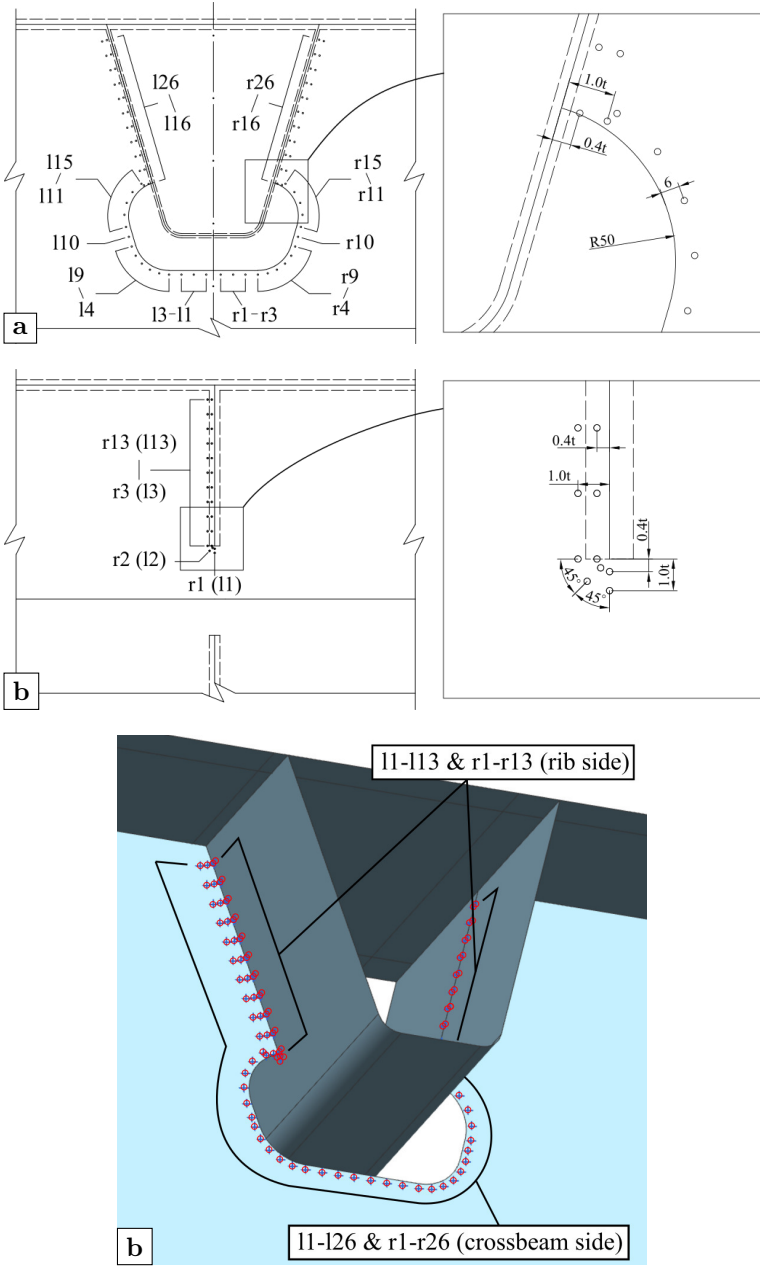


Figure 6.19: Locations of investigated points: (a) crossbeam side; (b) rib side; (c) 3-D illustration (unit: mm)

is given in the current Eurocode (CEN, 2005). With respect to the manual published by AISC(Connor *et al.*, 2012), AASHTO code (AASHTO, 2012) and previous research (Connor & Fisher, 2006), the principal stress at a distance of 6 mm from the free edge is used for the fatigue assessment.

Four models which are summarized in Table 6.2 are considered in total. In the model names, *CH* and *TF* are the abbreviations of “Cope Hole” and “Tight Fitted” respectively. *R6* or *R8* represents the rib thickness of 6 mm or 8 mm respectively. The model *CHR6* comes from the design of experiments which is also presented in Figure 6.19. *TFR6* has cancelled the cope hole on the basis of *CHR6*, but the rest of the design parameters remain the same. When choosing the design parameters for *TFR8*, the principal of equivalent rib stiffness is considered. According to Eurocode 3 (CEN, 2006), the minimum stiffness of ribs should be selected in accordance with the traffic category. The second moment of area I is calculated by the component composed of one rib plus the unit width deck which is the rib upper width plus the rib spacing. Therefore for *TFR8*, the height of the rib and the lower width of the rib decrease 25 mm respectively; the rib thickness changes from 6 mm to 8 mm; the thickness of the crossbeam is reduced to 12 mm and the rib radius increases from 25 mm to 50 mm. The thickness of the deck plate remains the same since its influence is not obvious. The difference between the second moment of area of *CHR6* and *TFR8* is 0.4%. The cross-section area of *TFR8* is 6.2% larger than *CHR6* which means a slightly heavier rib. Given the reduced weight from a thinner crossbeam, *TFR8* could be considered as an alternative for *CHR6*. *CHR8* has the same rib dimensions as *TFR8* but with cope holes. Note that the detailed coordinates of the reference points for calculating the hot spot stresses will change in accordance with the corresponding plate thickness.

Table 6.2: Relevant design parameters of the four models

Model name	CHR6	TFR6	TFR8	CHR8
Cope hole	Yes	No	No	Yes
Deck thickness [mm]	15	15	15	15
Rib thickness [mm]	6	6	8	8
Crossbeam thickness [mm]	15	15	12	15
Rib height [mm]	300	300	275	275
Rib upper width [mm]	300	300	300	300
Rib lower width [mm]	125	125	100	100
Rib radius [mm]	25	25	50	50
Second moment of area [$\times 10^8$ mm ⁴]	1.267	1.267	1.275	1.275
Cross-section area [mm ²]	13372.5	13372.5	14206.8	14206.8

The load cases and the boundary conditions are the same as in the previous section of the parametric analyses, as shown in Figure 6.8. The element size of 2 mm for the local refined area and 10 mm for the global coarse area are also adopted. Figure 6.20 presents the comparison of the two models with cope holes (i.e. *CHR6* and *CHR8*). The most critical position is at the lower end of the rib-to-crossbeam joint as anticipated. The maximum stress range at *l1* and *r1* on the rib wall is up to 182 MPa. After modifying the shape of the rib, the maximum stress range is diminished to 109 MPa on the rib side. However, the maximum stress ranges of *l16* and *r16* on the crossbeam side increase by 10 MPa, which is negative for the fatigue performance of this detail. Figure 6.21 shows the comparison of the two models without cope holes (i.e. *TFR6* and *TFR8*). The most critical position still appears at the curvature. Nevertheless, the maximum stress range at the middle point of the curvature is reduced to 74 MPa for *TFR6*. The maximum stress ranges of points at the soffit and the highest end of the rib wall from *TFR8* are slightly higher than from *TFR6*, either on rib side or on crossbeam side. The comparison shows that the stresses from *TFR8* are more evenly distributed. The calculated influence surfaces of *CHR8* and *TFR8* are presented in appendix B for reference.

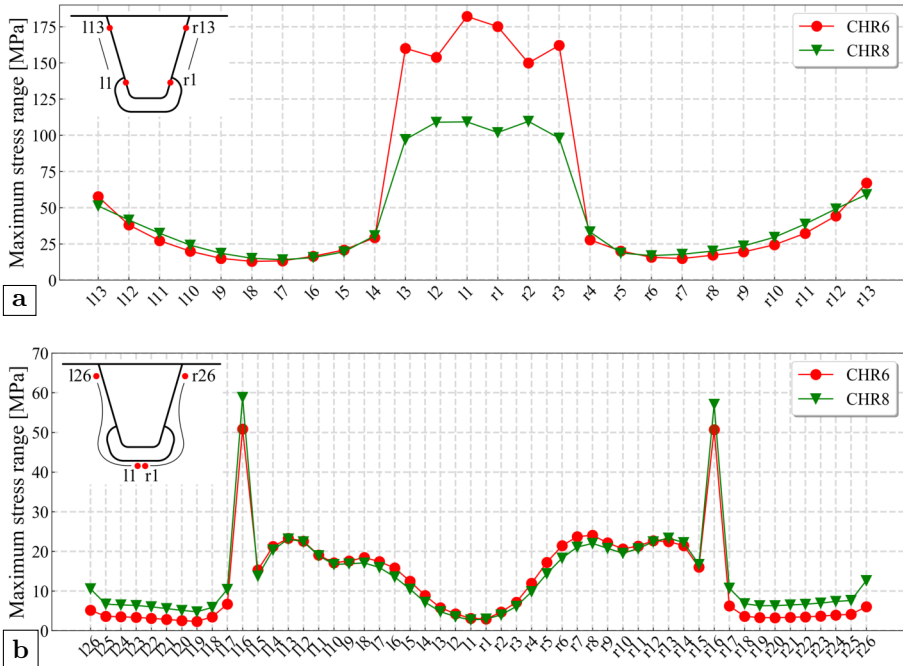


Figure 6.20: The comparison of maximum stress range of CHR6 and CHR8: (a) rib side; (b) crossbeam side

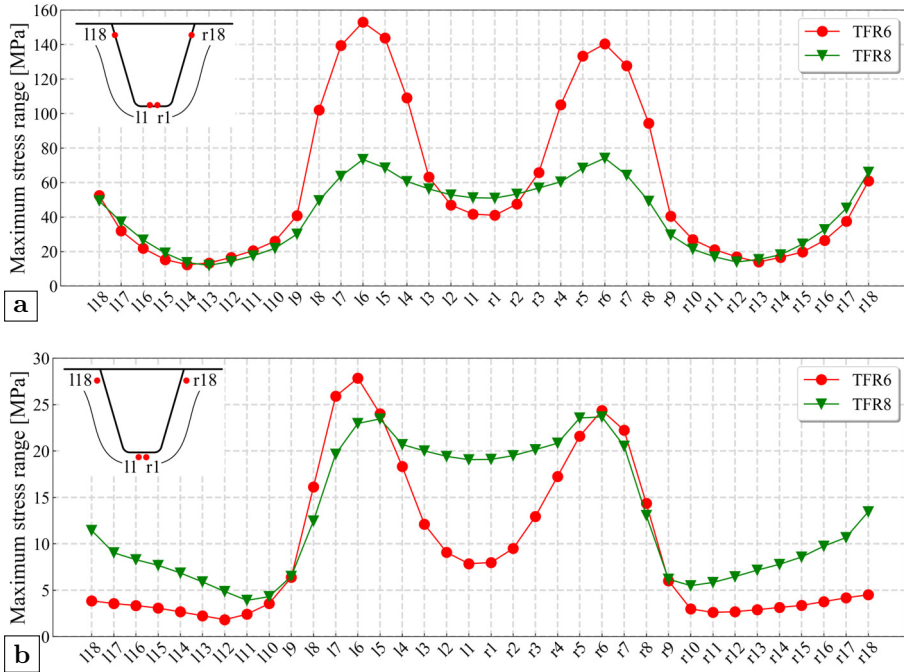


Figure 6.21: The comparison of maximum stress range of TFR6 and TFR8: (a) rib side; (b) crossbeam side

6.4.1 Fatigue life assessment based on influence surfaces

The fatigue life assessment of these four models is further conducted considering a simulated stochastic traffic flow. The workflow of the fatigue life assessment is shown in Figure 6.22.

The whole process is programmed in Python. Relevant manuscripts are shown in appendix A.6. With reference to Eurocode 1 (CEN, 2003), Fatigue Load Models 3 to 5 are intended to be used for fatigue assessment by reference to fatigue strength curves. Fatigue Load Model 3 is used for the direct verification of designs by simplified methods in which the influence of the annual traffic volume and of some bridge dimensions is taken into account by a material-dependent adjustment factor. Fatigue Load Model 4 is more accurate than Fatigue Load Model 3 for a variety of bridges and of the traffic when the simultaneous presence of several lorries on the bridge can be neglected. Fatigue Load Model 5 is the most general model, using actual traffic data. It is also stated in Eurocode that Fatigue Load Models 4 and 5 are intended to be used to determine stress range spectra resulting from the passage of lorries on the bridge. According to results

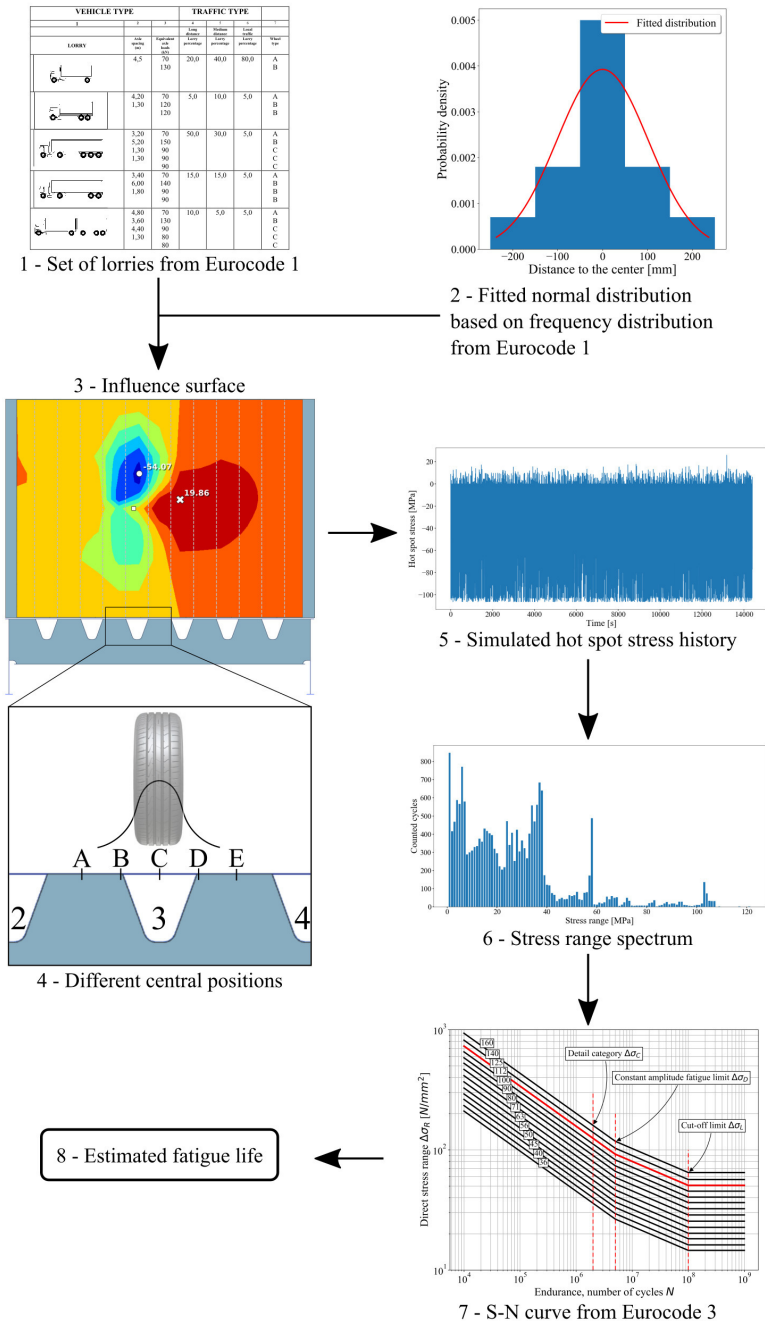


Figure 6.22: Workflow of the fatigue assessment (example of point 16 from the model TFR8)

from the previous chapter and the influence surfaces from the previous section, it can be concluded that the horizontal influence lines of OSDs are rather short. The simultaneous presence of several lorries can be neglected. Meanwhile, the actual traffic data for Fatigue Load Model 5 is unavailable. Hence, Fatigue Load Model 4 is adopted. The load dispersal through the pavement is not considered here. This is because of the interpolation procedure of the tire loads, which will be further explained in detail. In practical designs, the spread-to-depth ratio is 1 horizontally to 1 vertically down (i.e. 45°) to the level of the middle plane of the structural top plate. Fatigue Load Model 4 consists of sets of standard lorries. 5 different lorry types are defined as presented in step 1 of Figure 6.22. A Python class `FatigueLoadModel4` is defined to store relevant information, including the lorry names, the corresponding axle spacing and the equivalent axle loads. Relevant manuscript is shown in appendix A.4.

The transverse location of the vehicle is very important when assessing the fatigue performance since it will directly influence the induced stress ranges. A statistical distribution of the transverse location of the vehicle is given in Eurocode as shown in step 2 of Figure 6.22. The bar chart in blue is the frequency of distribution from Eurocode 1, in which the vehicles are assumed to be distributed in 5 positions with a specific width of 0.1 m. A normal distribution is fitted to represent the distribution of the transverse location. 7% vehicles are located outside the range of 0.15 m for each tail. The Z-score Z_{norm} is interpolated through

$$\begin{aligned} Z_{norm} &= (0.07 - 0.06944) * (1.48 - 1.47) / (0.07078 - 0.06944) - 1.48 \\ &\approx -1.4758 \end{aligned} \quad (6.1)$$

Then, the scale of the normal distribution s_{norm} can be calculated on the basis of the acquired Z_{norm} score by

$$\begin{aligned} s_{norm} &= -0.15 / Z_{norm} * 1000 \\ &\approx 101.64 \end{aligned} \quad (6.2)$$

The fitted curve of the normal distribution is shown as a red line in step 2 of Figure 6.22.

The location of the calculations is chosen as part of the slow lane. Traffic category 2 is selected, which represents roads and motorways with 2 or more lanes per direction with high flow rates of lorries. The number N_{obs} of heavy vehicles estimated per year per slow lane is 0.5 million (0.5×10^6). The traffic type of medium distance traffic is chosen. Accordingly, the percentages of lorry types are also confirmed as: 40% lorry type A, 10% lorry type B, 30% lorry type C, 15% lorry type D and 5% lorry type E. The lorry percentages are used to sample the whole traffic volumes.

At present, there is no clear suggestion about how the traffic lanes should be arranged on bridges using OSDs in current codes. Due to the relatively short horizontal influence lines, the transverse location of the assumed normal distribution of vehicles may influence the fatigue performance. Therefore, 5 positions of the central lines are considered as shown in step 4 of Figure 6.22. The dynamic load amplification appropriate for pavements of good quality is included in Fatigue Load Model 4, so the additional amplification factor is not considered. In order to finalize the programming, a few extra assumptions are needed. A fixed driving speed of 90 km/h is assumed. The distance between two consecutive vehicles is assumed to be 50 m. Moreover, it is also assumed that only one lorry would pass the target rib-to-crossbeam joint at each time as the simultaneous presence of several lorries was excluded before. Based on above assumptions, the main procedure of calculating the stress history is presented in Figure 6.23 and Algorithm 1.

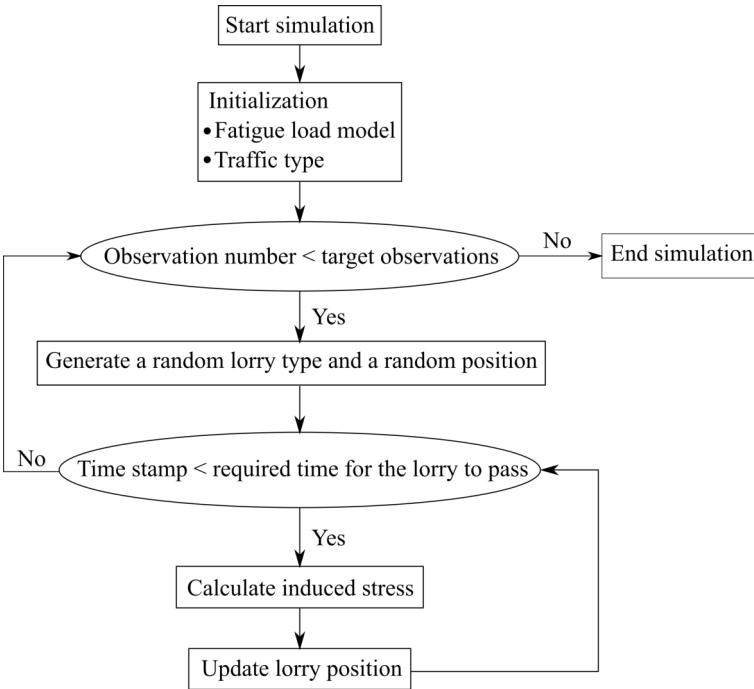


Figure 6.23: Illustration of the main function of calculating stress history

Algorithm 1: Main function of calculating stress history based on influence surfaces

Input: influence_surface, fatigue_load_model, observations,
 traffic_type, tire_central_location, distribution_scale

initiate the time point

```

1 time_stamp = 0
  # initiate data containers for time and stress
2 time_logger = []
3 stress_logger = []
  # start simulation
4 for observation in observations do
  # generate a random lorry with relevant information
  # RandomChoice will return a lorry type based on the lorry
  # percentages
5   lorry_type = RandomChoice(fatigue_load_model, traffic_type)
  # NormalDistribution will return a random variant based on
  # the central location and scale
6   lorry_location = NormalDistribution(tire_central_location,
  # based on the lorry type, the driving speed and the record
  # frequency, the time points needed for the lorry to pass
  # through is acquired
7   record_points = ...
  # iterate through all time points
8   for one_cal_loop in record_points do
  # StressStep will return the stress induced by the lorry
  # at current location
9     stress_point = StressStep(influence_surface,
  # store the stress result
10    stress_logger ← stress_point
  # update the lorry location and time logger
11    lorry_location = ...
12    time_logger ← time_stamp
  # insert the blank data between two consecutive lorries
13  time_stamp, time_logger, stress_logger = InsertBlank(...)
```

Output: time_logger, stress_logger

In the algorithm, the random sampling of lorry type (i.e. function RandomChoice) and transverse position (i.e. function NormalDistribution) is realized by calling the corresponding methods from NumPy (i.e. numpy.random.choice) and SciPy (i.e. scipy.stats.norm.rvs) respectively.

Numpy and SciPy are Python libraries for scientific computing.

The method `numpy.random.choice` is capable of generating a random sample from a given 1-D array. The probabilities associated with each entry in the given array can be specified. When sampling the lorry type in this case, the 1-D array is the list of lorries' names in Fatigue Load Model 4 and the percentages of lorry types are used as the probabilities that the corresponding lorry types will show up.

The method `scipy.stats.norm.rvs` will return a normal continuous random variable. The location keyword (`loc`) specifies the mean, and the scale keyword (`scale`) specifies the standard deviation. When sampling the transverse position, the center of the tire load distribution is used as the input for the location keyword (i.e. the mean of the normal distribution), as shown in the different central positions in Figure 6.22. The scale that is fitted in equation 6.2 is adopted as the input for the scale keyword.

For every moment when the OSD structure is loaded, the stress status of one target location induced by one tire load is interpolated from the relevant influence surface. In this procedure, the interpolation is finished based on the coordinate of the center point of the contact area. Therefore, the influence of different contact areas for different wheels is ignored. With respect to the assumption of linear-elastic material, the total stress of one investigated location at a specific moment is the superposition of all stresses induced by all effective tires at that moment. The procedure of calculating one stress point is as presented in Figure 6.24. Meanwhile, the algorithm of the function `StressStep` is shown in Algorithm 2.

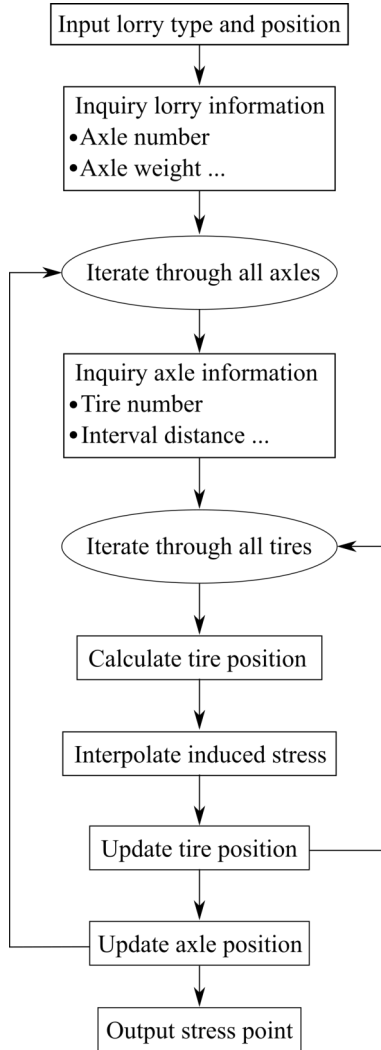


Figure 6.24: Work flow of the function StressStep

Algorithm 2: Calculate one stress point

```
Input: influence_surface, fatigue_load_model, lorry_type,
        lorry_location
# initiate the lorry model according to the lorry type
1 lorry_model = fatigue_load_model.lorry[lorry_type]
# retrieve the information of axles from the lorry model
2 axle_number = lorry_model.axle_number
# initiate a result container
3 stress_point = 0
# iterate through all axles
4 for number in axle_number do
    # retrieve the axle type according to the axle number
5    axle_type = lorry_model.tire_type[number]
6    axle_model = fatigue_load_model.axle[axle_type]
    # retrieve the tire number of the specific axle
7    tire_number = axle_model.tire_number
    # calculate first tire location of the axle
8    tire_location = ...
    # iterate through all tires
9    for tire in tire_number do
        # calculate stress induced by one tire
10       stress_step = InterpolateStress(influence_surface,
            tire_location)
        # store result
11       stress_point += stress_step
        # update tire location according to the axle model
12       tire_location = ...
    # update axle location
13    axle_location = ...
```

Output: stress_point

Once the stress histories are acquired, the stress range spectra can be derived through a cycle counting method. For counting stress range cycles, the widely known method is the rain-flow cycle counting method. It is based on the analogy of raindrops falling on a pagoda roof and running down the edges of the roof (Lee, 2005). Based on the original scheme, a number of variations have been reported which can be mainly divided into two categories: three-point method and four-point method.

The three-point cycle counting rule uses three consecutive points in a load-time history to determine whether a cycle is formed. The rules of the three-point rain-flow cycle counting method is shown in Figure 6.25. According to Lee

(2005), the three consecutive stress points (S_1, S_2, S_3) define two consecutive ranges as $\Delta S_1 = |S_1 - S_2|$ and $\Delta S_2 = |S_2 - S_3|$. If $\Delta S_1 \leq \Delta S_2$, one cycle from S_1 to S_2 is extracted. Otherwise, no cycle is counted. The three-point cycle counting method requires that the stress time history be rearranged so that it contains only the peaks and valleys and it starts with either the highest peak or the lowest valley, whichever is greater in absolute magnitude. Then, every three consecutive points from the beginning will be checked until a closed loop is defined. The two points forming the cycle are discarded and the remaining point will be connected. This procedure is repeated until the remaining data is exhausted. The range-pair counting method is a variation of the three-point counting method which does not require the load sequence to start with either the maximum peak or the minimum valley.

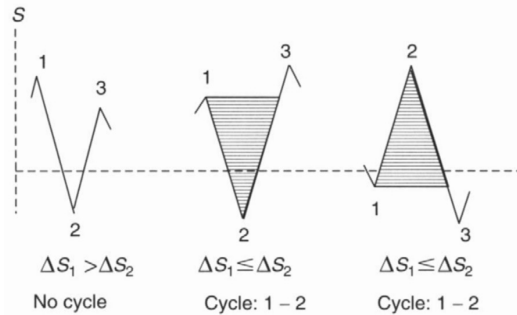


Figure 6.25: Rules of three-point rain-flow cycle counting (Lee, 2005)

Similar to the three-point counting method, the four-point counting method uses four consecutive points to extract a cycle. The detailed description of the four-point counting method can be found in Lee (2005). It is claimed that both rain-flow cycle counting methods lead to an identical range-mean rain-flow matrix. Therefore, the range-pair counting method is finally adopted to process these stress histories. As stated before, the stress histories are first processed to remain only peaks and valleys as illustrated in Figure 6.26. The algorithm used to filter the stress histories is presented in Algorithm 3. In the first step, the consecutive duplicates from the stress history are eliminated. This step is to make sure there is no zero slope for any line connecting two consecutive points. Then, the peak or valley point k is found under such condition: when the lines made of the point k with two points around it (i.e. point $k-1$ and point $k+1$) respectively have opposite signs.

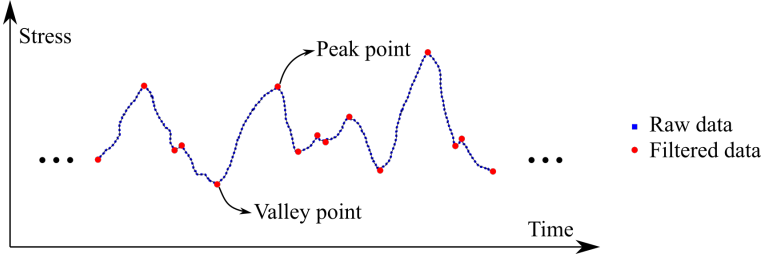


Figure 6.26: Illustration of preparing data for the range-pair counting method

Algorithm 3: Filter stress histories to remain only peaks and valleys

Input: stress_history

remove consecutive duplicates in stress_history

1 data ← DropDuplicates(stress_history)

initiate a result container

2 filtered_data = []

store the first data point

3 filtered_data ← data[0]

iterate through the second data point until the point before the last one

4 for k in range(1, len(stress_history)-1) do

calculate the slope before point k

5 slope1 = data[k] - data[k-1]

calculate the slope after point k

6 slope2 = data[k+1] - data[k]

store point k if the signs of slopes are different, otherwise point k is skipped

7 if slope1*slope2 < 0 then

8 filtered_data ← data[k]

store the last data point

9 filtered_data ← data[-1]

Output: filtered_data

Algorithm 4 shows the algorithm of the range-pair counting method. Three consecutive data points will be checked in sequence. Only when ΔS_1 is less or equal to ΔS_2 , a full stress cycle of ΔS_1 is recorded. If there does not exist points that fulfill the defined condition, the whole data will be reversed and the same checking procedure will be repeated. At last, there could be two points left by coincidence depending on the total number of data points. In theory, the remaining two points consist of only a half cycle. Here, it is simply counted as

a full cycle which has only a little influence on the final results since the whole data is rather large.

Algorithm 4: Range-pair counting method

```

Input: stress_history
# initiate a result container
1 counter = []
  # initiate the point index
2 k = 2
  # start processing data
3 while len(stress_history) > 2 do
  | # calculate stress ranges of consecutive three points
4   s1, s2 = RangeCalculator(stress_history, k)
5   if (s1 > s2) and (k < len(stress_history) - 1) then
  |   # skip to next point when the stress cycle condition is
  |   not fulfilled
6   |   k += 1
7   else if (s1 > s2) and (k == len(stress_history) - 1) then
  |   # reverse stress history data when reach the end of the
  |   data list
8   |   stress_history.reverse()
  |   # reset the point index
9   |   k = 2
10  else
  |   # store the stress range that meet the condition
11  |   counter ← s1
  |   # delete corresponding data points from the list
12  |   del data[k-2:k]
  |   # reset the point index
13  |   k = 2
  |
  # process the last stress cycle when there are two data points
  left
14 if len(stress_history) == 2 then
15 | counter ← abs(data[0] - data[1])

```

Output: counter

To finalize the simulation procedure, a record frequency has to be selected. The record frequency is actually controlling the number of interpolation points when a lorry is passing by. A record frequency that is too low would cause the peak values being missed since the interval distance between interpolation points are too far away. However, due to the limitation of the computation power, a record frequency that is too high would severely slow the calculation speed. It should

be noted that more interpolation points do not equal a higher precision if all most unfavorable load positions have already been captured. To determine a suitable record frequency, a series of five lorries from type A to E are considered. It is assumed that the lorry set will drive in a line and pass through the same transverse location. Five different record frequencies from 25 Hz to 125 Hz as well as the five locations of the tire center are considered. As an example, the calculation results of point *l6* on the rib side from the model *TFR8* are presented in Figure 6.27 to 6.31. Based on the calculation results, the record frequency has to be at least 75 Hz to achieve stable results under most situations. However, it is also noted that some peaks may be missed under 75 Hz especially for lorry type E. Once the record frequency is higher than 100 Hz, the difference of the raw data is not obvious. At some specific points, the record frequency of 125 Hz is able to capture some very small stress ranges. However, the small stress ranges are normally below the fatigue cut off limit, which would not have large impacts on the estimated fatigue lives. After comparing all results, the record frequency of 100 Hz is finally adopted.

After counting the cycles of stress ranges, the stress spectra are derived. Based on the Palmgren-Miner method (Hobbacher, 2019), the damage could be calculated with the stress ranges, the number of cycles and the design resistance S-N curve. At present, the structural hot spot stress is not covered in current codes. According to the recommendation from previous research (Kolstein, 2009), the detail category of 125 is used for the assessment of the welds. In addition, the assessment of the cope hole is based on the maximum compression stress and a detail category of 80 is chosen.

6.4.2 Results and discussion

The results of *CHR6* are shown in Figure 6.32. For the convenience of showing the results, a fatigue life higher than 100 year is defined as unlimited, which is the same for all following figures in the rest of this section. In general, the most critical position for *CHR6* is below the lower weld end as anticipated. On the rib side, the fatigue life of *l1-3* or *r1-3* is always less than 10 years for all schemes. The lowest fatigue life appears at *l1* for the scheme *location A*, which is 0.95 year. It should be noted that the estimated fatigue life is shorter than the common fatigue life of OSDs in practical projects. There are several possible explanations. On the one hand, the dispersal effect of the pavement is ignored when performing FEAs. The more concentrated load may overestimate the stress ranges and lead to the short fatigue life eventually. On the other hand, the multi-axle effect was not considered before when performing the fatigue life assessment for the rib-to-crossbeam joint. Hence, the adopted fatigue model as well as the lorry frequencies and the annual observation from Eurocode may not be very suitable for the assessment and directly affect the estimated fatigue life.

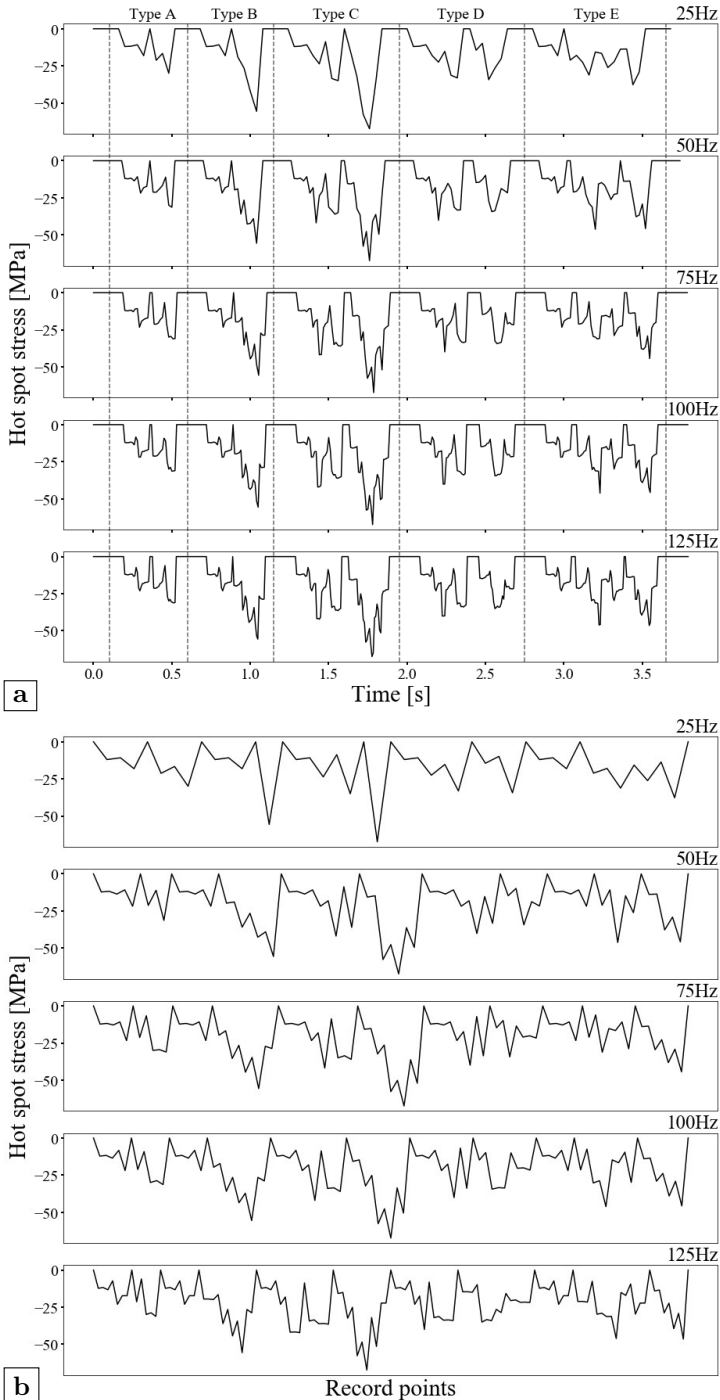
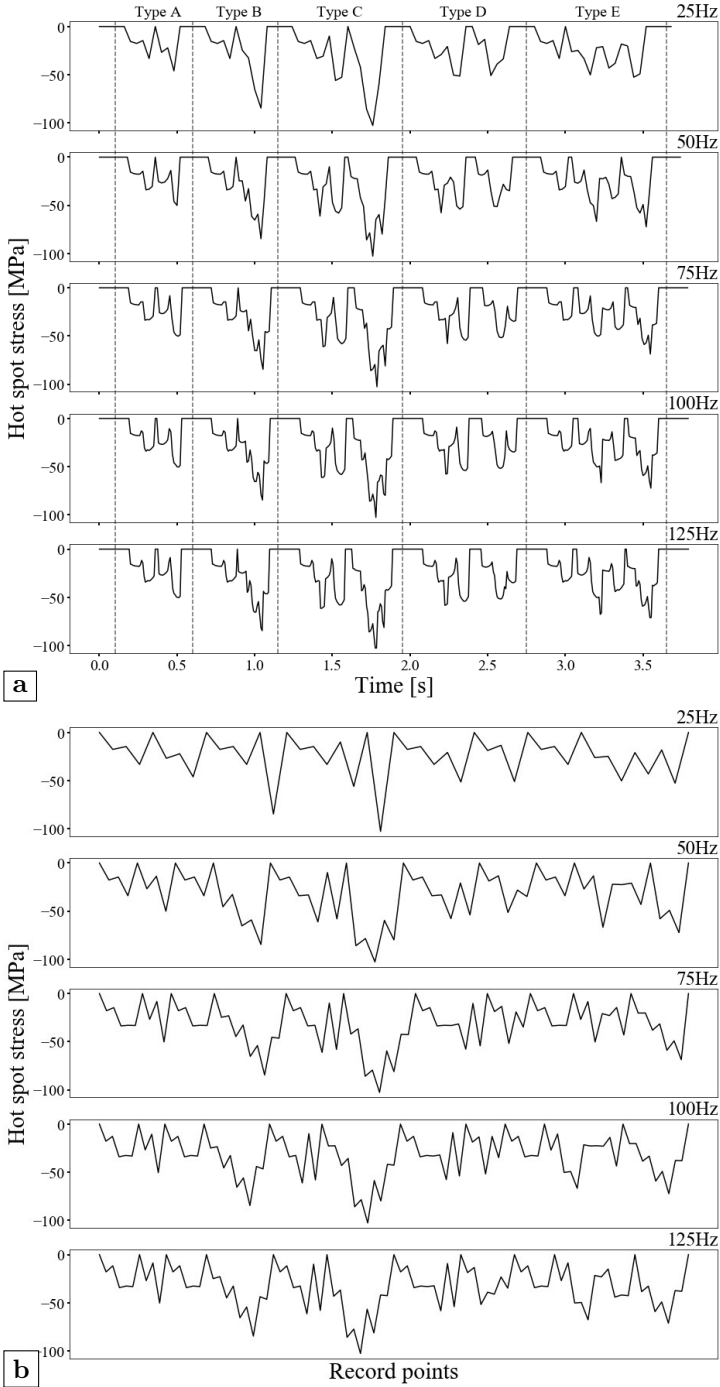


Figure 6.27: l_6 on rib side of TFR8 for location A: (a) raw data; (b) filtered data



148 **Figure 6.28:** l6 on rib side of TFR8 for location B: (a) raw data; (b) filtered data

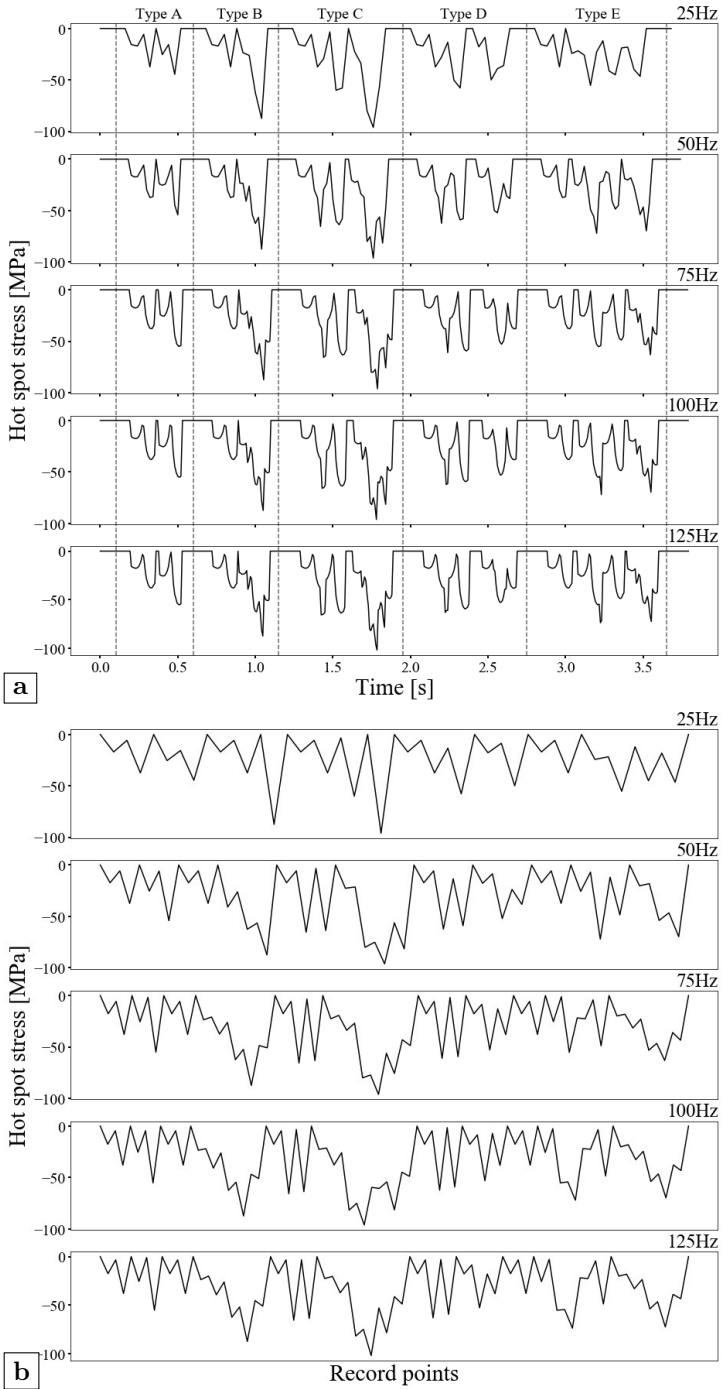


Figure 6.29: σ_{66} on rib side of TFR8 for location C: (a) raw data; (b) filtered data

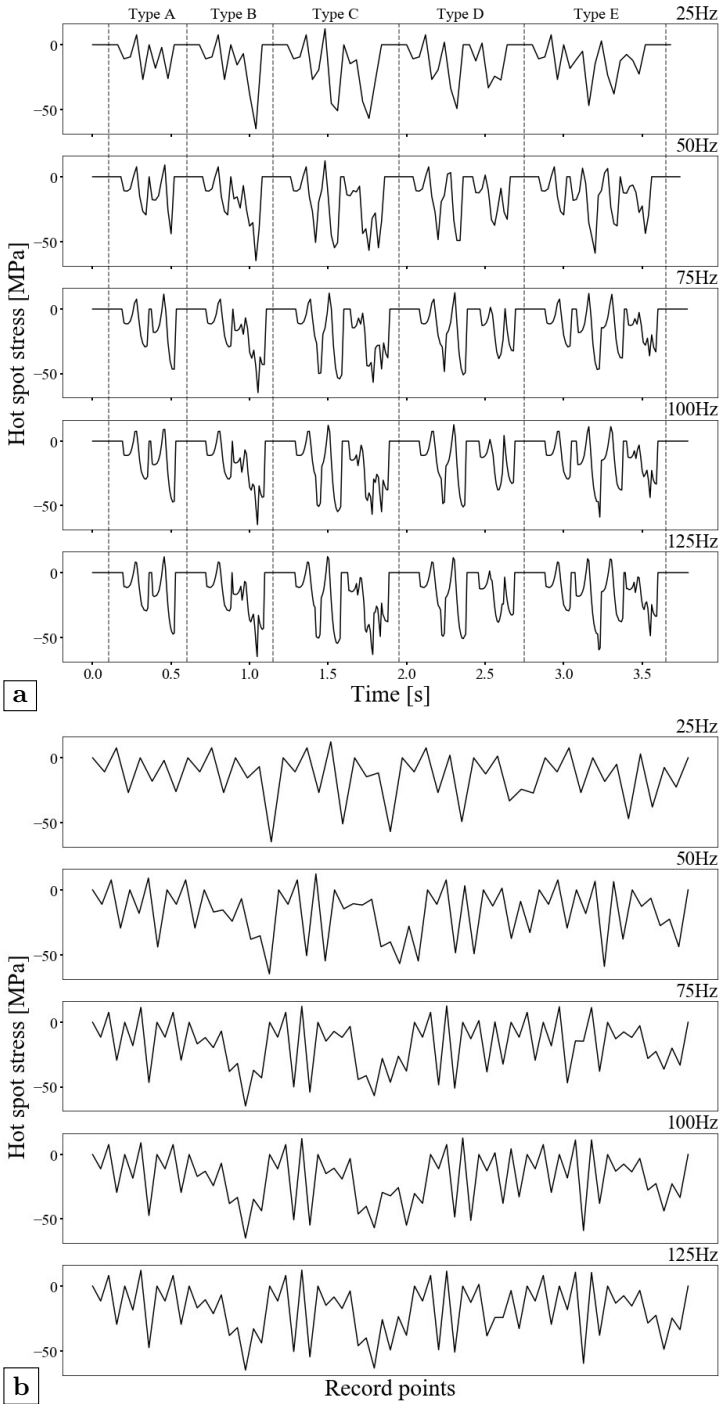


Figure 6.30: l_6 on rib side of TFR8 for location D: (a) raw data; (b) filtered data

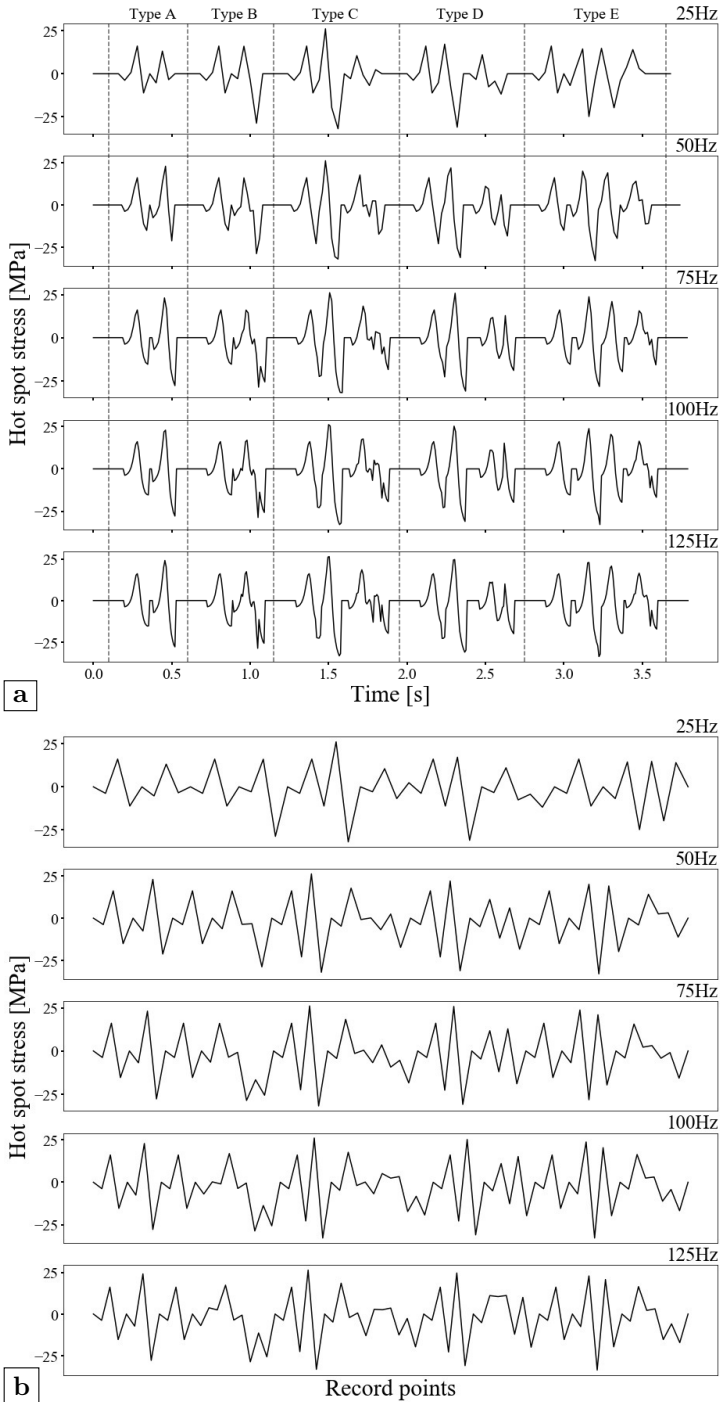


Figure 6.31: l6 on rib side of TFR8 for location E: (a) raw data; (b) filtered data

To get a better assessment result, different influence surfaces considering the pavement may be considered and the updated fatigue load model can be easily implemented in the framework. Except this position, the estimated fatigue life of rest points is longer than 100 year. On the crossbeam side, the lowest fatigue life also appears under the scheme *location A*, which is 34.35 year at *l16*. When the center of the tire load moves toward the other side, the fatigue life of *l16* would gradually increase to unlimited. However, the fatigue life of the curvature at the cope hole would decrease simultaneously. For example, the fatigue life of *r12* is 35.73 year under the scheme *location D* and the fatigue life of *r8* is 44.46 year under the scheme *location E*, while these two points have an unlimited fatigue life for the scheme *location A* and *B*.

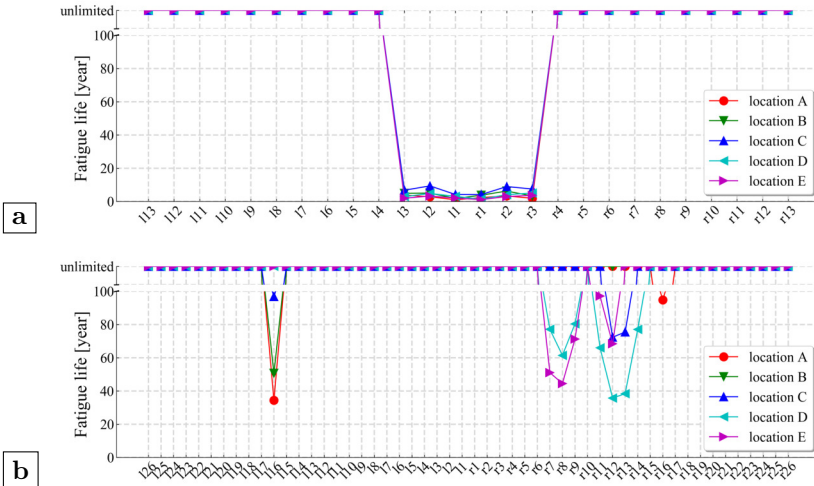


Figure 6.32: Estimated fatigue life of the model CHR6: (a) rib side; (b) crossbeam side

The results of *TFR6* are presented in Figure 6.33. When the cope hole is canceled directly on the basis of the original design (i.e. *CHR6*), the estimated fatigue life of all points on the crossbeam side would become unlimited. Nevertheless, the fatigue life of points at the curvature on the rib side (i.e. points *l4-8* and *r4-8*) is still generally low no matter where the central line of the tire load distribution is. Most of these points have a fatigue life of less than 20 year. The lowest fatigue life appears at *r6*, which is 0.98 year under the scheme *location D*. It is also observed that when the central line moves toward the center of rib (i.e. the scheme *location C*), the fatigue life of points under the soffit of the rib (i.e. *l1-3* and *r1-3*) would diminish. The fatigue life of *r13* is 13.66 year for the scheme *location C*.

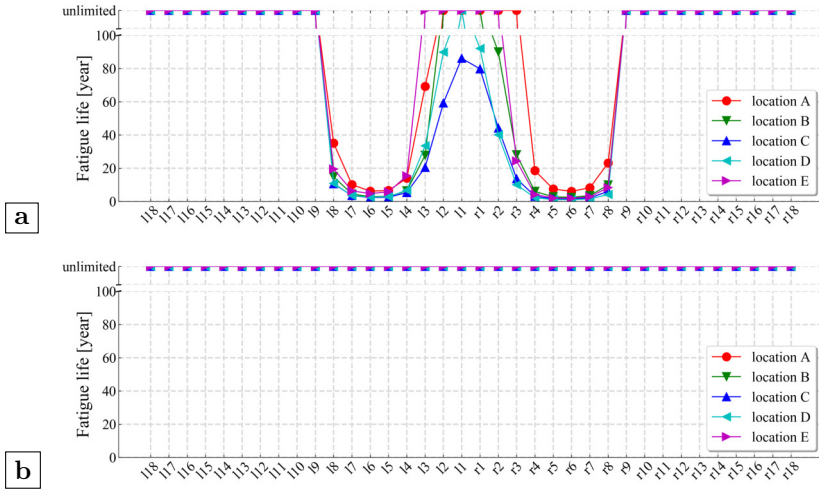


Figure 6.33: Estimated fatigue life of the model TFR6: (a) rib side; (b) crossbeam side

The results of *TFR8* are displayed in Figure 6.34. Compared with *TFR6*, the fatigue life of points on the crossbeam side remains unlimited. On the rib side, the fatigue life of points along the curvature zone has improved even though it is still the most critical position. The lowest fatigue life appears at *r6* for the scheme *location C* which is 9.16 year. Nevertheless, the influence of the stress concentrations at the soffit of the rib induced by the bending moment becomes more obvious. This may be proven by the lower fatigue life of *l1-3* and *r1-3* under the scheme of *location B, C* and *D*. However, it should be noted that if the central line of the tire load distribution is placed at the center of two ribs (i.e. the scheme *location A* and *E*), not only the fatigue life of most points under the rib soffit becomes unlimited but also the curvature zone has a higher fatigue life. For instance under the scheme *location A*, the lowest fatigue life appears at *r6* which is 38.87 year.

The results of *CHR8* are shown in Figure 6.35. On the rib side, the fatigue life of *CHR8* are longer than *CHR6*. For the critical points *l1-3* and *r1-3* below the weld end, the fatigue life is between 5 to 40 year. The lowest fatigue life appears at *r1* which is 5.26 year under the scheme *location E*. In general, the fatigue life of the critical points is slightly longer or more evenly distributed when the central line of the tire load distribution is at the center of rib (i.e. the scheme *location C*). But the influence of the location of load distribution is not as obvious as for *TFR8*. On the crossbeam side, the fatigue life of the point close to the cope hole termination and the curvature zone of cope hole

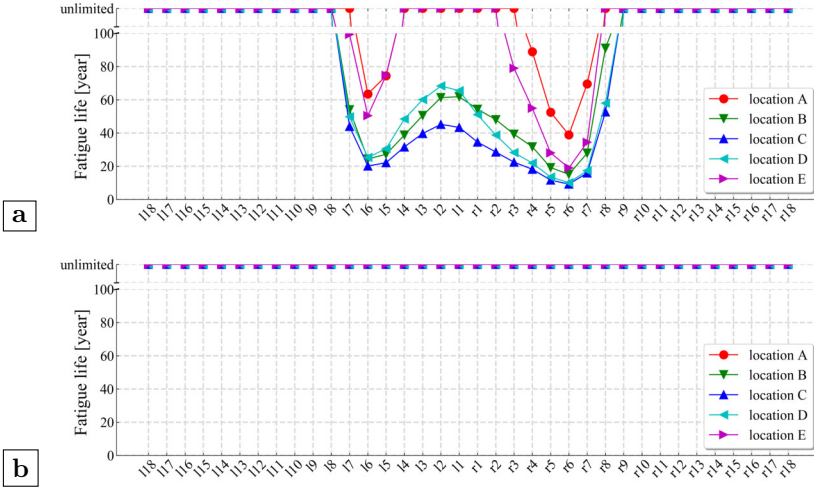


Figure 6.34: Estimated fatigue life of the model TFR8: (a) rib side; (b) crossbeam side

have improved. But a fatigue damage is still expected at either of these two locations. For the point close to the cope hole termination, the fatigue life of *l16* is 60.07 year under the scheme *location A*. For the curvature zone of cope hole, the fatigue life of *r12* is 34.35 year under the scheme *location D*.

6.5 Conclusions

The shell element model and the solid element model can both be adopted for the simulation of rib-to-crossbeam joints. The shell element model and the solid element model would generate consistent results under such conditions: a) the weld is modeled in the solid element model while omitted in the shell element model; b) the distance from the weld toe to the reference point on the rib wall should be calculated from the corner point of the rib-to-crossbeam intersection. The results of the shell element model tend to be higher than the solid element model when getting closer to the intersection point of rib and crossbeam. Thus, the result of the shell element model is more conservative when adopting the hot spot stress method.

The most critical position for the tight-fitted rib-to-crossbeam joint is at the curvature on the rib side. Increasing the thickness of the rib could reduce the maximum stress range on the rib side meanwhile changing the stress distribution on the crossbeam side. When the thickness of deck increases, the maximum

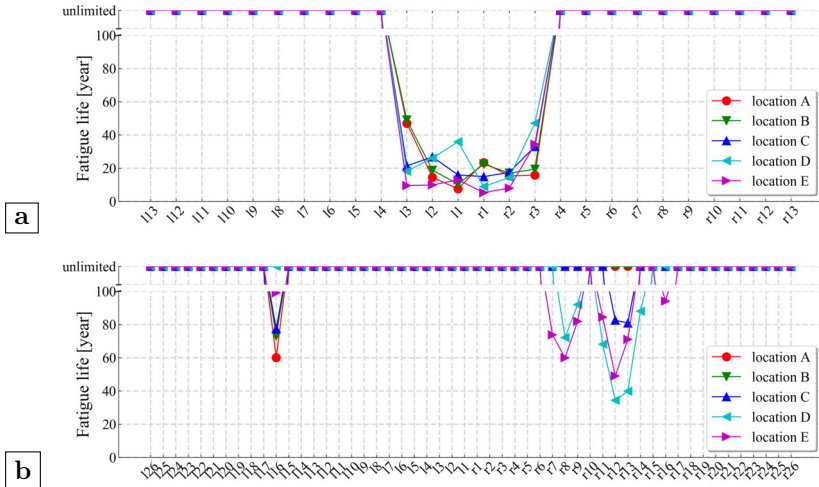


Figure 6.35: Estimated fatigue life of the model CHR8: (a) rib side; (b) crossbeam side

stress ranges on both sides decrease holistically. The radius of rib has a local influence on the points at the curvature. The larger radius could effectively lower the maximum stress range. Lastly, the thickness of the crossbeam and the maximum stress range on the crossbeam side have an obvious negative correlation. A more flexible crossbeam, i.e. decreasing its thickness, would reduce the maximum stress range at the bottom of ribs on the rib side.

A realization of the fatigue life assessment based on influence surfaces is proposed. According to the results of the fatigue life assessments, the multi-axle effect has to be considered. The fatigue performance of the rib-to-crossbeam joint is sensitive to not only the tire load but also the spacing between axles. Based on current Eurocode, a normal distribution of the vehicles is fitted to include the influence of different transverse position. For the rib-to-crossbeam joint with cope holes, it is preferred to place the central line of the load distribution closer to the center of the rib. In contrast, for the tight-fitted rib-to-crossbeam joint, it is preferred to place the central line of the load distribution closer to the center between two ribs. However, the load distribution mainly affects the controlling points on the rib side for both types of joints. Neither the rib dimensions nor the load distribution has an obvious improvement on the fatigue-prone details along the free edge of the cope hole. Hence, considering less possible fatigue-prone locations and reduced fabrication costs, the overall performance of the optimized tight-fitted rib-to-crossbeam joint is better.

7

Investigation of simplified calculation method

7.1 Introduction

Due to its complex structure, the design of OSDs is never an easy thing. With reference to the guide manual published by AISC (Connor *et al.*, 2012), three design levels, which are defined in accordance with the application and test data available to designers, as also presented in chapter 2, are as follows:

- Level 1 design is based on little or no structural analysis, but is accomplished by a selection of details that are verified to have adequate resistance by experimental testing.
- Level 2 design is based on the analysis of certain OSD details that can be evaluated with sufficient accuracy by simplified 1-D or 2-D analysis technique. Calculations normally focus on nominal stresses, and not local concentrations.
- Level 3 design is based on a refined 3-D analysis of the OSD to quantify the stresses on the most accurate extent reasonable expected for all components and connections. Calculations consider local stress concentrations at fatigue-prone details.

In the past, the analysis of an OSD is usually done by analytical methods that belong to level 2 design. These analytical methods are normally based on simplified models of OSD structures. Therefore, the results of these models are usually quite conservative. With the rapid development of computation power offered by modern computers, the 3-D analysis method based on FEA has become the primary option when performing design tasks. By introducing detailed submodels, FEA has the potential to provide precise results, which was also demonstrated in previous chapters. However, reliable analysis results always require a relatively high level of professional skill in manipulating the analysis software. Furthermore, FEA is also time-consuming. Even though many commercial analysis software provide useful tools for accelerating the modeling speed, for example the GUI of commonly used functions such as chamber and drill, modifying the FEA model is still quite laborious if it is not fully parameterized. Depending on the size of the model and the element type selected, the whole analysis procedure could be as long as tens of days. Therefore, simplified analytical methods could offer a quick determinations of the internal forces and initial design dimensions (Pipinato, 2016).

In 1957, Pelikan and Esslinger developed a simplified, yet sufficiently accurate method for the design of OSDs, although it mainly focused on those joints subjected to the longitudinal bending moment e.g. the rib-splice joint. A very important notion from the method of Pelikan and Esslinger is that the actual OSD is represented by an idealized substitute orthotropic plate. The deck plate with longitudinal ribs is treated as a continuous orthotropic plate supported

on rigid main girders and elastic crossbeams. The design computation is made in two steps: in the first step the crossbeams are considered rigid and the moments in the deck are computed in accordance with this assumption. In the second step, the effects of the actual elastic flexibility of the crossbeams are determined (AISC, 1963). Even though the Pelikan-Esslinger (PE) method is broadly accepted, one of the shortages is that it only considered the bending deformations of the idealized plate. Therefore, only the bending moment is derived. As stated before, the stress concentration at the rib wall induced by rib distortion is governing the fatigue performance of the rib-to-crossbeam joint. Hence, the PE method cannot be applied directly to evaluating the rib-to-crossbeam joint.

In this chapter, a simplified calculation method for evaluating the rib-to-crossbeam joint is developed based on the PE method. Compared with the original PE method, the shear deformation is now included for deriving the torsional moment. The purpose of this method is to offer a swift determination for the rib-to-crossbeam joint at the early design stage.

7.2 Analytical model

7.2.1 Basic assumptions

Similar to the original PE method, the OSD can be represented by an idealized orthotropic plate. The orthotropic plate is defined as a plate with different stiffness in two orthogonal directions x and y in the plane of the plate, as shown in Figure 7.1.

The assumptions for calculating deformations and stresses of an orthotropic plate in the original PE method are the same as used in the analysis of an isotropic plate (AISC, 1963), which are:

- The material of the plate is homogeneous, which means the physical properties of the material are identical at each point of the plate. Besides, the material is continuous all over the plate which precludes the existence of voids, slits, etc.
- The plate thickness is uniform and small, compared with the other two dimensions of the plate. Therefore, the stresses perpendicular to the middle plane of symmetry of the plate (x , y) and the effect of the shear stresses on the plate deformations may be disregarded.
- The deformations of a loaded plate are purely elastic and are in accordance with Hooke's law. The straight lines normal to the middle surface remain straight and normal to the deformed middle surface of the loaded plate.

- The deflections of the loaded plate are small compared with the plate thickness. This assumption precludes the occurrence of membrane stresses in the plate.

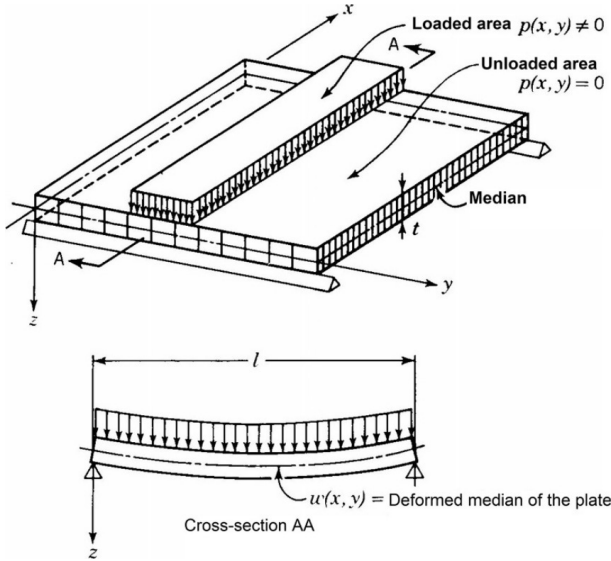


Figure 7.1: Idealized orthotropic plate (AISC, 1963)

The original PE method is based on the classical plate theory. With respect to the Kirchhoff-Love hypothesis, the lines being normal to the neutral surface before deformation remain straight and normal to the neutral surface after deformation and neglects the shear deformation. However, this assumption causes underestimation of the deflections (Takabatake, 2018). Being similar to the first-order shear deformation theory, the shear strain is considered and assumed to be constant along the thickness of the plate in this method. Since the distribution of the shear stress is constant, a shear correction factor is needed when analyzing a real plate. Otherwise it cannot satisfy the zero stress condition on the free surface. However, because the orthotropic plate is a virtual plate, the shear correction factor is therefore ignored. Other assumptions, e.g. the homogeneous and continuous material, the small and elastic deformations, are accordingly adopted.

7.2.2 Relevant expressions

For constructing the analytical model, the Cartesian coordinate system is adopted. The coordinate axis X and Y are located on the middle surface of the plate, and Y axis indicates the longitudinal direction along the ribs. The

coordinate Z axis represents the vertical direction. The positive direction of the external and internal forces and deflection components is defined as when they point towards the positive direction of the coordinate axes X, Y and Z. The moments are defined as positive when the bottom fibers of the plate produce tension.

For the convenience of easily indicating the partial differentiation, the simplified notations are used as

$$\frac{\partial}{\partial x} = ,x \quad \frac{\partial^2}{\partial x^2} = ,xx \quad \frac{\partial^2}{\partial x \partial y} = ,xy$$

Considering the middle surface of the plate, the horizontal displacements u_0 , v_0 and the vertical displacement ω_0 describe the displacements of the X, Y and Z directions, which are the functions of coordinates x and y . Therefore, the displacements u , v and ω of any points (x, y, z) could be written as

$$\begin{cases} u = u_0(x, y) + z\alpha \\ v = v_0(x, y) + z\beta \\ \omega = \omega_0(x, y) + z\rho \end{cases} \quad (7.1)$$

where α , β and ρ are the rotational angles at the middle surface. The linear strain-displacement relationships for thin plates are given as

$$\begin{cases} \varepsilon_x = u_{,x} & \gamma_{xy} = u_{,y} + v_{,x} \\ \varepsilon_y = v_{,y} & \gamma_{yz} = v_{,z} + \omega_{,y} \\ \varepsilon_z = \omega_{,z} & \gamma_{xz} = \omega_{,x} + u_{,z} \end{cases} \quad (7.2)$$

Substituting equations 7.1 into 7.2 and one gets

$$\begin{cases} \varepsilon_x = u_{0,x} + z\alpha_{,x} & \gamma_{xy} = u_{0,y} + v_{0,x} + z(\alpha_{,y} + \beta_{,x}) \\ \varepsilon_y = v_{0,y} + z\beta_{,y} & \gamma_{yz} = \beta_{,z} + \omega_{0,y} + z\rho_{,y} \\ \varepsilon_z = \rho & \gamma_{xz} = \alpha_{,z} + \omega_{0,x} + z\rho_{,x} \end{cases} \quad (7.3)$$

where $u_{0,x}$ and $v_{0,y}$ are the in-plane normal strains of the middle surfaces, which should be counted out ($u_0 = v_0 = 0$) since the membrane stresses are precluded in basic assumptions. According to the basic assumptions, the strain along the plate thickness is also negligible, therefore ε_z equals 0. The shear strain is neglected in the PE method but taken into account now. It should be noted that only the shear strain at the transversal direction γ_{xz} is considered, to simplify the calculations, so γ_{yz} equals 0. Hence, the rotational angles α , β and ρ may be solved as

$$\alpha = -\omega_{0,x} + \gamma_{xz} \quad \beta = -\omega_{0,y} \quad \rho = 0 \quad (7.4)$$

Substituting the expressions of the rotational angles (equations 7.4) back in equations 7.1, the expressions of displacements for the plate are reduced to

$$\begin{cases} u = -z(\omega_{0,x} - \gamma_{xz}) \\ v = -z\omega_{0,y} \\ \omega = \omega_0 \end{cases} \quad (7.5)$$

The derivation of displacement u is also illustrated in Figure 7.2, which shows a section ($y=const.$) of the plate before and after deformation.

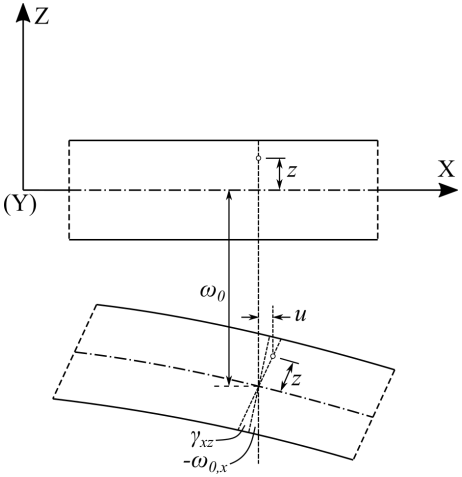


Figure 7.2: A section of the plate before and after deformation

Substituting equations 7.5 in 7.2, the nonzero strains are

$$\begin{cases} \varepsilon_x = -z(\omega_{0,xx} - \gamma_{xz,x}) \\ \varepsilon_y = -z\omega_{0,yy} \\ \gamma_{xy} = -z(2\omega_{0,xy} - \gamma_{xz,y}) \\ \gamma_{xz} = \gamma_{xz} \end{cases} \quad (7.6)$$

It should be noted that the shear strain γ_{xz} is treated as an independent variable as well as the vertical displacement ω_0 .

7.2.3 Equilibrium equations

Figure 7.3 presents the idealized plate subjected to an arbitrary vertical load $p(x, y)$. The equilibrium of the plate element is defined by three equations, which are equations 7.7, 7.9 and 7.11.

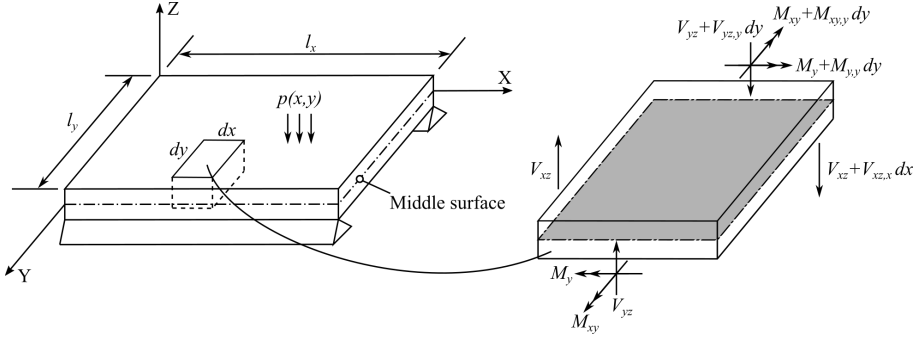


Figure 7.3: Vertically loaded plate

Based on the equilibrium for all the vertical forces acting on the element along the Z axis, the first equation is

$$V_{xz,x}dxdy + V_{yz,y}dydx + pdxdy = 0 \quad (7.7)$$

where V_{xz} and V_{yz} are the shear forces per unit length in the Y and X directions respectively. Divided by the common part $dxdy$ on both sides, equation 7.7 turns into

$$V_{xz,x} + V_{yz,y} = -p \quad (7.8)$$

According to the equilibrium for all the moments acting on the element with respect to the X axis, the second equation is

$$M_{y,y}dydx - V_{yz}dydx = 0 \quad (7.9)$$

wherein M_y is the bending moment per unit length in the X direction. Similarly, equation 7.9 is simplified to

$$M_{y,y} = V_{yz} \quad (7.10)$$

Concerning the equilibrium for all the moments acting on the element with respect to the Y axis, the third equation is

$$M_{xy,y}dydx - V_{xz}dxdy = 0 \quad (7.11)$$

and turns into

$$M_{xy,y} = V_{xz} \quad (7.12)$$

Combining equations 7.8, 7.10 and 7.12, and eliminating V_{yz} , the following system of partial differential equations is obtained

$$\begin{cases} V_{xz,x} + M_{y,yy} = -p \\ M_{xy,xy} + M_{y,yy} = -p \end{cases} \quad (7.13)$$

7.2.4 Relationships between stress, strain and displacement

By definition, the two-dimensional Hooke's law for elastic orthotropic plates may be written as

$$\sigma_x = \frac{E_x}{1 - \nu_x \nu_y} (\varepsilon_x + \nu_y \varepsilon_y) \quad (7.14)$$

$$\sigma_y = \frac{E_y}{1 - \nu_x \nu_y} (\varepsilon_y + \nu_x \varepsilon_x) \quad (7.15)$$

in which E is the Young's modulus of elasticity and ν is the Poisson's ratio. σ_x and σ_y are components of normal stresses in the X and Y directions. Nonetheless, the Poisson's ratio may be assumed to be negligible for the idealized plate representing the OSD ($\nu_x \cong \nu_y \cong 0$). This leads to a simpler relationship:

$$\sigma = E\varepsilon \quad (7.16)$$

Meanwhile, the shear stress τ is given by:

$$\tau = G\gamma \quad (7.17)$$

wherein G is the shear modulus of the plate and γ is the corresponding shear strain.

The expressions for moments and shear forces are defined by integrating the corresponding stress components over the thickness of plate:

$$\begin{cases} M_x = \int_{-h/2}^{h/2} \sigma_x z dz \\ M_y = \int_{-h/2}^{h/2} \sigma_y z dz \\ M_{xy} = \int_{-h/2}^{h/2} \tau_{xy} z dz \\ V_{xz} = \int_{-h/2}^{h/2} \tau_{xz} z dz \end{cases} \quad (7.18)$$

in which h is the thickness of the plate.

With respect to the stress-strain relationships and substituting equations 7.6 into the above expressions, the formulas of the moments and shear forces expressed in terms of ω_0 and γ_{xz} may be written as

$$\begin{cases} M_x = -K_x (\omega_{0,xx} - \gamma_{xz,x}) \\ M_y = -K_y \omega_{0,yy} \\ M_{xy} = -K_{xy} (2\omega_{0,xy} - \gamma_{xz,y}) \\ V_{xz} = K_{xz} \gamma_{xz} \end{cases} \quad (7.19)$$

where K_x and K_y are the flexural rigidity coefficients in the X and Y directions; K_{xy} is the torsional rigidity coefficient; K_{xz} is the shear rigidity coefficient. It should be noted, however, that these rigidity coefficients directly deducted from above equations are only suitable for a general orthotropic plate. For the substitute orthotropic plate used to represent the actual OSD system, the characteristic rigidity coefficients will be further discussed in the next section.

7.2.5 Rigidity coefficients

During the computation of the rigidity coefficients in this section, the designation of the dimensions used is shown in Figure 7.4.

In the figure, a is the upper width of the closed rib and e is the gap between two adjacent ribs. j is the bottom width of the rib. h_r is the vertical height of the rib while h_w is the actual height of the rib web. t_d and t_r are the thicknesses of the deck plate and the rib respectively. A is the size of the shadowed area which is defined as the area enclosed by a rib. u is defined as the developed width of one rib plate.

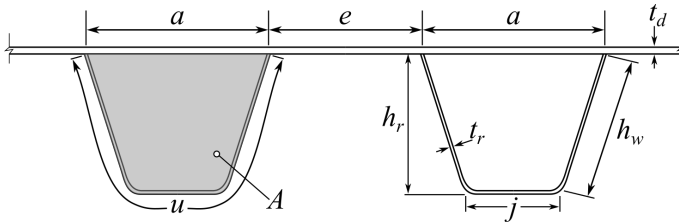


Figure 7.4: Rib dimensions

7.2.5.1 Flexural rigidity coefficient K_y

For the idealized orthotropic plate, K_x is the transverse rigidity of the system, which equals to the rigidity of the flat deck plate. K_y is the longitudinal rigidity, obtained by dividing the rigidity of one rib, acting in conjunction with the deck plate, by the rib spacing. In OSDs of the usual design, the longitudinal rigidity K_y is considerably larger than the horizontal rigidity K_x . The ratio K_y/K_x usually ranges between 500 and 2000, as stated in the original PE method (AISC, 1963). Therefore, the horizontal rigidity coefficient K_x may be neglected.

The flexural rigidity coefficient K_y is computed by

$$K_y = \frac{EI_R}{a + e} \quad (7.20)$$

where I_R is the moment of inertia of one rib.

7.2.5.2 Torsional rigidity coefficient K_{xy}

With reference to the original PE method, the torsional rigidity coefficient K_{xy} is expressed by the formula

$$K_{xy} = \frac{2GA^2}{(a + e)[(u/t_r) + (a/t_d)]} \tag{7.21}$$

It should be noted that the reduction coefficient μ is not taken into account.

7.2.5.3 Shear rigidity coefficient K_{xz}

The shear rigidity coefficient K_{xz} is achieved by performing a frame analysis as shown in Figure 7.5. The frame has 6 rods ψ_{1-6} and 6 nodes ϕ_{a-f} , which represents the base module of OSD consisting of one rib and part of the deck plate, as shown in Figure 7.5(a). Two hinge supports are placed at nodes ϕ_b and ϕ_e respectively. The virtual shear force V is assumed to be applied on both ends of the frame at nodes ϕ_a and ϕ_d , as illustrated in Figure 7.5(b). Once the vertical displacement between two ends of the deck plate δ is determined, the shear rigidity coefficient K_{xz} may be calculated by the formula

$$K_{xz} = \frac{V(a + e)}{\delta} \tag{7.22}$$

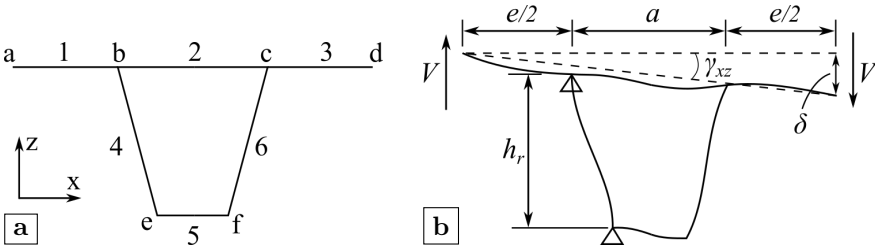


Figure 7.5: Frame analysis for shear rigidity coefficient: (a) base module; (b) shear deformation

In order to get the expression of the displacement δ , the frame analysis is programmed using the symbolic computing software Maple. The first step is to define the functions for the moment, the slope and the deflection for every rod sequentially. Considering an arbitrary rod ψ_i , the shear force is denoted as V_{ψ_i} . Assuming the node ϕ_j is the origin of the local coordinate system and the distance to ϕ_j along the rod is s , the moment function M_{ψ_i} is achieved by the integral of V_{ψ_i} with respect to s

$$\begin{aligned} M_{\psi_i} &= \int V_{\psi_i} ds + C_1 \\ &= V_{\psi_i} s + C_1 \end{aligned} \tag{7.23}$$

Integrating the moment function M_{ψ_i} , the slope function θ_{ψ_i} is acquired as

$$\begin{aligned}\theta_{\psi_i} &= \frac{\int M_{\psi_i} ds}{EI_{\psi_i}} + C_2 \\ &= \frac{V_{\psi_i} s^2}{2EI_{\psi_i}} + \frac{C_1 s}{EI_{\psi_i}} + C_2\end{aligned}\quad (7.24)$$

where I_{ψ_i} is the moment of inertia of rod ψ_i . Since the OSD is represented by the frame, the moment of inertia per unit length is calculated as

$$I_{\psi_i} = \frac{t_{\psi_i}^3}{12}$$

in which t_{ψ_i} is the thickness of the corresponding steel plate.

The deflection function δ_{ψ_i} is achieved by integrating the slope function θ_{ψ_i}

$$\begin{aligned}\delta_{\psi_i} &= \int \theta_{\psi_i} ds + C_3 \\ &= \frac{V_{\psi_i} s^3}{6EI_{\psi_i}} + \frac{C_1 s^2}{2EI_{\psi_i}} + C_2 s + C_3\end{aligned}\quad (7.25)$$

In functions 7.23 to 7.25, there are three constants (C_1, C_2 and C_3) due to the integral, which shall be determined by the boundary conditions. Taking the example of rod ψ_1 and choosing node ϕ_a as the local origin, functions 7.23 to 7.25 may be written as

$$\begin{aligned}M_{\psi_1} &= V_{\psi_1} s + M_{1a} \\ \theta_{\psi_1} &= \frac{V_{\psi_1} s^2}{2EI_{\psi_1}} + \frac{M_{1a} s}{EI_{\psi_1}} + \theta_{1a} \\ \delta_{\psi_1} &= \frac{V_{\psi_1} s^3}{6EI_{\psi_1}} + \frac{M_{1a} s^2}{2EI_{\psi_1}} + \theta_{1a} s + \delta_{1a}\end{aligned}\quad (7.26)$$

where M_{1a} , θ_{1a} and δ_{1a} are the end moment, slope and deflection at node ϕ_a of rod ψ_1 respectively. The same naming strategy will be used during the rest of this section.

The next step is to define the equilibrium equations at the intersection nodes as shown in Figure 7.6. The angle between the rib web and the vertical direction is denoted as α_r .

Taking the example of node ϕ_b , the force equilibrium equations along two axes are

$$V_{\psi_1} = R_{vb} + V_{\psi_2} + V_{\psi_4} \sin \alpha_r + N_{\psi_4} \cos \alpha_r \quad (7.27)$$

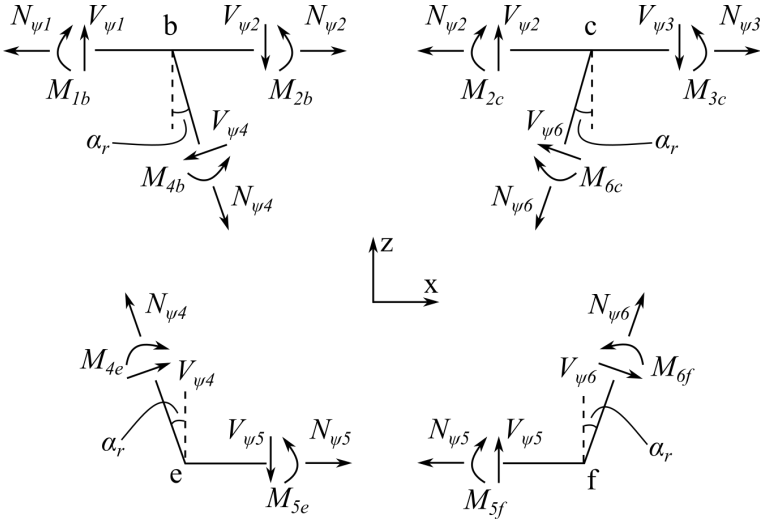


Figure 7.6: Illustration of node equilibrium

$$N_{\psi 2} + N_{\psi 4} \sin \alpha_r = R_{hb} + V_{\psi 4} \cos \alpha_r + N_{\psi 1} \quad (7.28)$$

in which R_{vb} and R_{hb} are the vertical and horizontal reaction force introduced by the hinged support.

According to the moment equilibrium about node ϕ_b :

$$M_{1b} = M_{2b} + M_{4b} \quad (7.29)$$

Since the rods are fixed, the end slope and displacement of each rod should be equal. Using u_{ij} and w_{ij} to denote the displacements along the X and Z axes, the relations of slope and displacement are

$$\begin{aligned} \theta_{1b} &= \theta_{2b} = \theta_{4b} \\ u_{1b} &= u_{2b} = u_{4b} \\ w_{1b} &= w_{2b} = w_{4b} \end{aligned} \quad (7.30)$$

The expressions for slope and displacement could be acquired by the corresponding functions 7.24 and 7.25.

Similarly, the equilibrium equations for other nodes are:

- for node ϕ_c

$$\begin{aligned}
V_{\psi 2} + V_{\psi 6} \sin \alpha_r &= V_{\psi 3} + N_{\psi 6} \cos \alpha_r \\
N_{\psi 2} + N_{\psi 6} \sin \alpha_r + V_{\psi 6} \cos \alpha_r &= N_{\psi 3} \\
M_{2c} + M_{6c} &= M_{3c} \\
\theta_{2c} &= \theta_{3c} = \theta_{6c} \\
u_{2c} &= u_{3c} = u_{6c} \\
w_{2c} &= w_{3c} = w_{6c}
\end{aligned} \tag{7.31}$$

- for node ϕ_e

$$\begin{aligned}
V_{\psi 4} \sin \alpha_r + N_{\psi 4} \cos \alpha_r &= R_{ve} + V_{\psi 5} \\
N_{\psi 4} \sin \alpha_r + R_{he} &= V_{\psi 4} \cos \alpha_r + N_{\psi 5} \\
M_{4e} &= M_{5e} \\
\theta_{4e} &= \theta_{5e} \\
u_{4e} &= u_{5e} \\
w_{4e} &= w_{5e}
\end{aligned} \tag{7.32}$$

- for node ϕ_f

$$\begin{aligned}
V_{\psi 5} + N_{\psi 6} \cos \alpha_r &= V_{\psi 6} \sin \alpha_r \\
N_{\psi 5} &= N_{\psi 6} \sin \alpha_r + V_{\psi 6} \cos \alpha_r \\
M_{5f} &= M_{6f} \\
\theta_{5f} &= \theta_{6f} \\
u_{5f} &= u_{6f} \\
w_{5f} &= w_{6f}
\end{aligned} \tag{7.33}$$

The last step is to define the load and boundary conditions for the whole system. As shown in Figure 7.5(b), the load and boundary conditions may be written as

$$\begin{aligned}
V_{\psi 1} &= V & u_{1b} &= 0 \\
M_{1a} &= 0 & w_{1b} &= 0 \\
V_{\psi 3} &= V & u_{5e} &= 0 \\
M_{3d} &= 0 & w_{5e} &= 0
\end{aligned} \tag{7.34}$$

Combine equations from 7.27 to 7.34 and solving for the unknown components, the expression for K_{xz} is finally acquired.

$$K_{xz} = \frac{12EI_d I_r (a+e)(a^3 I_r + I_d \alpha^*)}{2(a+e)^2 (j + 3h_w/2) h_w j^2 I_d^2 + 2I_r I_d (a+e) \beta^* + a^3 e^3 I_r^2} \tag{7.35}$$

with

$$\begin{aligned}\alpha^* &= 2h_w(a^2 + aj + j^2) + j^3 \\ \beta^* &= \left(\frac{j^3}{2} + h_w j^2\right)(a^2 - ae + e^2) - aeh_w j(a - e) + a^2 e^2 h_w\end{aligned}\quad (7.36)$$

where I_d and I_r are the moment of inertia calculated using the thickness of deck and rib respectively.

7.2.6 Partial differential equations

Substituting equations 7.19 into 7.13 and omitting the index ($\gamma = \gamma_{xz}$, $\omega = \omega_0$), the system of partial differential equations pending to be solved is

$$\begin{cases} K_{xz}\gamma_{,x} - K_y\omega_{,yyyy} = -p \\ -K_{xy}(2\omega_{,xxyy} - \gamma_{,xyy}) - K_y\omega_{,yyyy} = -p \end{cases}\quad (7.37)$$

in which all rigidity coefficients are defined in previous section. The general solution of the non-homogeneous differential equations is composed of a general solution to the corresponding homogeneous differential equations and a particular solution to the non-homogeneous differential equations.

7.2.6.1 Fourier analysis of loading

In order to solve either the homogeneous equations or the non-homogeneous equations, one of the keys is that the tire load acting on the bridge deck must be developed into Fourier series. The actual concentrated load is represented by a summation of sinusoidal component loads extending over the whole bridge deck.

1-D Fourier series

The 1-D Fourier series is utilized when solving the homogeneous equations to get the general solution. A cross-section of the substitute deck plate is shown in Figure 7.7.

The tire load $P = Q_0(x_2 - x_1)$ may be represented by

$$Q_{1d} = \sum_{n=1}^{\infty} Q_n \sin \frac{n\pi x}{b}\quad (7.38)$$

with

$$\begin{aligned}Q_n &= \frac{2Q_0}{b} \int_{x_1}^{x_2} \sin \frac{n\pi x}{b} dx \\ &= \frac{2Q_0}{n\pi} \left(\cos \frac{n\pi x_1}{b} - \cos \frac{n\pi x_2}{b} \right)\end{aligned}\quad (7.39)$$

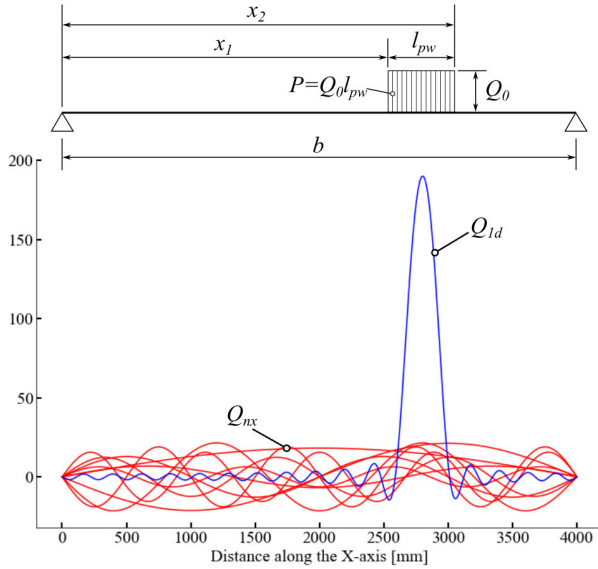


Figure 7.7: Illustration of 1-D Fourier series

where Q_{1d} is the load per unit width at the location x , represented by a Fourier series; Q_0 is the actual load on bridge deck per unit width; b is the width of the bridge deck.

The value of Q_n represents the maximum value of the n th sinusoidal component load of the series ($Q_{nx} = Q_n \sin(\frac{n\pi x}{b})$), as also illustrated in Figure 7.7.

2-D Fourier series

The 2-D Fourier series is utilized when solving the non-homogeneous equations to get the particular solution. The tire load $P = Q_0^* l_{pl} l_{pw}$ may be expressed as

$$Q_{2d} = \frac{4P}{l_{pl} l_{pw} \pi^2} \left[\sum_{m=1}^{\infty} \sum_{n=1}^{\infty} \frac{1}{nm} \sin\left(\frac{n\pi l_{pw}}{b}\right) \sin\left(\frac{n\pi x_p}{b}\right) \sin\left(\frac{n\pi x}{b}\right) \sin\left(\frac{m\pi l_{pl}}{s}\right) \sin\left(\frac{m\pi y_p}{s}\right) \sin\left(\frac{m\pi y}{s}\right) \right] \quad (7.40)$$

where l_{pl} and l_{pw} are the length and width of the load patch; x_p and y_p are the coordinates of the load center; b and s are the width and length of the bridge deck, respectively.

Figure 7.8 gives an example of the 2-D Fourier series. The tire load is placed

at the center of a bridge deck with 3600 mm wide and 4000 mm long. The load patch is a rectangle with a width of 270 mm and a length of 320 mm.

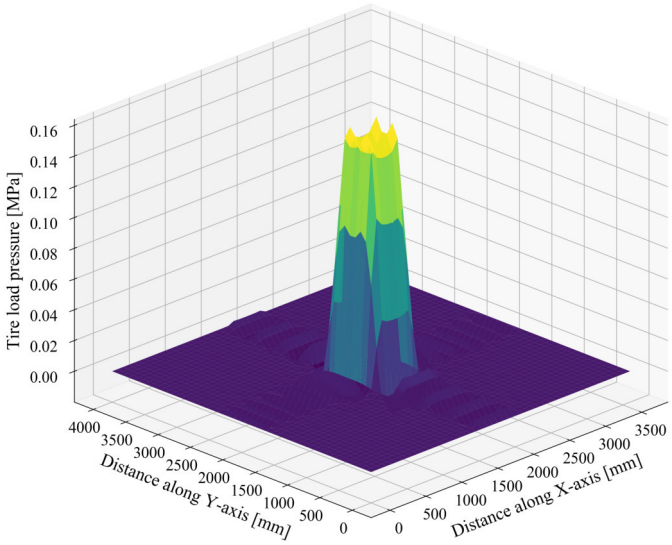


Figure 7.8: Illustration of 2-D Fourier series

7.2.6.2 General solution of the homogeneous equations

The corresponding homogeneous equations of equation 7.37 are

$$\begin{cases} K_{xz}\gamma_{,x} - K_y\omega_{,yyyy} = 0 \\ -K_{xy}(2\omega_{,xxyy} - \gamma_{,xyy}) - K_y\omega_{,yyyy} = 0 \end{cases} \tag{7.41}$$

Since the tire load is developed into a 1-D Fourier series, the general solutions of the homogeneous equations are also given as an infinite series.

$$\begin{aligned} \omega &= \sum_{n=1}^{\infty} \omega_n \\ \gamma &= \sum_{n=1}^{\infty} \gamma_n \end{aligned} \tag{7.42}$$

with

$$\begin{aligned}
\omega_n &= [C1_n \sinh(\alpha_n y) \sin(\beta_n y) + C2_n \cosh(\alpha_n y) \cos(\beta_n y) \\
&\quad + C3_n \sinh(\alpha_n y) \cos(\beta_n y) + C4_n \cosh(\alpha_n y) \sin(\beta_n y)] \sin\left(\frac{n\pi x}{b}\right) \\
\gamma_n &= [(C1_n \zeta_n - C2_n \eta_n) \sinh(\alpha_n y) \sin(\beta_n y) \\
&\quad + (C1_n \eta_n + C2_n \zeta_n) \cosh(\alpha_n y) \cos(\beta_n y) \\
&\quad + (C3_n \zeta_n + C4_n \eta_n) \sinh(\alpha_n y) \cos(\beta_n y) \\
&\quad + (C4_n \zeta_n - C3_n \eta_n) \cosh(\alpha_n y) \sin(\beta_n y)] \cos\left(\frac{n\pi x}{b}\right)
\end{aligned} \tag{7.43}$$

where $C1_n$, $C2_n$, $C3_n$ and $C4_n$ are the four integration constants to be determined from the boundary conditions for each term n of the series. α_n , β_n , ζ_n and η_n are four parameters to be determined by the functions.

Substituting equations 7.43 into 7.37, two very complicated polynomials about x and y on the left hand side of the equations are acquired. For every undetermined integration constant, its coefficient contains four unique common variables, which are:

- $\sinh(\alpha_n y) \sin(\beta_n y) \sin\left(\frac{n\pi x}{b}\right)$
- $\cosh(\alpha_n y) \cos(\beta_n y) \sin\left(\frac{n\pi x}{b}\right)$
- $\sinh(\alpha_n y) \cos(\beta_n y) \sin\left(\frac{n\pi x}{b}\right)$
- $\cosh(\alpha_n y) \sin(\beta_n y) \sin\left(\frac{n\pi x}{b}\right)$

In order for the polynomials to be zero, the coefficients of the integration constants should equal zero as well, which means the coefficients of the four variables stated above should be zero. Therefore, a system of equations is constructed for determining the expressions of parameters.

Considering the coefficients of $C1_n$ and $C4_n$, the system of equations is the same, which is:

$$\begin{cases}
K_{xy} \left[-\frac{2(\alpha_n^2 - \beta_n^2)n^2\pi^2}{b^2} + \frac{(\alpha_n^2\zeta_n - 2\alpha_n\beta_n\eta_n - \beta_n^2\zeta_n)n\pi}{b} \right] + K_y(\alpha_n^4 - 6\alpha_n^2\beta_n^2 + \beta_n^4) = 0 \\
K_{xy} \left[-\frac{4\alpha_n\beta_n n^2\pi^2}{b^2} + \frac{(\alpha_n^2\eta_n + 2\alpha_n\beta_n\zeta_n - \beta_n^2\eta_n)n\pi}{b} \right] + K_y(4\alpha_n^3\beta_n - 4\alpha_n\beta_n^3) = 0 \\
\frac{K_{xz}\zeta_n n\pi}{b} + K_y(\alpha_n^4 - 6\alpha_n^2\beta_n^2 + \beta_n^4) = 0 \\
\frac{K_{xz}\eta_n n\pi}{b} + K_y(4\alpha_n^3\beta_n - 4\alpha_n\beta_n^3) = 0
\end{cases} \tag{7.44}$$

Considering the coefficients of $C2_n$ and $C3_n$, the system of equations is the

same, which is:

$$\begin{cases} K_{xy} \left[-\frac{2(\alpha_n^2 - \beta_n^2)n^2\pi^2}{b^2} + \frac{(\alpha_n^2\zeta_n - 2\alpha_n\beta_n\eta_n - \beta_n^2\zeta_n)n\pi}{b} \right] + K_y(\alpha_n^4 - 6\alpha_n^2\beta_n^2 + \beta_n^4) = 0 \\ K_{xy} \left[\frac{4\alpha_n\beta_n n^2\pi^2}{b^2} + \frac{(-\alpha_n^2\eta_n - 2\alpha_n\beta_n\zeta_n + \beta_n^2\eta_n)n\pi}{b} \right] + K_y(-4\alpha_n^3\beta_n + 4\alpha_n\beta_n^3) = 0 \\ \frac{K_{xz}\zeta_n n\pi}{b} + K_y(\alpha_n^4 - 6\alpha_n^2\beta_n^2 + \beta_n^4) = 0 \\ -\frac{K_{xz}\eta_n n\pi}{b} + K_y(-4\alpha_n^3\beta_n + 4\alpha_n\beta_n^3) = 0 \end{cases} \quad (7.45)$$

When equations 7.44 and 7.45 are compared one by one carefully, it is observed that some equations are totally identical, i.e. the first and the third equations in 7.44 and in 7.45 are identical respectively. Meanwhile, only the signs are opposite for the other two pairs of equations, i.e. the left hand parts of the second and the fourth equations in both 7.44 and 7.45. Since the right hand part of these equations are all equal to zero, their solutions should be the same. Solving either system of equations presented above, the expressions for parameters may be determined. Using the symbolic computing software Maple to solve the system of equations 7.44, it is determined that there are in total five possible solutions. One possible solution is all zeros. The other three possible solutions contain imaginary parts. The last one possible solution with only real parts is

$$\begin{aligned} \alpha_n &= \sqrt{-\frac{-2\sqrt{2}\pi K_{xy}n\sqrt{K_{xz}K_y} - K_{xz}K_y b}{4K_{xy}K_y b}} \\ \beta_n &= \frac{\sqrt{K_{xy}K_y b(2\sqrt{2}\pi K_{xy}n\sqrt{K_{xz}K_y} - K_{xz}K_y b)}}{2K_{xy}K_y b} \\ \zeta_n &= \frac{4K_{xy}^2\pi^2 n^2 - K_{xz}K_y b^2}{2bK_{xy}^2\pi n} \\ \eta_n &= -\frac{2\alpha_n\beta_n K_y b}{K_{xy}\pi n} \end{aligned} \quad (7.46)$$

Substituting the expressions of parameters 7.46 back into equations 7.43, the general solution of the homogeneous equations may be determined.

7.2.6.3 Particular solution of the non-homogeneous equations

Recall the non-homogeneous equations, as presented in equation 7.37, which is

$$\begin{cases} K_{xz}\gamma_{,x} - K_y\omega_{,yyyy} = -p \\ -K_{xy}(2\omega_{,xxyy} - \gamma_{,xyy}) - K_y\omega_{,yyyy} = -p \end{cases} \quad (7.47)$$

As stated before, the load P may be expressed by a 2-D Fourier series as shown in 7.40. The expression may be further written as

$$Q_{2d} = \sum_{m=1}^{\infty} \sum_{n=1}^{\infty} a_{mn} \sin\left(\frac{n\pi x}{b}\right) \sin\left(\frac{m\pi y}{s}\right) \quad (7.48)$$

where

$$a_{mn} = \frac{4P}{l_{pl}l_{pw}\pi^2 mn} \sin\left(\frac{n\pi l_{pw}}{b}\right) \sin\left(\frac{n\pi x_p}{b}\right) \sin\left(\frac{m\pi l_{pl}}{s}\right) \sin\left(\frac{m\pi y_p}{s}\right) \quad (7.49)$$

To accommodate the infinite series form of the load, the particular solutions of the non-homogeneous equations are assumed to have the following form

$$\begin{aligned} \omega &= \sum_{m=1}^{\infty} \sum_{n=1}^{\infty} C1_{mn} \sin\left(\frac{n\pi x}{b}\right) \sin\left(\frac{m\pi y}{s}\right) \\ \gamma &= \sum_{m=1}^{\infty} \sum_{n=1}^{\infty} C2_{mn} \cos\left(\frac{n\pi x}{b}\right) \sin\left(\frac{m\pi y}{s}\right) \end{aligned} \quad (7.50)$$

where $C1_{mn}$ and $C2_{mn}$ are two parameters about both m and n need to be determined.

Utilizing the assumed solutions 7.50 to get the partial differentiation used in the system of non-homogeneous equations 7.47, following expressions are acquired:

$$\begin{aligned} \omega_{,xxyy} &= \sum_{m=1}^{\infty} \sum_{n=1}^{\infty} \frac{C1_{mn} n^2 \pi^4 m^2}{b^2 s^2} \sin\left(\frac{n\pi x}{b}\right) \sin\left(\frac{m\pi y}{s}\right) \\ \omega_{,yyyy} &= \sum_{m=1}^{\infty} \sum_{n=1}^{\infty} \frac{C1_{mn} m^4 \pi^4}{s^4} \sin\left(\frac{n\pi x}{b}\right) \sin\left(\frac{m\pi y}{s}\right) \\ \gamma_{,x} &= \sum_{m=1}^{\infty} \sum_{n=1}^{\infty} \left[-\frac{C2_{mn} n \pi}{b} \sin\left(\frac{n\pi x}{b}\right) \sin\left(\frac{m\pi y}{s}\right) \right] \\ \gamma_{,xyy} &= \sum_{m=1}^{\infty} \sum_{n=1}^{\infty} \frac{C2_{mn} n \pi^3 m^2}{b s^2} \sin\left(\frac{n\pi x}{b}\right) \sin\left(\frac{m\pi y}{s}\right) \end{aligned} \quad (7.51)$$

Substituting the equations 7.51 and 7.48 into 7.47, the system of equations for determining the parameters is acquired as

$$\begin{aligned} K_{xy} \left(2 * \frac{C1_{mn} n^2 \pi^4 m^2}{b^2 s^2} - \frac{C2_{mn} n \pi^3 m^2}{b s^2} \right) + \frac{K_y C1_{mn} m^4 \pi^4}{s^4} &= a_{mn} \\ \frac{K_{xz} C2_{mn} n \pi}{b} + \frac{K_y C1_{mn} m^4 \pi^4}{s^4} &= a_{mn} \end{aligned} \quad (7.52)$$

Solving equations 7.52, the parameters may be written as

$$\begin{aligned}
 C1_{mn} &= \frac{a_{mn}s^4b^2(K_{xy}\pi^2m^2 + K_{xz}s^2)}{m^2\pi^4(K_{xy}K_y\pi^2b^2m^4 + 2K_{xy}K_{xz}n^2s^4 + K_{xz}K_yb^2m^2s^2)} \\
 C2_{mn} &= \frac{2a_{mn}s^4bK_{xy}n}{\pi(K_{xy}K_y\pi^2b^2m^4 + 2K_{xy}K_{xz}n^2s^4 + K_{xz}K_yb^2m^2s^2)}
 \end{aligned}
 \tag{7.53}$$

Substituting the expressions of parameters 7.53 back into equations 7.50, the particular solution of the non-homogeneous equations is accordingly determined.

7.2.7 Carry-over factor

Similar to the original PE method, the carry-over factor κ_n is obtained from the three-moment equations. The carry-over factor is needed when analyzing a continuous orthotropic plate.

In order to find the expressions for the carry-over factor κ_n , a simply supported plate panel is considered as shown in Figure 7.9(a). At the edge of support 1, a sinusoidal bending moment $M_1 = M_1^* \sin(\frac{n\pi x}{b})$ is applied. The maximum value M_1^* appears at the location of $x = \frac{b}{2n}$.

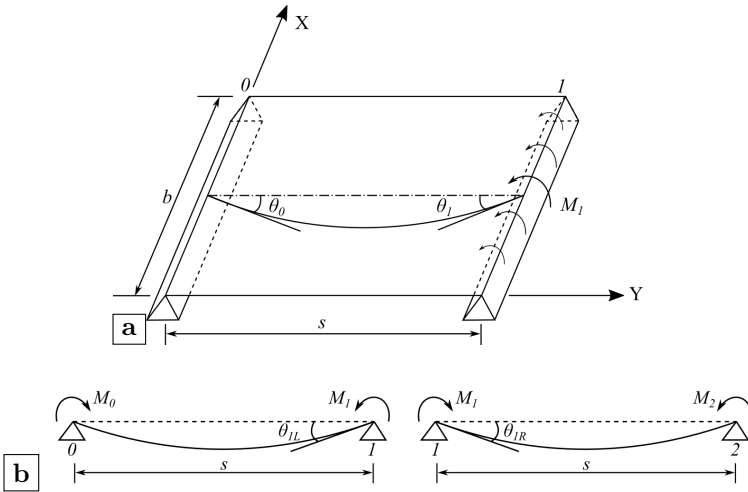


Figure 7.9: Derivation of the carry-over factor: (a) simply supported plate panel; (b) continuous beam (adapted from AISC (1963))

Since the plate is only loaded at the edges, it refers to the general solution (equations 7.43) deduced for the homogeneous equations. The boundary

conditions for the plate are:

$$\begin{aligned} y = 0 & \quad \omega = 0 & \quad M_y = 0 \\ y = s & \quad \omega = 0 & \quad M_y = M_1 \end{aligned} \quad (7.54)$$

Based on the above information, the four constants may be determined from equations 7.19 as

$$\begin{aligned} C1_n &= 0 \\ C2_n &= 0 \\ C3_n &= \frac{M_1 \cosh(\alpha_n s) \sin(\beta_n s)}{2K_y \sin\left(\frac{n\pi x}{b}\right) \alpha_n \beta_n [\sinh^2(\alpha_n) \cos^2(\beta_n s) + \sin^2(\beta_n s) \cosh^2(\alpha_n s)]} \\ C4_n &= -\frac{M_1 \sinh(\alpha_n s) \cos(\beta_n s)}{2K_y \sin\left(\frac{n\pi x}{b}\right) \alpha_n \beta_n [\sinh^2(\alpha_n) \cos^2(\beta_n s) + \sin^2(\beta_n s) \cosh^2(\alpha_n s)]} \end{aligned} \quad (7.55)$$

with the value of α_n and β_n defined by equations 7.46.

With these constants, the rotations due to the moment M_1 may be calculated using the formula

$$\theta_n = \omega_{n,y} \quad (7.56)$$

If the bending moments are applied at both supports of the plate, as shown in Figure 7.9(b), the values of the rotations at any support may be written as a function of the applied moments on both ends. For the continuous plate, the rotation at support 1 may be expressed as a function of either moments M_0 and M_1 in panel θ -1 or moments M_1 and M_2 in panel 1-2 simultaneously. According to the condition that the rotation θ_{1L} and θ_{1R} should be equal in a continuous plate, the three-moment equation of an unloaded continuous plate is obtained as

$$M_0 + 2kM_1 + M_2 = 0 \quad (7.57)$$

where k is calculated by

$$\begin{aligned} k &= -\frac{\theta_1}{\theta_0} \\ &= \frac{-\cosh(\alpha_n s) \sinh(\alpha_n s) \beta_n + \cos(\beta_n s) \sin(\beta_n s) \alpha_n}{\sinh(\alpha_n s) \cos(\beta_n s) \beta_n - \cosh(\alpha_n s) \sin(\beta_n s) \alpha_n} \end{aligned} \quad (7.58)$$

Similar to the continuous beam, when a sinusoidal moment is introduced at the support θ , the moments at further support (i.e. support 1 and 2) decrease by

a carry-over factor κ .

$$\begin{aligned} M_{1n} &= \kappa_n M_{0n} \\ M_{2n} &= \kappa_n M_{1n} = \kappa_n^2 M_{0n} \\ &\dots \end{aligned} \tag{7.59}$$

By substituting equations 7.59 into 7.57, the carry-over factor κ_n is obtained as

$$\kappa_n = -k + \sqrt{k^2 - 1} \tag{7.60}$$

7.2.8 Influence line

Influence line is required when calculating the general solution for the homogeneous equations. The tire load is transferred to the moment applied to the plate edge. Thus, the four constants required for the general solution may be computed.

The influence line is obtained in accordance with the Betti-Maxwell principle of reciprocity, as deflection lines of a continuous beam due to unit deformations (AISC, 1963). Thus, the influence line for the bending moment at any point of the continuous beam is defined as the deflection line due to a unit rotation applied at that point.

Given the general solutions as stated in equations 7.43, the same model as shown in Figure 7.9(a) is adopted. To get the influence line, a sinusoidal half unit rotation is considered since the other half unit rotation would be provided by the adjacent plate. The considered conditions may be expressed as

$$\begin{aligned} y = 0 & \quad \omega = 0 & \quad M_y = M_0 \sin\left(\frac{n\pi x}{b}\right) & \quad \theta = \frac{1}{2} \sin\left(\frac{n\pi x}{b}\right) \\ y = s & \quad \omega = 0 & \quad M_y = M_0 \sin\left(\frac{n\pi x}{b}\right) \kappa_n \end{aligned} \tag{7.61}$$

Based on these conditions, the four constants and the moment required to sustain the half unit rotation may be obtained. The four constants are

$$\begin{aligned} C1_n &= \frac{\cos^2(\beta_n s) - \cosh^2(\alpha_n s)}{C_{den}} \\ C2_n &= 0 \\ C3_n &= \frac{-\sin(\beta_n s)[- \cosh(\alpha_n s) \kappa_n + \cos(\beta_n s)]}{C_{den}} \\ C4_n &= \frac{-\sinh(\alpha_n s)[\cos(\beta_n s) \kappa_n - \cosh(\alpha_n s)]}{C_{den}} \end{aligned} \tag{7.62}$$

with

$$C_{den} = 2\beta_n [\cos(\beta_n s) \kappa_n - \cosh(\alpha_n s)] \sinh(\alpha_n s) - 2\alpha_n \sin(\beta_n s) [\cosh(\alpha_n s) \kappa_n - \cos(\beta_n s)] \quad (7.63)$$

7.2.9 Local model

Through the formulas presented in previous sections, the functions that describe the vertical deflections and the shear deformations are derived. According to the formulas of internal forces expressed in terms of deflections and deformations as presented in equation 7.19, the distributions of internal forces can also be calculated. By integrating through a defined width of one rib, the torsional moment and the shear force of the rib may be accordingly determined. With reference to the previous analyses, the distortional stress that appeared at the lower weld end on the rib wall is highly associated with the fatigue performance of the rib-to-crossbeam joint with cope holes. Therefore, a local model is required to connect the internal forces and the distortional stresses.

Figure 7.10 shows the illustration of the local model for the rib-to-crossbeam joint with cope holes. The local model is a frame model to represent the intersection. The width of the frame is the same as the crossbeam thickness. In practical structures, the bottom corners of the rib are curved. But in the local model, the curved corners are not modeled. Nevertheless, the influence of the curved corners (i.e. rib radius) are still included when calculating the flexural rigidity coefficient and the torsional rigidity coefficient.

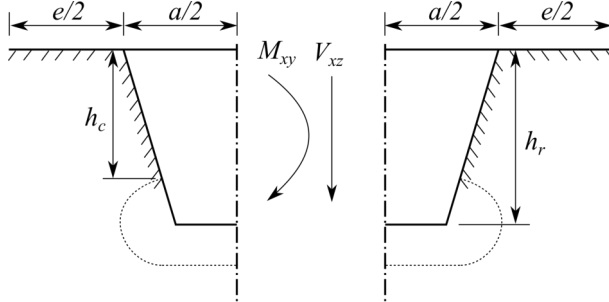


Figure 7.10: Local model at the rib-to-crossbeam joint

The average torsional moment at the central plane of the rib can be represented by a couple of forces with different directions. One force component is acting on the deck plate. The other force component is acting on the rib bottom. Meanwhile, part of the shear force is also assumed to be acting on the middle

end of the rib bottom. With respect to the combination of forces, the bending moment of the target point on the rib wall is calculated. Then, the distortional stress can be further determined. It should be noted that the acquired torsional stress is the nominal stress, which can be modified to the hot spot stress by using a proper stress concentration factor.

7.3 Case study

In this section, the nominal stress acquired from the analytical method and the hot spot stress acquired from FEA are compared to verify the analytical method. In practice, the nominal stress and the hot spot stress can be associated through the stress concentration factor (SCF). However, a reliable magnitude of the SCF is supposed to be determined through a regression analysis of numerous data. Due to the limitation of time, this procedure shall not be finished in this thesis. A case study based on two models from a previous chapter is presented to illustrate the feasibility of deriving a suitable SCF in future research. The models *CHR6* and *CHR8* used in chapter 6 are selected for the case study. Relevant dimensions of these two models can be found in Table 6.2.

For the convenience of using the analytical method, several Python classes are defined to pack the functions and relevant information. The workflow of using the Python classes is given in Figure 7.11. At first, two Python classes are defined to bundle all required information about the OSD and the applied load. The Python class `TrapezoidalSection` contains the geometrical information about the OSD, e.g. the dimensions of the rib and the crossbeam. The rigidity coefficients such as the flexural rigidity, the torsional rigidity and the shear rigidity are calculated based on the basic dimensions, which are also included in `TrapezoidalSection`. The Python class `LoadCase` includes the relevant information about the tire load, e.g. the magnitude of the tire load, the size of the load area and the load coordinates. Moreover, the functions for the 1-D Fourier analysis of load are also included in the `LoadCase`. Based on these two classes, the third Python class `AnalyticalModel` is defined to wrap the required functions of the analytical method as presented in the previous section. An instance of `AnalyticalModel` should be initiated from an instance of `TrapezoidalSection` and an instance of `LoadCase`. Therefore, it becomes very simple to consider different load cases for a specific OSD configuration or vice versa. Relevant manuscripts can be found in appendix A.7.

7.3.1 Trial calculation using the analytical method

In order to illustrate the analytical method, a trial calculation based on the model *CHR6* is first finished. As shown in Figure 7.12, the dimensions of the

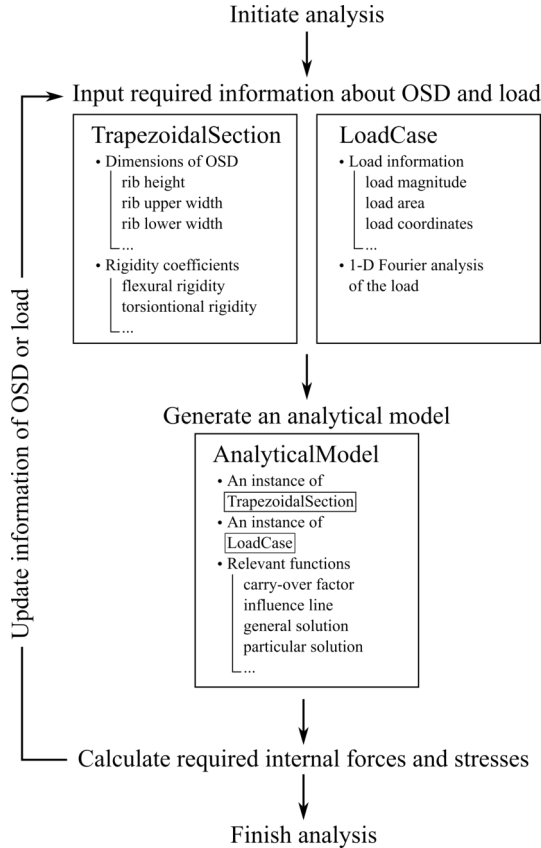


Figure 7.11: Workflow of the analytical method

OSD come from the model *CHR6*. Two spans of the OSD are named *plate 0* and *plate 1* respectively. A single tire load of 45 kN with the patch area of 270×320 mm is applied at the center of *plate 0*, as marked by red color.

Figure 7.13 to 7.17 show the calculation results in *plate 0* and Figure 7.18 to 7.22 present the calculation results in *plate 1* according to the analytical method. For each plate, the origin of the coordinate system used in these figures is at the corresponding location as shown in Figure 7.12, which means the figures of results and Figure 7.12 are presented from the same perspective angle. The description functions of these results are the summations of a series of trigonometric functions due to the Fourier analysis of the load. Two variables x and y represent the distances along the transversal (i.e. X axis) and longitudinal (i.e. Y axis) directions respectively.

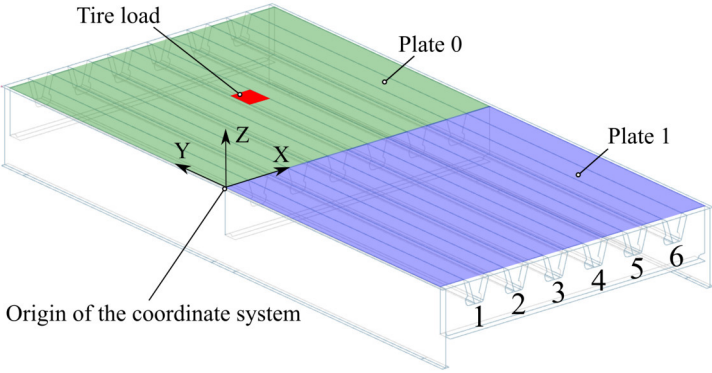


Figure 7.12: Calculation example of the analytical method

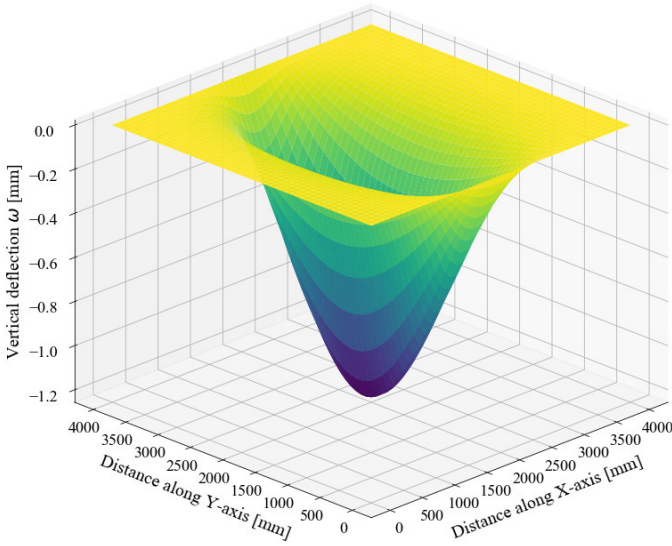


Figure 7.13: Vertical deflection ω in plate 0

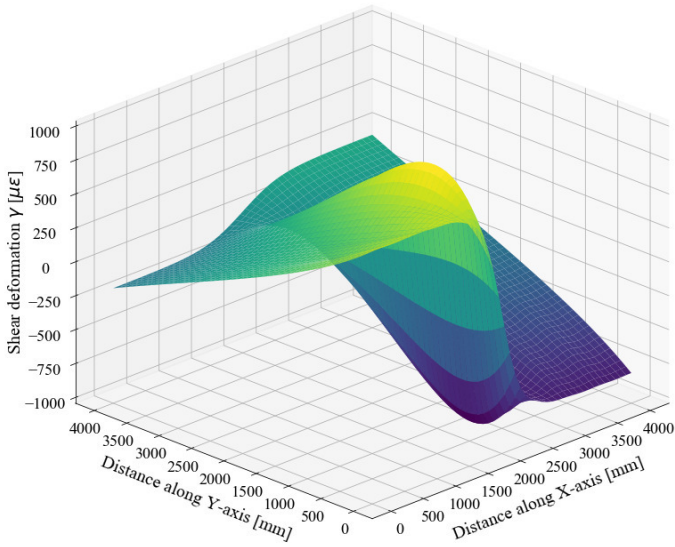


Figure 7.14: Shear deformation γ in plate 0

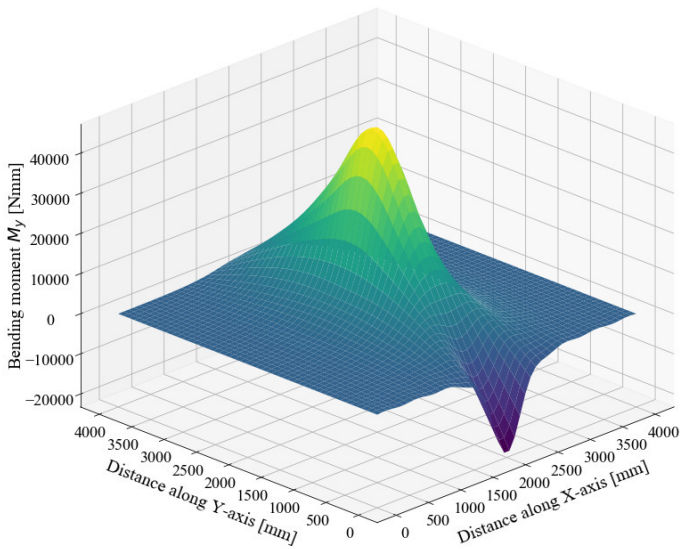


Figure 7.15: Bending moment M_y in plate 0

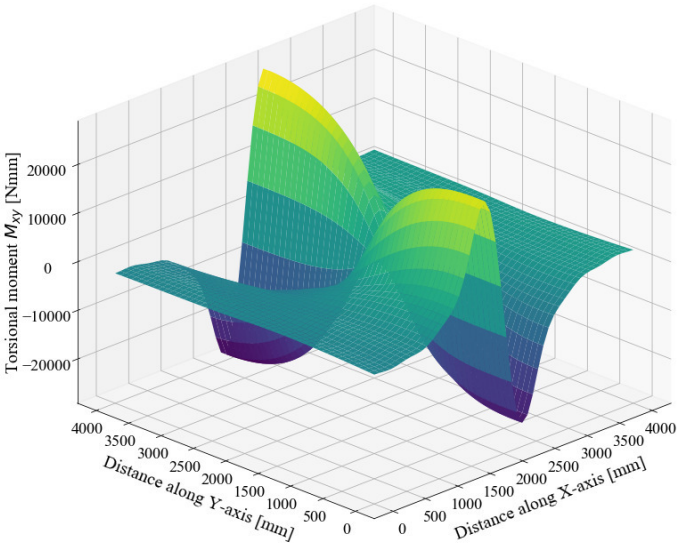


Figure 7.16: Torsional moment M_{xy} in plate 0

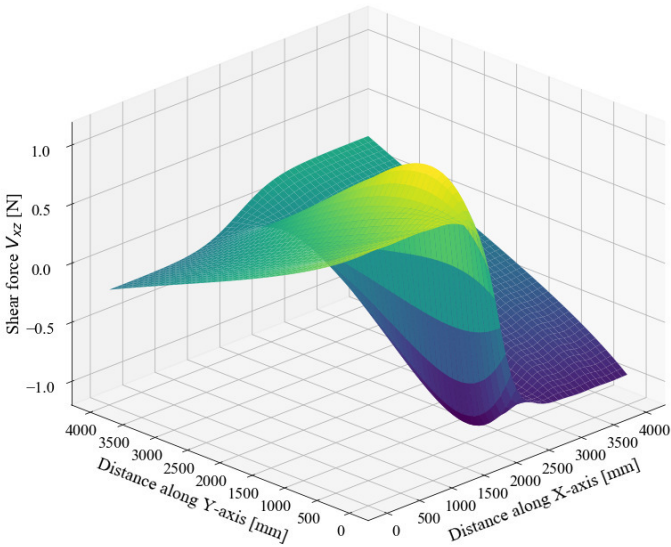


Figure 7.17: Shear force V_{xz} in plate 0

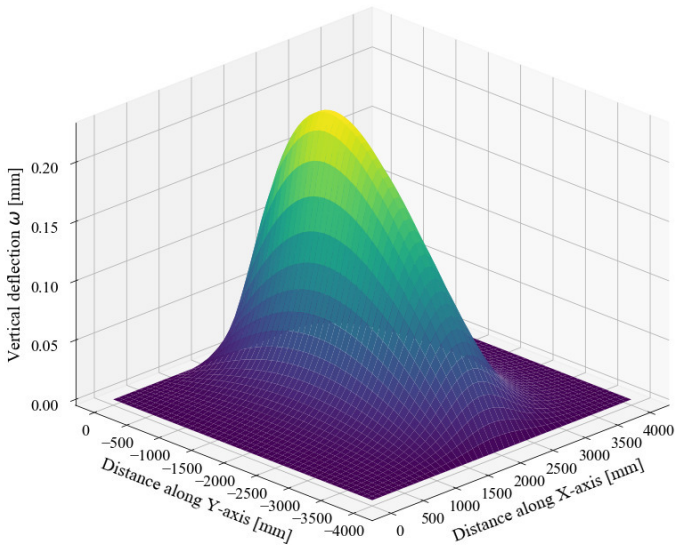


Figure 7.18: Vertical deflection ω in plate 1

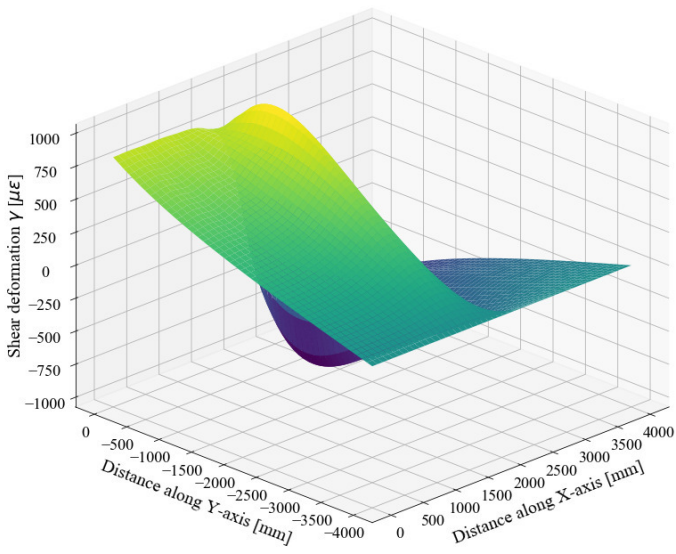


Figure 7.19: Shear deformation γ in plate 1

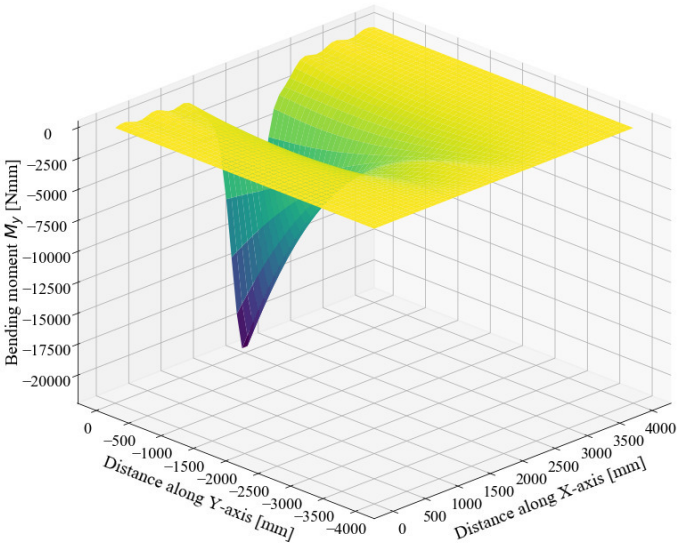


Figure 7.20: Bending moment M_y in plate 1

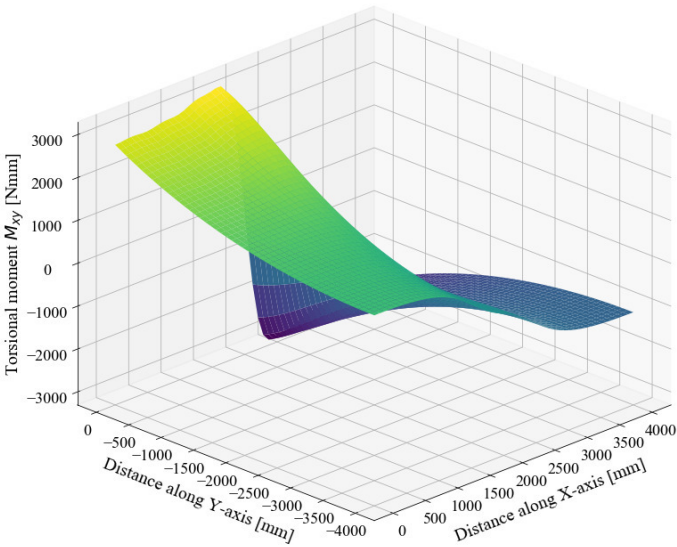


Figure 7.21: Torsional moment M_{xy} in plate 1

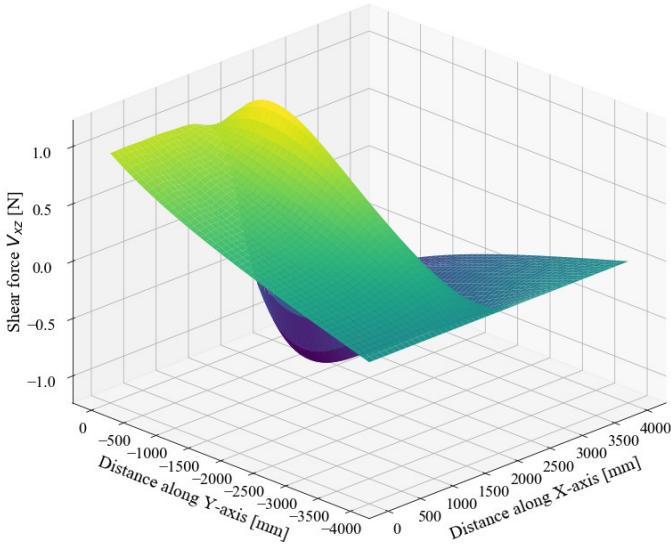


Figure 7.22: Shear force V_{xz} in plate 1

7.3.2 Comparison of results from analytical method and FEA

To compare the results from the analytical method and FEA, a moving single tire load is considered. Two load paths are defined as shown in Figure 7.23. The stress below the cope hole termination on the rib wall is considered for comparison. Therefore, the points $l1$ and $r1$ on rib 3 are selected as the reference points, the exact location of which points are also defined in Figure 6.19.

As for the results of FEA, the influence surfaces of reference points $l1$ and $r1$ from $CHR6$ and $CHR8$ are presented in Figure 7.24 and 7.25 respectively. The locations of load paths are also marked by dot lines. The influence surfaces are updated from the calculation results presented in section 6.4. Since the FEA results of two spans (i.e. *plate 0* and *plate 1*) are symmetrical to the X axis, only the results within one span (i.e. *plate 0*) are considered. It is assumed that the stress induced by the tire load is zero when the load is placed above the two crossbeams at the end. Therefore, the data points of the rest half span of the original influence surfaces could be acquired through interpolations.

As stated in the section of the trial calculation using the analytical method, the distribution of the required internal forces such as the torsional moment are described by a summations of a series of trigonometric functions. In order to

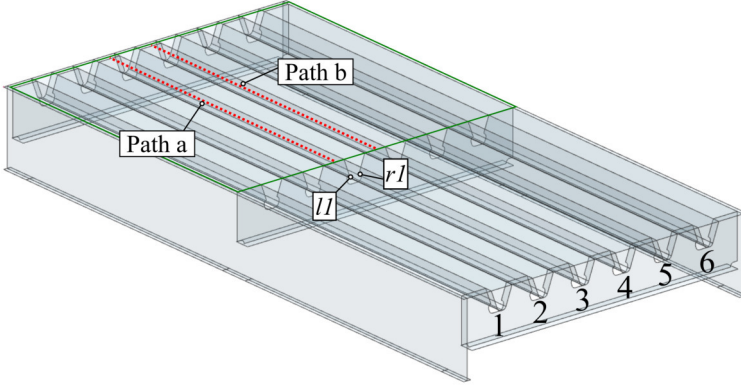


Figure 7.23: Load paths and reference pints for results comparison

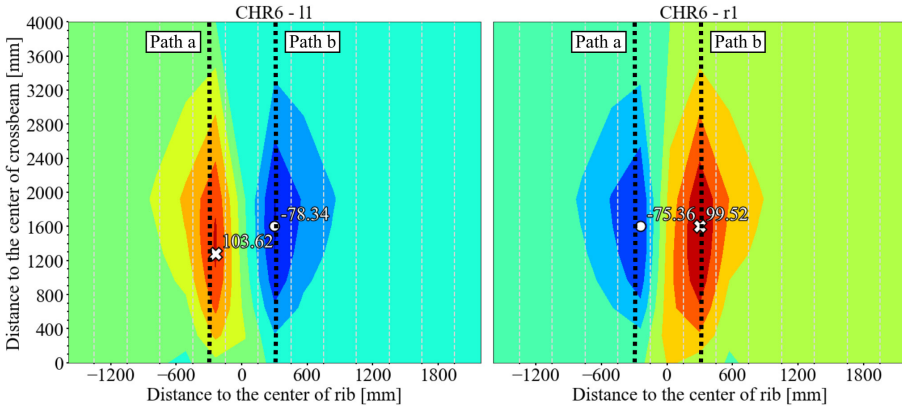


Figure 7.24: Influence surfaces of $l1$ and $r1$ from $CHR6$

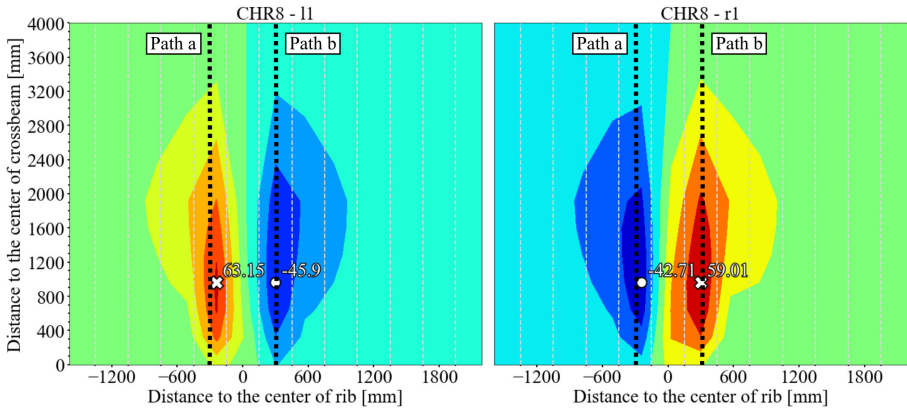


Figure 7.25: Influence surfaces of $l1$ and $r1$ from $CHR8$

get the internal forces over a specific rib at a specific cross-section, e.g. at the location of crossbeam, the variable y may first be substituted by the coordinate of the cross-section. Then, by integrating the acquired functions through the exact width of the specific rib, relevant internal forces can be determined.

In the original form of the local model, the calculated moment at the target point is positively correlated with the cope hole height. Hence, the calculated distortional stress would be also positively correlated with the cope hole height if the actual unconnected rib height is adopted for calculations in the local model. However as proven by the FEA results of the parametric analyses in section 3.4 and 5.6.1, it was found that the weld length of the rib-to-crossbeam joint (i.e. the height of the rib minus the height of the cope hole) is positively correlated with the distortional stress, which means the distortional stress should be negatively correlated with the cope hole height. To deal with this problem, the substituting unconnected rib height is defined as

$$h_{sub} = h_c / C_{reduction} \quad (7.64)$$

where the reduction coefficient $C_{reduction}$ is deducted from the FEA results and set to 2 in this case.

Figure 7.26 shows the comparison of stresses based on $CHR6$. Figure 7.27 displays the comparison of stresses based on $CHR8$. For $CHR6$, the nominal stresses from the analytical method are quite close to the hot spot stresses exported from FEA. For both two load paths, the absolute magnitude of stresses on the tension side is larger than the compression side. For $CHR8$, however, the differences between the analytical method and the FEA are relatively larger. It should be noted that the analytical method do not include the stress

concentration due to the weld. Therefore, a stress concentration factor K_{con} may be considered to transfer the nominal stresses to the hot spot stress. If only the maximum stresses are considered, for *CHR6*, the stress concentration factor of *path a* is 1.13, while the stress concentration factor of *path b* is 1.17. For *CHR8*, the stress concentration factor of *path a* is 1.78. Meanwhile, the stress concentration factor of *path b* is 1.84. Through the case study, the analytical method shows the potential to give a general and swift estimation for the design of the rib-to-crossbeam joint. However, the exact magnitude of the stress concentration factor K_{con} as well as the reduction coefficient $C_{reduction}$ require more calculations to be firmly decided.

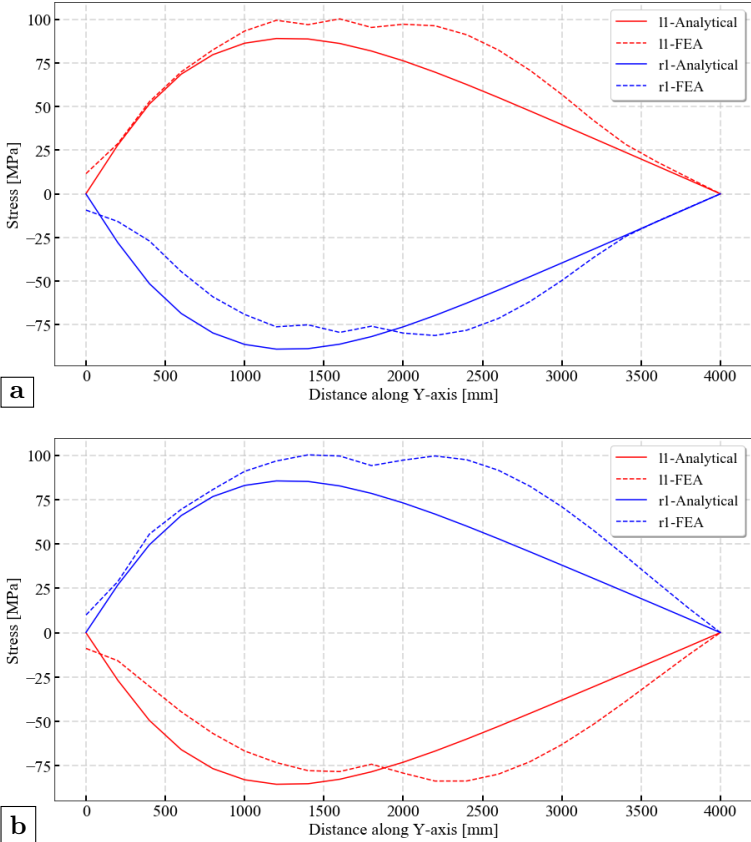


Figure 7.26: Calculation example based on CHR6: (a) path a; (b) path b

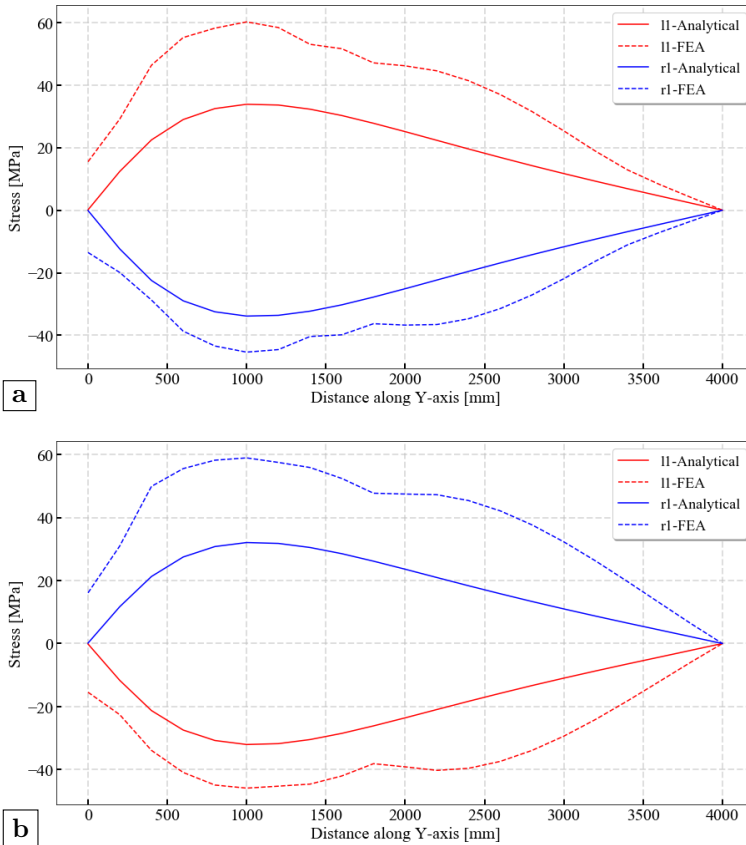


Figure 7.27: Calculation example based on CHR8: (a) path a; (b) path b

7.4 Conclusions

A simplified calculation method for quickly determining the dimensions of OSDs is developed in this chapter. The principle of this method is the same as the PE method. The actual OSD structure is substituted by an idealized orthotropic plate with different stiffness in two directions. However, only the bending moment is considered in the original PE method, which is not sufficient for the design of the rib-to-crossbeam joint. For the prevailing adopted rib-to-crossbeam joint with cope holes, the stress concentration at the lower weld induced by the distortional stresses is governing the fatigue performance of this joint as presented in previous chapters.

In order to calculate the distortional stress, the shear deformation is first

considered as an independent variable. Then, the system of partial differential equations are derived through the equilibrium relationships of the substituting plate. Three rigidity coefficients are needed in this method, namely the flexural rigidity coefficient, the torsional rigidity coefficient and the shear rigidity coefficient. The former two are calculated using the formulas given in the PE method. By performing a frame analysis, the formulas of the shear rigidity coefficient are achieved. The solutions of the system of the partial differential equations are acquired by using the symbolic computing software Maple. After getting the distributions of internal forces, a simple local model is proposed for calculating the nominal distortional stress at the target point, which is under the lower weld end on the rib wall. All of the formulas for the analytical method are packed together into three Python classes for the convenience of using.

The case study of the analytical method based on the models of the previous chapter is performed. The comparison of the results show that the hot spot stress could be achieved by considering a stress concentration factor on the basis of the nominal stress acquired by the analytical method. Nevertheless, the exact magnitude of the stress concentration factor requires more data to be finally determined.

8

Conclusions and future research

8.1 Conclusions

Up till now, the OSD is still the prior choice for long span bridges. However, the large amount of welds that are needed during the construction of OSDs would inevitably attract severe stress concentrations. Under repetitive loads, the locations that show high stress concentrations are easily prone to fatigue damage. Furthermore, the daily increased traffic intensity as well as overloaded vehicles makes the fatigue problem more and more prominent. Compared with the rib-to-deck joint, the rib-to-crossbeam joint does not attract enough attentions before, even though the fatigue cracks that appear at this joint normally stand for the largest portion of all fatigue cracks in OSDs.

Governing mode of fatigue cracking

During the evolution of OSDs, the rib-to-crossbeam joint has undergone the most drastic modifications. Numerous construction details of the rib-to-crossbeam joint appeared consecutively in the development history of OSD. At present, the most prevailing configuration is the closed rib of the trapezoidal cross-section that continuously passing through the crossbeam. An additional cope hole is set on the crossbeam under the bottom of the rib. As stated in the general introduction, four modes of fatigue cracking are possible for this type of rib-to-crossbeam joint. Two of them are in the rib wall and the other two are in the crossbeam as shown in Figure 2.3 and Figure 3.1.

In most cases, the fatigue mode of cracks initiating from the lower weld end and propagating longitudinally is the governing mode of fatigue cracking for the rib-to-crossbeam joint. This is also proven by the results of the fatigue life assessments based on influence surfaces, which indicates that the reference points below the lower weld end on rib wall have the shortest estimated fatigue life. Nonetheless, it should be noted that the influences of possible imperfections induced by the manufacturing process is not included here. For example, the possible notches along the free edge of cope holes due to the cutting procedure may cause higher stress concentrations that eventually lead to earlier fatigue cracks.

Structural hot spot stress (SHSS) method

Since the governing mode of fatigue cracking for the rib-to-crossbeam joint is tightly related to the rib distortions, corresponding stresses should be paid extra attentions when designing this joint. In current Eurocode, the design method for the rib-to-crossbeam joint is not clearly stated. On the one hand, the detail category corresponds to the stress induced by the rib distortion is still missing. Meanwhile, the governing mode of fatigue cracking is not included.

On the other hand, the recommended detail categories are still based on the nominal stress method. However, for the stress concentration induced by the rib distortion, a clear definition of the nominal stress is not possible. Due to these two reasons, the fatigue assessment method of OSDs, more specifically for the rib-to-crossbeam joint, has to be updated.

The SHSS method is more suitable to evaluate the fatigue performance of the rib-to-crossbeam joint. Compared with the other fatigue assessment method based on $S-N$ curves (i.e. the effective notch stress method), the hot spot stress is able to be measured directly which makes it possible to calibrate the calculation results through tests. Compared with the approaches based on fracture mechanics, the calculation procedure is much simpler and therefore easier to be popularized among bridge designers. Furthermore, an accurate definition of the initial crack length and shape is the prerequisite of generating realistic predictions for the fracture mechanics based approaches, which is still quite difficult as well as full of uncertainties.

Influence of design parameters

The distortional behavior of ribs would be influenced by the design parameters. According to the results of parametric analyses, the crossbeam spacing and the weld length of the rib-to-crossbeam joint are positively correlated with the distortional stress. The rib thickness has a negative correlation with the distortional stress. The influence of the rib distance on distortional stress depends on the relative size between the width of the load area and the parameter itself. If the load width of 270 mm from the fatigue load model of Eurocode is adopted, the distortional stress is generally negatively correlated with the rib spacing. The crossbeam height does not show an obvious influence on the distortional behavior. Through the parametric analyses, it is also found that the most unfavorable load position of the distortional stress is determined by the dimensions of ribs, whereas the other design parameters such as the rib distance, the crossbeam spacing, etc. do not show obvious effects. Since only the single tire load is considered in the parametric analyses, it should be noted that the influences of these design parameters on the magnitude of the distortional stress cannot be directly related to the estimated fatigue life. In another word, even though increasing the rib thickness would reduce the distortional stress of the target points on the rib wall, it is not guaranteed that the fatigue life of these target point would increase. This is because the influence of multi-axle should be included. Being different from the rib-to-deck joint, in which case the most unfavorable load position is when the tire load is directly above the specific joint, the maximum distortional stress of the rib-to-crossbeam joint is induced by the superposition of several load point on both sides of the target crossbeam. Therefore, the estimated fatigue life of target points on the rib

wall also depends on the most unfavorable load position and the lorry models adopted.

Through the tests on the full scale OSD specimen, two observations from the parametric analyses are verified. For the same rib dimensions of the OSD specimen, the most unfavorable load position with respect to the distortional stress is at about 1600 mm away from the investigated crossbeam rather than at the middle span. Meanwhile, the positive correlation between the weld length of the rib-to-crossbeam joint and the distortional stress is also verified. A longer weld length i.e. a lower termination position of the cope hole, would increase the stress induced by the rib distortion.

Conducting measurements

When measuring the hot spot stress, the first reference point is always at a distance of $0.4t$ away from the target weld toe. Given the normally used rib thickness of 6 mm, the distance between the strain gauge and the weld toe is merely 2.4 mm. For such a small distance, installing a single strain gauge at the exact location is rather difficult, especially for the rib-to-crossbeam joint. Due to the impediment of the crossbeam, the operating process is not easy if not possible. Using the strain gauge chain to measure the stress distribution of the vicinity to the target weld toe is therefore recommended for this joint. The required reference stress at reference points can be acquired through interpolations. However, since the construction of the rib-to-crossbeam joint is normally finished by a manual welding at present, the abnormal shape of the weld bead and the skew weld toe line may impose the difficulties of installing strain gauges.

It was observed that the raw data from the measurements show irregular results, especially for the strain gauge chains. One possible explanation for this phenomenon is that there exists an interfering signal. The interfering signal may be induced by factors other than the structural deformation. The influence of the possible interfering signal is more obvious on the strain gauge chains than the single strain gauges, which also means its influence is more obvious in the zone of stress concentrations than the normal locations. The ultimate reason for the existence of the interfering signal is still unclear. The assumption that the interfering signal is linear dependent about time is finally adopted for processing the raw data from measurements. It is concluded that this strategy is able to reduce the measurement errors induced by the possible interfering signal.

Finite element modeling (FEM)

The corresponding numerical simulations of the measurements were performed using the solid element and the shell element respectively. In general, similar

trends of stresses as the measurements are acquired. The calculation results of strain gauges that are far away from the zone of stress concentrations (i.e. the vicinity of weld toe) fit well with the measurement results. However, obviously divergent results appeared on strain gauges close to the weld toe (i.e. strain gauge chains). It is concluded that the deviation of strain gauges' locations and the deviation of load positions are the main causes that lead to the difference between measurement results and calculations results.

When performing numerical simulations using the solid elements, the actual weld shape is replaced by an idealized weld shape i.e. a triangular cross-section. Under a certain weld throat thickness, the concave weld profile would tend to decrease the calculated stress meanwhile the convex weld profile would tend to increase the calculated stress. In contrast, the influence of different throat thicknesses is limited under a certain weld profile. Unfortunately, the irregular weld shape in reality cannot be perfectly modeled in FEM.

When performing numerical simulations using the shell element, the actual weld bead is not modeled. However, the influence of weld can also be included by considering the virtual location of weld toes. The distance from the weld toe to the reference point could be counted either from the virtual location of the weld toe or from the intersection point of the cope hole termination.

In current Eurocode, the FEM based design method of OSDs is not clearly regulated. The key information of performing simulations e.g. the element selection, the weld modeling, etc. is still missing. For the simulation of the rib-to-crossbeam joint, the shell element model is preferred over the solid element model. Firstly, the influence of the actual weld shape is hard to be included. Secondly, the computation time of the solid model is much longer than the shell element model, which can up to four times in this case, yet the calculation results of the shell model and the solid model can be quite close. According to the comparison of different models versus measurement results, the shell element model and the solid element model would generate close results under such conditions:

- the weld is modeled in the solid element model while omitted in the shell element model;
- the distance from the weld toe to the reference point on the rib wall should be calculated from the intersection point of the cope hole termination.

Fatigue life assessment

The fatigue life assessment based on the theory of the damage accumulation is mentioned in the annex of Eurocode 3 *EN 1993-1-9*. The annex is defined as *normative*, and the general procedure of the fatigue life assessment is introduced.

Unfortunately, the code itself does not offer any information on how to actually realize the whole procedure. To the best of the author's knowledge, there does not exist a commercial software that offers such function. Therefore, the framework of fatigue life assessment procedure is proposed and programmed in Python. It is concluded that the fatigue life assessment based on either the influence lines or the influence surfaces is applicable, but the assessment based on influence surfaces is preferable. The proposed procedure of the fatigue life assessment is as follows.

- Step 1: define the loading sequence. In this dissertation, the Fatigue Load Model 4 from Eurocode 1 is adopted. The programmed Python class of the load model can effectively transfer the required information of the defined lorries, e.g. the lorry name, the corresponding axle spacing and the equivalent axle load, etc. Meanwhile, it is very simple to expand the class to include other fatigue load models or to accommodate actual traffic data.
- Step 2: prepare the required influence lines or influence surfaces of the target detail. In Siemens NX, this can be achieved by defining multiple sub-loadcases. When getting the influence surfaces, the width of the considered influence surface may not be too wide to limit the calculation time. For the rib-to-crossbeam joint, the width of the influence surfaces may be limited to the width of two ribs on each side.
- Step 3: get the stress history through interpolations. In this step, it is assumed that the vehicle will always drive in a line. A statistical distribution of the transverse location of the center line of vehicle is given in Eurocode. For the assessment based on influence surfaces, a normal distribution may be fitted to represent the distribution of the vehicle. For the assessment based on influence lines, five influence lines with the interval distance of 0.1 m may be considered.
- Step 4: count the cycles. It is concluded that the algorithm based on the range-pair counting method works well.
- Step 5: derive the estimated fatigue life. This step is accomplished based on the stress range spectra and the corresponding detail categories.

Optimizing suggestion

In retrospect, the tight-fitted rib-to-crossbeam joint appeared earlier in the development history of OSD than those with cope holes. However, two main problems impeded the application of this tight-fitted form. On the one hand, the fabrication accuracy of steel plates was quite low, which increased the assembly difficulties. On the other hand, the deck plate thickness of early

OSDs was usually much thinner than those used nowadays. This led to larger deformations under concentrated tire loads which caused high stresses at the bottom of the rib. Therefore, tight-fitted joints were gradually replaced by those with cope holes. Nevertheless, the fabrication accuracy has been improved with the help of modern computer numerically controlled (CNC) equipment. The commonly-used thickness of deck plates is also much thicker than before. These developments may encourage engineers to reconsider the applications of tight-fitted rib-to-crossbeam joints.

Through the parametric analyses, it is concluded that the most critical position for the rib-to-crossbeam joint without cope holes is at the curvature on the rib side. Furthermore, the closed rib of the trapezoidal section with a larger thickness and a larger bottom radius is suggested. The larger thickness of the rib could reduce the maximum stress range on the rib side meanwhile changing the stress distribution on the crossbeam side. The radius of rib has a local influence on the points at the curvature. The larger radius could effectively lower the maximum stress range. Meanwhile, the thickness of the crossbeam may be slightly decreased when adopting the tight-fitted rib-to-crossbeam joint. The thickness of the crossbeam and the maximum stress range on the crossbeam side have an obvious negative correlation. A more flexible crossbeam would help to reduce the maximum stress range at the bottom of ribs on the rib side.

According to the results of the fatigue life assessments, the multi-axle effect has to be considered. The fatigue performance of the rib-to-crossbeam joint is sensitive to not only the tire load but also the spacing between axles. Based on current Eurocode, a normal distribution of the vehicles is fitted to include the influence of different transverse position. For the rib-to-crossbeam joint with cope holes, it is preferred to place the central line of the load distribution closer to the center of the rib. In contrast, for the tight-fitted rib-to-crossbeam joint, it is preferred to place the central line of the load distribution closer to the center between two ribs. However, the load distribution mainly affects the controlling points on the rib side for both types of joints. Neither the rib dimensions nor the load distribution has an obvious improvement on the fatigue-prone details along the free edge of the cope hole. Overall, considering less possible fatigue-prone locations and reduced fabrication costs, the tight-fitted rib-to-crossbeam joint is suggested.

Simplified calculation method

A simplified calculation method for quick determining the dimensions of OSDs is proposed. The principle of the developed method is the same as the well-known Pelikan-Esslinger(PE) method. The actual OSD structure is substituted by an idealized orthotropic plate with different stiffness in two directions. However, only the bending moment is considered in the original PE method,

which is not sufficient for the design of the rib-to-crossbeam joint. In order to calculate the distortional stresses, the shear deformation is first considered as an independent variable. Then, the system of partial differential equations are derived through the equilibrium relationships of the substituting plate. Three rigidity coefficients are needed in this method, namely the flexural rigidity coefficient, the torsional rigidity coefficient and the shear rigidity coefficient. The former two are calculated using the formulas given in the PE method. By performing a frame analysis, the formulas of the shear rigidity coefficient are achieved. The solutions of the system of the partial differential equations are acquired by using the symbolic computing software Maple. After getting the distributions of internal forces, a simple local model is proposed for calculating the nominal distortional stress at the target point, which is under the lower weld end on the rib wall. All of the formulas for the analytical method are packed into three Python classes for the convenience of using. According to the results of the case study, it shows that the hot spot stress can be achieved by considering a stress concentration factor on the basis of the nominal stress acquired through the analytical method.

8.2 Future research

Experimental verification

For the rib-to-crossbeam joint in OSDs, the continuous closed rib with an additional cope hole is the most prevailing design at present. It is found that the cracks on the rib wall close to the lower end induced by the rib distortion is governing the fatigue performance at this joint. To deal with the rib distortion and to reduce the fabrication cost, the possibility of canceling the cope hole is discussed in this dissertation. Through the fatigue life assessments based on influence surfaces, the overall fatigue performance of the tight-fitted rib-to-crossbeam joint is considered better than the rib-to-crossbeam joint with cope hole. Meanwhile, it is also concluded that the fatigue performance of the rib-to-crossbeam joint is sensitive to the transverse location of the distribution of vehicles. However, a number of tests are still required to verify the acquired conclusions.

Firstly, correct influence surfaces are the prerequisite for a reliable fatigue life assessment. Static load tests on full-scale OSD specimens may be finished to verify the influence surfaces. As discussed in this dissertation, the measurements of SHSS are very sensitive to the exact location of strain gauges. For the tight-fitted rib-to-crossbeam joint, the automatic welding may be adopted to improve the quality of welds. For the rib-to-crossbeam joint with cope holes, the weld on rib wall may be ground carefully to generate a smooth weld toe line.

Secondly, the fatigue performance of the tight-fitted rib-to-crossbeam joint may be verified by fatigue tests. It should be noted that the stress range of the rib-to-crossbeam joint induced by a vehicle is not only related to the magnitude of the tire loads but also related to the distance between the tire axles. Hence, the effect of multi-axles has to be included. Since this is rather difficult to achieve in a laboratory environment, the long term monitoring of a real bridge seems to be a better choice. Meanwhile, the influence of the residual stress on fatigue resistance may also be an interesting topic, especially when new fabrication methods are introduced.

Fatigue design method

For the design purpose, the fatigue life assessment procedure based influence surfaces of SHSS presented in this dissertation is easy to understand and simple to use. Even though it only aims at the rib-to-crossbeam joint, the assessment procedure can be expanded to other fatigue-prone details of OSDs. Thanks to the open-source programming language Python, the program can be used anywhere without limitations. Nevertheless, future research may focus on following aspects to further improve the performance of the program.

Firstly, the calculation speed of the program can be further improved. At present, the simulation time can be as long as several days depending on the total number of investigated points and the assumed annual traffic volume. One of the reasons is that the Python manuscript only runs on one core by default. The advantage of common processors with multiple cores is not utilized. The algorithm of parallel computation may be incorporated or the current code can be optimized to accelerate the simulation speed.

Secondly, the assumptions of the simulation procedure may be further investigated. For instance, it is assumed in the program that the lorry will always drive along a straight line. However, the driving habit of human in the real world may not be so rigid. The horizontal deviation of the driving route may influence the stress history and distort the estimated fatigue life eventually since the simulated loops are quite large. The program can be expanded to incorporate the influence of the horizontal deviation when driving. Other assumptions, e.g. the normal distribution of vehicles and the representative lorry models, may also be studied to better represent the actual traffic information.

Simplified calculation method

The proposed simplified calculation method is able to give a general estimation of the stress concentration induced by the rib distortion when designing the rib-to-crossbeam joint with cope holes. Even though the formulas of the analytical

method are not extremely concise, they can be packed into the Python classes. When using these Python classes, the calculation procedure is invisible to users. Therefore, utilizing the analytical method is still easy. Moreover, the calculation speed of the analytical method is much faster than the FEA, which means the analytical method can offer a quick determination of the design parameters. Nevertheless, future research is required to improve the precision and to expand the applicable range.

Firstly, the precision of the simplified calculation method relies on a reliable stress concentration factor. A larger data set of the simplified calculation method and the corresponding FEM may be generated. Through the regression analysis of the data set, the stress concentration factor with a wider confidence level may be proposed.

Secondly, a local model that is able to evaluate the critical points for the tight-fitted rib-to-crossbeam joint may be developed. Though the fatigue life assessments, it is concluded that the most critical location for the tight-fitted rib-to-crossbeam joint is on the rib side at the lower curvature. The stress concentration at this location may be associated with the longitudinal bending moment. Since the distribution of the bending moment can also be acquired through the simplified calculation method, a more advanced local model may help to expand the applicable range of this method.

A

Manuscripts and templates

A.1 Process measurement data

```
import pandas as pd

def DataProcessHBM(input_filename, start_time, config_rows=47,
                  data_header=1, sheet='Sheet1'):
    """
    This function is used to pre-process measurement data. The
    output file is saved with the original name by default.

    input_filename
        str. Path of the measurement result file. The file should be
        exported by CatmanEasy with filetype of Excel2007 from HBM
        measurement system.
    start_time
        int. Example: 20181109151314, which means year 2018 month 09
        day 11 hour 15 minute 13 second 14.
    config_rows
        int. Rows with configuration information in the result file.
        Default is 47.
    data_header
        int. Row number used as column names. Default is 1.
    sheet
        str. Name of the sheet. Default is 'Sheet1'.
    """
    # read data from excel file
    df = pd.read_excel(input_filename, sheet_name=sheet,
                      header=data_header)
    # remove first 47 rows at the beginning, which contain information
    # of measurement system settings
    df = df.drop(index=np.arange(config_rows), axis=0)
    # edit labels of columns, which are names of strain gauges, remove
    # blank and symbols
    df.columns = df.columns.str.replace(" ", "")
    df.columns = df.columns.str.replace("-", "_")
    # set the time index column
    time_index =
    df.columns.values[0]
    df.rename(columns={time_index[0]: "Time_index"}, inplace=True)
    df = df.set_index(keys='Time_index')
    # finish time index using datetime
    time_origin = pd.Timestamp(str(start_time))
    df.index = pd.to_datetime(df.index, origin=time_origin, unit='s')
    # convert data type into number
    df = df.apply(pd.to_numeric)
    # write .csv file
    df.to_csv(f'{input_filename}.csv')

    return df
```

A.2 Generate nodes at specific coordinates

A.2.1 Required template of NX Open

```

import NXOpen
import NXOpen.CAE

def create_point(col_x, col_y, col_z):
    """
    This function creates a point in the NX space opened on
    the passed coordinates.

    col_x, col_y, col_z
        int or float. Coordinate (x, y, z) of the specific point.
    """
    theSession = NXOpen.Session.GetSession()
    workFemPart = theSession.Parts.BaseWork
    displayFemPart = theSession.Parts.BaseDisplay

    unit1 = workFemPart.UnitCollection.FindObject("MilliMeter")

    expression1 =
    workFemPart.Expressions.CreateSystemExpressionWithUnits(str(col_x),
    unit1)
    scalar1 = workFemPart.Scalars.CreateScalarExpression(expression1,
    NXOpen.Scalar.DimensionalityType.NotSet,
    NXOpen.SmartObject.UpdateOption.AfterModeling)

    expression2 =
    workFemPart.Expressions.CreateSystemExpressionWithUnits(str(col_y),
    unit1)
    scalar2 = workFemPart.Scalars.CreateScalarExpression(expression2,
    NXOpen.Scalar.DimensionalityType.NotSet,
    NXOpen.SmartObject.UpdateOption.AfterModeling)

    expression3 =
    workFemPart.Expressions.CreateSystemExpressionWithUnits(str(col_z),
    unit1)
    scalar3 = workFemPart.Scalars.CreateScalarExpression(expression3,
    NXOpen.Scalar.DimensionalityType.NotSet,
    NXOpen.SmartObject.UpdateOption.AfterModeling)

    point1 = workFemPart.Points.CreatePoint(scalar1, scalar2, scalar3,
    NXOpen.SmartObject.UpdateOption.AfterModeling)

    point1.SetVisibility(NXOpen.SmartObject.VisibilityOption.Visible)

if __name__ == '__main__':
    # invoking the defined function to create point, here is an
    # example of adding point at coordinate (4000, 1200, -300)
    create_point(4000, 1200, -300)

```

A.2.2 Coordinate transformation for large amount of points

```

import numpy as np
import pandas as pd
import math

def GeneratePointNX(input_filename, post_fix='new',
                    template_file='CreatPoint.py', data_header=1, sheet='Sheet1'):
    """
    This function is used to generate a Python-based NX open file,
    which is able to generate required points at specific coordinates.

    Two files will be generated. One is the NX open file for NX. The
    other one is an excel file with global coordinates.

    input_filename
        str. Path of the file contains coordinates of points. The
        input file should be an excel file contains predefined
        information. An example is available under the same folder.
    post_fix
        str. Add a postfix to the output file. Default is 'new'.
    template_file
        str. Path of the template for NX open file. An example is
        available under the same folder.
    data_header
        int. Row number used as column names. Default is 1.
    sheet
        str. Name of the sheet. Default is 'Sheet1'.
    """
    # read input file
    df = pd.read_excel(input_filename, sheet_name=sheet,
                      header=data_header)

    # calculate global coordinates of points
    for i in range(1, len(df)+1):
        origin_local = np.array([df['locoriginx'][i],
                                df['locoriginy'][i], df['locoriginz'][i]])
        basis_lx = np.array([df['basislx1'][i], df['basislx2'][i],
                              df['basislx3'][i]])
        basis_ly = np.array([df['basisly1'][i], df['basisly2'][i],
                              df['basisly3'][i]])
        basis_lz = np.array([df['basislz1'][i], df['basislz2'][i],
                              df['basislz3'][i]])
        point_local = np.array([df['locx'][i], df['locy'][i],
                                df['locz'][i], 1])
        global_point = Local2Global(origin_local, basis_lx, basis_ly,
                                    basis_lz, point_local)
        df.at[i, 'glox'] = global_point[0]
        df.at[i, 'gloy'] = global_point[1]
        df.at[i, 'gloz'] = global_point[2]
    # read the template file of NX open
    with open(template_file, 'r') as file:

```

```

        content_py = file.read()
    # write the NX open file for generating points
    with open('CreatPoint_{}.py'.format(post_fix), 'w') as file:
        file.write(content_py)
        for index, rows in df.iterrows():
            file.write('    creat_point({0:0.3f}, {1:0.3f},\
                {2:0.3f})\n'.format(rows['glox'], rows['gloy'],
                rows['gloz']))
    # update the inputfile with global coordinates and output a new
    # one at the same location
    df.to_excel('CoordinateOutput_{}.xlsx'.format(post_fix))

    return df

def Local2Global(origin_local, basis_lx, basis_ly, basis_lz,
    point_local):
    """
    This functino is used to transfer a point from local coordinate
    system to global coordinate system.

    origin_local
        array. Origin of the local coordinate system under the global
        coordinate system.
    basis_lx
        array. Vector of x-axis of local coordinate system.
    basis_ly
        array. Vector of y-axis of local coordinate system.
    basis_lz
        array. Vector of z-axis of local coordinate system.
    point_local
        array. Coordinate of target point under the local coordinate
        system.
    """
    # set the base vector of global coordinate, here is an example
    basis_x = np.array([1, 0, 0])
    basis_y = np.array([0, 1, 0])
    basis_z = np.array([0, 0, 1])
    origin_global = np.array([0, 0, 0])
    # calculate transformation matrix
    trans_vec = origin_local - origin_global
    trans_vec = np.append(trans_vec, 1)
    trans_matrix = np.zeros(12)
    trans_matrix[0] = np.dot(basis_x, basis_lx)
    trans_matrix[1] = np.dot(basis_x, basis_ly)
    trans_matrix[2] = np.dot(basis_x, basis_lz)
    trans_matrix[3] = np.dot(basis_y, basis_lx)
    trans_matrix[4] = np.dot(basis_y, basis_ly)
    trans_matrix[5] = np.dot(basis_y, basis_lz)
    trans_matrix[6] = np.dot(basis_z, basis_lx)
    trans_matrix[7] = np.dot(basis_z, basis_ly)
    trans_matrix[8] = np.dot(basis_z, basis_lz)
    trans_matrix = trans_matrix.reshape([4,3])
    trans_matrix = np.column_stack([trans_matrix, trans_vec.T])

```

```
# calculate point in global coordinate
point_global = np.dot(trans_matrix, point_local.T)
```

A.3 Export results using NX Open

```
import math
import NXOpen
import NXOpen.CAE
import NXOpen.UserDefinedObjects

def main(load_case, node_number):
    """
    This NX Open file is used to automatically export results for a
    number of load cases. It should be noted that the simulation file
    name, the number of load cases and the number of nodes must be
    updated accordingly when using.
    """
    theSession = NXOpen.Session.GetSession()
    workSimPart = theSession.Parts.BaseWork
    displaySimPart = theSession.Parts.BaseDisplay
    resultParameters1 =
    theSession.ResultManager.CreateResultParameters()
    resultParameters1.SetDBScaling(0)
    signalProcessingDBSettings1 = resultParameters1.GetDbSettings()
    # display results
    resultManager1 = theSession.ResultManager
    # the Filename should adapt to the target file name
    solutionResult1 =
    resultManager1.FindObject("SolutionResult[Filename.sim_Solution\
1]")
    loadcase1 =
    solutionResult1.Find("Loadcase[{}].format(load_case))
    iteration1 = loadcase1.Find("Iteration[1]")
    resultType1 =
    iteration1.Find("ResultType[[Stress][Element-Nodal]]")
    resultParameters1.SetGenericResultType(resultType1)
    resultParameters1.SetResultBeamSection(NXOpen.CAE.Result.Section.
        ValueOf(-1))
    resultParameters1.SetResultShellSection(NXOpen.CAE.Result.Section.
        Top)
    resultParameters1.SetResultComponent(NXOpen.CAE.Result.Component.
        MaximumPrincipal)
    resultParameters1.SetCoordinateSystem(NXOpen.CAE.Result.
        CoordinateSystem.
        AbsoluteRectangular)
    resultParameters1.SetSelectedCoordinateSystem(NXOpen.CAE.Result.
        CoordinateSystemSource.NotSet,
        -1)
    resultParameters1.SetRotationAxisOfAbsoluteCylindricalCSYS(NXOpen.CAE
        .Post.AxisymmetricAxis.X)
    resultParameters1.SetBeamResultsInLocalCoordinateSystem(True)
```

```

resultParameters1.MakeElementResult(False)
resultParameters1.SetElementValueCriterion(NXOpen.CAE.Result.
                                         ElementValueCriterion.Average)

average1 = NXOpen.CAE.Result.Averaging()
average1.DoAveraging = False
average1.AverageAcrossPropertyIds = True
average1.AverageAcrossMaterialIds = True
average1.AverageAcrossElementTypes = True
average1.AverageAcrossFeatangle = True
average1.AverageAcrossAnglevalue = 45.0
average1.IncludeInternalElementContributions = True
resultParameters1.SetAveragingCriteria(average1)
resultParameters1.SetComputationType(NXOpen.CAE.Result.
                                       ComputationType.NotSet)

resultParameters1.SetComputeOnVisible(False)
resultParameters1.SetComplexCriterion(NXOpen.CAE.Result.Complex.
                                       Amplitude)

resultParameters1.SetPhaseAngle(0.0)
resultParameters1.SetSectionPlyLayer(0, 0, 1)
resultParameters1.SetScale(1.0)
unit1 = workSimPart.UnitCollection.FindObject("MilliMeter")
resultParameters1.SetUnit(unit1)
resultParameters1.SetAbsoluteValue(False)
resultParameters1.SetTensorComponentAbsoluteValue(NXOpen.CAE.Result.
                                                    TensorDerivedAbsolute.
                                                    DerivedComponent)

resultParameters1.SetCalculateBeamStrResults(False)
resultParameters1.SetBeamFilletlets(True)
resultParameters1.SetBeamFilletRadius(0.5)
resultParameters1.DisplayMidnodeValue(True)
resultParameters1.SetIsReferenceNode(False)
resultParameters1.SetReferenceNodeLabel(0)
cyclicSymmetricParameters1 =
resultParameters1.GetCyclicSymmetricParameters()
cyclicSymmetricParameters1.ResultOption =
NXOpen.CAE.CyclicSymmetricParameters.GetResult.OnOriginalModel
cyclicSymmetricParameters1.OriginalResultOption =
NXOpen.CAE.CyclicSymmetricParameters.OriginalResult.BySector
cyclicSymmetricParameters1.SectCriteria =
NXOpen.CAE.CyclicSymmetricParameters.SectorCriteria.Index
cyclicSymmetricParameters1.SectorValue =
NXOpen.CAE.CyclicSymmetricParameters.Value.Maximum
cyclicSymmetricParameters1.EnvValue =
NXOpen.CAE.CyclicSymmetricParameters.EnvelopeValue.Average
cyclicSymmetricParameters1.SectorIndex = 1
sectors1 = []
cyclicSymmetricParameters1.SetSectorIndices(sectors1)
axisymmetricParameters1 =
resultParameters1.GetAxisymmetricParameters()
axisymmetricParameters1.ResultOption =
NXOpen.CAE.AxisymmetricParameters.GetResult.OnOriginalModel
axisymmetricParameters1.RotationAxis =
NXOpen.CAE.AxisymmetricParameters.AxisOfRotation.XAxis

```

```
axisymmetricParameters1.AxiOptions =
NXOpen.CAE.AxisymmetricParameters.Options.AtRevolveAngle
axisymmetricParameters1.EnvelopeVal =
NXOpen.CAE.AxisymmetricParameters.EnvVal.Average
axisymmetricParameters1.RevolveAngle = 0.0
axisymmetricParameters1.StartRevolveAngle = 0.0
axisymmetricParameters1.EndRevolveAngle = 360.0
axisymmetricParameters1.NumberOfSections = 40
postviewId1 = theSession.Post.CreatePostviewForResult(0,
solutionResult1, False, resultParameters1)
theSession.ResultManager.DeleteResultParameters(resultParameters1)

# get averaged nodal results
result1, resultParameters2 =
theSession.Post.GetResultForPostview(postviewId1)
signalProcessingDBSettings2 = resultParameters2.GetDbSettings()
average2 = NXOpen.CAE.Result.Averaging()
average2.DoAveraging = True
average2.AverageAcrossPropertyIds = True
average2.AverageAcrossMaterialIds = True
average2.AverageAcrossElementTypes = True
average2.AverageAcrossFeatangle = True
average2.AverageAcrossAngleValue = 45.0
average2.IncludeInternalElementContributions = True
resultParameters2.SetAveragingCriteria(average2)
theSession.Post.PostviewSetResult(postviewId1, resultParameters2)
colorbar1 = NXOpen.CAE.Post.Colorbar()
colorbar1.Spectrum = NXOpen.CAE.Post.Spectrum.Structural
colorbar1.InvertSpectrum = False
colorbar1.Scale = NXOpen.CAE.Post.Scale.Automatic
colorbar1.AutomaticLevel = False
colorbar1.NumberOfLevels = 12
colorbar1.Threshold = NXOpen.CAE.Post.Threshold.Displayed
colorbar1.ThresholdMinimum = -500
colorbar1.ThresholdMaximum = 500
colorbar1.ShowOverflowAbove = False
colorbar1.ShowOverflowBelow = False
colorbar1.OverflowAboveColor = workSimPart.Colors.Find("Silver\
Gray")
colorbar1.OverflowBelowColor = workSimPart.Colors.Find("Dark\
Gray")
colorbar1.Position = NXOpen.CAE.Post.Position.ValueOf(32757)
colorbar1.Overflow = NXOpen.CAE.Post.LimitDisplay.NotSet
colorbar1.Underflow = NXOpen.CAE.Post.LimitDisplay.NotSet
rangeValue1 = []
rangeColors1 = []
theSession.Post.PostviewSetColorbar(postviewId1, colorbar1, False,
rangeValue1, rangeColors1)
theSession.Post.PostviewSetShowHeader(postviewId1,
NXOpen.CAE.Post.ShowHeader.Automatic)
text1 = NXOpen.CAE.Post.Text()
text1.Font = 1420592
text1.Size = 1
```

```

text1.Color = workSimPart.Colors.Find("Deep Steel")
text1.Bold = 32767
theSession.Post.PostviewSetText(postviewId1, text1)
theSession.Post.PostviewSetFormat(postviewId1,
NXOpen.CAE.Post.Format.Auto, 4)
theSession.Post.PostviewSetFontSize(postviewId1, True, 1.0)
theSession.Post.PostviewUpdate(postviewId1)
theSession.ResultManager.DeleteResultParameters(resultParameters2)

# read nodal results and export results to files
# assign result access
resultaccess1 = resultManager1.CreateResultAccess(postviewId1)
# get components, return a tuple consisting of (description,
# components), description is a list of str
result_component = resultaccess1.AskResultComponents()
# generate file title
file_title1 = ['Node ID', 'X Coord', 'Y Coord', 'Z Coord']
file_title2 = [item for item in result_component[0]]
file_title = file_title1 + file_title2
# prepare to save data
node_data_all = []
for node in range(1, node_number+1):
    node_data = []
    node_data.append(node)
    coord_component = result1.AskNodeCoordinates([node])
    coord_list = [coord_component[0].X, coord_component[0].Y,
    coord_component[0].Z]
    stress_list = resultaccess1.AskNodalResultAllComponents(node)
    node_data = node_data + coord_list + stress_list
    node_data_all.append(node_data)
with open('{}{}.csv'.format(load_case, 'w') as file:
    file.write(','.join(item for item in file_title) + '\n')
    for node in range(0, node_number):
        file.write(','.join(str(item) for item in
        node_data_all[node]) + '\n')
# delete all result access to free up system resource
theSession.ResultManager.DeleteResultAccess(resultaccess1)

if __name__ == '__main__':
    # here is the example of 195 load cases
    for loadcases in range(1, 196):
        # here is the example of 576 nodes
        main(load_case=loadcases, node_number=576)

```

A.4 Class FatigueLoadModel4

```

class FatigueLoadModel4(object):
    """
    This is the class to bundle the information of Fatigue Load
    Model 4 from Eurocode 1. Relevant regulations may be referred to
    Table 4.7 - Set of equivalent lorries of EN 1991-2.
    """

```

```
unit: mm, N
"""
def __init__(self):
    # the list of 5 types of lorries
    self.lorry = [lorryA(), lorryB(), lorryC(), lorryD(),
lorryE()]
    self.lorrylist = ['A', 'B', 'C', 'D', 'E']
    # the list of 3 types of tires
    self.axle = [tireA(), tireB(), tireC()]
    self.axlelist = ['A', 'B', 'C']
    print('Load model is successfully initiated!')

class lorryA(FatigueLoadModel4):
    def __init__(self):
        self.lorry_type = 'A'
        self.axle_number = 2
        self.axle_spacing = [4500]
        self.axle_load = [70000, 130000]
        self.tire_type = ['A', 'B']

class lorryB(FatigueLoadModel4):
    def __init__(self):
        self.lorry_type = 'B'
        self.axle_number = 3
        self.axle_spacing = [4200, 1300]
        self.axle_load = [70000, 120000, 120000]
        self.tire_type = ['A', 'B', 'B']

class lorryC(FatigueLoadModel4):
    def __init__(self):
        self.lorry_type = 'C'
        self.axle_number = 5
        self.axle_spacing = [3200, 5200, 1300, 1300]
        self.axle_load = [70000, 150000, 90000, 90000, 90000]
        self.tire_type = ['A', 'B', 'C', 'C', 'C']

class lorryD(FatigueLoadModel4):
    def __init__(self):
        self.lorry_type = 'D'
        self.axle_number = 4
        self.axle_spacing = [3400, 6000, 1800]
        self.axle_load = [70000, 140000, 90000, 90000]
        self.tire_type = ['A', 'B', 'B', 'B']

class lorryE(FatigueLoadModel4):
    def __init__(self):
        self.lorry_type = 'E'
        self.axle_number = 5
        self.axle_spacing = [4800, 3600, 4400, 1300]
        self.axle_load = [70000, 130000, 90000, 80000, 80000]
        self.tire_type = ['A', 'B', 'C', 'C', 'C']

class tireA(FatigueLoadModel4):
```

```

def __init__(self):
    self.tire_number = 2
    self.tire_spacing = [2000]
    self.tire_width = 220
    self.tire_length = 320
    self.location_correction = 0

class tireB(FatigueLoadModel4):
    def __init__(self):
        self.tire_number = 4
        self.tire_spacing = [320, 1680, 320]
        self.tire_width = 220
        self.tire_length = 320
        self.location_correction = 160

class tireC(FatigueLoadModel4):
    def __init__(self):
        self.tire_number = 2
        self.tire_spacing = [2000]
        self.tire_width = 270
        self.tire_length = 320
        self.location_correction = 0

```

A.5 Functions for fatigue life assessment

```

import pandas as pd
import numpy as np
import scipy.optimize
from scipy.stats import norm
from scipy.interpolate import griddata
from itertools import groupby

def interpolate_stress(influence_surface, load_x, load_y,
                     x_lim=[160, 3940], y_lim=[0, 8000]):
    """
    This function is used to interpolate stress from influence surfaces
    .

    influence_surface
        dataframe like data. The data of influence surface.
    load_x, load_y
        float. Central point of tire contact area.
    x_lim, y_lim
        list. Gives the boundary of the influence surface. Load outside
        the boundary will return zero.
    """
    # prepare parameters for interpolation
    coordinates = influence_surface[['loadcoor_x', 'loadcoor_y']].
        values
    values = influence_surface['stress'].values
    # perform interpolation, note that the interpolation method may be

```

```
# changed
if (x_lim[0] <= load_x <= x_lim[1]) and (y_lim[0] <= load_y <=
y_lim[1]):
    x, y = np.mgrid[load_x:load_x+0.5:1, load_y:load_y+0.5:1]
    interpolated_point = griddata(coordinates, values, (x, y),
method='cubic')[0][0]
else:
    # return zero if the point is outside boundaries
    interpolated_point = 0.0

return interpolated_point

def stress_history_filter(data):
    """
    This function is used to filter data of stress histories and leave
    only peaks and valleys.

    data
        array like data. Corresponds to a stress history.
    """
    # transfer data to list
    data = list(data)
    # remove consecutive duplicates, especially for peaks and valleys
    data = [x[0] for x in groupby(data)]
    # initiate result containers
    filtered_data = []
    # store first data point
    filtered_data.append(data[0])
    for k in range(1, len(data)-1):
        slope1 = data[k] - data[k-1]
        slope2 = data[k+1] - data[k]
        # store points meet the condition
        if slope1*slope2 < 0:
            filtered_data.append(data[k])
    filtered_data.append(data[-1])
    # store last data point
    filtered_data = np.array(filtered_data)

return filtered_data

def rainflow_counting(data):
    """
    This function is used to perform the rainflow counting on a
    series of data. The algorithm is based on the range-pair
    counting method.

    data
        array like data. Make sure the data is filtered by
        the function stress_history_filter.
    """
    # initiate result container
    counter = []
    data = list(data)
```

```

# initiate point index
k = 2
while len(data) > 2:
    s1, s2 = cycle_calculus(data, k)
    if (s1 > s2) and (k < len(data)-1):
        k += 1
    elif (s1 > s2) and (k == len(data)-1):
        data.reverse()
        k = 2
    else:
        counter.append(s1)
        del data[k-2:k]
        k = 2
# if there are two points left, store them as one circle
if len(data) == 2:
    counter.append(abs(data[0] - data[1]))
counter = np.array(counter)

return counter

def cycle_calculus(data_list, k):
    """
    This is a transient function for the rainflow counting function.
    Calculate stress ranges around point k in data list.

    data_list
        list. Corresponds to a specific stress history.
    k
        int. Index of a point.
    """
    p1 = data_list[k-2]
    p2 = data_list[k-1]
    p3 = data_list[k]
    s1 = abs(p1 - p2)
    s2 = abs(p2 - p3)

    return s1, s2

def stress_step(influence_surface, lorry_type, lorry_location_x,
lorry_location_y, fatigue_load_model):
    """
    This function is one step in fatigue life assessment. It
    calculates and returns the stress induced by a specific lorry
    at a specific time point.

    influence_surface
        dataframe like data. The data of influence surface to
        interpolate.
    lorry_type
        str. Lorry type information.
    lorry_location_x, lorry_location_y
        float. Offer information of lorry at this specific moment.
    fatigue_load_model

```

```
    obj. An instance of fatigue load model object, which
        contains the information of lorry type, axle distance, etc.
    """
    # initiate load model
    model = fatigue_load_model
    # get lorry model according to lorry type
    lorry_model = model.lorry[model.lorrylist.index(lorry_type)]
    # get axle number
    axle_number = lorry_model.axle_number
    # initiate result container
    stress_result = 0
    # iterate all axles
    for number in range(0, axle_number):
        # get tire type
        axle_type = lorry_model.tire_type[number]
        # get tire model
        axle = model.axle[model.axlelist.index(axle_type)]
        # get tire load pad number
        tire_number = axle.tire_number
        # calculate first tire location
        tire_location_x = lorry_location_x - axle.location_correction
        tire_location_y = lorry_location_y
        # calculate one axle
        for tire in range(0, tire_number):
            # calculate one pad
            stress_step = interpolate_stress(influence_surface,
                tire_location_x, tire_location_y)
            # record one pad, here 45000 corresponds to the tire load
            # used when getting the influence surfaces
            stress_result +=
                stress_step/45000*lorry_model.axle_load[number]/tire_number
            # update tire location
            if tire == tire_number-1:
                break
            tire_location_x += axle.tire_spacing[tire]
            tire_location_y = tire_location_y
        # update axle location
        if number == axle_number-1:
            break
        lorry_location_x = lorry_location_x
        lorry_location_y -= lorry_model.axle_spacing[number]

    return stress_result

def time_blank(time_stamp, time_logger, stress_logger, blank_points,
    point_list):
    """
    This is a transient function for filling the time blank between
    two consecutive lorries.

    time_stamp
        int. The specific time point.
    time_logger
```

```

    list. Container of time data.
stress_logger
    list. Container of stress data.
blank_points
    int. The number of blank data points, calculated by the
        driving speed and the record frequency.
point_list
    list. The list of names when there are multiple points.
"""

blank_time = list(np.arange(time_stamp, time_stamp+blank_points))
blank_stress = len(blank_time)*[0]
time_logger += blank_time
for name in point_list:
    stress_logger[name] += blank_stress
# update time_stamp
time_stamp += blank_points

return time_stamp, time_logger, stress_logger
def get_fatigue_damage(stress_range, fatigue_detail_category,
    cycle_count):
    """
    This function is used to calculate the fatigue damage induced by
    a specific stress range.

    stress_range
        float. The specific stress range to be evaluated.
    fatigue_detail_category
        float or int. The fatigue detail category for the specific
            detail. For example, 125 for structural hot spot stress
            method.
    cycle_ount:
        float or int. The exact cycles recorded.
    """

    # define the constant amplitude fatigue limit
    sigma_caf1 = 0.737*fatigue_detail_category
    # define the fatigue cut off limit
    sigma_cutoff = 0.549*sigma_caf1
    # calculate fatigue damage according to stress range, with the
    # reference to Eurocode 1993 1-9.
    if stress_range < sigma_cutoff:
        fatigue_damage = 0
    elif sigma_cutoff <= stress_range < sigma_caf1:
        fatigue_damage = cycle_count*np.power(stress_range/sigma_caf1,
            5)/(5*np.power(10, 6))
    elif sigma_caf1 < stress_range:
        fatigue_damage =
            cycle_count*np.power(stress_range/fatigue_detail_category,
                3)/(2*np.power(10, 6))

```

A.6 Example of simulation procedure

```
#!/home/samcef/anaconda3/bin/python3.7

import pandas as pd
import numpy as np
import matplotlib.pyplot as plt
import scipy.optimize
import itertools
import time
from scipy.stats import norm
from scipy.interpolate import griddata
from fatigue_assessment_functions import *
from FatigueLoadModel4 import *

# generate the list of investigated points
point_list = [f'l{num}' for num in range(1, 19)] + [f'r{num}' for num
in range(1, 19)]
# generate the list of considered transverse locations
tire_location_list = [1450, 1600, 1750, 1900, 2050]
# prepare file name of influence surfaces
df_name = 'TFR8'
df_point = 's3'

# iterate from the central line of front left tire
for tire_location in tire_location_list:
    # read data of influence surfaces
    hss_df = pd.read_csv(f'./data/{df_name}_hss_{df_point}.csv')
    df_influence_surfaces = {}
    for name in point_list:
        df_influence_surfaces[name] = hss_df[hss_df['number'] ==
name].reset_index()
    # prepare the influence surface by adding extra points
    # above crossbeams
    for name in point_list:
        df_influence_surfaces[name] =
        add_extra_points(df_influence_surfaces[name])
    # initiate fatigue load model
    lm4 = FatigueLoadModel4()
    # prepare observations
    observations_year = 0.5*np.power(10, 6)
    observations_day = observations_year/365
    observations_month = observations_day*30
    observations_hour = observations_day/24
    # prepare different traffic types
    traffic_type_longdistance = [0.2, 0.05, 0.5, 0.15, 0.1]
    traffic_type_mediumdistance = [0.4, 0.1, 0.3, 0.15, 0.05]
    traffic_type_localtraffic = [0.8, 0.05, 0.05, 0.05, 0.05]
    # calculate z score according to the position of 7%
    z_score = (0.07-0.06944)*(-1.47+1.48)/(0.07078-0.06944)-1.48
    scale = -0.15/z_score*1000
    # prepare other parameters
    # simulated driving speed, unit: km/h
```

```

speed_real = 90
# interval distance between two consecutive lorries, unit: mm
distance_diff = 50000
# record frequency, unit: Hz
record_frequency = 100
time_step = 1/record_frequency
# transfer the unit of driving speed to mm/s
speed_cal = speed_real*1000000/3600
# generate blank data
time_diff = distance_diff/speed_cal
blank_points = time_diff/time_step
blank_time = np.arange(blank_points)
blank_stress = blank_time*0
# choose the number of observations to be simulated
observations = observations_day

# initiate start time
start = time.time()
# initiate time stamp
time_stamp = 0
# initiate time logger
time_logger = []
# initiate stress history loggers for all points
stress_logger = {}
for name in point_list:
    stress_logger[name] = []
# insert the initial blank data
time_stamp, time_logger, stress_logger = time_blank(time_stamp,
time_logger, stress_logger, blank_points, point_list)
# send notification
print('simulation has started!')

# start recording
for observation in range(0, int(observations)):
    # generate a random lorry type
    lorry_type = np.random.choice(lm4.lorrylist,
p=traffic_type_mediumdistance)
    # generate a random location
    lorry_location_x = norm.rvs(loc=tire_location, scale=scale)
    lorry_location_y = 0
    # calculate the time needed for the lorry to pass, note that
    # 8000 is the total length of the model considered
    lorry_length =
sum(lm4.lorry[lm4.lorrylist.index(lorry_type)].axle_spacing)
    drive_distance = lorry_length + 8000
    record_points = drive_distance/speed_cal/time_step

    # calculate one observation and record results
    for cal_loop in range(int(record_points)):
        # record one record point
        for name in point_list:
            stress_point =
            stress_step(df_influence_surfaces[name], lorry_type,

```

```
        lorry_location_x, lorry_location_y, lm4)
        stress_logger[name].append(stress_point)
    # update lorry location
    lorry_location_x = lorry_location_x
    lorry_location_y += speed_cal*time_step
    # update time logger
    time_logger.append(time_logger[-1]+1)
    time_stamp += 1

    # insert interval blank
    time_stamp, time_logger, stress_logger =
    time_blank(time_stamp, time_logger, stress_logger,
    blank_points, point_list)
end = time.time()

# save calculation results
stress_history = pd.DataFrame(stress_logger)
stress_history.to_csv(f'./fatigue/stress_history.csv',
index=False)
# send notification
print('stress history is saved!')

# post processing
# initiate a container for counted stress ranges
stress_range_count = pd.DataFrame()
# iterate through all investigated points
for name in point_list:
    raw_data = stress_logger[name]
    filtered_data = stress_history_filter(raw_data)
    counted_data = rainflow_counting(filtered_data)
    counted_data = counted_data.round()
    # count unique stress range numbers
    unique, count = np.unique(counted_data, return_counts=True)
    # convert final results to dict
    stress_range_raw = dict(zip(unique, count))
    stress_range = pd.DataFrame(stress_range_raw, index=[0])
    stress_range = stress_range.T.reset_index()
    stress_range.columns = ['stress_range', 'count']
    stress_range['point'] = name
    stress_range_count = pd.concat([stress_range_count,
    stress_range], ignore_index=True)
# initiate a data container for fatigue life
fatigue_life = {}
stress_damage = pd.DataFrame()
# iterate through all investigated points
for name in point_list:
    stress_range = stress_range_count[stress_range_count['point']
    == name]
    stress_range = stress_range.sort_values('stress_range',
ascending=True).reset_index(drop=True)
    # 125 is the considered detail category of SHSS
    stress_range['damage'] =
    [get_fatigue_damage(stress_range['stress_range'][num], 125,
```

```

stress_range['count'][num] for num in
range(len(stress_range))]
# calculate the fatigue life of one point
point_life = 1.0/stress_range['damage'].sum()/365
# store the result
fatigue_life[name] = point_life
# generate the dataframe of fatigue life for all investigated
# points and save relevant file
fatigue_life_df = pd.DataFrame(fatigue_life,
index=[0]).T.reset_index()
fatigue_life_df.columns = ['point', 'fatigue_life']
fatigue_life_df['location'] = tire_location
fatigue_life_df.to_csv(f'./fatigue/fatigue_life.csv', index=False)

```

A.7 Analytical method

A.7.1 Class TrapezoidalSection

```

import math

class TrapezoidalSection(object):
    """
    This class works as part of the analytical method for calculating
    orthotropic steel decks. It is defined specifically for the
    closed rib with trapezoidal cross-section.
    """
    def __init__(self, thickness_deck, thickness_rib,
thickness_crossbeam, upperwidth, height, lowerwidth, radius,
rib_span, copehole_height, crossbeam_width, crossbeam_height,
crossbeam_span, bottom_thickness=20, bottom_width=200):
        self.thickness_deck = thickness_deck
        self.thickness_rib = thickness_rib
        self.thickness_crossbeam = thickness_crossbeam
        self.upperwidth = upperwidth
        self.height = height
        self.lowerwidth = lowerwidth
        self.radius = radius
        self.rib_span = rib_span
        self.copehole_height = copehole_height
        self.crossbeam_width = crossbeam_width
        self.crossbeam_height = crossbeam_height
        self.crossbeam_span = crossbeam_span
        self.bottom_thickness = bottom_thickness
        self.bottom_width = bottom_width
        self.flexural_rigidity = self.FlexuralRigidity()
        self.torsional_rigidity = self.TorsionalRigidity()
        self.shear_rigidity = self.ShearRigidity()

    def MomentInertia(self):
        alpha = math.atan2((self.upperwidth - self.lowerwidth)/2,
self.height) actual_bottom_length = self.lowerwidth -

```

```

2*self.radius/math.tan(math.pi/4 + alpha/2)
actual_ribwall_length = (self.height -
self.thickness_rib/2)/math.cos(alpha) -
self.radius/math.tan(math.pi/4 + alpha/2)
curvature_length = math.sin(math.pi/4 - alpha/2)*self.radius*2
area_deck = (self.upperwidth +
self.rib_span)*self.thickness_deck
area_ribwall = self.thickness_rib*actual_ribwall_length
area_soffit = self.thickness_rib*actual_bottom_length
area_curvature = curvature_length*self.thickness_rib
y_deck = self.height + self.thickness_deck/2
y_ribwall = y_deck - actual_ribwall_length*math.cos(alpha)/2
y_soffit = self.thickness_rib/2
y_curvature = self.radius*math.cos(alpha)/math.tan(math.pi/4 +
alpha/2) + self.thickness_rib/2
sum_area = area_deck + area_ribwall*2 + area_soffit +
area_curvature*2
y_neutral_axis = (area_deck*y_deck +
2*area_ribwall*y_ribwall + 2*area_curvature*y_curvature +
area_soffit*y_soffit)/sum_area
I_deck = self.MomentInertiaBox((self.upperwidth +
self.rib_span), self.thickness_deck) +
self.ExtraMomentInertiaBox(area_deck, y_deck, y_neutral_axis)
I_ribwall =
self.MomentInertiaBox(self.thickness_rib/math.cos(alpha),
actual_ribwall_length*math.cos(alpha)) +
self.ExtraMomentInertiaBox(area_ribwall, y_ribwall,
y_neutral_axis)
I_soffit = self.MomentInertiaBox(actual_bottom_length,
self.thickness_rib) + self.ExtraMomentInertiaBox(area_soffit,
y_soffit, y_neutral_axis)
I_curvature =
self.MomentInertiaBox(self.thickness_rib/math.cos(math.pi/4 +
alpha/2), y_curvature - self.thickness_rib/2) +
self.ExtraMomentInertiaBox(area_curvature, y_curvature,
y_neutral_axis)
total_I = I_deck + I_ribwall*2 + I_soffit + I_curvature*2

return total_I

def SectionModule(self):
alpha = math.atan2((self.upperwidth - self.lowerwidth)/2,
self.height)
actual_bottom_length = self.lowerwidth -
2*self.radius/math.tan(math.pi/4 + alpha/2)
actual_ribwall_length = (self.height -
self.thickness_rib/2)/math.cos(alpha) -
self.radius/math.tan(math.pi/4 + alpha/2)
curvature_length = math.sin(math.pi/4 - alpha/2)*self.radius*2
updated_width = 2*(actual_ribwall_length + curvature_length) +
actual_bottom_length
area_deck = (self.upperwidth +
self.rib_span)*self.thickness_deck
area_ribwall = self.thickness_rib*actual_ribwall_length

```

```

area_soffit = self.thickness_rib*actual_bottom_length
area_curvature = curvature_length*self.thickness_rib
y_deck = self.height + self.thickness_deck/2
y_ribwall = y_deck - actual_ribwall_length*math.cos(alpha)/2
y_soffit = self.thickness_rib/2
y_curvature = self.radius*math.cos(alpha)/math.tan(math.pi/4 +
alpha/2) + self.thickness_rib/2
sum_area = area_deck + area_ribwall*2 + area_soffit +
area_curvature*2
y_neutral_axis = (area_deck*y_deck + 2*area_ribwall*y_ribwall
+ 2*area_curvature*y_curvature +
area_soffit*y_soffit)/sum_area
lower_section_module = self.MomentInertia()/y_neutral_axis
upper_section_module = self.MomentInertia()/(self.height +
self.thickness_deck - y_neutral_axis)

return upper_section_module, lower_section_module,
y_neutral_axis, updated_width

def MomentInertiaCrossbeam(self, effective_width_coefficient=0):
    effective_width = self.crossbeam_span*
        effective_width_coefficient
    area_deck = self.thickness_deck*effective_width
    area_crossbeam = self.thickness_crossbeam*self.crossbeam_height
    area_bottom = self.bottom_width*self.bottom_thickness
    y_deck = self.crossbeam_height +self.thickness_deck/2
    y_crossbeam = self.height/2
    y_bottom = self.bottom_thickness/2
    sum_area = area_deck + area_crossbeam + area_bottom
    y_neutral_axis = (area_deck*y_deck + area_crossbeam*y_crossbeam
        +
    area_bottom*y_bottom)/sum_area
    I_deck = self.MomentInertiaBox(effective_width,
self.thickness_deck) + self.ExtraMomentInertiaBox(area_deck,
y_deck, y_neutral_axis)
    I_crossbeam = self.MomentInertiaBox(self.thickness_crossbeam,
self.crossbeam_height - self.bottom_thickness) +
self.ExtraMomentInertiaBox(area_crossbeam, y_crossbeam,
y_neutral_axis)
    I_bottom = self.MomentInertiaBox(self.bottom_width,
self.bottom_thickness) +
self.ExtraMomentInertiaBox(area_bottom, y_bottom,
y_neutral_axis)
    total_I = I_deck + I_crossbeam + I_bottom

return total_I

def CrossbeamSectionArea(self, effective_width_coefficient=0):
    effective_width = self.crossbeam_span*
        effective_width_coefficient
    area_deck = self.thickness_deck*effective_width
    area_crossbeam = self.thickness_crossbeam*self.crossbeam_height
    area_bottom = self.bottom_width*self.bottom_thickness

```

```
sum_area = area_deck + area_crossbeam + area_bottom

return sum_area

def FlexuralRigidity(self):
    elasticity_modulus_steel = 210000
    felxural_rigidity =
    elasticity_modulus_steel*self.MomentInertia()/(self.upperwidth
    + self.rib_span)

    return felxural_rigidity

def TorsionalRigidity(self):
    shear_modulus_steel = 81000
    elasticity_modulus_steel = 210000
    developed_width = self.SectionModule()[3]
    section_property = 4*math.pow(self.AreaEnclosed(),
    2)/(developed_width/self.thickness_rib +
    self.upperwidth/self.thickness_deck)
    torsional_rigidity =
    shear_modulus_steel*section_property/(self.upperwidth +
    self.rib_span)/2

    return torsional_rigidity

def ShearRigidity(self):
    E = 210000
    a = self.upperwidth
    e = self.rib_span
    j = self.lowerwidth
    hw = self.RibWallHeight()
    Id = self.MomentInertiaBox(1, self.thickness_deck)
    Ir = self.MomentInertiaBox(1, self.thickness_rib)
    alpha = 2*hw*(math.pow(a, 2) + a*j + math.pow(j, 2)) +
    math.pow(j, 3)
    beta = (math.pow(j, 3)/2 + hw*math.pow(j, 2))*(math.pow(a, 2)
    - a*e + math.pow(e, 2)) - a*e*hw*j*(a - e) + math.pow(a,
    2)*math.pow(e, 2)*hw
    shear_rigidity = 12*E*Id*Ir*(a + e)*(math.pow(a, 3)*Ir +
    Id*alpha)/(2*math.pow(a+e, 2)*(j + 3*hw/2)*hw*math.pow(j,
    2)*math.pow(Id, 2) + 2*Ir*Id*(a + e)*beta + math.pow(a,
    3)*math.pow(e, 3)*math.pow(Ir, 2))

    return shear_rigidity

def RibWallHeight(self):
    alpha = math.atan2((self.upperwidth - self.lowerwidth)/2,
    self.height)
    actual_bottom_length = self.lowerwidth -
    2*self.radius/math.tan(math.pi/4 + alpha/2)
    actual_ribwall_length = (self.height -
    self.thickness_rib/2)/math.cos(alpha) -
```

```

self.radius/math.tan(math.pi/4 + alpha/2)

return actual_ribwall_length

def AreaEnclosed(self):
    alpha = math.atan2((self.upperwidth - self.lowerwidth)/2,
self.height)
    actual_bottom_length = self.lowerwidth -
2*self.radius/math.tan(math.pi/4 + alpha/2)
    actual_ribwall_length = (self.height -
self.thickness_rib/2)/math.cos(alpha) -
self.radius/math.tan(math.pi/4 + alpha/2)
    curvature_length = math.sin(math.pi/4 - alpha/2)*self.radius*2
    area_box1 = (self.upperwidth -
actual_ribwall_length*math.sin(alpha)*2)*\
actual_ribwall_length*math.cos(alpha)
    area_box2 =
2*actual_bottom_length*self.radius*math.cos(alpha)/\
math.tan(math.pi/4 + alpha/2)
    area_triangle1 = math.pow(actual_ribwall_length,
2)*math.cos(alpha)*math.sin(alpha)
    area_triangle2 = (self.upperwidth - actual_bottom_length -
2*actual_ribwall_length*math.sin(alpha))*self.radius*\
math.cos(alpha)/math.tan(math.pi/4 + alpha/2)
    total_area = area_box1 + area_box2 + area_triangle1 +
area_triangle2

return total_area

def MomentInertiaBox(self, width, height):

return width*height**3/12

def ExtraMomentInertiaBox(self, area, area_center, neutral_axis):

return area*(area_center - neutral_axis)**2

def RibWallAngle(self):

return math.atan2((self.upperwidth - self.lowerwidth)/2,
self.height)

```

A.7.2 Class LoadCase

```

import numpy as np

class LoadCase(object):
    """
    This class works as part of the analytical method for calculating
    orthotropic steel decks. It is defined specifically for the load
    on an idealized plate.
    """

```

```

def __init__(self, load_size, load_width, load_length,
load_position_x, load_position_y, plate_width, plate_span,
series_number_n, series_number_m, impact_factor, step=1):
    self.load_size = load_size
    self.load_width = load_width
    self.load_length = load_length
    self.load_x = load_position_x
    self.load_y = load_position_y
    self.impact_factor = impact_factor
    self.series_number_n = series_number_n
    self.series_number_m = series_number_m
    self.plate_width = plate_width
    self.plate_span = plate_span
    self.step = step

def LoadQn(self):
    load_q0 = self.load_size*self.impact_factor/self.load_width/
                self.load_length

    series_number_n_list = np.arange(1, self.series_number_n+1, 1)
    npi = series_number_n_list*np.pi
    load_x1 = self.load_x - self.load_width/2
    load_x2 = self.load_x + self.load_width/2
    qn = 2*load_q0*(np.cos(npi*load_x1/self.plate_width) - np.cos(
                npi*load_x2/self.
                plate_width))/npi

    return qn

def FourierAnalysisOne1D(self, specific_series_number_n):
    qn = self.LoadQn()
    npi = specific_series_number_n*np.pi
    x_coor = np.arange(0, self.plate_width+1, self.step)
    one_series = qn[specific_series_number_n-1]*np.sin(npi*x_coor/
                self.plate_width)

    return x_coor, one_series

def FourierAnalysisSum1D(self):
    x_coor = np.arange(0, self.plate_width+1, self.step)
    sum_series = np.zeros(len(x_coor))
    qn = self.LoadQn()
    for series in range(1, self.series_number_n+1):
        series = self.FourierAnalysisOne1D(series)[1]
        sum_series += series

    return x_coor, sum_series

```

A.7.3 Class AnalyticalModel

```

import numpy as np
import sympy as sp

```

```

class AnalyticalModel(object):
    """
    This class works as part of the analytical method for calculating
    orthotropic steel decks. To initiate an instance of this class,
    an instance of the class TrapezoidalSection and an instance of
    the class LoadCase are required.
    """
    def __init__(self, rib_model, load_model):
        self.rib = rib_model
        self.load = load_model
        self.n = np.arange(1, load_model.series_number_n+1)
        self.m = np.arange(1, load_model.series_number_m+1)
        self.alpha, self.beta, self.zeta, self.eta = self.
            get_parameters()

        self.kappa = self.get_carry_over_factor()
        self.x, self.y = sp.symbols('x y')

    def get_parameters(self):
        ky = self.rib.flexural_rigidity
        kxy = self.rib.torsional_rigidity
        kxz = self.rib.shear_rigidity
        b = self.rib.crossbeam_width
        s = self.rib.crossbeam_span
        n = self.n
        alpha = np.sqrt(-(-2*np.sqrt(2)*np.pi*kxy*n*np.sqrt(kxz*ky)-\
            kxz*ky*b)/(4*kxy*ky*b))
        beta = np.sqrt(kxy*ky*b*(2*np.sqrt(2)*np.pi*kxy*n*\
            np.sqrt(kxz*ky)-kxz*ky*b)/(2*kxy*ky*b))
        zeta = (4*kxy**2*np.pi**2*np.power(n,
            2)-kxz*ky*b**2)/(2*b*kxy**2*np.pi*n)
        eta = -2*alpha*beta*ky*b/(kxy*np.pi*n)

        return alpha, beta, zeta, eta

    def get_carry_over_factor(self):
        s = self.rib.crossbeam_span
        alpha = self.alpha
        beta = self.beta
        zeta = self.zeta
        eta = self.eta
        k = (-np.cosh(alpha*s)*np.sinh(alpha*s)*beta+np.cos(beta*s)*\
            np.sin(beta*s)*alpha)/(np.sinh(alpha*s)*np.cos(beta*s)*\
            beta-np.cosh(alpha*s)*np.sin(beta*s)*alpha)
        kappa = -k + np.sign(k)*np.sqrt(np.power(k, 2) - 1)

        return kappa

    def get_constants_influenceline(self):
        kappa = self.kappa
        alpha = self.alpha
        beta = self.beta
        zeta = self.zeta
        eta = self.eta

```

```

s = self.rib.crossbeam_span
C_den = 2*beta*(np.cos(beta*s)*kappa - np.cosh(alpha*s))*\
np.sinh(alpha*s) - 2*alpha*np.sin(beta*s)*(np.cosh(alpha*s)*\
kappa - np.cos(beta*s))
C1 = (np.power(np.cos(beta*s), 2) - np.power(np.cosh(alpha*s),
2))/C_den
C2 = 0/C_den
C3 = (-np.sin(beta*s)*(-np.cosh(alpha*s)*kappa +
np.cos(beta*s)))/C_den
C4 = (-np.sinh(alpha*s)*(np.cos(beta*s)*kappa -
np.cosh(alpha*s)))/C_den

return C1, C2, C3, C4

def get_constants_general_solution(self):
M0, M1 = self.get_moment_general_solution()
alpha = self.alpha
beta = self.beta
zeta = self.zeta
eta = self.eta
ky = self.rib.flexural_rigidity
kxy = self.rib.torsional_rigidity
kxz = self.rib.shear_rigidity
b = self.rib.crossbeam_width
s = self.rib.crossbeam_span
C1 = -M0/(2*ky*alpha*beta)
C2 = 0*C1
C3 = np.sin(beta*s)*(np.power(np.sinh(alpha*s),
2)*np.cos(beta*s)*M0 - np.power(np.cosh(alpha*s),
2)*np.cos(beta*s)*M0 +
np.cosh(alpha*s)*M1)/(2*ky*alpha*beta*(np.power(np.sinh(\
alpha*s), 2)*np.power(np.cos(beta*s), 2) +\
np.power(np.sin(beta*s), 2)*np.power(np.cosh(alpha*s), 2)))
C4 = np.sinh(alpha*s)*(np.power(np.sin(beta*s),
2)*np.cosh(alpha*s)*M0 + np.power(np.cos(beta*s),
2)*np.cosh(alpha*s)*M0 -
np.cos(beta*s)*M1)/(2*ky*alpha*beta*(np.power(np.sinh(\
alpha*s), 2)*np.power(np.cos(beta*s), 2) +\
np.power(np.sin(beta*s), 2)*np.power(np.cosh(alpha*s), 2)))

return C1, C2, C3, C4

def construct_general_solution(self, C1, C2, C3, C4):
alpha = self.alpha
beta = self.beta
zeta = self.zeta
eta = self.eta
n = self.n
b = self.rib.crossbeam_width
s = self.rib.crossbeam_span
x = self.x
y = self.y

```

```

w = [None]*len(n)
r = [None]*len(n)
for i in range(0, len(n)):
    w[i] = (C1[i]*sp.sinh(alpha[i]*y)*sp.sin(beta[i]*y) +
            C2[i]*sp.cosh(alpha[i]*y)*sp.cos(beta[i]*y) +
            C3[i]*sp.sinh(alpha[i]*y)*sp.cos(beta[i]*y) +
            C4[i]*sp.cosh(alpha[i]*y)*sp.sin(beta[i]*y))*\
            sp.sin(n[i]*np.pi*x/b)

    r[i] = ((C1[i]*zeta[i] -
            C2[i]*eta[i])*sp.sinh(alpha[i]*y)*sp.sin(beta[i]*y) +
            (C1[i]*eta[i] +
            C2[i]*zeta[i])*sp.cosh(alpha[i]*y)*sp.cos(beta[i]*y) +
            (C3[i]*zeta[i] +
            C4[i]*eta[i])*sp.sinh(alpha[i]*y)*sp.cos(beta[i]*y) +
            (C4[i]*zeta[i] -
            C3[i]*eta[i])*sp.cosh(alpha[i]*y)*sp.sin(beta[i]*y))*\
            sp.cos(n[i]*np.pi*x/b)

    return w, r

def get_moment_general_solution(self):
    w, r = self.construct_general_solution(\
        *self.get_constants_influenceline())
    n = self.n
    b = self.rib.crossbeam_width
    s = self.rib.crossbeam_span
    x = self.x
    y = self.y
    M0 = [None]*len(n)
    M1 = [None]*len(n)
    Qn = self.load.LoadQn()
    y1 = self.load.load_y - self.load.load_length/2
    y2 = self.load.load_y + self.load.load_length/2
    kappa = self.kappa
    for i in range(0, len(n)):
        M0[i] = Qn[i]*sp.integrate(w[i]/sp.sin(n[i]*np.pi*x/b),
            (y, y1, y2))
        M1[i] = M0[i]*kappa[i]
    M0 = np.array(M0)
    M1 = np.array(M1)

    return M0, M1

def construct_particular_solution(self):
    load = self.load
    n = self.n
    m = self.m
    ky = self.rib.flexural_rigidity
    kxy = self.rib.torsional_rigidity
    kxz = self.rib.shear_rigidity
    b = self.rib.crossbeam_width
    s = self.rib.crossbeam_span

```

```

x = self.x
y = self.y
w = []
r = []
for i in range(1, len(n)+1):
    for j in range(1, len(m)+1):
        amn = 4*load.load_size/(load.load_width*\
            load.load_length*np.pi**2*i*j)*np.sin(i*\
            np.pi*load.load_width/b)*np.sin(i*np.pi*\
            load.load_x/b)*np.sin(j*np.pi*load.load_length/s)*\
            np.sin(j*np.pi*load.load_y/s)

        C1p = amn*s**4*b**2*(kxy*np.pi**2*j**2 +
            kxz*s**2)/(j**2*np.pi**4*(kxy*ky*np.pi**2*b**2*j**4 +
            2*kxy*kkz*i**2*s**4 + kxz*ky*b**2*j**2*s**2))

        C2p = 2*amn*np.power(s,
            4)*b*kxy*i/(np.pi*(kxy*ky*np.power(np.pi,
            2)*np.power(b, 2)*np.power(j, 4) +
            2*kxy*kkz*np.power(i, 2)*np.power(s, 4) +
            kxz*ky*np.power(b, 2)*np.power(j, 2)*np.power(s, 2))

        wp_exp = C1p*sp.sin(i*np.pi*x/b)*sp.sin(j*np.pi*y/s)
        rp_exp = C2p*sp.cos(i*np.pi*x/b)*sp.sin(j*np.pi*y/s)
        w.append(wp_exp)
        r.append(rp_exp)

return w, r

def construct_solution(self):
    wg, rg = self.construct_general_solution(\
        *self.get_constants_general_solution())
    wp, rp = self.construct_particular_solution()
    w = sp.add.Add(sum(wp), sum(wg))
    r = sp.add.Add(sum(rp), sum(rg))
    self.w = w
    self.r = r

return w, r

def get_bending_moment(self):
    ky = self.rib.flexural_rigidity
    my = ky*sp.diff(self.w, self.y, 2)

return my

def get_torsional_moment(self):
    kxy = self.rib.torsional_rigidity
    mxy = -kxy*(2*sp.diff(self.w, self.x, self.y) -
        sp.diff(self.r, self.y))

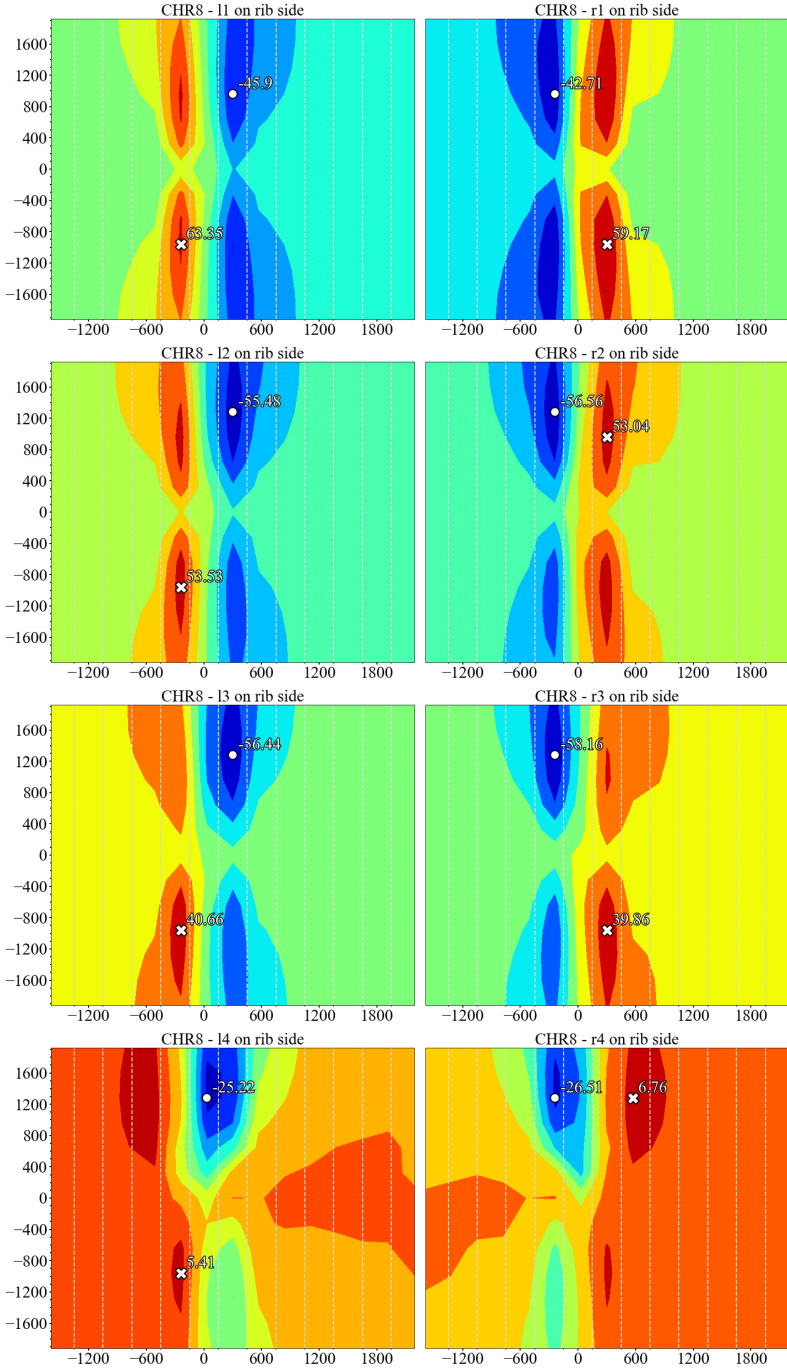
return mxy

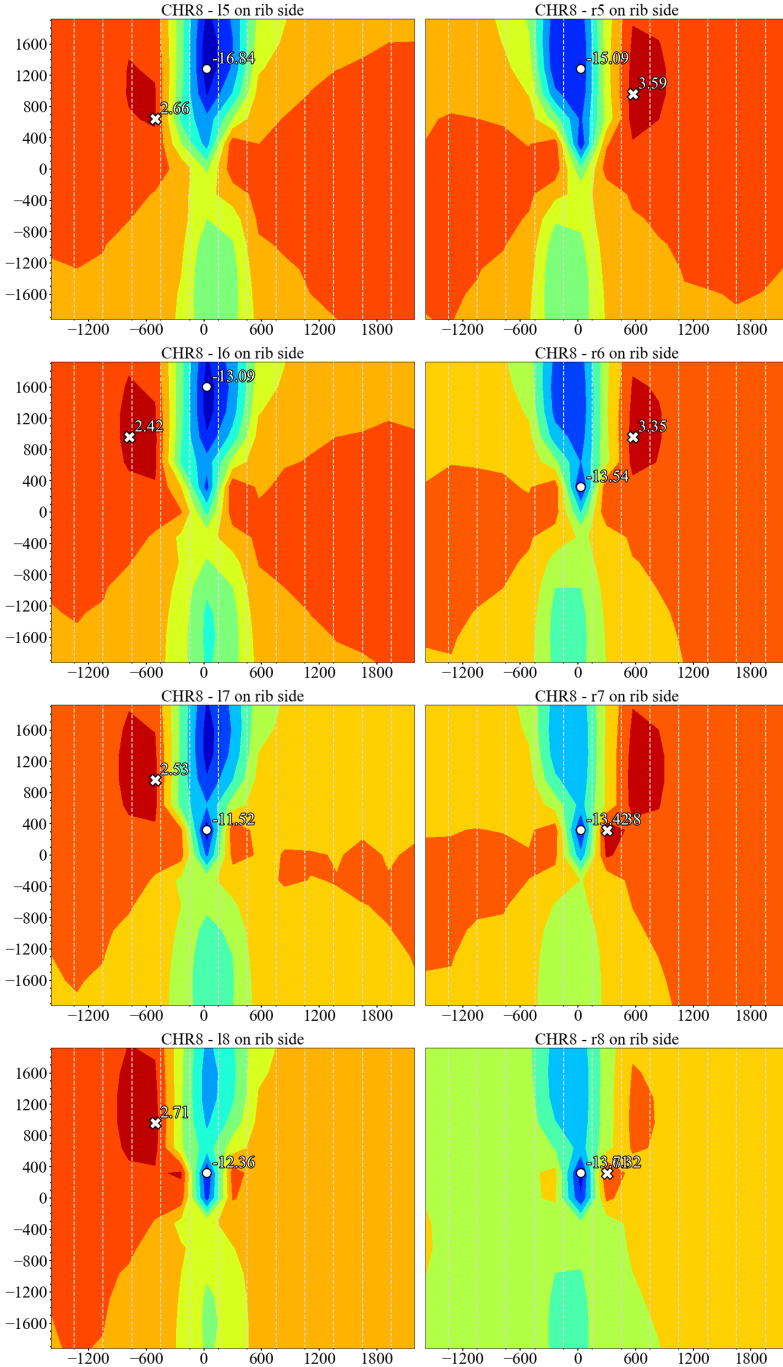
```

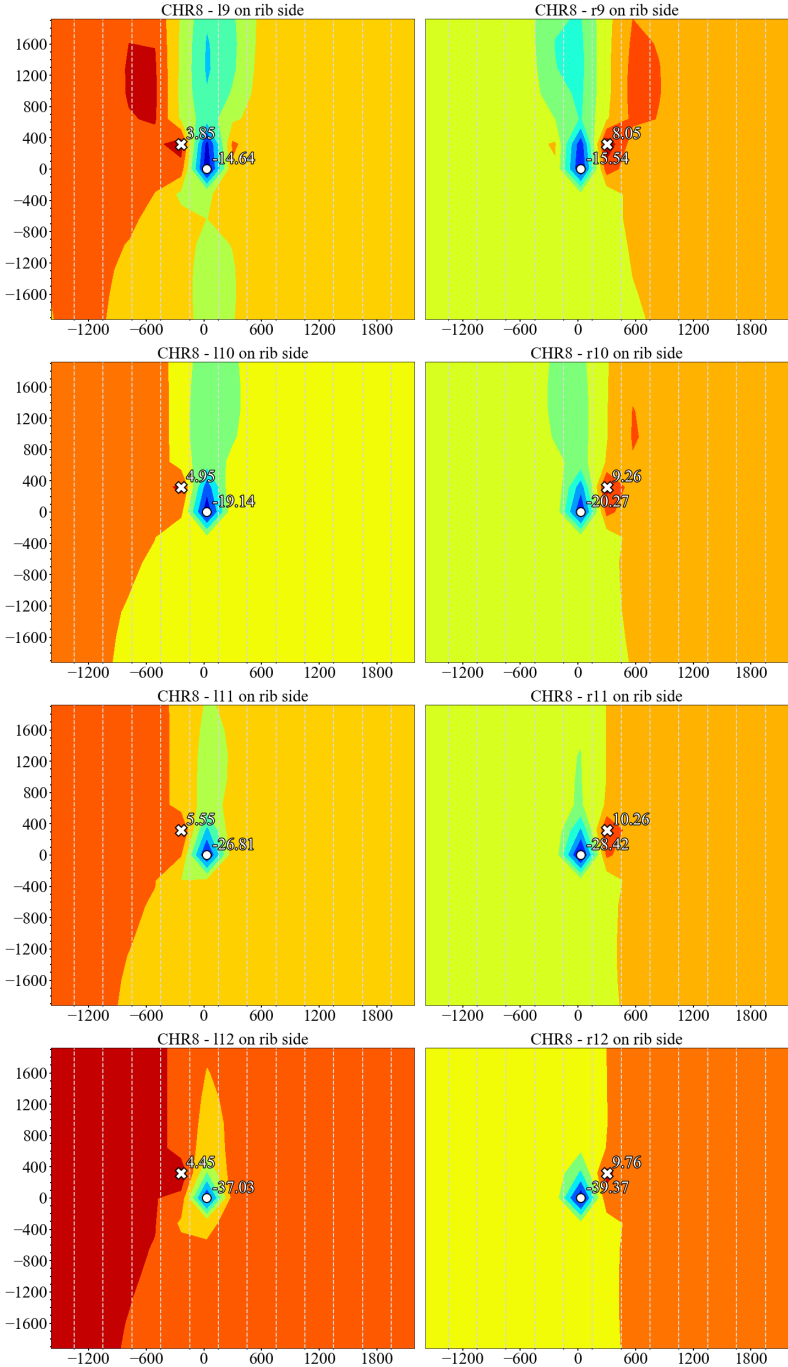
```
def get_shear_force(self):  
    kxz = self.rib.shear_rigidity  
    vxz = kxz*self.r  
  
    return vxz
```

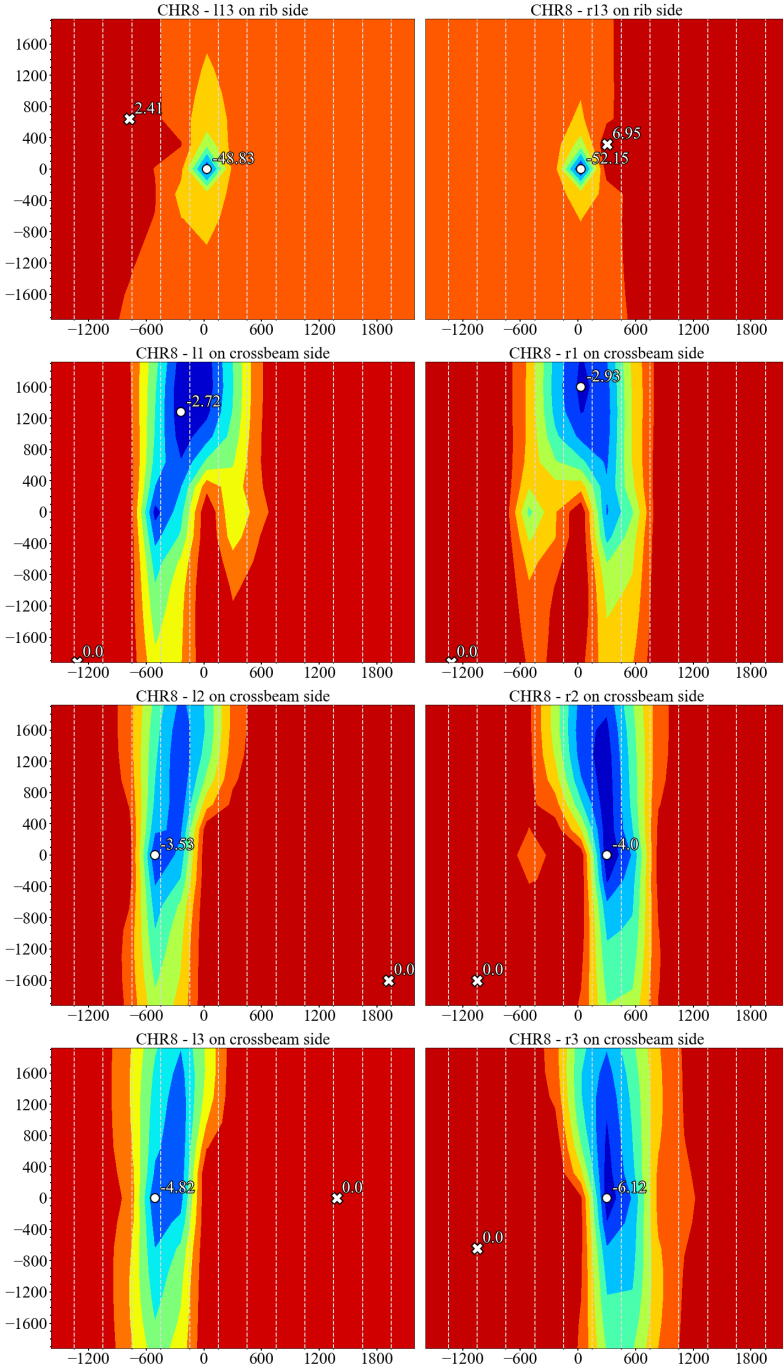

B

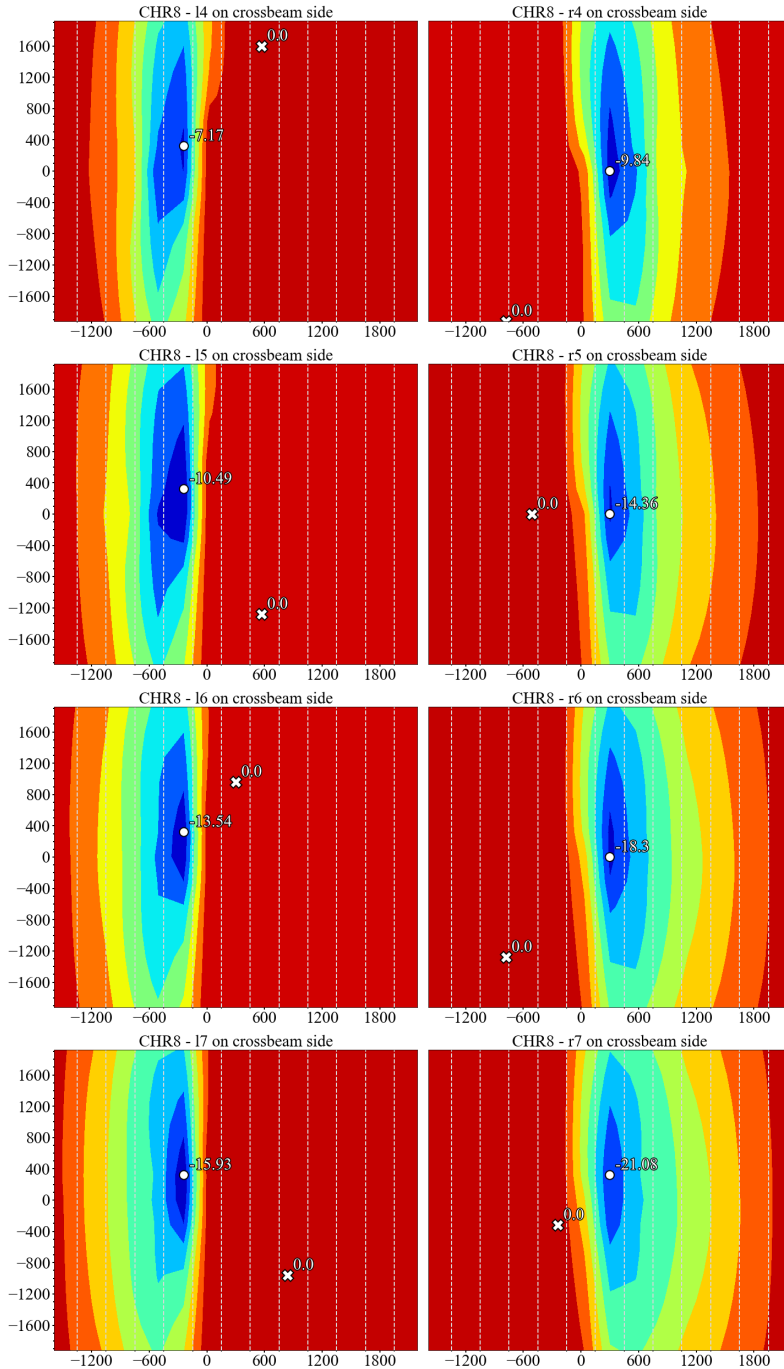
Supplementary calculation results

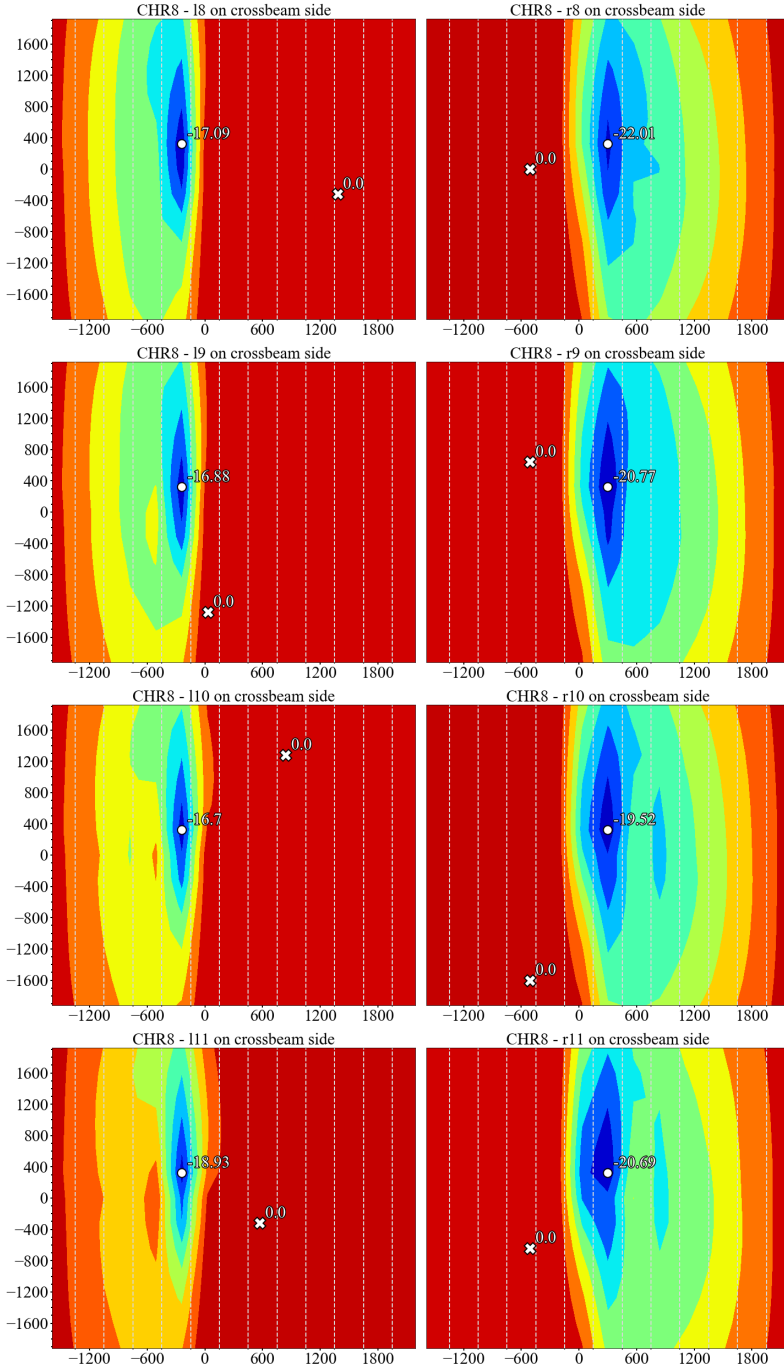


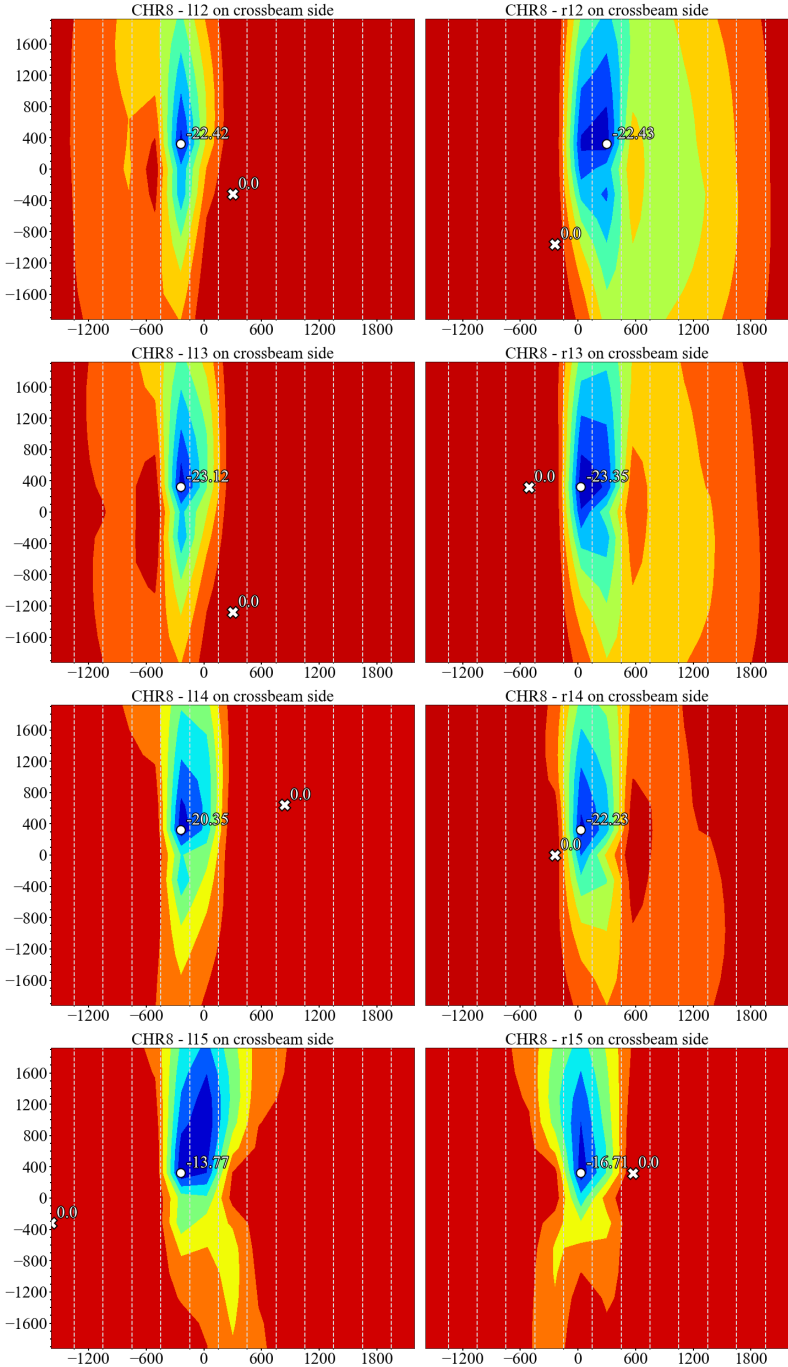


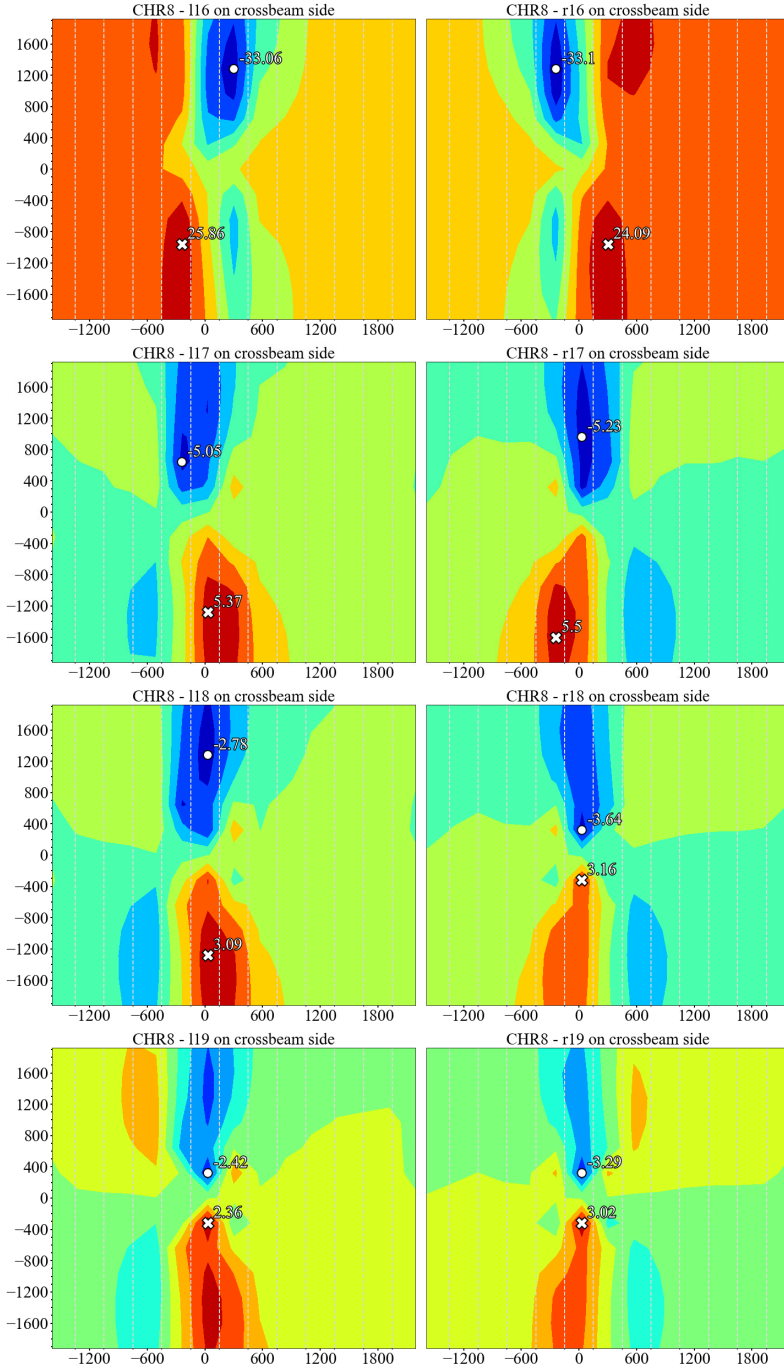


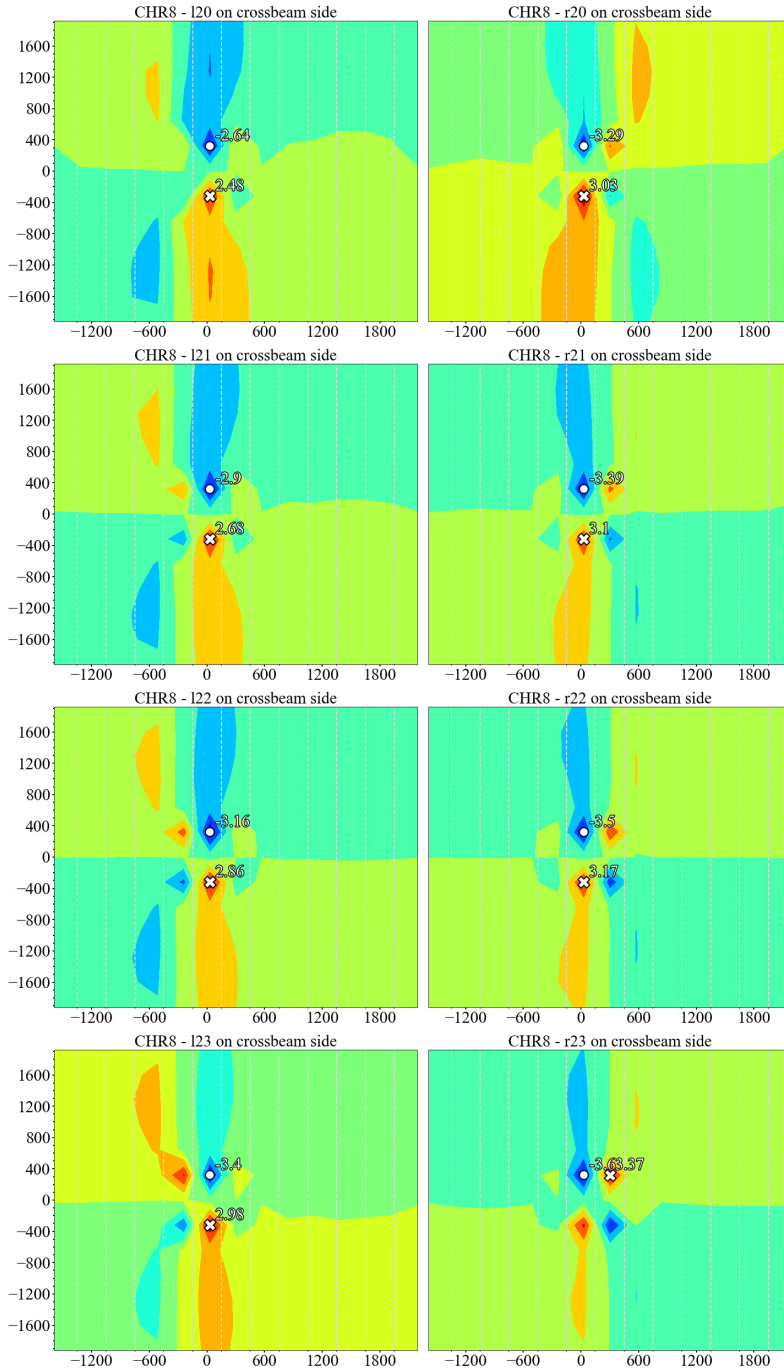


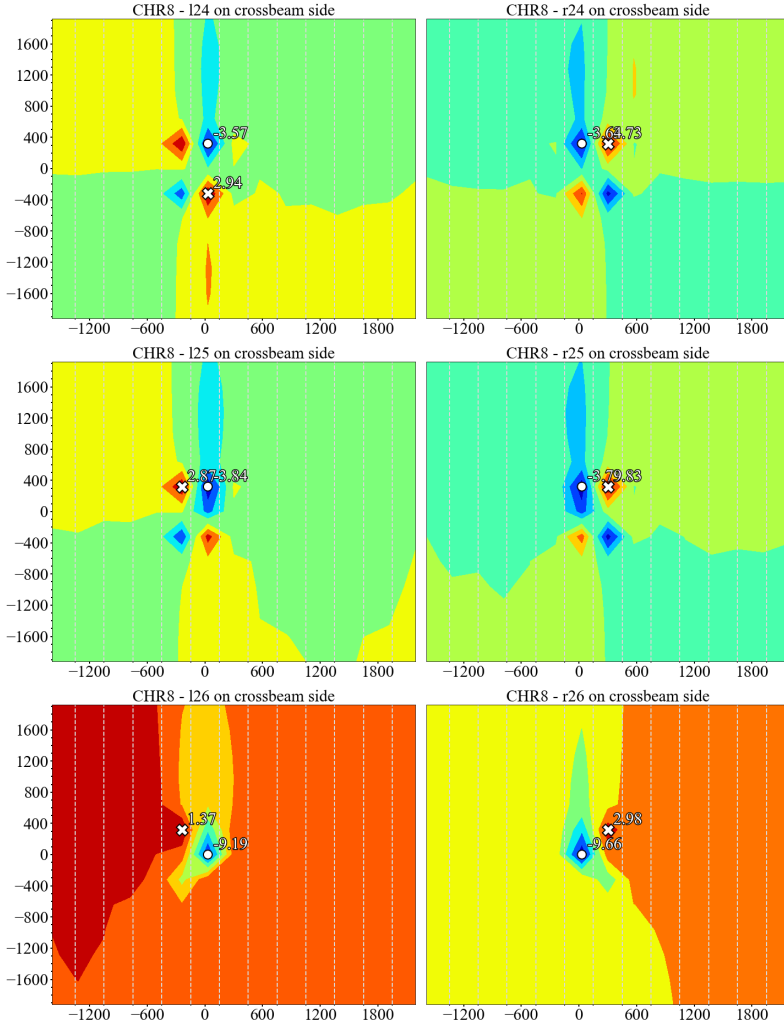


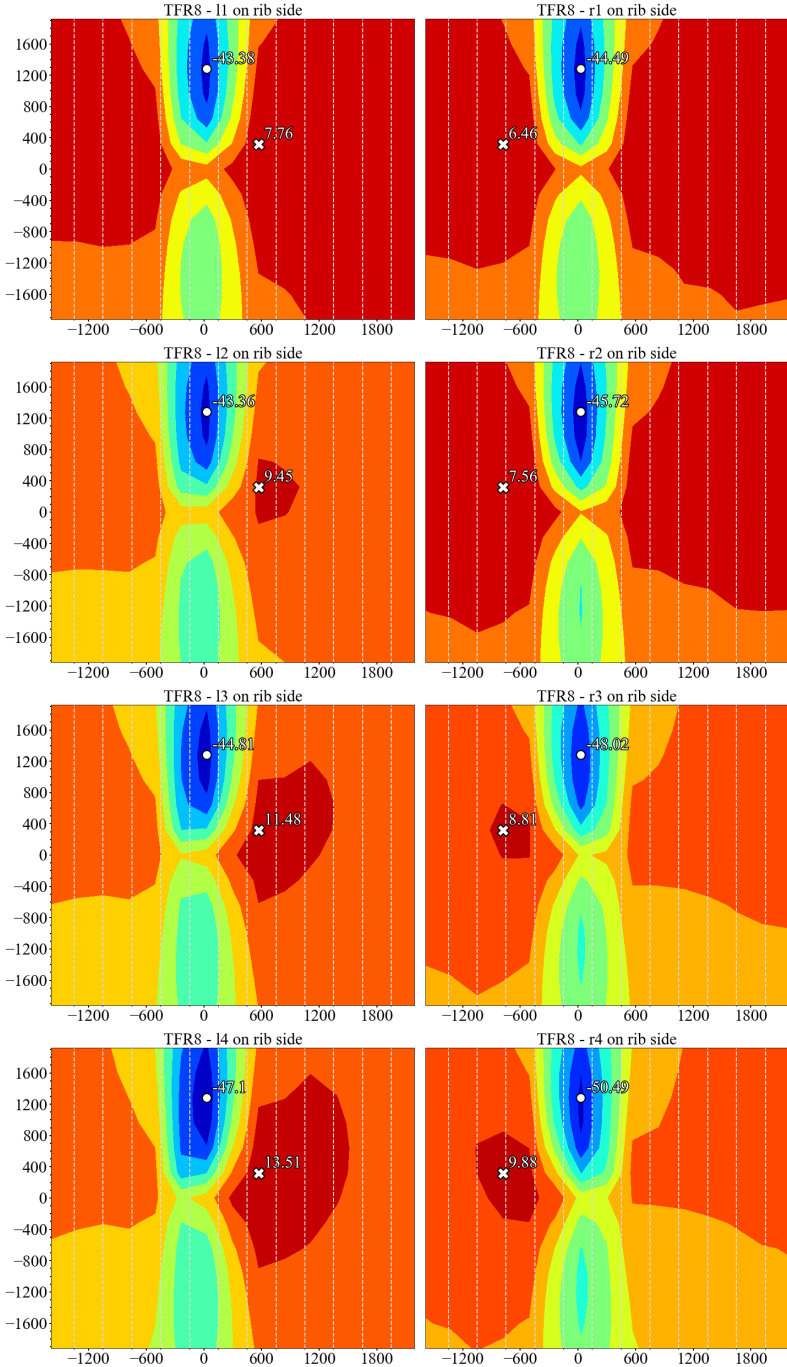


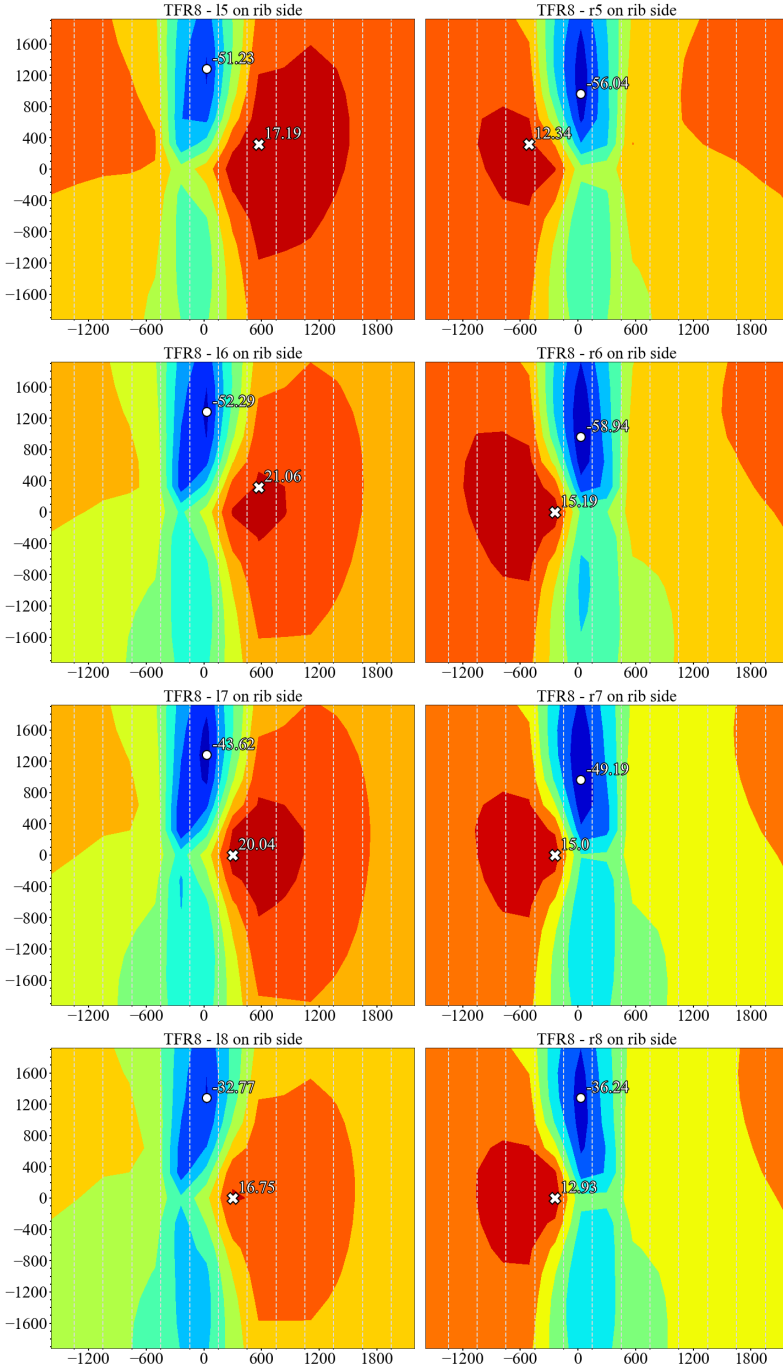


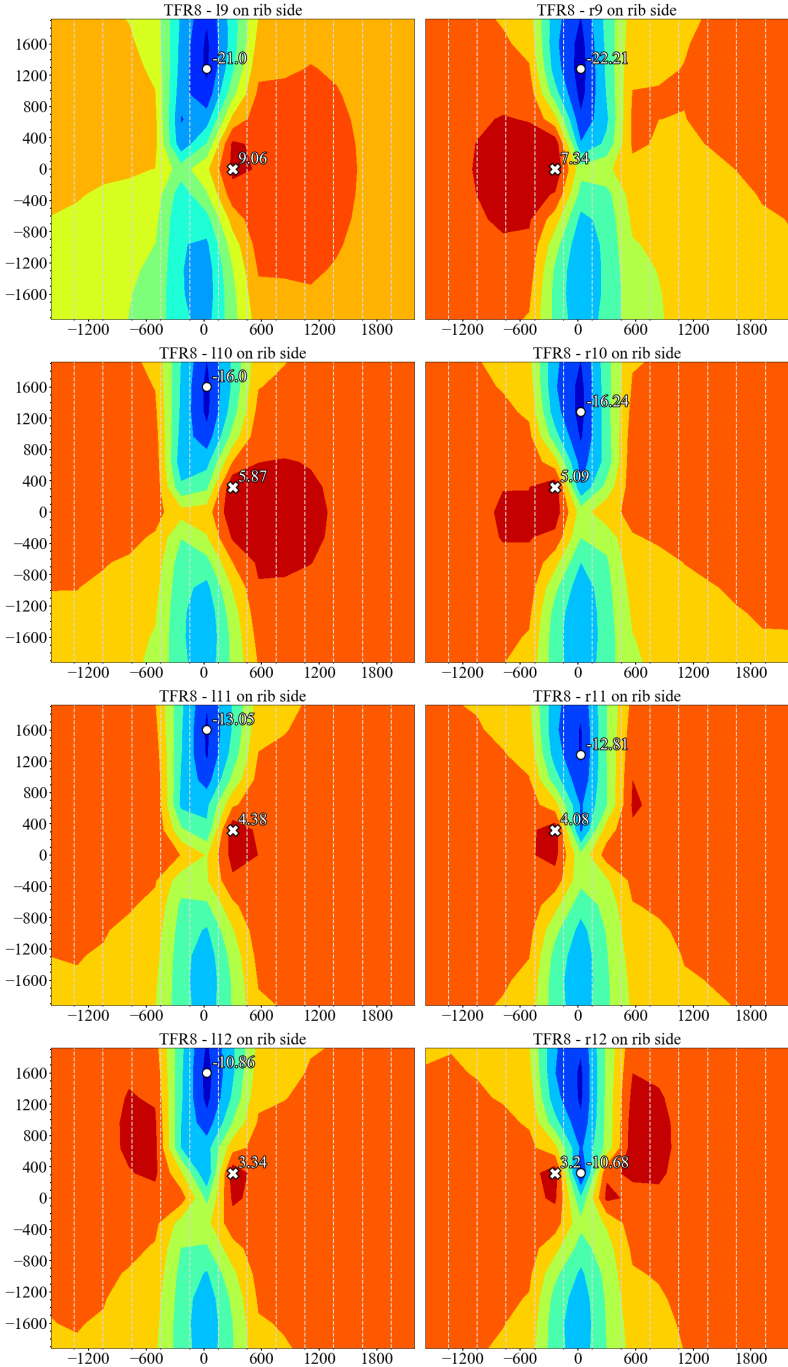


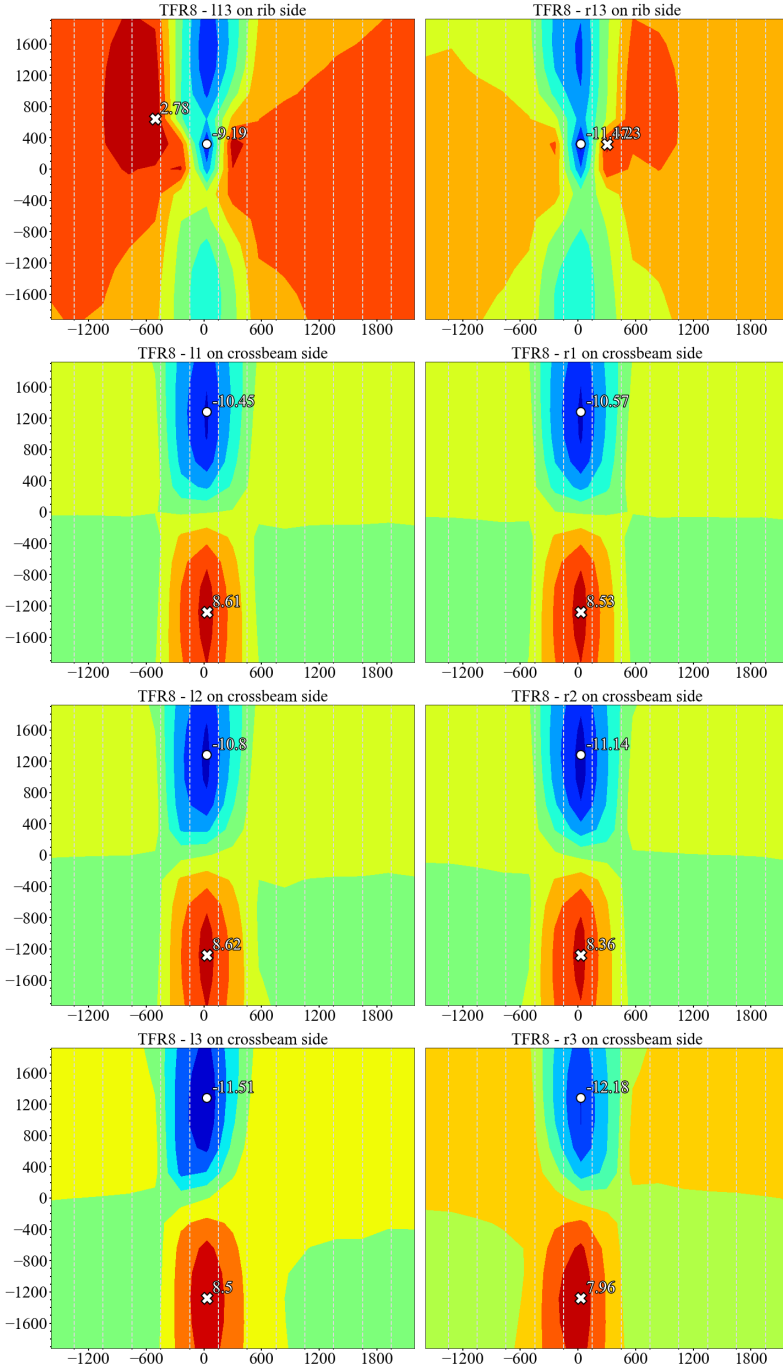


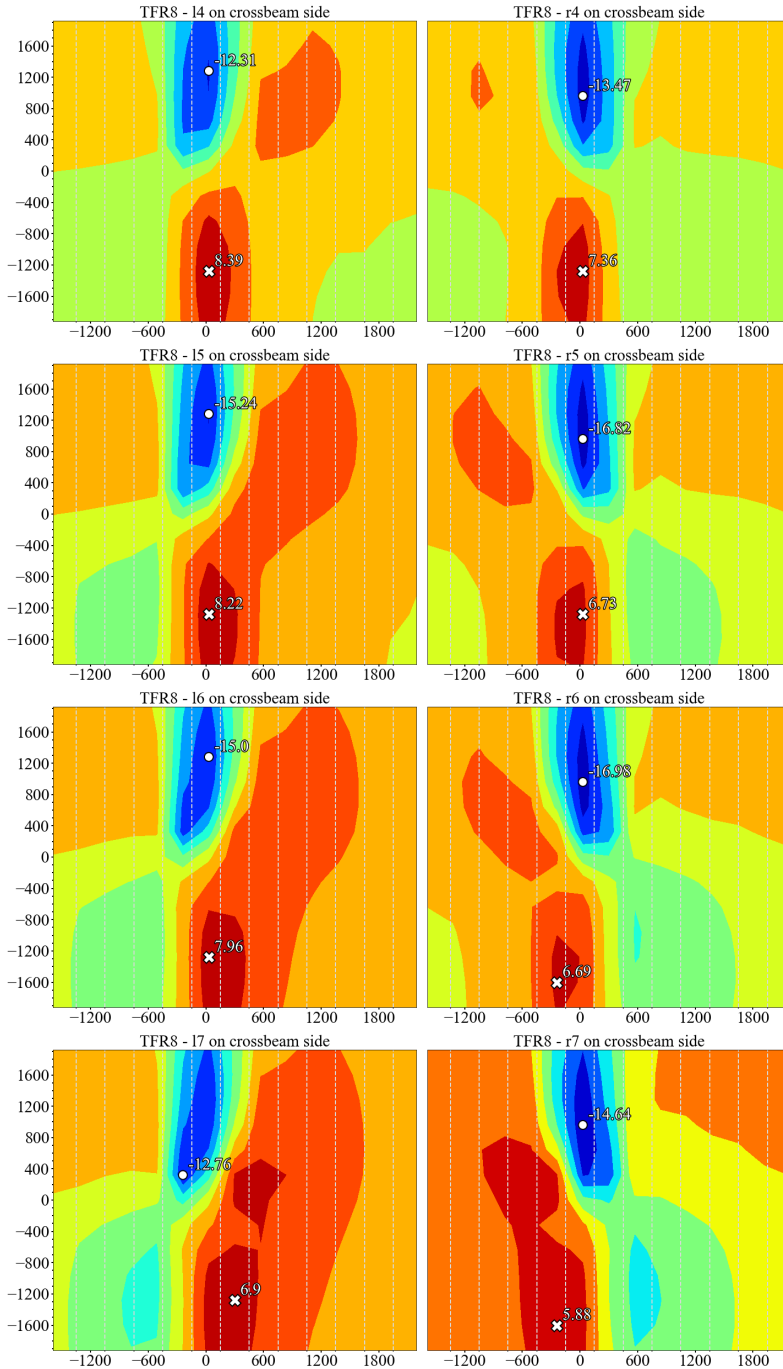


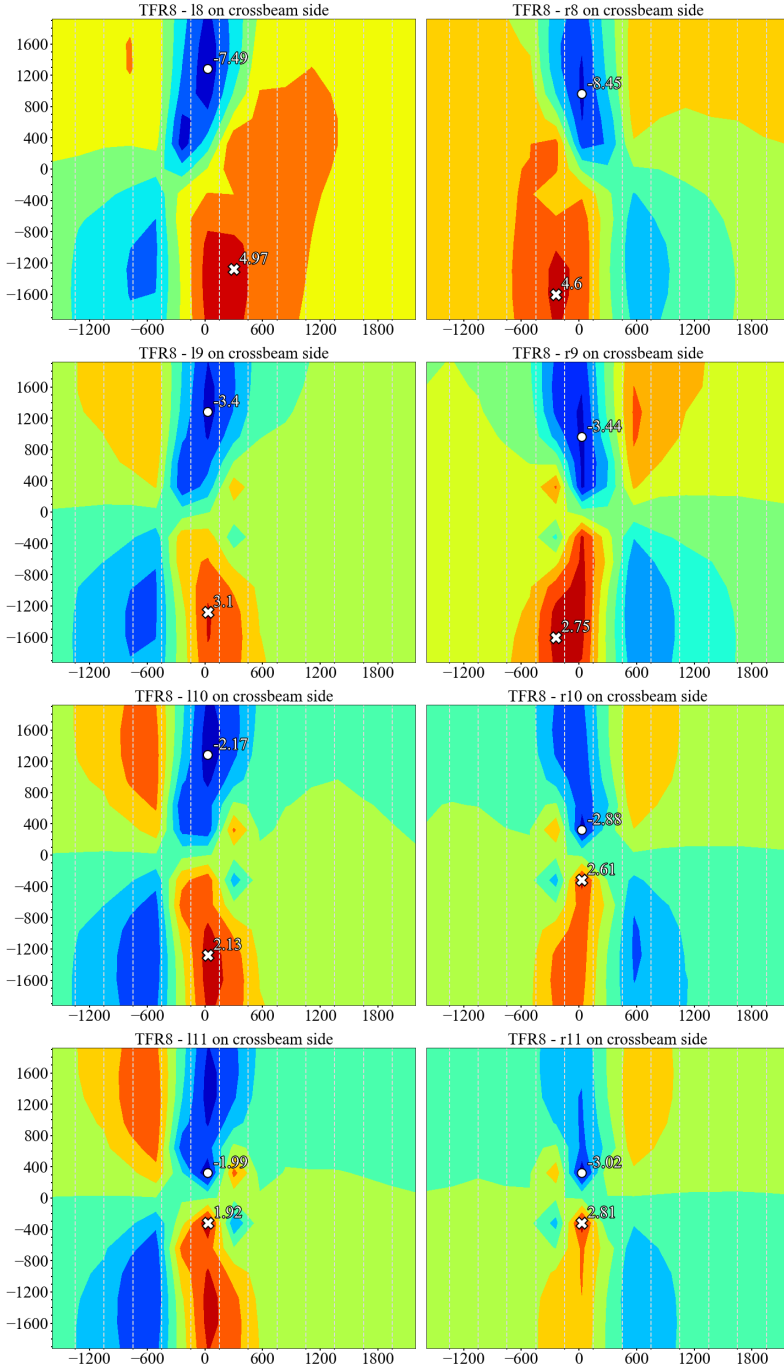


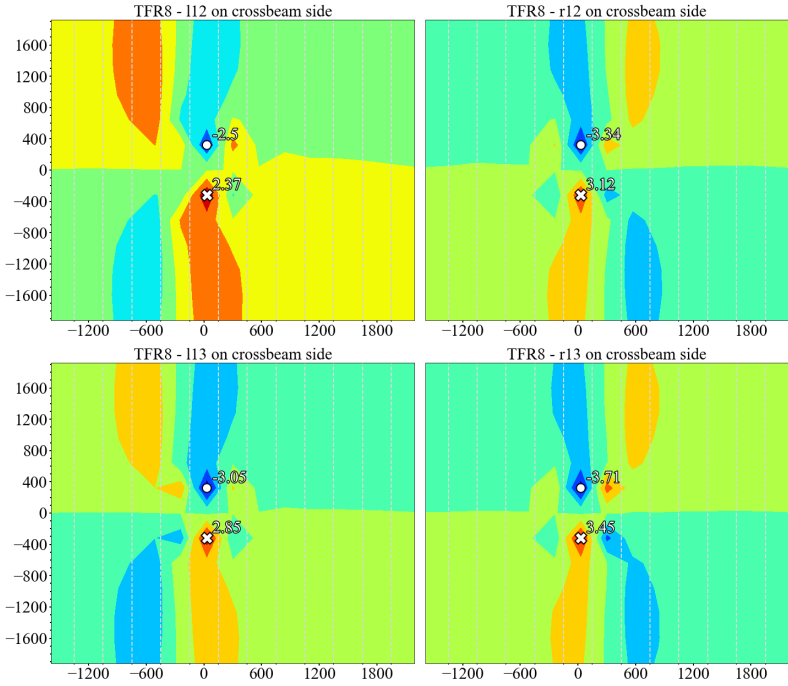












References

- AASHTO (2012). *AASHTO LRFD bridge*. American Association of State Highway and Transportation Officials, Washington, DC.
- Abdelbaset, H., Cheng, B., Tian, L., Li, H. T. & Zhang, Q. H. (2020). Reduce hot spot stresses in welded connections of orthotropic steel bridge decks by using UHPC layer: Experimental and numerical investigation. *Eng. Struct.*, 220(June):110988.
- AISC (1963). *Design Manual for Orthotropic Steel Plate Deck Bridges*. American Institute of Steel Construction, New York.
- Alipour, M., Harris, D. K., Barnes, L. E., Ozbulut, O. E. & Carroll, J. (2017). Load-capacity rating of bridge populations through machine learning: application of decision trees and random forests. *J. Bridg. Eng.*, 22(10):04017076.
- ANSYS Inc. (2007). *ANSYS advanced analysis techniques guide*. November.
- Aygül, M., Al-Emrani, M. & Urushadze, S. (2012). Modelling and fatigue life assessment of orthotropic bridge deck details using FEM. *Int. J. Fatigue*, 40:129–142.
- Baandrup, M., Noe Poulsen, P., Forbes Olesen, J. & Polk, H. (2019). Parametric optimization of orthotropic girders in a cable-Supported Bridge. *J. Bridg. Eng.*, 24(12):04019118.
- Battista, R. C., Pfeil, M. S. & Carvalho, E. M. (2008). Fatigue life estimates for a slender orthotropic steel deck. *J. Constr. Steel Res.*, 64(1):134–143.
- Beghini, M., Bertini, L. & Fontanari, V. (1997). Fatigue life evaluation by weight functions for orthotropic bridge decks. *Theor. Appl. Fract. Mech.*, 28(1):41–50.

References

- Boeters, T. (2017). *Concrete overlay of movable steel orthotropic bridges*. Ph.D. thesis, Delft University of Technology.
- Buckland, P. G. (2004). Four decades of experience with orthotropic decks. In *2004 Orthotropic Bridg. Conf.* Sacramento, California, USA.
- Buitelaar, P., Braam, C. R. & Kaptijn, N. . (2004). Reinforced high performance concrete overlay system for steel bridges. In *2004 Orthotropic Bridg. Conf.* Sacramento, California, USA.
- CEN (2003). *Eurocode 1: Actions on Structures - Part 2: Traffic loads on bridges*.
- CEN (2005). *Eurocode 3: Design of steel structures - Part 1-9: Fatigue*.
- CEN (2006). *Eurocode 3: Design of steel structures - Part 2: Steel bridges*.
- Chen, B., Chen, Z., Xie, X. & Ye, X. (2020). Fatigue performance evaluation for an orthotropic steel bridge deck based on field hotspot stress measurements. *J. Test. Eval.*, 48(2):1175–1187.
- Chen, S., Huang, Y., Gu, P. & Wang, J. Y. (2019a). Experimental study on fatigue performance of UHPC-orthotropic steel composite deck. *Thin-Walled Struct.*, 142(May):1–18.
- Chen, Y., Lv, P. & Li, D. (2019b). Research on fatigue strength for weld structure details of deck with U-rib and diaphragm in orthotropic steel bridge deck. *Metals (Basel)*, 9(5).
- Chen, Z., Li, C. & Ke, L. (2016). Fatigue cracks and stress amplitude analysis of orthotropic steel deck in a suspension bridge. *Adv. Eng. Res.*, 63(Icsee):343–347.
- Cheng, B., Cao, X., Ye, X., Cao, Y. & Teng, N. (2019). Stringer longitudinal bending-induced fatigue failure of stringer-to-floor beam welded connections in orthotropic steel railway bridge decks. *J. Bridg. Eng.*, 24(6):04019055.
- Choi, J. H. & Kim, D. H. (2008). Stress characteristics and fatigue crack behaviour of the longitudinal rib-to-cross beam joints in an orthotropic steel deck. *Adv. Struct. Eng.*, 11(2):189–198.
- Connor, R., Fisher, J., Gatti, W., Gopalaratnam, V., Kozy, B., Leshko, B., McQuaid, D. L., Medlock, R., Mertz, D., Murphy, T., Paterson, D., Sorensen, O. & Yadlosky, J. (2012). *Manual for Design, Construction, and Maintenance of Orthotropic Steel Deck Bridges*. Federal Highway Administration.

-
- Connor, R. J. (2004). Influence of cutout geometry on stresses at welded rib-to-diaphragm connections in steel orthotropic bridge decks. *Transp. Res. Rec.*, (1892):78–87.
- Connor, R. J. & Fisher, J. W. (2005). Identifying effective and ineffective retrofits for fatigue cracking in steel bridges using field instrumentation. *Proc. Struct. Congr. Expo.*, 11(6):107–115.
- Connor, R. J. & Fisher, J. W. (2006). Consistent approach to calculating stresses for fatigue design of welded rib-to-web connections in steel orthotropic bridge decks. *J. Bridg. Eng.*, 11(5):517–525.
- Cui, C., Xu, Y. L., Zhang, Q. H. & Wang, F. Y. (2020). Vehicle-induced dynamic stress analysis of orthotropic steel decks of cable-stayed bridges. *Struct. Infrastruct. Eng.*, 16(8):1067–1081.
- Cui, C., Zhang, Q., Bao, Y., Bu, Y. & Ye, Z. (2018). Fatigue Damage Evaluation of Orthotropic Steel Deck Considering Weld Residual Stress Relaxation Based on Continuum Damage Mechanics. *J. Bridg. Eng.*, 23(10):04018073.
- D’Angelo, L. & Nussbaumer, A. (2017). Estimation of fatigue S-N curves of welded joints using advanced probabilistic approach. *Int. J. Fatigue*, 97:98–113.
- De Corte, W. (2009). Parametric study of floorbeam cutouts for orthotropic bridge decks to determine shape factors. *Bridg. Struct.*, 5(2-3):75–85.
- De Corte, W., Delesie, C. & Van Bogaert, P. (2007). Examination of local stresses in relation to fatigue failure at the rib to floorbeam joint of orthotropic plated bridge decks. *Bridg. Struct.*, 3(3-4):183–191.
- De Corte, W. & Jansseune, A. (2015). Review of FE-based fatigue evaluation methods for the rib to floorbeam welds in orthotropic bridge decks. *Key Eng. Mater.*, 627:337–340.
- De Corte, W. & Van Bogaert, P. (2006). The effect of shear deformations in floorbeams on the moment distribution in orthotropic plated bridge decks. *J. Constr. Steel Res.*, 62(10):1007–1015.
- De Corte, W. & Van Bogaert, P. (2007). An evaluation of the use of fracture mechanics techniques for the design of orthotropic decks. *Key Eng. Mater.*, 348-349:285–288.
- De Freitas, S. T., Kolstein, H. & Bijlaard, F. (2013). Lightweight reinforcement systems for fatigue-cracked orthotropic bridge decks. *Struct. Eng. Int. J. Int. Assoc. Bridg. Struct. Eng.*, 23(4):458–467.

References

- de Jong, F. (2004). Overview fatigue phenomenon in orthotropic bridge decks in the Netherlands. In *2004 Orthotropic Bridg. Conf.*, pp. 489–512. Sacarmento, California, USA.
- de Jong, F. (2007). *Renovation techniques for fatigue cracked orthotropic steel bridge decks*. Ph.D. thesis, Delft University of Technology.
- Delesie, C. & Van Bogaert, P. (2011). Experimental and numerical simulation of stress concentrations in orthotropic bridge decks induced by stiffener distortion. In *Eurosteel 2011*. Budapest, Hungary.
- Dieng, L., Marchand, P., Gomes, F., Tessier, C. & Toutlemonde, F. (2013). Use of UHPFRC overlay to reduce stresses in orthotropic steel decks. *J. Constr. Steel Res.*, 89:30–41.
- Fu, Z., Ji, B., Kong, X. & Chen, X. (2018). Effects of Hammer Peening on Fatigue Performance of Roof and U-Rib Welds in Orthotropic Steel Bridge Decks. *J. Mater. Civ. Eng.*, 30(11):04018306.
- Haagensen, P. J. & Maddox, S. J. (2006). *IIW Recommendations on Post Weld Improvement of Steel and Aluminium*.
- Haibach, E. & Plasil, E. (1983). Untersuchungen zur betriebsfestigkeit von stahlleichtfahrbahnen mit trapezhohlstreifen im eisenbahnbrueckenbau. *Stahlbau*, 52(9):269–74.
- Heng, J., Zheng, K., Kaewunruen, S. & Baniotopoulos, C. (2019a). Stochastic traffic-based fatigue life assessment of rib-to-deck welding joints in orthotropic steel decks with thickened edge U-ribs. *Appl. Sci.*, 9(13).
- Heng, J., Zheng, K., Kaewunruen, S., Zhu, J. & Baniotopoulos, C. (2019b). Dynamic Bayesian network-based system-level evaluation on fatigue reliability of orthotropic steel decks. *Eng. Fail. Anal.*, 105(June):1212–1228.
- Hobbacher, A. F. (2019). *Recommendations for Fatigue Design of Welded Joints and Components*. Springer, Villepinte, France, second edi edition.
- Huang, W., Pei, M., Liu, X., Yan, C. & Wei, Y. (2020). Nonlinear Optimization of Orthotropic Steel Deck System Based on Response Surface Methodology. *Research*, 2020:1–22.
- Huang, Y., Zhang, Q., Bao, Y. & Bu, Y. (2019a). Fatigue assessment of longitudinal rib-to-crossbeam welded joints in orthotropic steel bridge decks. *J. Constr. Steel Res.*, 159:53–66.
- Huang, Y., Zhang, Q., Bao, Y. & Bu, Y. (2019b). Fatigue assessment of longitudinal rib-to-crossbeam welded joints in orthotropic steel bridge decks. *J. Constr. Steel Res.*, 159:53–66.

-
- Jiang, X., Yuan, Y., Wu, C. & Luo, C. (2017). Fatigue life assessment of orthotropic steel deck with UHPC pavement. *J. Eng. (United Kingdom)*, 2017.
- Kato, K., Hanji, T., Tateishi, K., Choi, S. M. & Hirayama, S. (2013). Local stress behavior at closed rib to crossbeam connections in orthotropic steel bridge decks. *EASEC 2013*.
- Kitner, K. J. (2016). A study of manufacturable rib-to-floor beam connections in steel orthotropic bridge decks. Technical report, Lehigh University.
- Kolstein, M. H. (2009). *Fatigue classification of welded joints in orthotropic steel bridge decks*. Ph.D. thesis, Delft University of Technology.
- Kozy, B. M., Connor, R. J., Paterson, D. & Mertz, D. R. (2011). Proposed revisions to AASHTO-LRFD bridge design specifications for orthotropic steel deck bridges. *J. Bridg. Eng.*, 16(6):759–767.
- Ladinek, M., Niederwanger, A. & Lang, R. (2018a). An individual fatigue assessment approach considering real notch strains and local hardness applied to welded joints. *J. Constr. Steel Res.*, 148:314–325.
- Ladinek, M., Niederwanger, A., Lang, R., Schmid, J., Timmers, R. & Lener, G. (2018b). The strain-life approach applied to welded joints: Considering the real weld geometry. *J. Constr. Steel Res.*, 148:180–188.
- Lee, Y.-L. (2005). *Fatigue testing and analysis: Theory and Practice*. Elsevier Inc.
- Leendertz, J. (2008). *Fatigue Behaviour of Closed Stiffener to Crossbeam Connections in Orthotropic Steel Bridge Decks*. Ph.D. thesis, Delft University of Technology.
- Leonetti, D., Maljaars, J. & Snijder, H. H. (2020). Probabilistic fatigue resistance model for steel welded details under variable amplitude loading – Inference and uncertainty estimation. *Int. J. Fatigue*, 135:105515.
- Li, D., Zhang, C. & Lu, P. (2020). Fatigue property and improvement of a rounded welding region between the diaphragm plate and closed rib of an orthotropic steel bridge deck. *Metals (Basel)*, 10(2).
- Li, H. & Wu, G. (2020). Fatigue evaluation of steel bridge details integrating multi-scale dynamic analysis of coupled train-track-bridge system and fracture mechanics. *Appl. Sci.*, 10(9).
- Liu, R., Wang, B. & Liu, Y. (2015). Distortion induced fatigue of deck plate at rib intersection with diaphragm in orthotropic steel deck. *Int. J. Steel Struct.*, 15(3):623–632.

References

- Lu, N., Noori, M. & Liu, Y. (2017). Fatigue reliability assessment of welded steel bridge decks under stochastic truck loads via machine learning. *J. Bridg. Eng.*, 22(1):04016105.
- Lyse, I. & Madsen, I. (1938). Structural behavior of battle-deck floor systems. Technical report, Lehigh University.
- Mangus, A. R. (2015). Steel orthotropic deck systems for short spans less than 140-ft [42.672 m] of North America. Technical Report March.
- Marks, J. (2018). Fatigue investigation of slit rib-to-floor beam connections in steel orthotropic bridge decks. Technical Report May, Lehigh University.
- Medani, T. O. (2006). *Design principles of surfacings on orthotropic steel bridge decks*. Ph.D. thesis, Delft University of Technology.
- Mukherjee, S. (2016). *Laboratory fatigue evaluation of a full scale steel orthotropic bridge deck with round bottom ribs and fitted floor beams*. Ph.D. thesis, Lehigh University.
- Nagy, W. (2017). *Fatigue assessment of orthotropic steel decks based on fracture mechanics*. Ph.D. thesis, Ghent University.
- Nagy, W., Schotte, K., Van Bogaert, P. & De Backer, H. (2016). Fatigue strength application of fracture mechanics to orthotropic steel decks. *Adv. Struct. Eng.*, 19(11):1696–1709.
- Nagy, W., Van Bogaert, P. & De Backer, H. (2015). LEM based fatigue design for welded connections in orthotropic steel bridge decks. *Procedia Eng.*, 133:758–769.
- Nykänen, T., Mettänen, H., Björk, T. & Ahola, A. (2017). Fatigue assessment of welded joints under variable amplitude loading using a novel notch stress approach. *Int. J. Fatigue*, 101:177–191.
- Pipinato, A. (2016). *Innovative bridge design handbook*. Elsevier Inc.
- Poutiainen, I., Tanskanen, P. & Marquis, G. (2004). Finite element methods for structural hot spot stress determination - A comparison of procedures. *Int. J. Fatigue*, 26(11):1147–1157.
- S Chatterjee, P. (1992). Strengthening and refurbishment of Severn Crossing Part 1: introduction. In *Proc. Inst. Civ. Eng. Struct. Build.*, volume 94, pp. 1–5.
- Saunders, J., Chen, Y., Marks, J., Hodgson, I., Sause, R. & Marks, J. (2019). Fatigue resistant rib-to-floor beam connections for orthotropic steel decks. Technical report, Lehigh University.

-
- Shao, X. & Cao, J. (2018). Fatigue assessment of steel-UHPC lightweight composite deck based on multiscale FE analysis: Case study. *J. Bridg. Eng.*, 23(1):05017015.
- Shi, Z., Yang, S., Pu, Q. & Zhang, Y. (2019). Fatigue performance of orthotropic steel decks in long-span cable-stayed steel-box girder railway bridges. *J. Bridg. Eng.*, 24(5):04019035.
- Sim, H.-B., Uang, C.-M. & Sikorsky, C. (2009). Effects of fabrication procedures on fatigue resistance of welded joints in steel orthotropic decks. *J. Bridg. Eng.*, 14(5):366–373.
- Siwowski, T., Kulpa, M. & Janas, L. (2019). Remaining fatigue life prediction of welded details in an orthotropic steel bridge deck. *J. Bridg. Eng.*, 24(12):05019013.
- Su, L., Wang, S., Gao, Y., Liu, J. & Shao, X. (2020). In situ experimental study on the behavior of UHPC composite orthotropic steel bridge deck. *Materials (Basel)*, 13(1):1–13.
- Su, Q., Dai, C. & Xu, C. (2018). Full-scale experimental study on the negative flexural behavior of orthotropic steel–concrete composite bridge deck. *J. Bridg. Eng.*, 23(12):04018097.
- Takabatake, H. (2018). *Simplified analytical methods of elastic plates*. Springer.
- Tang, M. C. (2011). A new concept of orthotropic steel bridge deck. *Struct. Infrastruct. Eng.*, 7(7-8):587–595.
- Teixeira de Freitas, S. (2012). *Steel plate reinforcement of orthotropic bridge decks*. Ph.D. thesis, Delft University of Technology.
- Teixeira de Freitas, S., Kolstein, H. & Bijlaard, F. (2017). Fatigue assessment of full-scale retrofitted orthotropic bridge decks. *J. Bridg. Eng.*, 22(11):04017092.
- Tsakopoulos, P. A. & Fisher, J. W. (2002). Fatigue resistance investigation for the orthotropic deck on the Bronx-Whitestone bridge. Technical Report 02, Lehigh University.
- Tsakopoulos, P. A. & Fisher, J. W. (2005). Full-scale fatigue tests of steel orthotropic deck panel for the Bronx-Whitestone Bridge rehabilitation. *Bridg. Struct.*, 1(1):55–66.
- Ugural, A. C. & Fenster, S. K. (2012). *Advanced mechanics of materials and applied elasticity*. Pearson Education, fifth edition.

References

- Van Es, S. H., Kolstein, M. H., Pijpers, R. J. & Bijlaard, F. S. (2013). TIG-dressing of high strength steel butt welded connections - Part 1: Weld toe geometry and local hardness. *Procedia Eng.*, 66:216–225.
- Walter, R. (2005). *Cement-based overlay for orthotropic steel bridge decks: a multi-scale modeling approach*. Ph.D. thesis, Technical University of Denmark.
- Wang, B. (2014). Fatigue assessment of the diaphragm-to-rib welded connection in orthotropic steel deck using effective notch stress approach. *J. Fail. Anal. Prev.*, 15(1):65–73.
- Wang, B. (2017). *A multiscale study on fatigue mechanism and life estimation on welded joints of orthotropic steel decks*. Ph.D. thesis, Ghent University.
- Wang, B., De Backer, H., Zhou, X. Y. & Chen, A. (2020). Two-stage crack growth-based fatigue damage evaluation of orthotropic steel decks considering vehicle overload. *Struct. Infrastruct. Eng.*, 0(0):1–14.
- Wang, C., Zhai, M., Duan, L. & Wang, Y. (2018a). Cold reinforcement and evaluation of steel bridges with fatigue cracks. *J. Bridg. Eng.*, 23(4):04018014.
- Wang, Q. D., Ji, B. H. & Fu, Z. Q. (2018b). Fatigue performance of hammer-Peened diaphragm-to-rib welds in orthotropic steel decks. In *IABMAS 2018*, pp. 528–533.
- Wang, Y., Fu, Z., Ge, H., Ji, B. & Hayakawa, N. (2019a). Cracking reasons and features of fatigue details in the diaphragm of curved steel box girder. *Eng. Struct.*, 201(March):109767.
- Wang, Y., Wang, Z. & Zheng, Y. (2019b). Analysis of fatigue crack propagation of an orthotropic bridge deck based on the extended finite element method. *Adv. Civ. Eng.*, 2019:80–90.
- Weber, C. (2012). *“Leichtbau - eine Forderung unserer Zeit. Anregungen für den Hoch- und Brückenbau“*. Zur Einführung baukonstruktiver Prinzipien in den 1930er und 1940er Jahren. Von Fritz Leonhardt, volume 81.
- Wolchuk, R. (1990). Lessons from weld cracks in orthotropic decks on three european bridges. *J. Struct. Eng.*, 116(1):75–84.
- Wolchuk, R. (2004). Orthotropic decks with long rib spans. In *2004 Orthotropic Bridg. Conf.*, pp. 762–772. Sacramento, California, USA.
- Wolchuk, R. (2014). Empirical Design Rules for Effective Utilization of Orthotropic Decks. *J. Bridg. Eng.*, 19(2):152–158.

-
- Wu, Z., Zheng, K., Cui, Y. & Feng, Y. (2010). Study on detailed stresses of crossbeam web cutout for steel orthotropic deck. *2010 Int. Conf. Futur. Inf. Technol. Manag. Eng. FITME 2010*, 2:483–486.
- Xiao, Z. & Yamada, K. (2004). A method of determining geometric stress for fatigue strength evaluation of steel welded joints. *Int. J. Fatigue*, 26(12):1277–1293.
- Yan, F., Chen, W. & Lin, Z. (2016). Prediction of fatigue life of welded details in cable-stayed orthotropic steel deck bridges. *Eng. Struct.*, 127:344–358.
- Yao, Y., Ji, B., Ye, Z., Fu, Z. & Zhu, Q. (2020). Prediction for key damaged parts in steel bridge decks based on the stress influence area. *Structures*, 26(1):745–754.
- Yokozeki, K. (2017). *High fatigue resistant orthotropic steel bridge decks*. Ph.D. thesis, Tokyo City University.
- Yokozeki, K. & Miki, C. (2016). Fatigue evaluation for longitudinal-to-transverse rib connection of orthotropic steel deck by using structural hot spot stress. *Weld. World*, 60(1):83–92.
- Yokozeki, K. & Miki, C. (2017). Fatigue assessment of various types of longitudinal-to-transverse rib connection in orthotropic steel decks. *Weld. World*, 61(3):539–550.
- Zhang, H., Liu, Y. & Deng, Y. (2020a). Fatigue crack assessment for orthotropic steel deck based on compound poisson process. *J. Bridg. Eng.*, 25(8):04020057.
- Zhang, Q., Cui, C., Bu, Y., Liu, Y. & Ye, H. (2015). Fatigue tests and fatigue assessment approaches for rib-to-diaphragm in steel orthotropic decks. *J. Constr. Steel Res.*, 114:110–118.
- Zhang, Q., Liu, Y., Bao, Y., Jia, D., Bu, Y. & Li, Q. (2017). Fatigue performance of orthotropic steel-concrete composite deck with large-size longitudinal U-shaped ribs. *Eng. Struct.*, 150:864–874.
- Zhang, X., Li, X., Liu, R., Hao, C. & Cao, Z. (2020b). Dynamic properties of a steel-UHPC composite deck with large U-ribs: Experimental measurement and numerical analysis. *Eng. Struct.*, 213(April).
- Zhi, Y., Wang, Y. X., Sun, H. B. & Ji, B. H. (2018). Fatigue stress analysis of diaphragm-U-rib welding joints and local optimization. In *IABMAS 2018*, pp. 534–540.

References

- Zhou, H., Shi, G., Wang, Y., Chen, H. & De Roeck, G. (2016a). Fatigue evaluation of a composite railway bridge based on fracture mechanics through global-local dynamic analysis. *J. Constr. Steel Res.*, 122:1–13.
- Zhou, H., Wen, J., Wang, Z., Zhang, Y. & Du, X. (2016b). Fatigue crack initiation prediction of cope hole details in orthotropic steel deck using the theory of critical distances. *Fatigue Fract. Eng. Mater. Struct.*, 39(9):1051–1066.
- Zhu, A., Li, M., Zhu, H., Xu, G., Xiao, H. & Ge, H. (2018a). Fatigue behaviour of orthotropic steel bridge decks with inner bulkheads. *J. Constr. Steel Res.*, 146:63–75.
- Zhu, J., Zhang, W. & Li, X. (2019a). Fatigue damage assessment of orthotropic steel deck using dynamic Bayesian networks. *Int. J. Fatigue*, 118:44–53.
- Zhu, Z. & Xiang, Z. (2019). Fatigue cracking investigation on diaphragm cutout in a self-anchored suspension bridge with orthotropic steel deck. *Struct. Infrastruct. Eng.*, 15(10):1279–1291.
- Zhu, Z., Xiang, Z., Li, J., Huang, Y. & Ruan, S. (2020). Fatigue behavior of orthotropic bridge decks with two types of cutout geometry based on field monitoring and FEM analysis. *Eng. Struct.*, 209:109926.
- Zhu, Z., Xiang, Z. & Zhou, Y. E. (2019b). Fatigue behavior of orthotropic steel bridge stiffened with ultra-high performance concrete layer. *J. Constr. Steel Res.*, 157:132–142.
- Zhu, Z., Yuan, T., Xiang, Z., Huang, Y., Zhou, Y. E. & Shao, X. (2018b). Behavior and fatigue performance of details in an orthotropic steel bridge with UHPC-deck plate composite system under in-Service traffic flows. *J. Bridg. Eng.*, 23(3):04017142.



Orthotropic steel bridge deck.